UNIVERSITY OF CAMBRIDGE
INSTITUTE OF ASTRONOMY

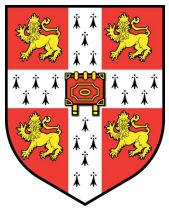

EXOCOMETS AT LARGE ORBITAL RADII AND THEIR INWARD TRANSPORT IN DEBRIS DISCS

SEBASTIÁN MARINO ESTAY
CORPUS CHRISTI COLLEGE

A dissertation submitted to the
University of Cambridge for the
Degree of Doctor of Philosophy
September 24, 2018

SUPERVISORS:
PROF. M. C. WYATT, DR. A. BONSOR AND DR. G. M. KENNEDY

"L'essentiel est invisible pour les yeux"

Le Petit Prince, Antoine de Saint-Exupéry

Dedicado a mi familia, allá en mi querido Chile

DECLARATION OF ORIGINALITY

I, Sebastián Marino Estay, declare that this dissertation entitled Exocomets at large orbital radii and their inward transport in debris discs, solely contains work undertaken while in candidature for a research degree at this University. I confirm that this manuscript has not previously been submitted for a degree or any other qualification at this University or any other institution. This dissertation is the result of my own research and contains no outcomes from other research collaborations. The detailed analysis and written work were done exclusively by me. The length of this Thesis is within the 60,000 words limit set by the Degree Committee of Physics and Chemistry. The following parts of this Thesis have already been published in, or submitted to, academic journals:

- **Chapter 2** was adapted from the published work
  Exocometary gas in the HD 181327 debris ring
  S. Marino, L. Matra, C. Stark, M. C. Wyatt, S. Casassus, G. Kennedy, D. Rodriguez, B. Zuckerman, S. Perez, W. R. F. Dent, M. Kuchner, A. M. Hughes, G. Schneider, A. Steele, A. Roberge, J. Donaldson, and E. Nesvold. MNRAS, 460, 2933, August 2016.

- **Chapter 3** was adapted from the published work
  ALMA observations of the Corvi debris disc: inward scattering of CO-rich exocomets by a chain of 3-30 $M_{\oplus}$ planets?
  S. Marino, M. C. Wyatt, O. Panic, L. Matra, G. M. Kennedy, A. Bonsor, Q. Kral, W. R. F. Dent, G. Duchene, D. Wilner, C. M. Lisse, J.-F. Lestrade, and B. Matthews. MNRAS, 465, 2595, March 2017.

- **Chapter 4** was adapted from the published work
  ALMA observations of the multiplanet system 61 Vir: what lies outside super-Earth systems?
  S. Marino, M. C. Wyatt, G. M. Kennedy, W. Holland, L. Matra, A. Shannon, and R. J. Ivison. MNRAS, 469, 3518, August 2017

- **Chapter 5** was adapted from the published work
  A gap in the planetesimal disc around HD 107146 and asymmetric warm dust emission revealed by ALMA
  S. Marino, J. Carpenter, M. C. Wyatt, M. Booth, S. Casassus, V. Faramaz, V. Guzman, A. M. Hughes, A. Isella, G. M. Kennedy, L. Matrà, L. Ricci and S. Corder. MNRAS, 479, 5423, October 2018.

- **Chapter 6** was adapted from the published work
  Inward scattering of exocomets by a planet chain: exozodi levels, impacts and the scattered disc between the planets
  S. Marino, A. Bonsor, M. C. Wyatt, and Q. Kral. MNRAS, 479, 1651, September 2018.

The co-authors of the publications listed above only contributed indirectly to this dissertation, by their work done during multiple application processes which secured the observational data presented and analysed in this dissertation, and by providing useful feedback on the analysis, results and writing during the drafting process of the above manuscripts.

Sebastián Marino Estay
Cambridge, September 24, 2018

EXOCOMETS AT LARGE ORBITAL RADII AND THEIR INWARD TRANSPORT IN DEBRIS DISCS

Sebastián Marino Estay

SUMMARY

Planetary systems are not only composed of planets, but also of km-sized rocky and icy bodies that are confined within belts similar to the Asteroid and Kuiper belt in the Solar System. Mutual collisions within these belts grind down solids producing dust and giving rise to *debris discs*. Primitive asteroids and comets likely played a major role in the emergence of life on Earth through their delivery of volatiles early in the lifetime of our planet. Cometary impacts, therefore, could be a necessary condition for the emergence of life in exoplanets and the study of debris discs essential to determine the ubiquity of such phenomenon. Moreover, exocometary discs provide a unique window into the origins and outer regions of planetary systems as comets do within our Solar System.

Initially, in Chapter 1 I present an overview of the study of exoplanetary systems, focusing on debris discs. I discuss the basics of planet formation, its connection with debris discs, and how these evolve and interact with planets. I also describe how we observe these discs and probe their volatile component that is locked inside exocomets, and some evidence supporting the idea of exocomets venturing into the inner regions of planetary systems.

Then, in Chapters 2, 3, 4 and 5 I present new ALMA observations of the systems HD 181327, η Corvi, the multiplanet system 61 Vir and HD 107146, which host debris discs. In the first two, I highlight the derivation of the density structure of their discs and the detection of volatiles being released by exocomets; while in the third and fourth I compare the observations with simulations, which I use to set constraints on the underlying planetesimal distribution and mass and orbital distance of unseen planets.

Finally, in Chapter 6 I present result obtained from N-body simulations to study the process of inward transport of comets by a multiplanetary system and how these can deliver material to inner planets and explain the frequently observed exozodiacal dust. To conclude, in Chapter 7 I summarise the results and conclusions of this dissertation and discuss ongoing and future work.

ACKNOWLEDGEMENTS

It is so strange to realise that this episode of my life is close to an end, three enlightening years studying the Universe at a place that I never dreamed I could reach. I would like to first thank Mark, who believed in my skills and supported my case when applying to do a PhD in Cambridge; and made a great job as a supervisor, teaching and guiding me throughout the multiple scientific projects that we worked on. I am also grateful to Grant and Amy, who had always their doors open, ready to provide help, support, advice and feedback, especially during the stressful period of job applications. I also want to thank Simon Casassus as he pushed me and gave me the confidence to apply to Cambridge and start a PhD in Astronomy.

También debo agradecer a mi familia, que desde Chile siempre me apoyaron, hicieron sentir que era poca la distancia y que mi hogar todavía estaba en Chile para cuando quisiera volver. Quiero agradecer especialmente a mi madre, que me inspiró a soñar que es posible romper las barreras que creemos preestablecidas, a mi padre porque me empujó a encontrar mi equilibrio entre los estudios y la vida fuera de la astronomia, y a mi hermano Gabriel porque como hermano mayor me dejó despejados muchos caminos que recorrí. También infinitos agradecimientos al resto de mi familia y amigos en Chile, Víctor, Álvaro, Julián, Tomás, Gato y todos los cabros que me recibían con el mejor de los abrazos cada vez que volví a Chile. Además, me gustaría reconocer a mi profesor de colegio Rafael Cautivo, que me motivó e inspiró a elegir una carrera como Astronomía.

I must also thank Eleanor, who made my life in Cambridge not just magical, but the best years of my life as an adult, and gave me all the love and support that I needed being so far from home. I should also thank the new and amazing friends I have made in Cam, the Khoalition, the Barton road gang, the Corpus FC crew, and the office H27. You all made the last three years of my life an incredible journey to go through, which could not have been better. Special thanks to Luca, who supported me as a friend, taught me so much about debris discs at the start of my PhD, made the stressful moments of going through ALMA deadlines actually fun, and motivated me to start very fruitful collaborations that I hope they continue for a long time.

Sebastián Marino Estay, Cambridge, September 24, 2018

Contents

List of Figures

List of Tables

1

Introduction

Since the discovery of 51 Pegasi b in 1995, the first known extrasolar planet (exoplanet) orbiting around a main-sequence star (Mayor & Queloz, 1995), multiple campaigns have searched for exoplanets around hundreds of thousands of stars seeking to characterize them, understand their frequency and diversity, and ultimately discover if some of these exoplanets could sustain life. Two decades later, thousands of exoplanets have been discovered, using a variety of different techniques such as transits (e.g., Batalha et al., 2013), radial velocities (e.g., Mayor et al., 2011; Wittenmyer et al., 2014), microlensing (e.g., Cassan et al., 2012), and direct imaging (e.g., Kalas et al., 2008; Marois et al., 2008; Lagrange et al., 2009a; Rameau et al., 2013); each one optimised to detect specific types of planets, thus with their own biases (see Figure 1.1). These studies have demonstrated that planetary systems are common, with an overall planet occurrence rate of $\sim 50\%$ (Winn & Fabrycky, 2015), and vastly diverse. For example, transiting and direct imaging surveys have found extreme systems, some of which have multiple low mass planets on orbits smaller than that of Mercury, and others multiple giant planets at tens of astronomical units (au). All these discoveries have shown that our Solar System may not be as unique as we thought in the past.

Planetary systems are nonetheless not just composed of planets, but also of smaller bodies with a wide size distribution, from dwarf planets or asteroids down to the size of dust grains. Our Solar System is the most well known example, with the majority of minor bodies

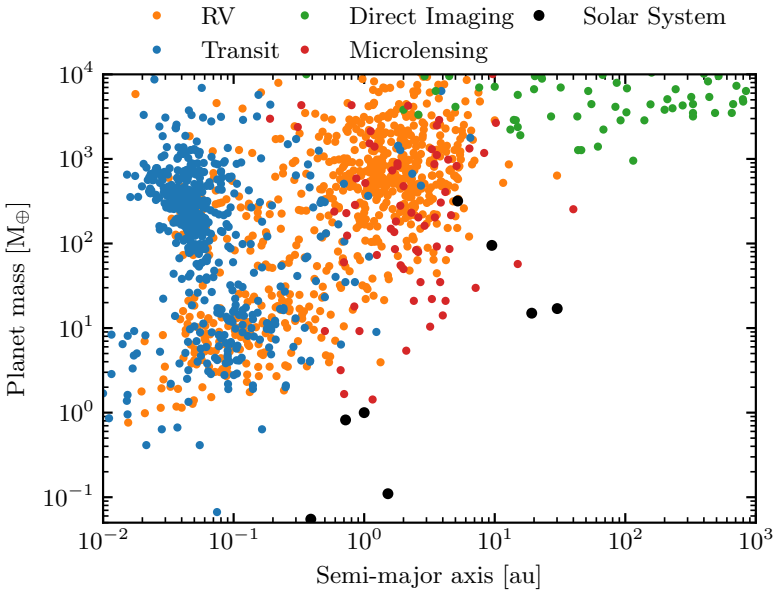

Figure 1.1: Discovered exoplanets by radial velocities (orange), transits (blue), direct imaging (green) and microlensing (red). The data to make this figure was obtained from http://exoplanet.eu.

concentrated in two belts: the asteroid belt spanning 2 to 4 au between the orbits of Mars and Jupiter, and the Kuiper belt located beyond the orbit of Neptune from 30 up to 50 au. Beyond that resides a large reservoir of long period comets that surrounds our Solar System in a shell known as the Oort cloud extending out to thousands of au. These minor bodies are not in a steady state, but undergoing evolution. They can collide, sublimate and even be tidally disrupted, processes that can release and replenish the dust orbiting the Sun. For example, the Zodiacal cloud primarily found within 5 au is composed of dust continually being replenished and released by such mechanisms (Nesvorný et al., 2010). Planetary systems are therefore also expected to be composed of solids on a wide size distribution, with perhaps no clear boundaries between planets, dwarf planets, comets, asteroids and dust. This dissertation focuses on the study of these minor bodies around nearby stars.

How a small fraction of the material that gives form to stars results in a planetary system and our own Solar System, is today a major topic of research and debate. In the next section, I summarise the overall picture that we have today and in my opinion the most important questions that remain to be answered.

1.1 From interstellar μm-sized dust to planets

It is widely accepted that planetary systems (and our own Solar System) must have formed from a circumstellar disc, rich in gas and interstellar dust, formed during the gravitational

collapse of a molecular core and as a consequence of angular momentum conservation. These so-called protoplanetary discs can contain tens to hundreds of Earth masses in the form of dust grains, and enough gas to form multiple gas giant planets (see review by Williams & Cieza, 2011). However, how this actually happens is a matter of debate. Because giant planets such as Jupiter are mostly composed of gas, they must have formed and grown close to their final mass before the protoplanetary disc dispersal. Two main pathways could lead to the formation of gas giants, either through gravitational instabilities and fragmentations during the early evolution of massive circumstellar discs (e.g. Boss, 1997; Boley, 2009), or by the formation of solid cores and subsequent gas accretion (Pollack et al., 1996; Rafikov, 2004; Levison et al., 2010). Terrestrial planet formation, on the other hand, could extend beyond disc dispersal in its final stages, but as well as core accretion it requires the previous formation of km-sized building blocks (planetesimals) from the available solid material in the disc while gas is still present to damp their orbits (Morbidelli et al., 2012).

In order to form these planetesimals, dust must grow at least nine orders of magnitude, from μm- to km-sized bodies before the dispersal of these discs on 3-10 Myr timescales (Ercolano & Pascucci, 2017). Mutual collisions of μm-sized grains are expected to lead to the formation of mm-sized grains (e.g. Birnstiel et al., 2010), and this is observed in discs (e.g. van Boekel et al., 2004; Marino et al., 2015; Tazzari et al., 2016). However, growth beyond a few cm is particularly challenging. This is because mutual collisions of large grains result in either bouncing, fragmentation or erosion (Zsom et al., 2010; Blum & Wurm, 2008), but no net growth. Moreover, once dust grains grow beyond the size of a $\sim$mm, they start to decouple from the gas[1], and start to quickly drift inwards since they feel a drag force due to the sub-Keplerian speed at which the gas orbits the star (Weidenschilling, 1977a). These different barriers must be overcome in order to form planetesimals that can then grow, assisted by gravity, to form planets.

A few mechanisms have been proposed that could lead to planetesimal formation (see review by Blum, 2018). For example, dust grains could grow as fractals composed of monomers that remain sticky and well coupled to the gas, bypassing both the bouncing and radial drift barrier (Kataoka et al., 2013). However, this relies on the assumption of a high stickiness. A second proposed mechanism is that the above mentioned barriers are bypassed through the gravitational collapse of a concentrated cloud of pebbles, a scenario known as streaming instability (Youdin & Goodman, 2005; Johansen et al., 2007; Yang et al., 2017). This requires, however, particular conditions such as *Stokes* numbers[2] of $10^{-3} - 5$ and a high dust-to-gas ratio.

Once planetesimals are formed they can continue growing through mutual collisions in what

[1]The exact size at which grains decouple from the gas depends on the gas densities and grain bulk densities.
[2]The Stoke number is defined as the ratio between the stopping time and orbital period.

is called runaway growth, forming planetary embryos with masses ranging between the mass of the Moon and Mars for typical models at 1 au (Ida & Makino, 1993). After reaching such a mass, they start to dynamically stir the material near their orbits, reducing their collisional cross-section and slowing down their growth. Subsequent growth could either happen by the accretion of pebbles that are strongly affected by gas drag (Johansen & Lacerda, 2010) leading to the formation of a gas giant core or an ice giant planet; or collisions between embryos after disc dispersal (Chambers & Wetherill, 1998) resulting in terrestrial planets. Despite the apparent difficulties in the formation of planetesimals, observations suggest that planet formation might be an efficient process that could happen early on in the protoplanetary disc lifetime, as observations with the *Atacama Large Millimeter/submillimeter Array* (ALMA) of ringed protoplanetary discs suggest (see Figure 1.2).

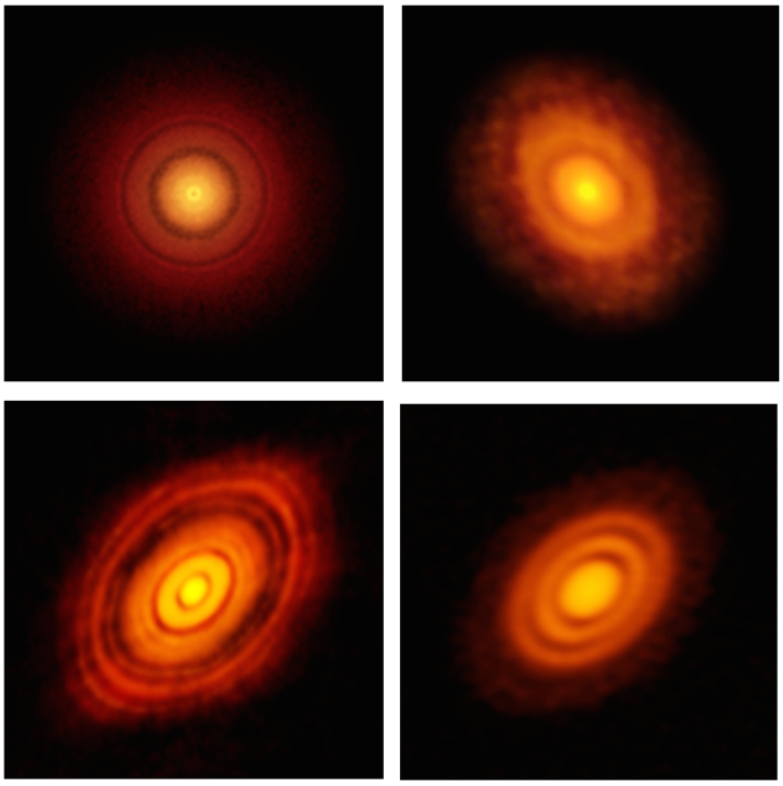

Figure 1.2: ALMA continuum observations of four protoplanetary discs showing evidence of gaps or rings in the dust distribution (Andrews et al., 2016; Cieza et al., 2016; Isella et al., 2016; ALMA Partnership et al., 2015). One potential explanation for these is the presence of forming planets creating gaps in the distribution of dust in the disc (Dipierro et al., 2015). Credit: ESO.

The processes mentioned above do not only only result in planet formation, but also in the formation of planetesimal belts (Lissauer, 1993), similar to the Asteroid or Kuiper belt. After disc dispersal, mutual collisions can grind down these planetesimals if relative velocities are high enough, releasing solids in a wide size distribution (from μm-sized dust grains up to km-sized planetesimals). This triggers a collisional cascade, where solids of a given size are

destroyed by collisions and replaced by fragments of larger bodies, ultimately forming a *debris disc* (e.g., Backman & Paresce, 1993; Krivov et al., 2000; Wyatt et al., 2007b). Debris disc studies therefore provide unique information about the nature of planetesimals, i.e *exoasteroids* or *exocomets*, around mature exoplanetary systems and their connection with planet formation (see reviews by Wyatt, 2008; Krivov, 2010; Hughes et al., 2018).

1.2 Debris disc observations

Given the expected size distribution of solids in a debris disc (see §1.4), the bulk of the cross sectional area is dominated by the bottom of the collisional cascade, i.e. dust. The presence of circumstellar dust around other main sequence stars has been known since the launch of the *Infrared Astronomical Satellite* (IRAS) three decades ago, which found hundreds of nearby stars with infrared excess produced by dust orders of magnitude higher than the Solar System (e.g., Aumann et al., 1984; Oudmaijer et al., 1992; Mannings & Barlow, 1998). Since the dust orbiting a star is short-lived, as it is ground down by collisions and removed by radiation forces (see §1.3.2), these dusty systems must host debris discs.

The dust in these discs can be characterised at different wavelengths, from the optical with the *Hubble Space Telescope* (HST) to the radio with the Very Large Array (VLA), allowing the characterisation of their spectral energy distributions (SEDs). Unresolved discs are generally parametrized with a temperature, T, and a fractional luminosity, $f_{\rm IR} \equiv L_{\rm dust}/L_\star$, which defines the level of emission at all wavelengths. Figure 1.3 shows some model SEDs of a star with different $f_{\rm IR}$ produced by dust at different temperatures. The peak of the disc emission or of the fractional excess, $F_{\nu,\rm dust}/F_{\nu,\star}$, strongly depends on the dust temperature, thus any single wavelength observation searching for debris discs will be biased to detect dust at specific temperatures. Assuming that dust grains behave approximately as *black body* spheres, then their temperature and radial location, $r_{\rm BB}$, are related by

$$T(r) = 278.3 \left(\frac{L_\star}{L_\odot}\right)^{1/4} \left(\frac{r_{\rm BB}}{1\ {\rm au}}\right)^{-1/2}, \tag{1.1}$$

where $L_\star$ is the star luminosity. However, this is only a first order approximation because depending on its composition and size, dust grains can have large albedos or very inefficient emission at infrared wavelengths; thus being at lower or higher temperatures compared to a black body, respectively. Using more realistic dust size distribution and grain optical properties, it is possible to model SEDs with infrared excess, and obtain more accurate estimates of both temperature and the radial distance of dust in debris discs (e.g., Ballering et al., 2014; Kennedy & Wyatt, 2014; Pawellek et al., 2014).

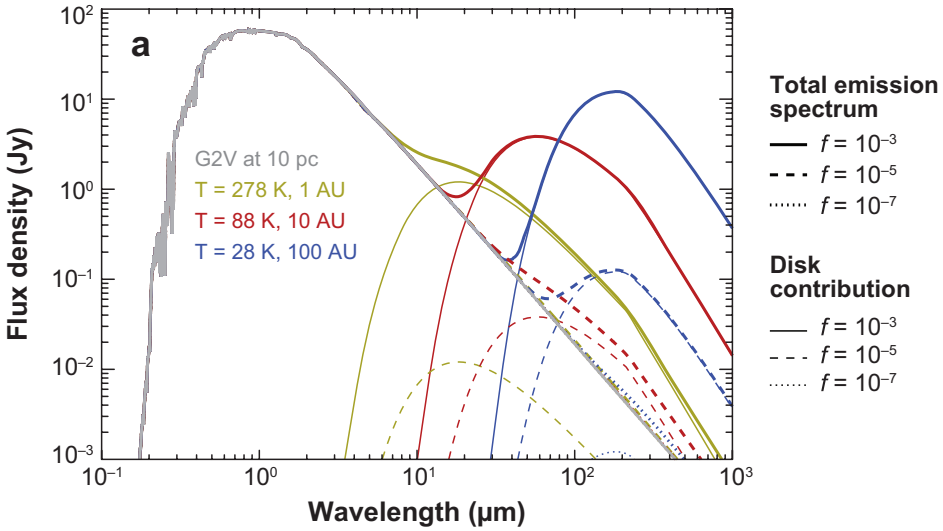

Figure 1.3: Synthetic spectra of a G2V star located at 10 pc and surrounded by circumstellar dust (taken from Wyatt, 2008). The yellow, red and blue lines represent dust located at 1, 10 and 100 au from the star, respectively. The continuous, dashed and dotted lines represent discs with fractional luminosities of 10^{-3}, 10^{-5} and 10^{-7}, respectively.

Most of the systems with known excess show evidence of dust located in narrow belts at tens of au, analogous to the Kuiper belt in the Solar System. Debris disc surveys in the far-infrared (FIR) with *Spitzer* and *Herschel* have shown that these type of discs, i.e. Kuiper belt analogues, are present around at least $\sim 20\%$ of AFGK-type stars (e.g., Su et al., 2006; Hillenbrand et al., 2008; Carpenter et al., 2009a; Eiroa et al., 2013; Chen et al., 2014; Thureau et al., 2014), with the fraction decreasing with stellar age as expected from collisional models (see §1.4). Other surveys in the near- and mid-infrared (NIR and MIR) have searched for warm/hot dust located within a few au, analogous to the asteroid belt or Zodiacal dust in the Solar System. Such surveys have found tens of nearby stars with dust at temperatures higher than 300 K, with an occurrence rate of $\sim 20\%$ around nearby AFGK-type stars (e.g., Absil et al., 2013; Ertel et al., 2014, see §1.6).

1.2.1 From protoplanetary to debris discs

Although both debris and protoplanetary discs are primarily studied based on the dust emission, they correspond to significantly different evolutionary stages in the life of a planetary system. While protoplanetary discs are gas rich and have large amounts of millimetre-sized dust ($30 - 300$ $M_\oplus$, Andrews et al., 2011) which is the result of the grain growth though sticking collisions, debris discs are generally gas poor (see §1.5) with dust masses below $\lesssim 1$ $M_\oplus$. For example, studies at millimetre wavelength have found an abrupt drop in the derived sub-cm dust mass for systems older than ~ 10 Myr (see Figure 1.4), an age

at which protoplanetary discs should have been dispersed (e.g. via viscous evolution and photoevaporation, Alexander et al., 2006; Clarke, 2007)). Moreover, even their dust size distributions inferred from their SEDs differ. In protoplanetary discs it extends from sub-μm sizes up to mm- or cm-sized grains as a result of the grain growth. On the other hand, debris disc SEDs show no evidence of sub-μm grains, traced by the lack of NIR, and have spectral slopes at millimetre wavelengths that indicate the presence of solids much bigger than the observed wavelengths ($\gtrsim 10$ cm).

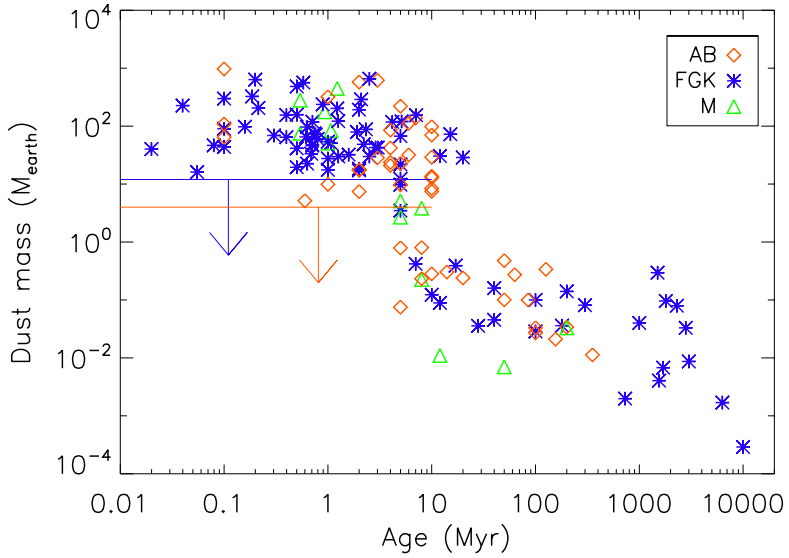

Figure 1.4: Dust mass derived from submillimetre observations towards pre-main sequence and main sequence stars (taken from Panić et al., 2013). Observational upper limits are shown with blue and red arrows for T Tauri stars and Herbig Ae stars, respectively.

It is worth noting that the distinction between protoplanetary and debris discs has become less clear in the recent years due to the development of more sensitive instruments (see Wyatt et al., 2015). First, it is not clear at what age debris discs actually form, i.e. when does secondary dust start being produced by collisions between larger bodies. This could happen either before or after protoplanetary disc dispersal. The population of known massive debris discs could appear at a young age, being coeval to some $\sim 1-5$ Myr old protoplanetary discs, or evolve from some of the massive long lived protoplanetary discs. However, the upper limits of circumstellar dust around young (< 10 Myr) systems in nearby star forming regions are generally higher than the dust masses observed in the massive nearby debris discs (e.g. Ansdell et al., 2016). Because of this, it is impossible to conclude what type of protoplanetary discs form the observed debris disc population. Secondly, there are protoplanetary discs with ages significantly longer than 10 Myr (Scicluna et al., 2014), and a few massive debris discs in young star forming regions definitely younger than 10 Myr (Carpenter et al., 2009b; Riviere-Marichalar et al., 2013). Finally, some young systems with debris disc-like SEDs show significant amounts of gas that could be comparable to protoplanetary discs (see §1.5).

1.3 Dust dynamics

Debris disc observations provide a unique tool to study planetary systems where unseen planets could lie. This is because the total cross sectional area of these dusty discs is generally much greater than of a planet, and thus they are brighter and easier to detect. However, in order to correctly interpret debris disc observations it is fundamental to understand the different factors that can shape the distribution of dust in a system. Although it has been shown that some debris discs have vast amounts of gas (see §1.5), for the majority gas is absent or present at such low densities that its effect is negligible. In such case dust dynamics are only affected by the gravitational field, radiation forces and stellar winds.

1.3.1 Gravitational interactions

In the presence of planets or stellar companions the Keplerian orbits of solids (e.g. dust, planetesimals, etc.) can be dramatically perturbed with dynamics that can appear complex. However, it is possible to simplify the analysis of dynamical interactions by considering them as the sum of three distinct types of interactions (Murray & Dermott, 1999). These are secular interactions that act over long timescales and separations; resonant interactions that act when the ratio between the orbital periods is approximately equal to the ratio of two integers, thus they are localised; and short-period interactions that can become important in close encounters (e.g. scattering). These types of interactions have been subject of multiple studies related to debris discs, predicting a wide variety of disc structures that could be observed (e.g. Mouillet et al., 1997; Wyatt, 2003, 2005, 2006; Nesvold et al., 2013; Pearce & Wyatt, 2014).

1.3.2 Radiation forces

Small dust grains, which dominate the total surface area in a disc and are responsible for the bulk of the infrared excess, can be significantly affected by non-gravitational forces such as radiation pressure and stellar winds. The effect of radiation force is usually parametrized by the ratio between the radiation and gravitational force

$$\beta = \frac{F_{\rm rad}}{F_{\rm grav}} = \left(\frac{\sigma}{m}\right)\left(\frac{L_\star \langle Q_{\rm pr}\rangle}{4\pi c G M_\star}\right), \tag{1.2}$$

where $M_\star$ is the stellar mass and σ, m, and $\langle Q_{\rm pr}\rangle$ are the cross-sectional area, mass and Mie scattering coefficient of a dust grain (averaged over all wavelengths). Hence, grains subject to radiation pressure will experience an effective gravitational force $F_{\rm eff} = F_{\rm grav}(1-\beta)$. Assuming that dust grains are released from much bigger bodies (parent planetesimals) on circular orbits at Keplerian speed (or at velocities with respect to the parent body much

smaller than Keplerian), grains with $\beta \geq 0.5$ will be put on orbits with eccentricities larger than 1 and thus will abandon the system on a short timescale. Therefore, we expect that debris discs will lack dust grains smaller than a characteristic size corresponding approximately to $\beta = 0.5$. Such size is called the blow-out size, $D_{\rm bl}$, and can be written as

$$D_{\rm bl} = 0.8 \left(\frac{L_\star}{L_\odot}\right) \left(\frac{M_\star}{M_\odot}\right)^{-1} \left(\frac{\rho}{2.7 \text{ g cm}^{-3}}\right)^{-1} \mu\text{m}, \tag{1.3}$$

where ρ is the bulk density of dust grains and we have assumed that grains act like black bodies (i.e. $\langle Q_{\rm pr} \rangle = 1$). Slightly bigger grains are quickly lost by destructive collisions in a few orbits if the dust densities are high (generally true for the observed bright debris discs) or they can be lost through Poynting-Robertson (P-R) drag when the densities are low enough, making dust grains spiral inwards until they reach sublimation temperatures or are accreted by the central star (Burns et al., 1979). Therefore, dust grains cannot be primordial or leftovers of the protoplanetary disc phase, they must be rather a product of recent collisions between larger bodies (see Backman & Paresce, 1993). It is worth noting that despite the simple physics defining $D_{\rm bl}$, the minimum grain size inferred from SED modelling of resolved discs, $D_{\rm min}$, does not necessarily match exactly $D_{\rm bl}$ as expected from collisional modelling of discs (Krivov et al., 2006; Thébault & Augereau, 2007; Thébault & Wu, 2008; Krivov et al., 2013). Moreover, the ratio $D_{\rm min}/D_{\rm bl}$ is found to vary systematically with stellar luminosity from about 10 for Solar-type stars to unity for A stars (Pawellek et al., 2014; Pawellek & Krivov, 2015), which could be due to higher dynamical stirring around early type stars or surface energy constraints (Krijt & Kama, 2014).

1.3.3 The implication for multiwavelength observations

Multiwavelength high resolution images of debris discs have revealed a diversity of disc features: ring-like structures (e.g. HR 4796A, Perrin et al., 2015), warps (e.g. β Pic, Heap et al., 2000), gaps or double ring structures (e.g. HD 107146, Ricci et al., 2015a), eccentric rings (e.g. Fomalhaut, Kalas et al., 2005) and clumps (e.g. Vega, Wyatt, 2003). Most of these features can be attributed to the dynamical presence of planets shaping the debris spatial distribution. However, some of these features can vary significantly depending on the wavelength at which they are observed as they trace totally different grain sizes which can have significantly different dynamics as shown above (e.g. Wyatt, 2006; Krivov et al., 2007). For example, optical observations of discs are dominated by light scattered by small grains in the disc. These observations can give insights into the spatial distribution of μm-sized dust grains, near the blow-out size and thus highly affected by radiation pressure (Thébault & Wu, 2008), even displaying in some cases variable features that can be attributed to interaction with stellar winds (e.g., Boccaletti et al., 2015). Additionally, the unknown scattering phase function,

which depends on the size distribution and composition of grains, can result in spurious asymmetries that may look like overdensities, making scattered light observations even harder to analyse. On the other hand, because dust opacities decrease steeply with wavelengths larger than the grain size, dust thermal emission at millimetre wavelengths is dominated by big grains ($\sim 0.1 - 10$ mm), for which radiation forces and the effect of stellar winds are negligible ($\beta \ll 1$). Therefore, mm-sized grains are approximately only affected by the gravitational potential of the system and mutual collisions; and so can be thought of as test particles in the disc that can trace the location of the parent planetesimals and perturbing planets in the system.

1.4 Collisional evolution

After gas is dispersed in young planetary systems, the orbits of minor bodies can be readily excited or *stirred* by planets, either through secular interactions with planets (Mustill & Wyatt, 2009) or through gravitational perturbations caused by the growth of Pluto-sized objects within a planetesimal disc (Kenyon & Bromley, 2008). Such stirring ignites a collisional cascade removing solid mass by grinding down bodies down to μm-sized dust which is subsequently removed by radiation forces. The collisional evolution after disc stirring has been studied in detail through both analytic (Dominik & Decin, 2003; Wyatt et al., 2007a; Löhne et al., 2008; Geiler & Krivov, 2017) and numerical models (Krivov et al., 2006; Thébault & Augereau, 2007). Here, I summarise the analytic approximations from Wyatt et al. (2007a). Later in Chapter 4 I present a numerical prescription to compute such evolution taking into account the more detailed size distribution and strength of solids.

As a first approximation we can assume that a disc is composed of a population of solids that can be described by a power-law size distribution, i.e.

$$N(D) \propto \begin{cases} D^{2-3q} & D_{\rm min} < D < D_{\rm max}, \\ 0 & \text{if not,} \end{cases} \tag{1.4}$$

where q is 11/6 for an infinite collisional cascade (Dohnanyi, 1969). Equation 1.4 implies that if q takes values between 5/3 to 2 and $D_{\rm min} \ll D_{\rm max}$ most of the disc mass will be in the largest solids while the surface area or the total cross section is dominated by the smallest particles. Thus, the total emission or fractional luminosity of a debris disc will generally be a function of the minimum grain size.

In §1.3.2 I showed that dust grains smaller than the blow-out size will be quickly lost from the system and thus we can approximate $D_{\rm min} = D_{\rm bl}$. Larger grains will experience catastrophic collisions grinding down solids to the blow-out size on a longer timescale. It is possible to

estimate the timescale t_c at which a particle of size D_c will experience a catastrophic collision. This can be approximated by the product of the orbital period, $T = \sqrt{r^3/(GM_\star)}$, the ratio of the relative velocity of collisions to the Keplerian velocity ,$f(e, I) = v_{\rm rel}/v_{\rm K}$, and the cross-sectional area of the belt, $A = dr\ r\ 2I$, divided by the cross-sectional area of particles in the belt that can cause a catastrophic collision, $\sigma_c = \sigma_{\rm tot} f_{cc}(D_c)$, i.e.

$$t_c(D_c) = \sqrt{\frac{r^3}{GM_\star}} \frac{r\ dr\ 2I}{\sigma_{\rm tot} f_{cc}(D_c) f(e, I)}, \tag{1.5}$$

where e and I are the mean eccentricity and orbital inclination of particles in the disc. For Rayleigh distributions of e and I, $f(e, I)$ can be approximated by $(1.24e^2 + I^2)^{1/2}$ (Lissauer & Stewart, 1993; Wetherill & Stewart, 1993). While $\sigma_{\rm tot}$ can be estimated almost directly from observations ($\sim 4\pi r^2 f_{\rm IR}$), $f_{cc}(D_c)$ depends on the internal strength of particles which can be a function of the particle size. For example, small particles can be highly bound by electrostatic force. On the other hand, km-sized bodies can be strongly bound by gravity. Typically $f_{cc}(D_c)$ is a function of the size distribution (q) and $X_c = D_{cc}/D_c$, with D_{cc} being the size of the smallest solid that has enough energy to catastrophically destroy a body of size D_c. This will depend on the planetesimal strength or disruption threshold, $Q^\star_{\rm D}$, which can be a function of the particle size. Then, X_c can be approximated by $(2Q^\star_{\rm D}/v^2_{\rm rel})^{1/3}$. Setting $D_c = D_{\rm max}$ and assuming $q = 11/6$ (only valid for a constant $Q^\star_{\rm D}$), $e \approx\ I$ and $X_c \ll 1$, we find (see Wyatt et al., 2007a),

$$f_{cc} = 6.3 \times 10^6 \left(\frac{D_{\rm bl}}{D_c}\right)^{0.5} \left(\frac{r}{1\ {\rm au}}\right)^{-5/6} \left(\frac{Q^\star_{\rm D}}{1\ {\rm J\ kg^{-1}}}\right)^{-5/6} e^{5/3} \left(\frac{M_\star}{M_\odot}\right)^{5/6}, \tag{1.6}$$

finally obtaining

$$t_c = 1.4 \times 10^{-9} \left(\frac{r}{1\ {\rm au}}\right)^{13/3} \left(\frac{dr}{r}\right) \left(\frac{D_c}{1\ {\rm km}}\right) \left(\frac{Q^\star_{\rm D}}{1\ {\rm J\ kg^{-1}}}\right)^{5/6} e^{-5/3} \left(\frac{M_\star}{M_\odot}\right)^{-4/3} \left(\frac{M_{\rm tot}}{M_\oplus}\right)^{-1} {\rm Myr}, \tag{1.7}$$

where $M_{\rm tot}$ is the total mass in solids that can be expressed as

$$M_{\rm tot} = 2.7 \times 10^{-9} f_{\rm IR} \left(\frac{r}{1\ {\rm au}}\right)^2 \left(\frac{D_c}{D_{\rm bl}}\right)^{0.5} {\rm M_\oplus}, \tag{1.8}$$

for the assumed size distribution. Eq. 1.7 represents the timescale at which mass is lost from the cascade through the removal of the largest planetesimals. It is possible to estimate the collisional lifetime of solids of a specific size D (e.g. traced at a particular wavelength) as the collisional timescale for destructive collisions should scale as $(D/D_c)^{0.5}$. This is important to keep in mind when analysing and interpreting observations of debris discs as the dust density distribution can depend on the lifetime of dust, and thus, on the grain size that an observation is tracing. For example, μm-sized grains could last a few or less than an orbit, while mm-sized

grains could remain in the disc for tens of orbits. If dust is produced at a particular radial and azimuthal location in a disc, then scattered light images tracing the small grains would show an asymmetric disc with a clump at the dust production location, while millimetre thermal emission observations would be consistent with an axisymmetric disc as millimetre grains can survive for timescales long enough to spread azimuthally around the disc. Note that we have assumed that the the disruption threshold is independent of size, and thus the size distribution can be represented by a single power law. This is not necessarily the case as $Q_{\rm D}^{\star}$ is expected to be a function of size, in which case the size distribution is no longer a single power law (Löhne et al., 2008).

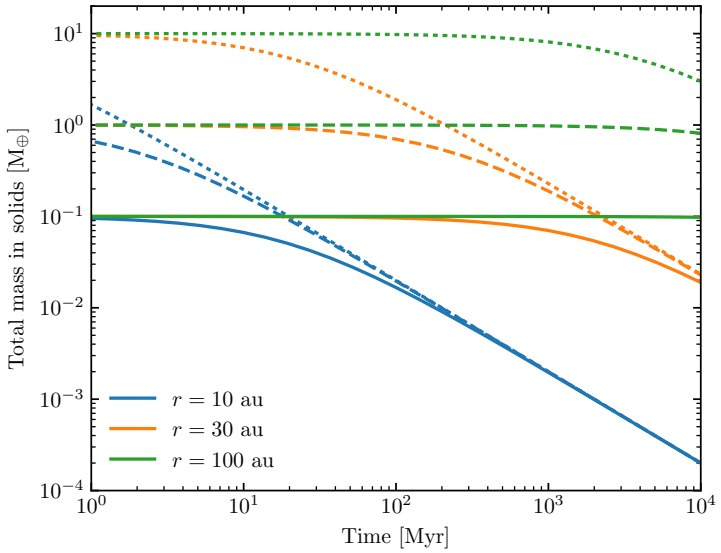

Figure 1.5: Collisional evolution of the total mass in a debris disc according to Equation 1.9. The blue, orange and green lines represent discs with a radius of 10, 30 and 100 au, respectively. The continuous, dashed and dotted lines represent initial solid masses of 0.1, 1 and 10 $M_{\oplus}$, respectively. I have assumed $dr/r = 0.3$, $e = 0.05$, $D_c = 10$ km, $M_{\star} = 1\,M_{\odot}$ and $Q_{\rm D}^{\star} = 150$ J kg^{-1}.

Assuming that collisions are the only mechanism of mass loss in the disc we can solve $\dot{M}_{\rm tot} = -M_{\rm tot}/t_c$ to obtain

$$M_{\rm tot}(t) = M_{\rm tot}(0)/(1 + t/t_c(0)), \tag{1.9}$$

where $M_{\rm tot}(0)$ is the initial total mass in the disc and $t_c(0)$ is the collisional lifetime of the biggest particles in the disc at the initial epoch. This equation assumes that the disc was initially stirred, i.e. e and I have had their current distribution since $t = 0$. This is not necessarily true if no massive planets are present in the system, in which case the disc will start its collisional evolution delayed by a time $t_{\rm stir}$. Eq. 1.9 implies that the dust mass and fractional luminosity of a disc will decay as $1/t$ for $t \gg t_c$ independently of the initial disc mass. This is because more massive discs will collisionally evolve more quickly ending up at the same level that they would have if they started with a lower disc mass (see Figure 1.5). This unavoidable collisional

evolution implies that the older a system is, the harder it is to detect any debris in the system. Although it is true that the disc mass is expected to decrease with time, more detailed modelling considering a size dependent disruption threshold by Löhne et al. (2008) showed that the disc brightness has a flatter evolution than t^{-1} and that the dust mass and total disc mass have a different evolution as the size distribution evolves with time.

1.5 Gas in debris discs

Although debris discs are generally assumed to be gas depleted, in some of these systems significant amounts of gas have been detected, especially in young debris discs that should have recently left the protoplanetary disc phase. The gas component in these systems has been studied through the observations of neutral atomic carbon (CI) and carbon monoxide (CO) emissions, two species that are bright in the submillimetre and can be observed using ground based telescopes (e.g. APEX or ALMA), and ionised atomic carbon (CII) and neutral atomic oxygen (OI) emission in the far-IR using Herschel. Table 1.1 lists the debris discs where gas has been detected.

Despite the increasing number of gas detections in debris discs, the origin of this gas is still unclear. There is ongoing debate of whether the observed gas is primordial (gas still remaining from the protoplanetary disc phase), or secondary (gas released from solids rich in volatiles such as comets in the Solar System). About 10 out of 15 systems with detected CO gas are consistent with a primordial origin (e.g. HD 21997, Kóspál et al., 2013) as the inferred column densities of CO are high enough to be self-shielded against photodissociation due to the interstellar UV radiation field (Visser et al., 2009), and thus CO could be long-lived. These systems are usually called hybrid discs as they display features that are generally associated with both protoplanetary (abundant gas that is radially extended) and debris disc-like SEDs (lack of high near-IR excess). However, in a few systems the CO column densities are not high enough (even if primordial H_2 is present) and the CO should be photodissociated in timescales as short as ~ 120 yr. This has favoured a secondary origin scenario in the case of β Pictoris (Dent et al., 2014), HD 181327 (Marino et al., 2016), η Corvi (Marino et al., 2017b) and Fomalhaut (Matrà et al., 2017b), in which gas is most likely released from icy bodies, e.g through destructive collisions or photodesorption.

It is worth noting that 13 out of 17 of the gas detections have been around A-type stars, which could hint at a specific origin. For example, primordial gas in debris disc could be more likely to be found around A-type stars compared to FGK-type stars due to more massive primordial discs (e.g. Andrews et al., 2013). Prior to writing this dissertation, gas had only been found around A stars and β Pic was the only system where the gas was inconsistent with a primordial

Table 1.1: Main parameters of debris disc systems with gas detections prior to May 2018.

ID	Age [Myr]	$L_\star$ [$L_\odot$]	$L_{\rm IR}/L_\star$	$M_{\rm dust}$ [$M_\oplus$]	Gas detection	$M_{\rm CO}$ [$M_\oplus$]
η Tel	23 ± 4 (1)	20.9 (6)	2.4×10^{-4} (6)	$1.3 \pm 0.08 \times 10^{-2}$ (12)	CII (12)	$< 6.8 \times 10^{-5}$ (8)
49 Ceti	40 ± 10 (2,3)	16.4 (7)	1.1×10^{-3} (7)	$2.7 \pm 0.4 \times 10^{-1}$ (7)	CO, OI, CII, CI (15, 16, 17)	1.4×10^{-4} (25)
β Pic	23 ± 4 (1)	8.7 (9)	2.6×10^{-3} (11)	$7.8 \pm 0.8 \times 10^{-2}$ (13)	CO, OI, CII, CI (19, 20, 21)	2.8×10^{-5} (19)
Fomalhaut	440	16.6	7.8×10^{-5}	1.5×10^{-2}	CO (29)	$0.65 - 42 \times 10^{-6}$ (29)
η Corvi	1000-2000	5.0	1.5×10^{-4}	1.4×10^{-2} (30)	CO (30)	$\sim 10^{-7}$ (30)
HD 21997	30 ± 10 (2,3)	11.2 (7)	5.7×10^{-4} (7)	$1.6 \pm 0.5 \times 10^{-1}$ (7)	CO (18)	6×10^{-2} (25)
HD 32297	$15 - 500$ (5)	6.2 (5)	4.4×10^{-3} (6)	$3.7 \pm 1.1 \times 10^{-1}$ (14)	CO, CII (22, 24)	1.3×10^{-3} (25)
HD 110058	10	5.9	1.9×10^{-3}	3×10^{-3}	CO (26)	2.1×10^{-5} (25)
HD 121191	16	8.2	4.7×10^{-3}	9.5×10^{-3}	CO (28)	2.7×10^{-3} (28)
HD 121617	16	17.0	4.8×10^{-3}	1.4×10^{-1}	CO (28)	1.8×10^{-2} (28)
HD 131488	16	13.1	5.5×10^{-3}	3.2×10^{-1}	CO (28)	8.9×10^{-2} (28)
HD 131835	16 ± 1 (4)	9.2 (8)	3.0×10^{-3} (8)	$4.7 \pm 1.6 \times 10^{-1}$ (8)	CO (8)	6×10^{-2} (25)
HD 138813	10	24.5	1.5×10^{-3}	7.6×10^{-3}	CO (26)	7.4×10^{-4} (25)
HD 146897	10	3.1	5.3×10^{-3}	2×10^{-2}	CO (26)	2.1×10^{-4} (25)
HD 156623	10	14.8	5.5×10^{-3}	2.4×10^{-4}	CO (26)	2.0×10^{-3} (25)
HD 172555	23 ± 4 (1)	7.8 (10)	7.3×10^{-4} (10)	$4.8 \pm 0.006 \times 10^{-4}$ (10)	OI (10)	$< 2.4 \times 10^{-5}$ (18)
HD 181327	23 (1)	3.1	2×10^{-3}	0.44	CO (27)	1.8×10^{-6} (27)

References used in this table: (1) Mamajek & Bell (2014); (2) Gagné et al. (2014); (3) Torres et al. (2008); (4) Pecaut et al. (2012); (5) Rodigas et al. (2014); (6) Chen et al. (2014); (7) Moór et al. (2015b); (8) Moór et al. (2015a); (9) Crifo et al. (1997); (10) Riviere-Marichalar et al. (2012); (11) Rhee et al. (2007); (12) Riviere-Marichalar et al. (2014); (13) Dent et al. (2005); (14) Meeus et al. (2012); (15) Zuckerman et al. (1995); (16) Roberge et al. (2013); (17) Roberge et al. (2014); (18) Moór et al. (2011); (19) Dent et al. (2014); (20) Roberge et al. (2006); (21) Cataldi et al. (2014); (22) Donaldson et al. (2013); (23) Kóspál et al. (2013); (24) Greaves et al. (2016); (25) Kral et al. (2017b); (26) Lieman-Sifry et al. (2016); (27) Marino et al. (2016); (28) Moór et al. (2017); (29) Matrà et al. (2017b); (30) Marino et al. (2017b).

origin. Chapters 2 and 3 present the first gas detection around Solar-type stars (HD 181327 and η Corvi), and in both cases the gas cannot be explained as being primordial.

The presence or absence of gas has important consequences for the understanding of the physical processes and evolution in protoplanetary and debris discs. Although, it is uncertain how long primordial gaseous discs can survive against photoevaporation and accretion onto the star, debris discs surveys looking for gas and deeper observations of star forming regions could place important constraints on disc dispersal models. Moreover, if gas is of primordial origin the gas densities in the disc could be high enough (of the order of the dust densities) to trigger instabilities through dust-gas interactions, potentially modifying the dust density distribution (as is the case for protoplanetary discs). These instabilities can produce low eccentricity ring-like structures that can be mistakenly attributed to perturbing planets (e.g. Lyra & Kuchner, 2013).

When the gas is of secondary origin it must somehow be replenished by volatiles contained in solids, either in the form of ices or trapped in pockets (Collings et al., 2004) as in Solar System comets. If the gas is co-located with the dust (where the collisional rates are highest), then the gas is expected to be released in collisions of solids at some point down the collisional cascade as μm-sized grains would hardly retain any volatiles. As a first approximation we can estimate the rate at which gas species will be released by the product of the mass loss rate in the disc, and the mass fraction of the gas species trapped in planetesimals, i.e. $\dot{M}^{+}_{\rm gas} = \dot{M}_{\rm tot} f_{\rm gas}$, where $f_{\rm gas}$ is the gas mass fraction of planetesimals. In steady state, this should be equal to the mass loss rate of gas (e.g. due to photodissociation). Thus, if we can estimate the mass loss rate of gas and dust, $\dot{M}_{\rm dust} = \dot{M}_{\rm tot}(1 - f_{\rm gas})$, we can infer the fraction of volatiles contained in planetesimals as

$$f_{\rm gas} = 1 / \left(\frac{\dot{M}_{\rm dust}}{\dot{M}_{\rm gas}} + 1 \right). \tag{1.10}$$

I will use this equation or its first order approximation (considering $f_{\rm gas} \ll 1$) in Chapter 2 to estimate the fraction of CO locked in planetesimals around HD 181327. Finally, if gas is of secondary origin but is not co-located with the dust, then the presence of gas could hint at planetesimal outgassing driven by sublimation, as comets do when they venture into the inner regions of the Solar System. This is described in Chapter 3.

1.5.1 Metallic gas

Volatiles such as CO are not the only kind of gas that has been detected in systems with debris discs, metallic atomic species are known to be present in a few debris disc systems. β Pic was the first system in which metallic gas was identified by detecting a narrow Ca II K line centered at the stellar velocity and super-imposed on the broad photospheric stellar

absorption (Slettebak, 1975). Additionally, a weaker red- or blue-shifted component has also been seen, varying both in strength and velocity (e.g. Slettebak & Carpenter, 1983). But β Pic is not the only system in which this has been observed. In recent years this phenomenon has been seen in several systems, in particular in systems with edge-on outer discs (Welsh et al., 1998; Montgomery & Welsh, 2012; Eiroa et al., 2016; Miles et al., 2016; Hales et al., 2017; Rebollido et al., 2018).

This phenomenon has historically been attributed to the presence of star-grazer objects or *falling evaporating bodies* (FEBs) on highly eccentric orbits, which evaporate/start evaporating when they come within a few stellar radii of the star (Ferlet et al., 1987; Beust et al., 1990; Beust & Morbidelli, 1996; Kiefer et al., 2014). Although it is tempting to relate this phenomenon to Sun-grazing comets, observed FEB activity is several orders of magnitude higher (Dutrey et al., 2004) and no molecular species have been found to display a variable component, which would indicate that these FEBs are icy.

1.6 Hot dust & volatile delivery

While most of the systems with cold and warm dust are consistent with Asteroid or Kuiper belt analogues located beyond a few au (e.g., Wyatt et al., 2007b; Schüppler et al., 2016; Geiler & Krivov, 2017), a few systems present levels of warm/hot dust ($\gtrsim 300$ K) detected in the NIR and MIR that are incompatible with such scenarios. This is because there are limits on how bright a debris disc can be at any given age (Wyatt et al., 2007a; Löhne et al., 2008). At tens of au a belt of km-sized or larger planetesimals can survive collisions on Gyr timescales, but within a few au debris discs collisionally evolve much faster setting a limit on their brightness. This incompatibility implies that the hot dust or material sustaining it must be either transient, e.g. as a result of a giant collision between planetary embryos or a giant impact on a planet (e.g., Jackson et al., 2014; Kral et al., 2015), or be continually fed from material formed further out in the system where it can survive for much longer timescales. These inner dust components are analogous to the Zodiacal dust, which is replenished from dust that originates from comets that disintegrate as they pass through the inner Solar System (Nesvorný et al., 2010), and thus they are usually referred as exozodiacal dust or exozodis (see review by Kral et al., 2017a). Well studied systems like the 450 Myr old A-star Vega (Absil et al., 2006; Defrère et al., 2011; Su et al., 2013) and the 1-2 Gyr old F-star η Corvi (Stencel & Backman, 1991; Wyatt et al., 2005; Smith et al., 2009) have bright exozodis and outer planetesimal belts that could act as the source of material that is replenishing the dust in their inner regions. Based on the NIR excess measured in nearby stars using interferometry, it has been estimated that $\sim 10-30\%$ of AFGK-type stars have exozodi levels above 1% of the stellar flux (Absil et al., 2013; Ertel et al., 2014), with a tentative correlation with the existence of an outer reservoir of cold dust for

FGK-type stars (Nuñez et al., 2017). In Chapter 3 I study the system η Corvi using ALMA observations constraining the structure of its outer belt and mechanism feeding its exozodi.

Different mechanisms have been invoked that could explain the bright hot dust: P-R drag (van Lieshout et al., 2014; Kennedy & Piette, 2015), inward scattering of solids from an outer debris belt by a chain of planets (e.g., Bonsor & Wyatt, 2012); planetesimals evolving into cometary orbits due to mean motion resonances with an exterior high mass planet on an eccentric orbit (Beust & Morbidelli, 1996; Faramaz et al., 2017); instabilities in the system after which a planet could disrupt a planetesimal belt scattering large amounts of material inwards (Bonsor et al., 2013). The latter is analogous to the the Late Heavy Bombardment in the Solar System (LHB), caused by the outward migration of Neptune after Jupiter and Saturn crossed the 1:2 resonance causing a massive delivery of planetesimals to the inner Solar System (Gomes et al., 2005). In Chapter 6 I study how the architecture of a planetary system affects the inward scattering of comets, which could feed an exozodi or deliver volatiles to inner planets via impacts.

Understanding these phenomena is of great importance as it can set constraints on the architecture of planetary systems (e.g. Bonsor & Wyatt, 2012; Bonsor et al., 2012), but it can also be used to assess the possibility that material formed at large radii, i.e. rich in volatiles in the form of ices and organic molecules, could be transported into the inner regions of planetary systems where it could be accreted by Earth-like planets. Impacts and volatile delivery by comets and asteroids originating in the outer asteroid belt has been proposed to account for the water on Earth, which may have formed dry (Morbidelli et al., 2000; O'Brien et al., 2006; Raymond et al., 2009). In the particular case of the Solar System, the formation of Jupiter and Saturn could have been a determinant in the delivery of water and volatiles to its inner regions (Raymond & Izidoro, 2017). Moreover, impacts could have also acted as chemical activators and the energy source for amino acid formation in primitive atmospheres (e.g., Civs et al., 2004; Rotelli et al., 2016). For other systems where terrestrial planets formed closer in, volatile delivery could be essential for the development of an atmosphere that could support life (e.g., Raymond et al., 2007; Lissauer, 2007). As mentioned in §1.5, thanks to the unprecedented sensitivity of ALMA, it has been possible to detect exocometary gas and constrain the volatile composition of planetesimals in exo-Kuiper belts (e.g., Dent et al., 2014; Marino et al., 2016; Kral et al., 2016; Matrà et al., 2017a,b). This supports the general picture that volatiles can be locked in planetesimals that could be later delivered to planets (e.g. de Niem et al., 2012).

1.7 The Atacama Large Millimeter/submillimeter Array

ALMA is currently the most sensitive instrument to study debris discs. At millimetre wavelengths, this array of fifty 12 m diameter antennas (12-m array) and twelve 7 m plus four 12 m antennas (Atacama Compact Array), is able to detect and resolve nearby debris discs with a high signal-to-noise in the dust thermal emission and even look for gas molecules if present. As an interferometer its angular resolution, $\theta_{\rm res}$, can be adjusted since it depends on the wavelength and projected baselines,

$$\theta_{\rm res} \approx \lambda / L_{\rm max}, \tag{1.11}$$

where $L_{\rm max}$ is the maximum projected baseline in the array. With maximum baselines ranging from 45 m to 16 km, ALMA's resolution can vary from from $\sim 5''$ down to $\sim 0\farcs02$ (at 230 GHz).

Because ALMA is an interferometer, it does not take an image from the sky, but instead measures visibilities, $V(u, v)$, which are defined as the Fourier transform of the sky brightness distribution, $I(l, m)$, attenuated by the Airy function or primary beam of the Antenna, $A(l, m)$,

$$V(u, v) = \int\int A(l, m) I(l, m) \exp^{-2\pi i(ul+vm)} \, dldm. \tag{1.12}$$

In this manner, visibilities represent an alternative representation of the spatial information of the sky brightness distribution. It is only when combining multiple visibilities with a well sampled uv-coverage (as it is the case with ALMA) that it is possible to synthesise a reconstructed image. Alternatively, visibilities can be studied directly, for example, by comparing to model visibilities of discs as done in Chapters 2, 3, 4 and 5, where I also present new ALMA observations of four discs. Therefore, we can use ALMA to study the structure of debris discs in detail, trace the location of planetesimals, and look for asymmetries in the disc emission that could, for example, be attributed to unseen planets perturbing the orbits of planetesimals.

2

Exocometary gas in the HD 181327 debris ring

2.1 Introduction

In this chapter I study the debris disc around the F5/6 main sequence star HD 181327 (Nordström et al., 2004; Torres et al., 2006), member of the 23 ± 3 Myr old β Pic moving group (Mamajek & Bell, 2014) and located at a distance of 51.8 ± 1.7 pc (van Leeuwen, 2007). The star has an IR excess with a fractional luminosity of $L_{\rm IR}/L_\star \sim 0.2\%$ (Lebreton et al., 2012) that comes from dust thermal emission that has been marginally resolved at different wavelengths: at 18.3 μm by Chen et al. (2008) and at 70 μm, 100 μm and 3.2 mm by Lebreton et al. (2012). HST scattered light observations resolved a debris ring of μm-sized grains with a peak at ~ 90 au and 36 au wide (Schneider et al., 2006; Stark et al., 2014). The latter study identified a possible radial dust size segregation due to radiation pressure, based on variations of the scattering phase function with radius. Moreover, they found asymmetries that could be interpreted as an increase in the optical depth in the west side of the ring, potentially due to either a recent catastrophic disruption or warping of the disc by the ISM.

In this chapter I present the first ALMA observations to study the dust continuum at 220 GHz, the presence of CO gas in the system, constrain the location of planetesimals, look for asymmetries that could give hints on the origin of the asymmetric features observed by the HST, and study the origin of the CO gas. In §2.2 I present the observations and imaging of the

dust continuum and CO line emission. In §2.3 I compare the observations with an axisymmetric disc model for the dust continuum and CO (2-1), using a Markov chain Monte Carlo (MCMC) method coupled with radiative transfer simulations to sample the parameter space and estimate the debris spatial distribution, CO gas mass and the disc orientation in the sky. In §2.4 I discuss the implications of the dust continuum and CO observations, I compare them with the previous HST observations, and I derive a cometary composition based on the CO observations. Finally in §2.5 I summarise the main results and conclusions.

2.2 ALMA observations and imaging

HD 181327 was observed by ALMA in band 6 on 10 March 2014 as part of the cycle 1 project 2012.1.00437.S. The total number of antennas was 26 with minimum and maximum projected baselines of 12 and 365 m, respectively. The total time on source excluding overheads was 34 min. Three months later, on the 4 and 12 June, three new observation runs using the same band were carried out corresponding to the cycle 2 project 2013.1.00523.S. The total number of antennas was 39 with a minimum and maximum projected baselines of 15 and 650 m, respectively. The total time on source excluding overheads was 129 min. Calibrations were applied using the pipeline provided by ALMA.

On both projects, the ALMA correlator provided 4 spectral windows (spws), 3 exclusively dedicated to study the dust continuum with 128 channels and a total bandwidth of 2 GHz centered at: 212.9, 214.9 and 228.1 GHz in the first project, and 214.6, 216.6 and 232.5 GHz in the second. The fourth spw was configured with a higher spectral resolution of 244 KHz and total bandwidth of 937.5 MHz (3840 channels), centered at 230.5 GHz to target the ^{12}CO (2-1) transition at 230.538 GHz in both projects. I combined the two datasets from both projects to achieve the most complete $u - v$ coverage and the highest signal-to-noise ratio (S/N) on the reconstructed continuum image and CO line emission.

2.2.1 Dust continuum

The image synthesis of the dust continuum was carried out using a non-parametric least-squares modeling technique that incorporates a regularization term called "entropy" from a family of Maximum Entropy Methods (MEMs). Examples of usage of MEM for image synthesis in Astronomy can be found in Pantin & Starck 1996; Casassus et al. 2006; Levanda & Leshem 2010; Casassus et al. 2013; Warmuth & Mann 2013; Coughlan & Gabuzda 2013; Marino et al. 2015. These deconvolved images "superresolve" the interferometric data, as the entropy prior allows an extrapolation of spatial frequencies beyond those sampled by the interferometer. The whole algorithm is called *uvmem* and the resulting images "MEM

models". The deconvolved image can then be "restored" by convolving with a *Clean* beam corresponding to *natural* or *Briggs* weighting and adding the dirty map of the residuals. The restored maps are comparable to standard Clean images. While the resolution or point-spread-function on the deconvolved image can vary at different locations, the resolution on the restored images is well characterised by a synthetic beam of $0\farcs47 \times 0\farcs36$ and $0\farcs69 \times 0\farcs58$, corresponding to Briggs and natural weighting respectively.

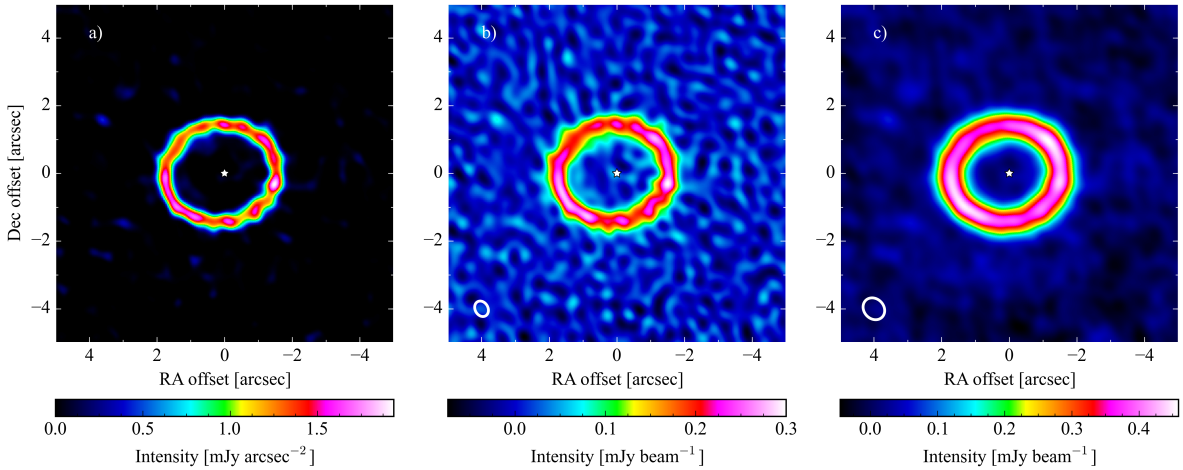

Figure 2.1: ALMA dust continuum maps at 220 GHz (Band 6). ***a)*** MEM non-parametric model (regularized with the maximum entropy method). ***b)*** Restored image adding residuals and convolving with a synthetic beam corresponding to *Briggs* weighting ($0\farcs47 \times 0\farcs36$). ***c)*** Restored image adding residuals and convolving with a synthetic beam corresponding to *natural* weighting ($0\farcs69 \times 0\farcs58$). The respective beams are represented by white ellipses. The x- and y-axes indicate the offset from the stellar position in R.A. and decl. in arcsec, i.e. north is up and east is left. The stellar position is marked with a white star.

In Figure 2.1 I present the results of the image synthesis on the continuum emission: (a) MEM model, (b) restored image with Briggs weighting (Briggs map hereafter) and (c) restored image with natural weights (natural map hereafter). To smooth the artefacts due to thermal noise on the visibilities and characterize the noise level in the image space, I perform a Monte Carlo simulation bootstrapping the measured visibilities, i.e. adding a random Gaussian noise according to the observed dispersion on each base-line and repeating the image synthesis described above. The presented images are the median of 200 iterations. I observe a noise level of 0.022 mJy beam^{-1} on the Briggs map, while 0.015 mJy beam^{-1} on the natural map, estimated from the median absolute deviation and from the rms on the dirty map of the residuals. The total flux in the Natural map inside a ellipse of semi-major axis $4''$ and oriented as the best-fit model (see §2.3) is 7.9 ± 0.2 mJy (which does not take into account the error on the absolute flux calibration of $\sim 10\%$). This is consistent with the trend of the spectral energy distribution (SED) between 170 μm (Moór et al., 2006, ISO) and 3.2 mm (Lebreton et al., 2012, ATCA), but too low compared to the 0.05 Jy at 870 μm observed by LABOCA-APEX (Nilsson et al., 2009), possibly due to a background galaxy in the primary beam. Inside the primary

beam I also detect two compact sources with peak intensities of 0.14 and 0.08 mJy beam^{-1}, located at $8''$ with a PA=9.5° and $9''$ with a PA of 210°, respectively. These are probably background galaxies (see Figure 2.8) as the position of the southern compact source is consistent with an edge-on galaxy observed in the STIS/HST observations in 2011 (Stark et al., 2014).

Similar to previous observations of scattered light, the disc presents a ring-like morphology. The bulk of the emission is radially confined between $\sim 50 - 125$ au ($\sim 1\farcs0 - 2\farcs4$) with a peak intensity at 85.8 ± 0.3 au obtained by fitting an ellipse to the peak intensities along the ring of the MEM model. When I compare these results with the HST observations I find that the ring is slightly narrower and shifted inwards in the millimetre, while the inner edge in scattered light (82.3 ± 1.1) is close to the peak radius in the millimetre. This is consistent with what would be expected from grain size segregation due to radiation pressure, previously suggested in this disc by Stark et al. (2014). Radiation pressure causes small dust grains to extend farther out in radius compared with millimetre grains, shifting the density maximum of small grains to larger radii (see discussion in §2.4.3).

The disc emission appears consistent with an axisymmetric ring and most of the observed intensity variations along the ring in the panels of Figure 2.1 and the small offset from the star can be explained by the PA of the beam, the noise level and the ALMA astrometric error (see §2.4.1). In §2.3.1 I compare the observations with an axisymmetric disc model.

In Figure 2.2 I present intensity profiles of the maps presented in Figure 2.1a and 2.1b, along the ring's major and minor axis, together with the deprojected mean intensity at all azimuths extracted from Figure 2.1c. In the top and middle panels the MEM model profile is represented by a red line, while the Briggs map profile is represented in blue with blue shaded areas equivalent to 1 $\sigma = 0.022/\sqrt{2}$ mJy beam^{-1} (the factor $1/\sqrt{2}$ is due to the mean between the opposite sides of the disc). The projected Briggs Clean beam is presented with dashed black lines. The radial extent of the emission both along the major and minor axis is wider than the beam, demonstrating that the width of the ring is marginally resolved. The full width half maximum (FWHM) of the ring is $\sim 0\farcs5$, which at a distance of 51.8 pc translates to ~ 25 au. A more accurate estimation is presented in §2.3.1. The bottom panel shows that the disc emission extends out to $\sim 4''$ (200 au) in either a second ring or a halo component. The grey area in the bottom panel represents the 99.7% confidence region equivalent to $3\sigma = 0.015/\sqrt{N_{\rm beams}}$ mJy beam^{-1} (the factor $1/\sqrt{N_{\rm beams}}$ is due to the mean at all azimuth and the number of independent points). In Figure 2.1c this emission is also just visible as a broad ring around $4''$. To test the significance of this detection and whether this could be a product of the image synthesis method, I produce Clean images obtaining roughly the same results. Moreover, the second component is recovered in the dirty map of the residuals when a best-fit ring model is subtracted to the data (see §2.3 for a description of the ring model). A brief

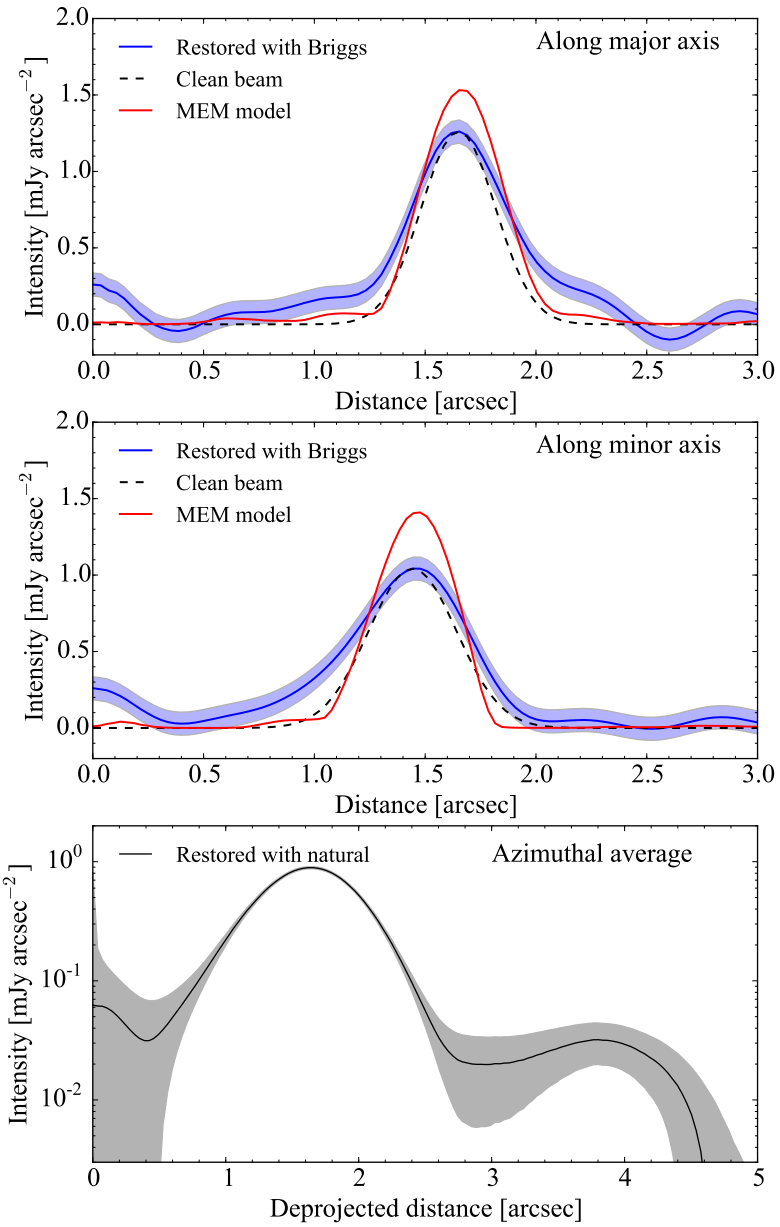

Figure 2.2: Intensity radial profiles of the dust continuum vs distance to the star along the major (top panel) and minor axis of the disc (middle panel). In the bottom panel I present the mean intensity at all azimuths vs the deprojected distance to the star. The red, blue, black dashed and black continuous lines represent the MEM model, Briggs map, projected Briggs Clean beam and natural map, respectively. The blue and grey areas represent the 68% and 99.7% confidence regions, respectively.

discussion about the origin of this emission and the dirty map of the residuals is presented in §2.4.

2.2.2 ^{12}CO (2-1)

To study the ^{12}CO (2-1) transition line at 230.538 GHz (rest frequency), I first subtract the continuum emission from the visibilities fitting a polynomial of the first order at the frequencies where no line emission is expected. The dirty map of the continuum subtracted data does not show any significant emission above 3σ which could be attributed to CO. With natural weights the noise level is 1.0 mJy beam^{-1} per channel. To search for any low level CO emission I compute the total flux inside an elliptic mask and between a frequency or velocity range that I vary, both spatially and in frequency, to maximise the S/N of the integrated flux. The S/N is maximised inside an elliptic mask of minimum and maximum semi-major axes of $1\farcs4$ and $2\farcs1$ (assuming the same orientation and aspect ratio as the main ring) and a velocity range of -2.8 to 2.0 km s^{-1}(Barycentric reference frame). These parameters match the location of the main ring and the expected Doppler shift due to Keplerian rotation, i.e. $v_0 = 0.1 \pm 0.4$ km s^{-1} (Gontcharov, 2006) and $v_{max} = 1.9$ km s^{-1} for $M_\star = 1.36$ $M_\odot$ (Lebreton et al., 2012). The spectrum extracted from the data cube inside the elliptic mask and smoothed with a Gaussian kernel is presented in Figure 2.3. The horizontal lines represent ±1, 3, 4 and 5σ levels. The line peak is $\sim 5\sigma$. The integrated flux where the S/N is maximised is 30.1 ± 5.4 mJy km s^{-1} (5.6σ). Moreover, I find that the CO emission in the south east and north west side of the disc are consistent with being blue and red shifted, respectively. As the disc north side is the brightest in scattered light due to forward scattering, I can infer that it is also the closest side. This implies that the disc is rotating clockwise in the sky.

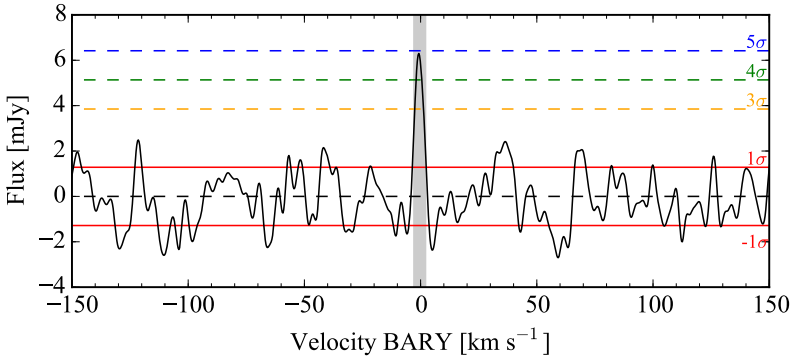

Figure 2.3: Continuum subtracted integrated spectrum inside an elliptic mask of minimum and maximum semi-major axis of $1\farcs4$ and $2\farcs1$, and oriented as the dust continuum ring. The original spectrum was smoothed with a Gaussian kernel with standard deviation of 4 channels. The horizontal lines represent ±1, 3, 4 and 5σ levels. The grey region represents velocities between -2.8 km s^{-1}and 2.0 km s^{-1}where the S/N is maximised. The velocities represent the Doppler shift with respect to 230.538 GHz in the Barycentric reference frame.

In Figure 2.4 I present the integrated intensity over the velocity range specified above and averaging at all azimuths. The grey area represents the 68% confidence region. The CO line peaks at 90 ± 4 au (error=$0.5\times$ beam semi-major axis $\times$ distance / (S/N)), close to the ring radius in the continuum, suggesting that gas and dust are co-located. This favours a secondary origin scenario, where the CO is being released from icy bodies in the disc. I study the azimuthal profile of the emission along the ring and I find no evidence for non-axisymmetry, similar to the dust continuum. In §2.3.2 I study the CO gas distribution by modeling the CO emission in the non-LTE regime, with different excitation temperatures and electron densities which act as the main collisional partner. Using an MCMC technique I constrain the distribution of CO gas in the disc to quantify its similarity to the dust distribution.

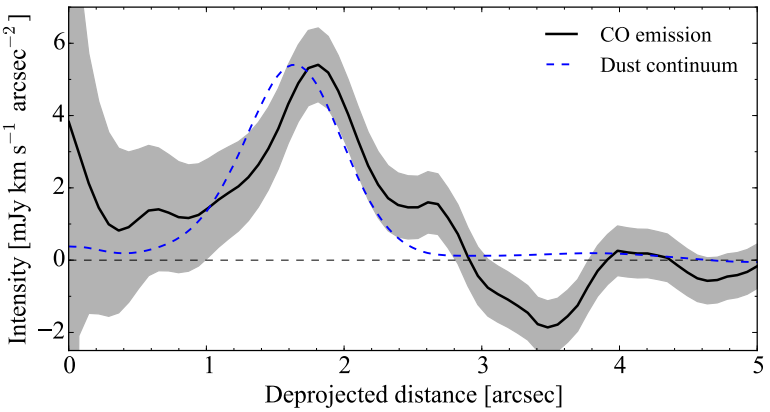

Figure 2.4: Mean intensity at all azimuths (black line) integrating from -2.8 km s^{-1}and 2.0 km s^{-1}with respect to 230.538 GHz, in the Barycentric reference frame. The profile is extracted from the dirty map with natural weights of the continuum subtracted visibilities. The grey area represents the 68% confidence region. In blue I also present the mean intensity of the dust continuum presented in Fig. 2.2 in an arbitrary scale.

2.3 Disc modelling

2.3.1 Dust continuum

To constrain the location of the millimetre-sized dust population, I compare the observations with an axisymmetric debris disc model in the visibility space. The dust density distribution is parametrized as a ring of radius r_0, with a Gaussian radial profile of width Δr (FWHM) and a Gaussian vertical profile with a scale height H (vertical standard deviation) or aspect ratio $h = H/r$:

$$\rho(r,z) = \rho_0 \exp\left[-\frac{(r-r_0)^2}{2\sigma_r^2} - \frac{z^2}{2H^2}\right], \sigma_r = \frac{\Delta r}{2\sqrt{2\log 2}}. \quad (2.1)$$

For the dust optical properties I use a mass-weighted mean opacity of astrosilicate grains with

an internal density of 3.5 g cm^{-3} (Draine, 2003). I assume a Dohnanyi-like size distribution with a power law index of -3.5, and minimum and maximum grain size $a_{\rm min} = 1.3\mu$m and $a_{\rm max} = 1.0$ cm. These values were roughly estimated comparing the model and observed SED in an iterative procedure. The resulting mass-weighted absorption opacity ,$\kappa_{\rm abs}$, is 1.1 cm^2 g^{-1} at 1.3 mm, computed using the "Mie Theory" code written by Bohren & Huffman (1983). While $(a_{\rm min}, a_{\rm max})$, $\kappa_{\rm abs}$ and the derived total dust mass are highly dependent on the choice on the grain composition and size distribution, these assumptions have very little effect on the derived disc structure. A detailed study on the grain properties of this disc can be found in Lebreton et al. (2012). Synthetic images are computed using RADMC-3D[1] (Dullemond et al., 2015), while the corresponding model visibilities were derived using the tool *uvsim* that is part of the *uvmem* algorithm. The free parameters in the model image and visibilities are r_0, h, Δr, $M_{\rm dust}$, PA, inclination (i) and RA- and decl-offset. The last two to account for astrometric uncertainty and disc eccentricity.

I use a Bayesian approach to constrain the different parameters of the ring model, sampling the parameter space to recover the posterior distribution with the public python module *emcee* that implements the Goodman & Weare's Affine Invariant MCMC Ensemble sampler (Foreman-Mackey et al., 2013). The posterior distribution is defined as the product of the likelihood function and the prior probability distribution functions for each parameter, which I assume are uniform. The likelihood function is defined proportional to $\exp[-\chi^2/2]$, where χ^2 is

$$\chi^2 = \sum_i \frac{||V_{\rm data,i} - V_{\rm model,i}||^2}{\delta V^2_{\rm data,i}}, \tag{2.2}$$

i.e. the sum over the squared difference of the model and measured visibilities, divided by the variance. In my priors, I impose a lower limit to h equivalent to 0.03 due to model resolution constraints.

The posterior distribution of h, Δr and r_0 are presented in Figure 2.5, while in Table 2.1 I summarise the best fit values extracted from the marginalised distribution. As previously mentioned, the ring is marginally resolved with $\Delta r = 23.2 \pm 1.0$ au in the radial direction. Although the width of the ring is well constrained under the assumption of a Gaussian radial profile, a detailed analysis of the radial structure of the main ring is impossible with the current angular resolution. The width of the ring is significantly larger than in the Fomalhaut ring (Boley et al., 2012). This could be related to the age of the systems as well as any possible planet- or star-disc interactions in the case of Fomalhaut (Faramaz et al., 2015; Shannon et al., 2014). In agreement with the ring radius derived in §2.2, I find $r_0 = 86.0 \pm 0.4$ au.

On the other hand the scale height is not fully constrained. In principle, it should be possible

[1]http://www.ita.uni-heidelberg.de/∼dullemond/software/radmc-3d/

Table 2.1: Best fit values for the dust continuum model. Median ± uncertainty based on the 16th and 84th percentile of the marginalised distributions.

Parameter	Best fit value
$M_{\rm dust}$ [$M_\oplus$]	0.422 ± 0.005
r_0 [au]	86.0 ± 0.4
Δr [au]	23.2 ± 1.0
h	0.07 ± 0.03
PA [°]	98.8 ± 1.4
i [°]	30.0 ± 0.7
RA offset [mas]	96 ± 5
Dec offset [mas]	-42 ± 5

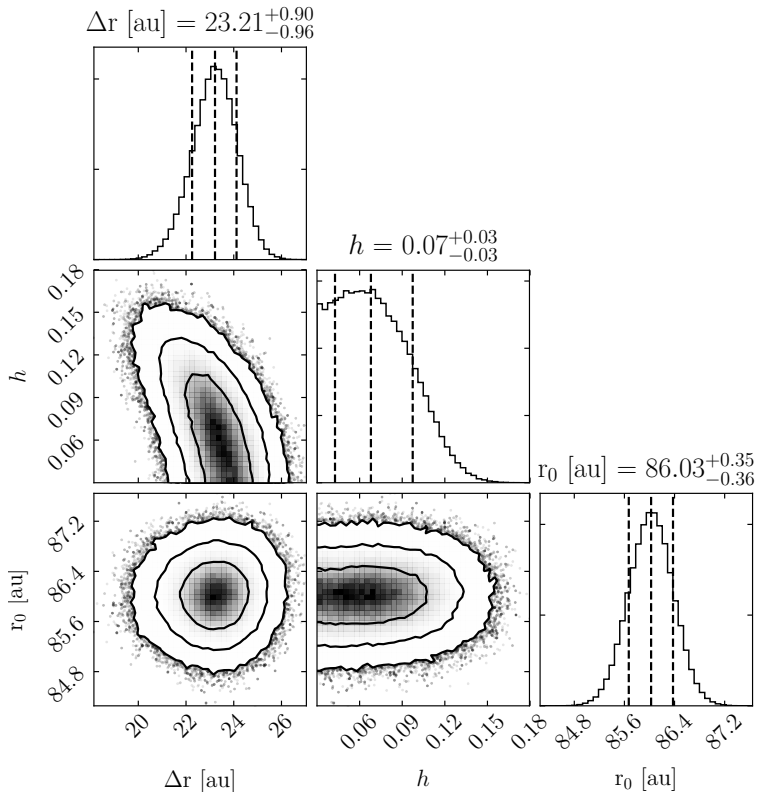

Figure 2.5: Posterior distribution of $h = H/r$, r_0 and Δr. The marginalised distributions of Δr, $h = H/r$ and r_0 are presented in the top, middle right and bottom right panel, respectively. The vertical dashed lines represent the 16th, 50th and 84th percentiles. ***Left middle panel:*** marginalised distribution of h and Δr. ***Left bottom panel:*** marginalised distribution of r_0 and Δr. ***Middle bottom panel:*** marginalised distribution of r_0 and h. Contours correspond to 68%, 95% and 99.7% confidence regions and the black dots to points of the MCMC outside the 99.7% confidence region. This plot was generated using the python module *corner* (Foreman-Mackey et al., 2014).

to derive h from the ratio of the ring's width or surface brightness along the major and minor axis of the projected ring, causing h and Δr to be correlated. In addition to this, in this case the estimation of h is limited as the observations only marginally resolve the ring's width. However, I can put a 99.7% confidence upper limit of 0.14 for h. Both upper limit and best

fit value (see Table 2.1) are consistent with the upper limit of 0.11 from Stark et al. (2014) and 0.09 from Schneider et al. (2006). The same figure shows that h and Δr are anticorrelated. The derived total dust mass in the main ring is 0.442 ± 0.005 $M_\oplus$. This value is highly dependant on the choice of dust internal density (3.5 g cm^{-3}) and for the assumed dust size distribution it scales as $(a_{\max}/1\ \mathrm{cm})^{0.5}$, noting that $a_{\max}$ is unconstrained. Moreover, the uncertainty on the dust mass quoted above does not include the uncertainty on the absolute flux calibration, or the uncertainty on the stellar distance. Including these systematics, the uncertainty should be $\sim 12\%$.

2.3.2 ^{12}CO (2-1)

To derive the CO gas distribution I follow a procedure similar to the dust continuum modeling in the previous Section. I fit the data with an axisymmetric disc of gas with a density distribution parametrized similar to the dust density distribution, but with a fixed vertical aspect ratio h of 0.07 and fixed disc orientation, that corresponds to the best fit of the dust continuum (see Table 2.1). The gas is in Keplerian circular orbits with a fixed systemic radial velocity of 0.1 km s^{-1} in the Barycentric frame. Instead of simulating visibilities as in the dust continuum analysis, I fit the data with the gas models in the image space. The model images produced with RADMC-3D at different frequencies (tracing different radial velocities) are convolved with the dirty beam and then compared directly with the dirty map of the CO data, both corresponding to natural weights. This method is analogous to comparing model visibilities with gridded visibility data, but computationally more efficient. The likelihood function is defined proportional to $\exp[-\chi^2/2]$, where χ^2 is the sum over the image and frequency space of the squared difference between the model and observed dirty map, divided by the variance, and taking into account the number of independent beams in the image and the correlation between adjacent channels in ALMA data. The free parameters in the MCMC are the CO gas mass (M_{CO}), ring radius (r_0) and FWHM of the ring (Δr).

However, the CO emission is not only constrained by the density distribution. Matrà et al. (2015) showed that local thermodynamic equilibrium (LTE) does not necessarily apply in the low gas density environments of debris discs. Depending on the gas kinetic temperature and collisional partner densities, the derived gas mass can vary by orders of magnitude. Thus, to model the ^{12}CO (2-1) emission it is necessary to include non-LTE effects, i.e to solve the population levels including (de-)excitations through radiative process, where the CMB photons and dust thermal emission dominate the radiation field at 230 GHz, as well as through collisions. The similarity between the dust and gas distribution showed in §2.2.2 suggest that the CO is of secondary origin, e.g. produced by collisions between icy planetesimals that release volatile species such as CO or H_2O. This implies that the main

collisional partner of CO molecules are electrons produced by carbon ionization and H_2O, which I neglect as it is a much less efficient collider compared to electrons (Matrà et al., 2015). However, I stress that the derived CO gas distribution and total mass (in both the extremes of radiation dominated and LTE) are independent of the specific collisional partner because it is the density of the partners that matters. That is, a different partner would yield a different range of values on the x-axis, but the same CO masses. The CO-e^- collisional rates are computed using expressions described by Dickinson & Richards (1975). In §2.4.6 I discuss the origin of the CO gas. I also use as input the best fit model of the dust continuum to compute the dust contribution to the radiation field at 230 GHz.

I consider different kinetic temperatures ranging from half to twice the dust temperature derived in the previous section (50 K at the ring radius). The electron density is defined as $n_{e^-}(r)=n^0_{e^-}(r/86\text{ au})^{-1.1}$, where the power law index was assumed equal to the one derived for β Pic (Matrà et al., 2017a). I vary $n^0_{e^-}$ between 10^{-2}-10^7 cm^{-3} to cover from the radiation-dominated regime to LTE. Scattered light images suggest that the north east side of the disc is the closest as it is brighter in scattered light because of forwards scattering; thus, if the CO is in Keplerian rotation it should be possible to determine the direction at which the CO moves in the sky. Hence, I consider models of the disc rotating clockwise as well as anticlockwise. I find a best fit with the gas rotating clockwise on the sky. The best model is five times more likely than the best anticlockwise model and 300 times more likely than no CO emission. In §2.4.1 I discuss the implications for the observed asymmetries in scattered light. Below, I concentrate only on the clockwise case.

In Figure 2.6 I present the CO gas masses derived with my MCMC-modeling technique for different kinetic temperatures and electron densities. I find that the best fit value of M_{CO} can vary due to the uncertainty in the excitation temperature between $1.2 \pm 0.4 \times 10^{-6}$ - $2.9 \pm 0.9 \times 10^{-6}$ $M_\oplus$ in the worst case (LTE), while it is well constrained around $1.8 \pm 0.6 \times 10^{-6}$ $M_\oplus$ in the radiation dominated regime (low n_{e^-}). Recent ALMA observations of the β Pic disc suggest $n^0_{e^-} \sim 10^2$ cm^{-3} (Matrà et al., 2017a), which for HD 181327 corresponds to a scenario close to the radiation dominated regime. In Figure 2.7 I present the posterior distributions, assuming $n^0_{e^-} = 10^2$ cm^{-3} and equal gas and dust temperatures. I find $M_{CO} = 1.8 \pm 0.6 \times 10^{-6}$ $M_\oplus$, $r_0 = 81^{+10}_{-9}$ au and $\Delta r = 48^{+17}_{-21}$ au. This model has a total flux of $\sim$ 18 mJy km s^{-1}, a CO peak density of $\sim$0.15 cm^{-3} and peak optical depth of ~ 0.007. I also notice that when both gas and dust temperature are equal, the difference in the derived CO mass between the radiation dominated regime and LTE is negligible because the radiation in the ring is actually dominated by the dust thermal emission rather than the CMB, as it was found to be the case in the Fomalhaut debris ring (Matrà et al., 2015). I also find that the derived values of r_0 and Δr are independent of $n^0_{e^-}$ and the gas kinetic temperature. Table 2.2 summarises the best fit values of the CO distribution.

The radius of the CO ring matches with the dust ring, confirming what I found averaging the

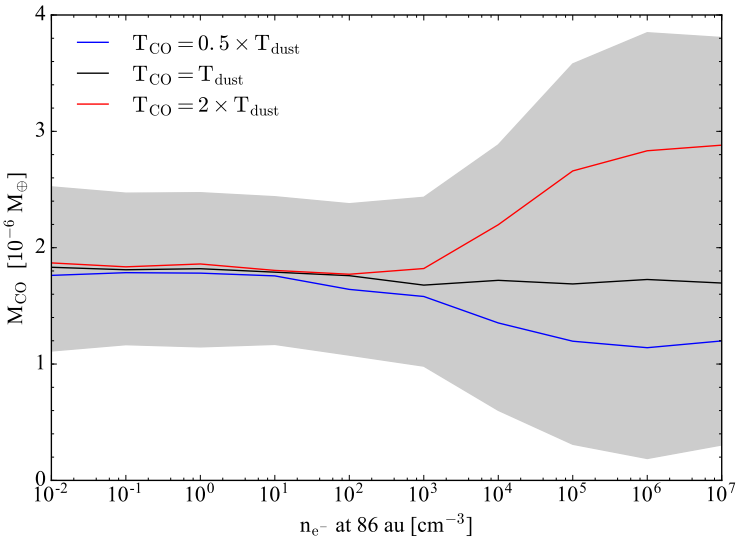

Figure 2.6: Best fit CO gas mass values obtained from my MCMC analysis using different kinetic temperatures and electron densities ($n^0_{e^-}$, main collisional partner). The blue, black and red lines correspond to kinetic temperatures equal to 0.5, 1 and 2.0 times the dust temperature in the disc, respectively. The grey area represents the 68% confidence region with gas temperatures ranging between $0.5 - 2.0$ times the dust temperature.

Table 2.2: Best fit values for the CO model. Median $\pm$ uncertainty based on the 16th and 84th percentile of the marginalised distributions.

Parameter	Best fit value
M_{CO} [$M_\oplus$]	$1.2 \pm 0.4 \times 10^{-6}$ - $2.9 \pm 0.9 \times 10^{-6}$
r_0 [au]	81^{+10}_{-9}
Δr [au]	48^{+17}_{-21}

data in §2.2.2, that gas and dust are co-located. Given the derived dust and CO densities it is unlikely that the CO is self shielded enough to avoid the photodissociation due to the ISM radiation field, which occurs in a timescale of $\sim$ 120 yr (Visser et al., 2009) (see discussion in §2.4.6). This implies that the CO must be replenished and produced in the main ring; therefore, I conclude that the CO is of secondary origin and released by icy bodies. In §2.4.6 I discuss its origin. I also find that the CO ring could have a radial width similar to the dust distribution, although it is not well constrained.

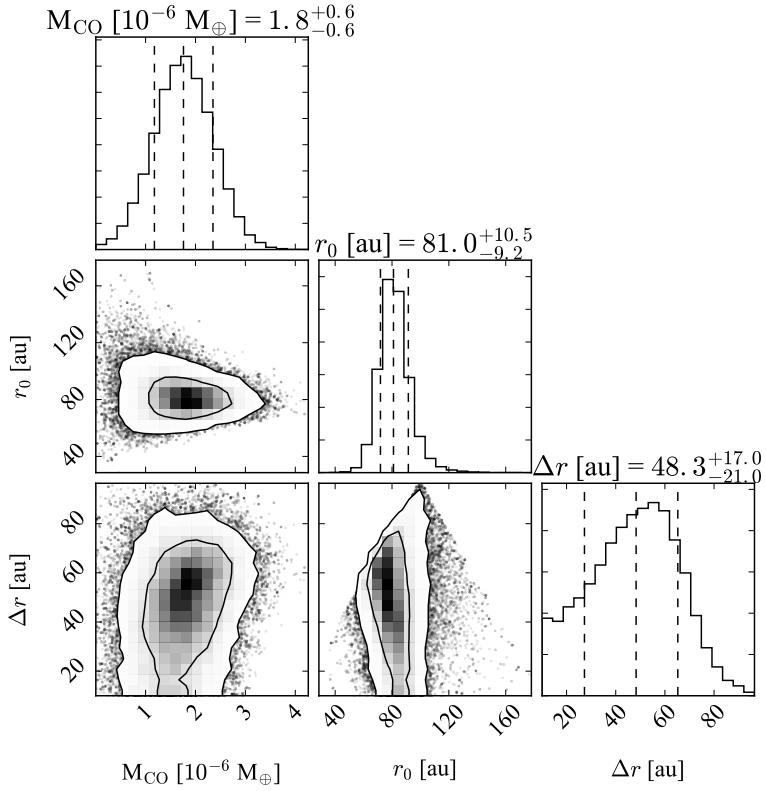

Figure 2.7: Posterior distribution of M_{CO}, r_0 and Δr of the CO disc. The marginalised distributions of M_{CO}, r_0 and Δr are presented in the top, middle right and bottom right panel, respectively. The vertical dashed lines represent the 16th, 50th and 84th percentiles. ***Left middle panel:*** marginalised distribution of M_{CO} and r_0. ***Left bottom panel:*** marginalised distribution of Δr and M_{CO}. ***Middle bottom panel:*** marginalised distribution of r_0 and Δr. Contours correspond to 68%, and 95% confidence regions and the black dots to points of the MCMC outside the 99.7% confidence region. This plot was generated using the python module *corner* (Foreman-Mackey et al., 2014).

2.4 Discussion

2.4.1 Axisymmetry

In §2.3 I analysed the observations assuming an axisymmetric disc, however Stark et al. (2014) found large scale asymmetries consistent with either a recent catastrophic disruption of a large body or disc warping due to interactions with the ISM. Figure 2.8 shows the best axisymmetric ring model image (a, with the inclusion of a second ring), the dirty map of the residuals when the best model is subtracted from the observed visibilities using natural weighting (b), and when the best double ring model is subtracted (c, see Section below). The map of residuals of a single ring is consistent with pure thermal noise without any peak intensity greater than 3σ along the main ring or where scattered light observations suggested an increase in the optical depth (black contours). The same image shows the two compact sources at $\sim 8''$ N and $9''$ SW from the star described in §2.2.1. I can put an upper limit on any fractional enhancement of

emission in the millimetre of ∼10%, which is lower than the asymmetries derived in scattered light (10-42%). This can be translated to a mass upper limit of any dust density enhancement of 5×10^{-3} $M_{\oplus}$ beam^{-1} ($\sim$ 3 Pluto mass), assuming the dust composition and grain size distribution ($a_{\rm max} = 1.0$ cm) described in §2.3. This mass upper limit scales roughly as ($a_{\rm max}$/1 cm)$^{1/2}$ with the Dohnanyi-like size distribution, as noted in §2.3.1.

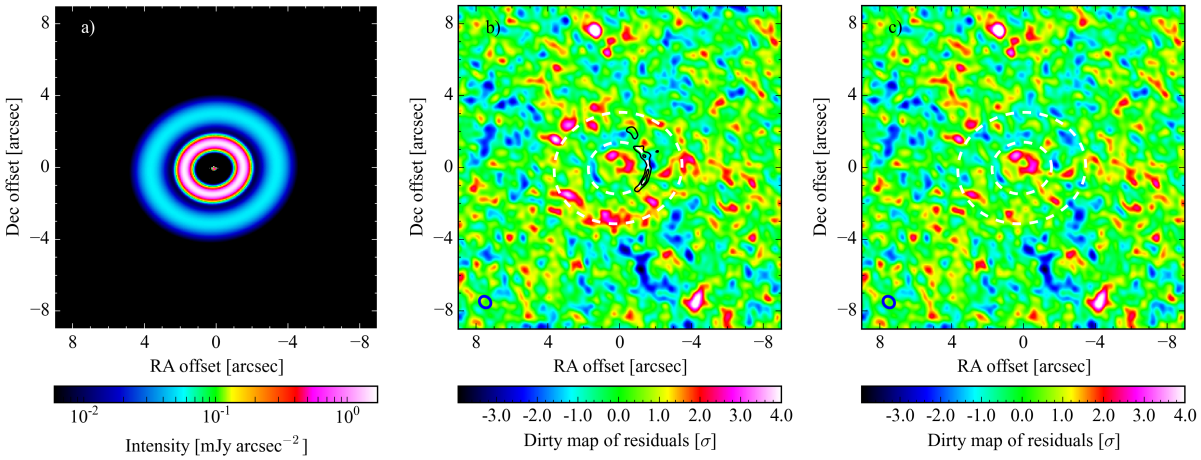

Figure 2.8: ***a)*** Synthetic model image of the best fit model with two rings at 220 GHz. ***b)*** Dirty map of the residuals of the best fit model with a single ring corresponding to natural weighting. The black contours represent the optical depth deviations from a uniform disc derived from *HST* images (Stark et al., 2014, left panel Figure 1). ***c)*** Dirty map of the residuals of the best fit model with two rings corresponding to natural weighting. The white dashed contours in panels b) and c) correspond to radius of the main and second ring of the best fit two rings model. The Clean beam is represented by a blue ellipse ($0\farcs67 \times 0\farcs58$) in the bottom left corner. The x- and y-axes indicate the offset from the stellar position in R.A. and decl. in arcsec, i.e. north is up and east is left.

In a giant collision scenario, the small dust produced from the collision would initially form a trailing outward-propagating spiral structure due to radiation pressure that would orbit the star (Kral et al., 2013). After one orbit the fragments would collide again in the "pinch point" and would continually produce new debris in this region where the density is higher. The small dust produced by collisions would form a leading outward-propagating spiral structure from the pinch point as it is affected by radiation pressure (Jackson et al., 2014), and I would expect the millimetre-sized dust distribution to be narrower at the collision point, increasing the surface brightness. In addition, such a collision would produce a CO excess that would extend from the collision point, along the ring in the direction of motion as far as it can spread in $\sim$ 120 yr at which point is photodissociated, as the disc is optically thin, similar to the case of β Pictoris (Dent et al., 2014; Jackson et al., 2014).

Such features are not present in the millimetre continuum, nor in the CO emission. In §2.2.2 and

§2.3.2 I found that the CO and, thus, all the debris rotates clockwise in the sky. This has strong implications for the interpretation of the asymmetries in scattered light that extend outwards in an anticlockwise direction, forming a trailing spiral. The giant collision scenario could only explain the asymmetry if the collision has occurred in the last 4×10^3 yr or 5 orbits; thus, very unlikely. An alternative explanation of the asymmetry in scattered light could be that the disc is being warped by ISM interactions as suggested by Stark et al. (2014) or that the excess is being produced by a large body releasing small dust (e.g Rappaport et al., 2014), in which case the asymmetric structure would form a trailing spiral of small grains that would orbit the star in clockwise direction.

2.4.2 Extended emission

Even though I model the disc as a single ring, I detect emission that extends at least to $4''$ (see §2.2.1). This emission is recovered both at the east and west side of the disc with no significant differences, and using the image synthesis method as well as using the Clean algorithm. Moreover, it appears in the residuals presented in Figure 2.8b. Assuming the same dust composition and grain size distribution as in the original ring, I model it with a second component in the dust density distribution. I find that this emission can be fitted by a power law surface density distribution, that starts in the main ring with a surface density 25 times lower and that decreases as r^{-1}. An alternative is to add a second ring, in which case I find that the observations are best fitted with a second ring of radius ~ 185 au, FWHM~ 76 au and peak surface density 25 times lower than the maximum of the main ring. In both alternative models I obtain a total flux of 8.6 ± 0.4 mJy and a dust mass of $\sim 0.57 \pm 0.04$ $M_\oplus$, assuming the same grain size distribution for the two components, an assumption which, as noted before, has significant influence on the derived dust mass. The flux uncertainty does not consider the uncertainty on the absolute flux calibration ($\sim 10\%$). Figure 2.8c shows the residuals when the double ring model is subtracted, obtaining a map with pure thermal noise. The origin of this emission could be dust on eccentric orbits produced in the main ring from eccentric planetesimals, or even primordial dust from the protoplanetary disc phase as this is a young system ($\sim$ 23 Myr). This extended component could be related to the change in slope of the derived surface density near 150 au in scattered light (see figure 9 in Stark et al., 2014). Deeper ALMA observations at a different wavelength or even ACA observations coupled with detailed modeling are necessary to conclude about its origin. If the dust surface density distribution has a local minimum between $2''$ and $4''$, this could be evidence of a perturbing planet orbiting in the gap or on a highly eccentric orbit (Pearce & Wyatt, 2015).

2.4.3 Dust size segregation

From the MCMC analysis and the fit of an ellipse to the intensity maxima along the ring, I find that its radius is 86.0 ± 0.4, significantly smaller than at optical wavelengths ($r_0 = 90.5 \pm 1.1$). On the other hand, the distribution of small and millimetre grains overlaps. The main ring of millimetre grains extends roughly from 63 to 110 au, while the small dust is found roughly from 70 au and beyond 200 au. The difference in peak radius of 4.5 ± 1.2 au reveals grain size segregation. Due to radiation pressure, small dust grains released from larger bodies on circular orbits should be put on eccentric orbits with larger semi-major axes that depend on the grain sizes. The net effect is that the larger grains traced at millimetre wavelengths should remain in almost circular orbits at the radius of the parent planetesimal belt, while the spatial distribution of small grains shifts to larger radii (see Thébault & Wu, 2008; Krivov et al., 2008, for detailed modelling). The same segregation has been proposed for other debris discs, e.g. in AU Microscopii Strubbe & Chiang (2006) suggested a parent planetesimal belt at a specific radius to explain the surface brightness profile from scattered light images. This was later corroborated by millimetre observations (MacGregor et al., 2013).

2.4.4 Collisional timescales

Rough estimates of the time scale at which mass is being lost ($\dot{\mathrm{M}}$) from planetesimals in the steady state collisional cascade can be made under the following assumptions: (1) the particles in the disc have small mean eccentricities and inclinations (e and I) equal to 0.05; (2) the relative velocities between particles is equal to $\mathrm{v_K}(1.25e^2 + I^2)^{1/2}$ (valid for Rayleigh distributions of e and I, Lissauer, 1993; Wetherill & Stewart, 1993); (3) planetesimal strengths ($Q^\star_\mathrm{D}$) independent of size and equal to 230 J kg^{-1} (appropiate for km-sized weak ice bodies, Benz & Asphaug, 1999; Wyatt & Dent, 2002). Constant $Q^\star_\mathrm{D}$ leads to a universal particle size distribution with a power law index of -3.5, consistent with the assumptions in §2.3.1. Under these assumptions and using Equations 1.7 and 1.8 I find $\dot{\mathrm{M}} \sim 3\,\mathrm{M}_\oplus\,\mathrm{Myr}^{-1}$. By equating the collisional lifetime of bodies of different size with the age of the system (23 Myr), I also infer a maximum planetesimal size in the collisional cascade (D_c) of at least 1.8 km in diameter. Larger planetesimals may be present, but they would not yet have collided, thus they do not contribute to the collisional cascade. The collisional lifetime scales with the size of the body, D_c, roughly as $(\mathrm{D}_c/1.8\ \mathrm{km})^{0.5}$. I can then extrapolate this to obtain a collisional lifetime of mm-sized grains of 24×10^3 yr (~ 34 orbits).

Note that this collision timescale is broadly consistent with equation 16 in Wyatt et al. (1999) given the different assumptions for these calculations. This emphasises that the collisional lifetime of the mm-sized grains is set by the cross-sectional area in small grains, which is

relatively well constrained from the observations, and is not dependent on the details of the collisional lifetimes of the largest objects discussed above.

2.4.5 Eccentric ring?

In my analysis I also found that the ring center is offset by 96 ± 5 mas in RA and -42 ± 5 mas in decl with respect to the phase center, which was centered at the expected stellar position at epoch. However, the offset is within the astrometric rms of ALMA ($\sim$ $0\farcs1$; private communication with ALMA helpdesk). An upper limit for the eccentricity of the ring can be estimated using a 3σ astrometric error of $0.3''$. This results in an eccentricity upper limit of 0.18, consistent with the eccentricity of 0.02 ± 0.01 measured by Stark et al. (2014).

2.4.6 CO origin

I found that the CO is co-located with the dust, consistent with being axisymmetric and havng the same radial extention as the main ring, although not well constrained. Given the CO derived mass and limits, I can estimate a vertical and radial column density of about 10^{13} and 10^{14} cm^{-2} depending on the gas kinetic temperature and electron densities (see §2.3.2), which implies a CO self shielding coefficient of $\sim 0.7 - 0.9$ (low self-shielding, Visser et al., 2009) and a photodissociation timescale of $\sim$ $140 - 170$ yr due to the interstellar radiation field (see details in Matrà et al., 2015). Even if I assume that the CO is primordial and there is 10^4 times more H_2 than CO, the column density is still too low to shield the CO. Hence, the CO gas must have been produced recently and is probably continually replenished through destructive collisions or photodesorption of icy planetesimals, i.e. it has a secondary origin. Furthermore, given that the CO cannot exist for an orbital period at these distances (680 yr at 86 au), the majority of detected CO must be produced roughly axisymmetrically throughout the disc ring.

If I compare the derived CO mass with other debris discs with CO gas detected and of secondary origin (49 Ceti and β Pic, Dent et al., 2005, 2014), I find that for HD 181327 M_{CO} is at least an order of magnitude lower. Moreover, the CO/dust mass ratio is between $3 - 7 \times 10^{-6}$ in HD 181327, two orders of magnitude lower compared to β Pic (CO/dust mass ratio $\sim 3 \times 10^{-4}$). The difference could be in the host star as 49 Ceti and β Pic are A stars, which could naturally favour the release of volatiles due to stronger radiation environments.

2.4.7 Cometary composition

In §2.4.4 I derived the mass loss rate from planetesimals ($\dot{\mathrm{M}}$) and in §2.4.6 I determined that the CO must be of secondary origin. Assuming that the mass of CO present in gas phase is in steady state, I can derive the CO ice mass fraction f_{CO} of planetesimals as a function of $\dot{\mathrm{M}}$ and the photodissociation timescale of CO τ_{co}. In steady state I expect $f_{\mathrm{CO}} \times \dot{\mathrm{M}} \approx \mathrm{M_{CO}} \times \tau_{\mathrm{co}}^{-1}$ (Equation 1.10), thus

$$f_{\mathrm{CO}} = 4.3 \times 10^{-3} \left(\frac{\mathrm{M_{CO}}}{1.8 \times 10^{-6}\ \mathrm{M_\oplus}} \right) \left(\frac{\dot{\mathrm{M}}}{3\ \mathrm{M_\oplus\ Myr^{-1}}} \right)^{-1} \left(\frac{\tau_{\mathrm{co}}}{140\ \mathrm{yr}} \right)^{-1}. \quad (2.3)$$

This value could vary from $2{\times}10^{-3}$ to $7{\times}10^{-3}$ due to systematic uncertainties in $\mathrm{M_{CO}}$ and $\tau_{\mathrm{co}}(\mathrm{M_{CO}})$. Moreover, the value of $\dot{\mathrm{M}}$ is highly dependant on $Q_{\mathrm{D}}^{\star}$ which could vary between 200 and 10^4 J kg^{-1} for km-sized bodies, making $\mathrm{f_{CO}}$ range between $2{\times}10^{-3}$ to 0.1. Another big uncertainty is that an important fraction of CO could also be a product of CO_2, released from icy bodies and that photodissociates in a shorter timescale of ~ 30 yr (Hudson, 1971; Lewis & Carver, 1983), or produced by CO_2 ice photodesorption. Thus, the CO ice fraction above can be interpreted as CO+CO_2 ice mass fraction of planetesimals. The net effect is that $f_{\mathrm{CO+CO_2}}$ is probably between 0.2%-18% which is consistent with the CO+CO_2 abundances in Solar system comets (CO+CO_2 mass fraction of 3-27%, Mumma & Charnley, 2011). If the planetesimals have an ice to rock fraction similar to the Solar System of about unity, I can extrapolate and obtain an (CO+CO_2)/H_2O ice abundance ratio between 0.3-13%. Note that the CO and CO_2 production rate does not depend on the unknown mechanism that is releasing CO, as it will always be limited by the destruction rate of icy solids that sublimate CO or expose an icy surface.

2.4.8 Dust-gas interactions

The origin of the ring-like morphology of the HD 181327 disc is unclear. Lyra & Kuchner (2013) showed that dust-gas interactions can be non-negligible in debris discs and produce instabilities that shape the dust and gas distribution in narrow ring-like structures. These instabilities arise if: the dust stopping time τ_f is in the range of $0.1 - 10/\Omega_{\mathrm{K}}$, with Ω_{k} the Keplerian rotation frequency, and dust to gas ratio $\varepsilon \lesssim 1$. To ascertain if this could explain the dust distribution in the HD 181327 debris disc I estimate τ_f and ε. A reasonable value for the stopping time as a function of the grain size can be obtained using the CO gas mass derived in the modeling, i.e. $\mathrm{M_{CO}} = 1.2 \times 10^{-6} - 2.9 \times 10^{-6}\ \mathrm{M_\oplus}$, and if I assume: (1) the gas is dominated by CO, H_2O and their photodissociaton products; (2) the CO/H_2O ice abundance ratio in planetesimals derived above (0.3-13%); (3) the C/CO abundance ratio is ~ 100, the same as in β Pic (Roberge et al., 2006). Under these assumptions I find a total gas mass that could vary

between 7×10^{-4} and 0.06 $\mathrm{M}_{\oplus}$.

The stopping time defined as $\tau_s = m\mathrm{v}_{\mathrm{rel}}/F_{\mathrm{drag}}$ can be estimated considering the Epstein drag force that gas exerts on dust grains. I approximate the dust grain velocities with the same expression for the relative velocities presented in §2.4.4. The gas drag force depends on the gas density, gas kinetic temperature (T_k) and the grain size (a_d). The first can be derived assuming a gas density distribution proportional to the dust density distribution, while the second is assumed to be close to the mm-dust dust grain temperature in the ring (∼50 K). Finally I obtain

$$\tau_{\mathrm{s}} \simeq 2 \times 10^3 \left(\frac{\mathrm{M}_{\mathrm{gas}}}{0.06\ \mathrm{M}_{\oplus}}\right)^{-1} \left(\frac{a_d}{1\ \mathrm{mm}}\right) \left(\frac{T_k}{50\ \mathrm{K}}\right)^{-1/2} \Omega_K^{-1}. \tag{2.4}$$

Thus, for mm-sized particles $\tau_{\mathrm{s}} \gtrsim 2 \times 10^3 \Omega^{-1}$, much longer than the necessary to trigger the instability. Moreover, the stopping time is even longer than the collisional lifetime calculated in §2.4.4 ($\sim$ 34 orbits). Only for grains at the bottom of the collisional cascade, with sizes $\lesssim 10$ μm, the stopping time is in the range where the instability could be triggered. The dust-to-gas mass ratio of grains smaller than 10 μm is of the order of unity. However, given that this instability does not apply to the mm-sized grains, and the distribution of micron-sized grains is consistent with being derived from the mm-sized grains, with any differences in their distribution attributable to radiation pressure without the need for the photoelectric instability, I conclude that this instability does not play a significant role in this disc. Furthermore, the collisional lifetime of μm-sized grains can be obtained using the fractional luminosity of the disc (Wyatt et al., 1999), which translates to ∼5 orbits, while the timescale for the instability to occur is tens of orbital periods (Lyra & Kuchner, 2013).

2.5 Conclusions

I resolved the HD 181327 debris ring in dust continuum for the first time at millimetre wavelengths with an angular resolution of $0\farcs47 \times 0\farcs36$ and I detected ^{12}CO (2-1) emission for the first time in a debris disc around a solar-type star. Assuming an axisymmetric disc, I found that the dust continuum is best fitted with a ring of radius 86 ± 0.4 au and width 23.1 ± 1.0 au.

The ALMA observations are consistent with an axisymmetric ring and no significant residuals along the main ring remain after subtracting the best fit model to the continuum data. I also derived an upper limit for any dust overdensity along the primary ring. When I compared to previous HST observations at optical wavelengths I found that the derived orientations of the disc on the sky are consistent, but the ring radius derived from the data is significantly smaller. This result is consistent with grain size segregation due to radiation pressure.

Additionally, I detected low-level emission that extends beyond the primary ring, consistent with either an extended halo of dust or a secondary ring. This result is robust against different image synthesis methods and is also recovered in the residuals of the best-fit ring model. Deeper ALMA or ACA observations could help to study the origin of this emission.

Finally, I found that the CO is co-located with the dust, favouring a secondary origin scenario. Assuming axisymmetry I model the CO emission in the non-LTE regime with different kinetic gas temperatures and collisional partner densities. With gas kinetic temperatures of 50 K and electron densities similar to the ones found in β Pic, the emission is best fitted with a total CO gas mass of $1.8 \pm 0.6 \times 10^{-6} \mathrm{M}_{\oplus}$. In addition, I derived CO+CO_2 ice abundances in planetesimals and I found that they are consistent with the composition observed in Solar system comets. Furthermore, it is unlikely that the effect of hydrodynamics can affect the structure of the disc.

3

ALMA observations of the η Corvi debris disc: inward scattering of CO-rich exocomets by a chain of 3-30 $M_\oplus$ planets?

3.1 Introduction

Among the sample of old stars with hot dust, the $1-2$ Gyr old F2V star η Corvi (HD 109085, HIP 61174, Ibukiyama & Arimoto, 2002; Mallik et al., 2003; Vican, 2012, hereafter assumed to be 1.4 Gyr old, consistent with isochrone fitting in the HR diagram), located 18.3 pc away (van Leeuwen, 2007), is particularly interesting because it presents both a hot and a cold dust component in its SED, where the hot dust exceeds the brightness limit mentioned in §1.6. Its infrared excess was first detected with *IRAS* (Stencel & Backman, 1991), after which several observations from the optical to the millimetre have targeted this system. From MIR observations, Smith et al. (2009) determined that the hot dust must be located within 3 au from the star. More recent observations with the Large Binocular Telescope Interferometer (LBTI) and the Keck Interferometer have confirmed this and determined that the hot component is located at projected separations of $\sim$ 1.4 au and 0.2-0.8 au from the star, respectively (Defrère et al., 2015; Kennedy et al., 2015b; Lebreton et al., 2016). Moreover, it is known that the the hot dust luminosity has stayed almost constant over the last three decades

(Duchêne et al., 2014). On the other hand, Wyatt et al. (2005) resolved the cold component of the system with SCUBA/JCMT at millimetre wavelengths, finding that it has a mean radius of ~ 150 au. At 70 μm *Herschel* imaged both hot and cold components, resolving the outer belt and confirming that the hot dust has large amounts of small dust below the blow-out size (previously known from *IRS*, Chen et al., 2006) providing further evidence that the hot dust cannot be explained by a steady-state collisional cascade and suggesting a more violent origin (Duchêne et al., 2014).

Several scenarios have been proposed to explain the high levels of MIR emission in η Corvi. Wyatt et al. (2010) suggested that the system could host a population of highly eccentric planetesimals, colliding at pericentre within a few au producing the hot dust and observed excess. These planetesimals would survive for longer timescales due to their large apocentre in the cold belt. While this scenario is appealing in connecting the the inner and outer dust components in the system, it was ruled out by *Herschel* resolved observations (Duchêne et al., 2014) as no emission is detected between the hot dust location and the outer belt. The hot dust could be also a product of a giant impact on a planet close in or recent giant collision in an in situ asteroid belt rather than an ongoing collisional cascade. This would be consistent with the spectroscopic features of impact produced silica and high-temperature carbonaceous phases revealed by *Spitzer* (Chen et al., 2006; Lisse et al., 2012). However, these events are expected to be rare and the produced small dust short lived compared to the age of the system (Kral et al., 2015), although η Corvi is one of just two FGK stars with hot dust at this level out of the DEBRIS sample of ~ 300 stars, i.e. it is not possible to exclude an unlikely scenario as we could be witnessing the system at a special time. On the other hand, the hot dust also displays spectral features of primitive cometary material consistent with icy solids formed further out in the system (Lisse et al., 2012), and thus, transported by an unknown process to within a few au. There are two known mechanisms that can transport material inwards, Poynting-Robertson (P-R) drag and interactions with a single or multiple planets. The first can deliver small grains from the outer disc to the inner regions, but this mechanism is not efficient enough to explain the hot dust in η Corvi given the low optical depth or fractional luminosity of the outer belt (Kennedy & Piette, 2015). Thus, it seems necessary to invoke the presence of planets in the system.

Three scenarios remain that could explain the hot dust level and its composition:

1. the system is going through an instability, analogous to the Late Heavy Bombardment (LHB) in the Solar System, scattering comets from the outer belt to the innermost regions (e.g., Bonsor et al., 2013);

2. planets in a rather stable configuration in the system are scattering dust from the outer disc feeding the hot dust or bigger icy solids that then collide closer in producing the hot

dust (e.g., Bonsor et al., 2012, see Chapter 6);

3. planetesimals are scattered by planets in the system, colliding with a planet within a few au releasing large amounts of debris.

In this chapter I present the first continuum observations of η Corvi with ALMA to study in detail the continuum dust emission of its cold outer belt at 0.88 mm, and look for features that can hint at one of the three possible planet-driven scenarios described above to explain the hot dust. In §3.2 I describe the ALMA observations, continuum imaging and search for any CO emission in the disc. Then, in §3.3 I model the continuum data with parametric disc models to study the distribution of planetesimals in the disc. I also derive CO gas masses and upper limits considering non-LTE. In §3.4 I discuss the implications of the ALMA continuum data, how it fits with the hypothesis of material being transported from the outer to the inner regions of the disc; I also discuss the origin of a tentative CO gas detection, and I place some constraints on a planet between the hot dust and outer belt based on the continuum observations. Finally in §3.5 I summarise the main results and conclusions of this chapter.

3.2 Observations

ALMA band 7 observations (340 GHz) of η Corvi were carried out from 2013 Dec 15 to 2015 Jan 1 under the project 2012.1.00385.S (PI: M. C. Wyatt), resulting in 6 successful executions. Each set of observations is a 3-point mosaic along the disc major axis, separated by 8.″8 and centered on η Corvi. The primary beam FWHM of a single pointing is 17.″9, which allowed to reach a combined primary beam efficiency above 50% in a elongated region of 36″x18″ oriented as the disc in the sky. Array configurations were very compact, with baselines ranging from 26 to 240 m (5th and 95th percentiles). This allows to recover angular scales from 1″ up to 7″.

The band 7 spectral setup consisted of four spectral windows. Three were set to observe the continuum emission centered at 335.744, 337.644 and 347.455 GHz, each one with 128 channels of 14 km/s width (effective spectral resolution of 28 km s^{-1}), obtaining a 2 GHz total bandwidth per spectral window. The fourth included the ^{12}CO 3–2 line at 345.798 GHz and was set with 3840 finer channels, each one with a width of 0.42 km s^{-1}(effective spectral resolution of 0.82 km s^{-1}), obtaining a total bandwidth of 1.9 GHz. The four together provided an effective bandwidth of 7.9 GHz to study the continuum emission. The total time on source, t_{sci}, was 4.5 h, so the actual time spent on source with the pointing on the location of η Corvi itself is 1.5 h.

3.2.1 Continuum emission

The image reconstruction of the dust continuum is performed with the CLEAN algorithm and task in CASA 4.4 (McMullin et al., 2007a), using natural weights, and combining the four spectral windows to recover the highest S/N. Using natural weights, the beam has a size of $1\farcs18 \times 0\farcs65$ (equivalent to 22×12 au), with a position angle (PA) of 89°. The image noise level before correcting by the primary beam is 20 μJy beam^{-1}, and after correcting by the primary beam it increases with distance to the star as the primary beam efficiency decreases. The image noise around the outer belt varies from 22 μJy beam^{-1} near the disc major axis up to 30 μJy beam^{-1} close to the minor axis. In Figure 3.1 I present the Clean image tapering the visibilities with the Fourier transform of a Gaussian of FWHM of $1\farcs2$, to obtain a less elongated beam of $1\farcs5 \times 1\farcs3$ with a PA of $88°$, and higher S/N per beam. At the center of the tapered image, the noise level is 30 μJy beam^{-1}, varying from 33 to 45 μJy beam^{-1} around the outer belt. Substructure is present along the belt in the Clean image, with two minima to the south west of the star. However, the emission is still consistent with an axisymmetric belt given the S/N (see §3.3). Compared with the PACS image at 70 μm obtained by *Herschel* (previous best image of the outer belt), I obtain a spatial resolution four times higher and a 50% higher S/N if I degrade the ALMA image to the PACS resolution.

Using the non-tapered image, I obtain an intensity peak of 287 ± 20 μJy beam^{-1} at the stellar location, which is consistent with the expected photospheric emission of 250 ± 7 μJy, extrapolated from the available photometry at 2.2, 3.6, 3.8, and 4.8 μm assuming a spectral index of 2 (Sylvester et al., 1996). However, the stellar emission at these wavelengths could deviate significantly from Rayleigh-Jeans as observed for the Sun (e.g., Loukitcheva et al., 2004; Fontenla et al., 2007). Subtracting the extrapolated stellar flux I can place an upper limit on any extra emission, e.g. hot dust. Considering the different uncertainties I find a 3σ upper limit of 100 μJy on the hot dust flux at 0.88 mm, higher than the 44 μJy extrapolated from the 70 μm flux excess detected with *Herschel* (Duchêne et al., 2014) using a spectral index of 2.0 (optimistic prediction), and far above the 1.5 μJy predicted by the hot dust model presented in the same study to fit the SED. Therefore, it is not surprising that no hot dust emission is detected.

I measure a total disc flux of 13.7 ± 0.5 mJy by integrating the continuum emission inside an elliptic mask with the same orientation and ellipticity as the disc, i.e. inclination (i) of $35°$ and a position angle (PA) of $117°$, and within a semi-major axis of $11''$[1]. At a similar wavelength of 0.85 mm, SCUBA-2/JCMT observed η Corvi measuring a total flux of 15.5 ± 1.4 mJy, which extrapolated to 0.88 mm with a spectral index of 3.0 (i.e. 14.0 ± 1.3 mJy) is consistent with the

[1]The estimation of i and PA is presented in §3.3, obtaining values consistent with previous Herschel observations, (Lebreton et al., 2016).

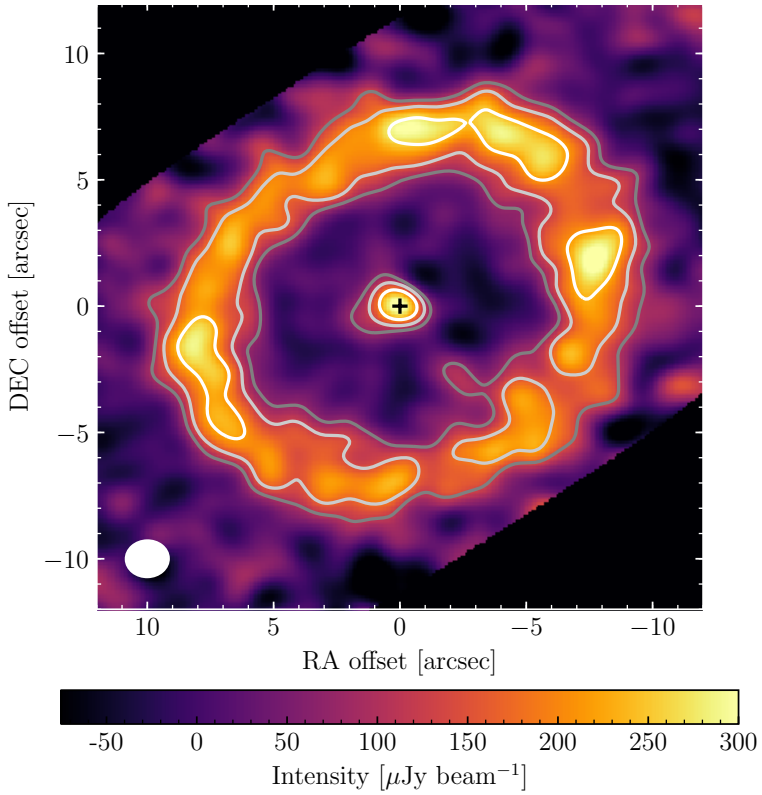

Figure 3.1: ALMA dust continuum Clean image at 0.88 mm (Band 7), with natural weights, primary beam corrected, and tapered by a Gaussian of FWHM of 1.″2. The beam size is $1.''5 \times 1.''3$ and is represented by a white ellipse in the bottom left corner. At the center of the image, the noise level is 25 μJy beam^{-1}. The black masked region indicates a primary beam response below 40%. The contours represent emission above 3, 5 and 8 times the local noise level. The x- and y-axes indicate the offset from the stellar position in R.A. and decl. in arcsec, i.e. north is up and east is left. The stellar position is marked with a black "+".

ALMA observations.

To study the radial profile of the surface brightness I compute the average intensity over 40° wide wedges along the major and minor axes, and the average intensity profile at all azimuths around ellipses oriented as the disc in the sky. Figure 3.2 shows the intensity profiles. Note that points in the radial profile separated by less than $\sim 1''$ (beam size) are not independent. The peak intensity along the major and minor axes are 90 ± 6 μJy beam^{-1} and 82 ± 9 μJy beam^{-1}, respectively, both consistent within the uncertainties, while the average profile at all azimuths has a peak intensity of 93 ± 4 μJy beam^{-1}. Along the major axis of the disc, the belt peaks at $8''.30 \pm 0''.06$ (151 ± 1 au), where the error is estimated as $\sim$Beam$_{\rm fwhm}/(S/N)$, with S/N~ 23 at the peak – this uncertainty could be underestimated as the relation above is strictly valid only for point sources. The deprojected radial profile in the lower panel of Figure 3.2 shows that the belt is clearly spatially resolved, spanning over $\sim 5''$, or ~ 90 au in radial extent.

Similarly, I study the surface brightness variations along position angle averaging the disc emission radially between 120 and 180 au, and over arcs of 18°. This is shown in Figure 3.3. Unlike Duchêne et al. (2014) where they found evidence of asymmetric disc emission at 70 μm with the north-west side having a peak intensity higher by a factor of 1.4 compared to the south-east side (see their Figure 5), I find no evidence of such asymmetries around the azimuthal profile of the belt. In fact, following the same procedure as they did, I compare the peak intensity of the averaged radial profile of the north-west with the south-east ansae, finding that they are consistent within uncertainties (ratio of 0.9 ± 0.1 with the south-east being brighter) and the first cannot be brighter by more than a factor of 1.2 (3σ limit). However, when studying the contribution to the total flux from the north-west and south-east halves of the disc (divided by the minor axis of the disc), I find that they have fluxes of 7.5 ± 0.3 and 6.2 ± 0.3 mJy, respectively. This is marginal evidence for emission excess on the north-west side of the disc as the Herschel showed, but still consistent with being axisymmetric.

3.2.2 CO (3-2)

After subtracting the continuum emission from the visibilities using the CASA task *uvcontsub*, I search for any CO $J = 3 - 2$ gas emission that could be present in the system. I find no significant CO gas emission along the continuum subtracted dirty channel maps (no Clean iterations are necessary since there is no significant emission in the dirty channel maps). As shown in Chapter 2, the detection limits can be improved by azimuthally averaging the dirty channel maps and integrating in frequency. Similar to the method presented in the previous section, I calculate the mean CO intensity at different radii azimuthally averaging the continuum subtracted dirty channel maps around ellipses oriented as the outer belt (see

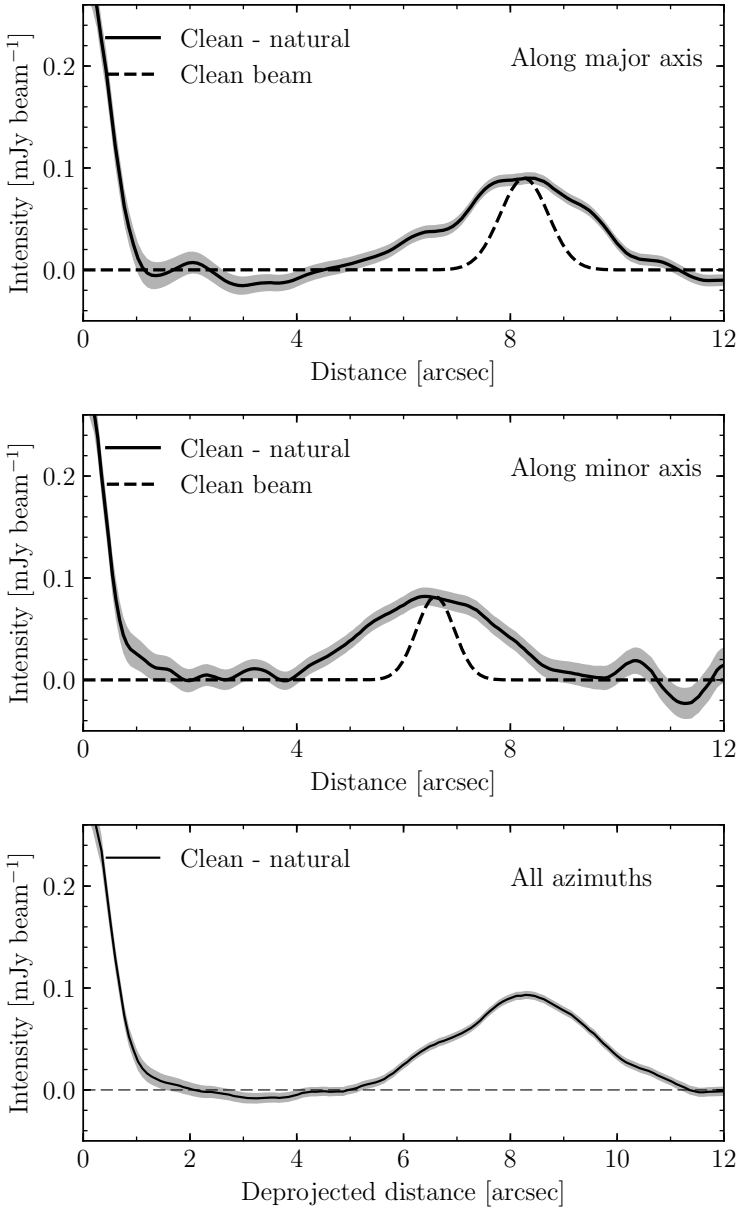

Figure 3.2: Intensity radial profiles of the dust continuum vs distance to the star along the major (top panel) and minor axis of the disc (middle panel) obtained averaging over 40° wide wedges. In the bottom panel I present the mean intensity at all azimuths vs the deprojected distance to the star. The grey areas represent the 68% confidence region.

§3.3.1). I also integrate the emission in frequency or radial velocity (RV) between the minimum and maximum RV expected from Keplerian rotation at each radii, and assuming the same inclination as the outer belt (37°). I restrict the maximum RV to 6 km s^{-1}, equivalent to the maximum RV at 10 au from the star, as it is not possible to spatially resolve emission within 10 au. The stellar radial velocity, $v_\star$, is not well constrained for this system, with Gaia DR2 providing the best constraint of 0.7 ± 0.7 km s^{-1} (Gaia Collaboration et al., 2016b, 2018). Therefore, I vary $v_\star$ between -1.4 to 2.8 km s^{-1}to search for any significant CO disc emission

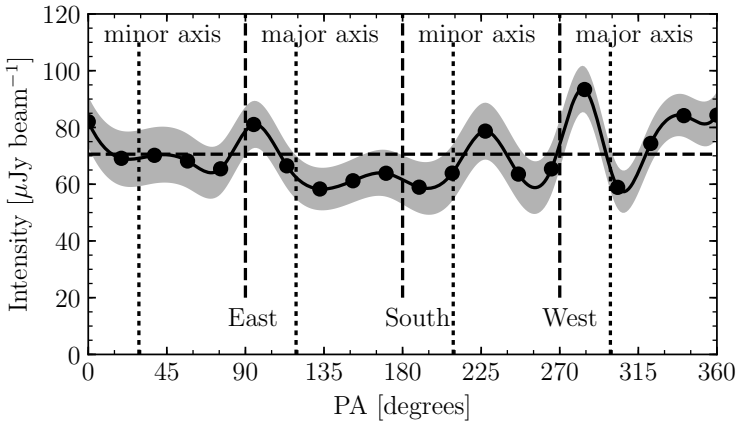

Figure 3.3: Intensity azimuthal profiles of the dust continuum emission vs position angle (PA) obtained averaging over elliptic annuli of semi-major axes between $0\farcs8$ and $9\farcs8$ (equivalent to 125 and 180 au) and over 18° wide wedges (centered at the black dots). The continuous line is obtained with a cubic spline interpolation between the black dots. The horizontal dashed line represents the mean intensity around the outer belt. The grey area represents the 68% confidence region.

that could be present in the data. At each radius I estimate the uncertainty based on the rms on each channel, the number of independent spectral resolution elements considered ($\sim$ $\frac{\text{number of channels}}{2.667}$, due to Hanning smoothing[2]) and the number of independent beams around each ellipse ($\sim \frac{\text{Perimeter of ellipse}}{\text{beam major axis}}$).

In Figure 3.4 I present the mean intensity profile spectrally integrated assuming $v_\star = 1.5$ km s^{-1}. The continuum radial profile is overlayed in blue dashed line. I find an intensity peak of 4.7 ± 1.1 mJy beam^{-1} km s^{-1}at $\sim 1\farcs2$. This peak is present above 3σ for $v_\star$ ranging from -0.5 to 2.8 km s^{-1}. Apart from the peak at $\sim 1\farcs2$ from the star, no significant emission is detected. The peak of the emission corresponds to a radius of 22 ± 6 au, where the uncertainty is estimated as the beam semi-major axis divided by the S/N. This implies that the putative detection is not strictly co-located with the hot dust. Note that the sensitivity of the intensity profile varies with radius because the number of beams and spectral resolution elements over which I integrate changes with radius. Therefore, it is possible that similar or even higher CO levels are present within $1\farcs2$, where the integrated sensitivity is lower.

In Figure 3.5 I present a spectrum obtained by integrating the dirty map over an elliptic mask oriented as the outer belt and with an inner and outer semi-major axes of $0\farcs8$ to $2\farcs0$ (15 to 37 au), respectively, to maximise the S/N. I also smoothed the spectrum convolving it with a Gaussian kernel with a standard deviation of 2.5 channels or 1.1 km s^{-1}. The spectrum shows a line centered at 1.8 km s^{-1}, consistent with the expected profile for a ring of CO gas rotating around the star at a radius of ~ 20 au. The total line flux between -2.7 km s^{-1}and 6.3 km s^{-1}is

[2]https://safe.nrao.edu/wiki/pub/Main/ALMAWindowFunctions/Note_on_Spectral_Response.pdf

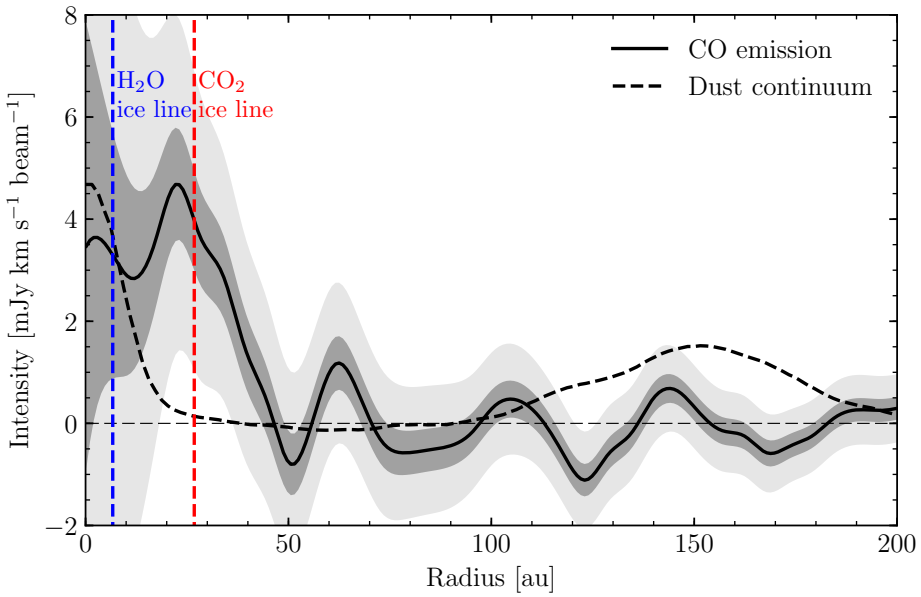

Figure 3.4: Mean CO intensity vs distance to the star obtained by azimuthally averaging the continuum subtracted dirty channel maps and integrating over the line width expected due to Keplerian rotation, assuming an heliocentric stellar radial velocity of 1.5 km s^{-1}. The grey areas represent the 68% confidence region. The dust continuum radial profile is overlayed with a black dashed line. The vertical blue and red dashed lines represent the water and CO_2 ice lines assuming black body temperatures.

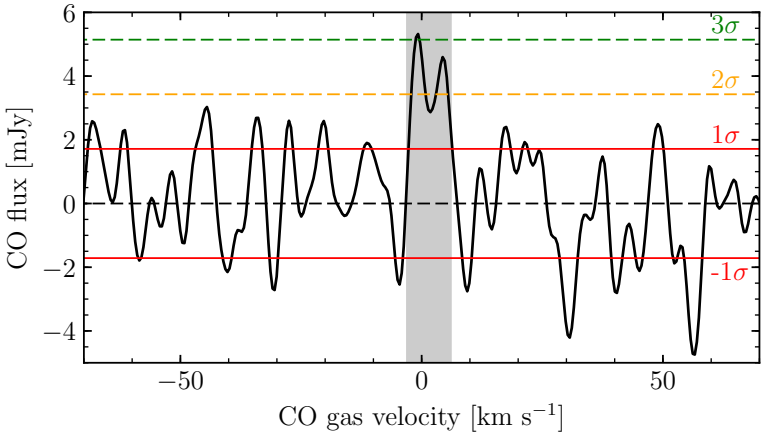

Figure 3.5: Continuum subtracted integrated spectrum inside an elliptic mask of minimum and maximum semi-major axis of $0\farcs8$ and $2\farcs0$, and oriented as the dust continuum outer belt. The original spectrum was smoothed with a Gaussian kernel with standard deviation of 2.5 channels. The horizontal lines represent ±1, 2, 3 and 4σ levels. The grey region represents velocities between -2.7 km s^{-1}and 6.3 km s^{-1}, equivalent to the line width expected due to Keplerian rotation at $\sim$20 au ($1''$). The velocities represent the Doppler shift with respect to 345.796 GHz in the Barycentric reference frame.

38 ± 9 mJy km s^{-1}(4σ). This is used in §3.3.7 to estimate the mass of CO that could be present at this location. If the gas is in Keplerian rotation, the emission should have a butterfly

pattern, with half of the emission having a positive or negative Doppler shift and arise from either the south east or north west half of the disc (separated by the minor axis of the disc). Thus, I try to integrate the emission on one half of the disc for positive Doppler shifts and on the other half for negative Doppler shifts to reduce the integrated noise. I find similar S/N ratios for both possible disc orientations, slightly preferring the north-western and south-eastern halves having positive and negative Doppler shifts, respectively, but not at a significant level. With the preferred orientation I obtain a S/N of 3.9 for the integrated flux, while with the opposite the S/N is 3.4. The small difference in S/N shows that there is emission with the same Doppler shift on both halves of the disc, in contradiction with the Keplerian and disc orientation assumption. This could be due to the emission being not very well constrained in position as I am using the dirty channel maps, the uncertain stellar radial velocity, the disc orientation being different compared to the outer belt, or deviations from Keplerian rotation. I can also estimate the likelihood of that any search of CO conducted over the range $v_\star = 0.7 \pm 0.7$ km s^{-1} and over annuli with semi-major axes within the range $0 - 8''$ would result in a 4σ detection. I find that this has a probability of 0.3%. The origin of this emission if real is discussed in §3.4.2. Deeper ALMA observations are necessary to confirm this detection and study the gas rotation pattern.

In order to place upper limits on the total CO emission from the outer belt and inner component (co-located with the hot dust), I compute the uncertainty on the total flux given the noise level on each channel map and the number of velocity channels to consider. Around the outer belt I obtain an integrated noise level of 12 mJy km s^{-1} integrating azimuthally and radially along the belt seen in continuum emission (from 130 au to 170 au), and in velocity at the expected radial velocity on each pixel due to Keplerian rotation and 37° inclination. For the inner component, I integrate the emission inside $1\farcs2$ between ± 21 km s^{-1}(expected line width assuming no emission is coming from a radii smaller than 1 au) obtaining an integrated noise level of 11 mJy km s^{-1}. Based on this, in §3.3.7 I also calculate a 3σ upper limit on the CO mass that could be in the outer belt and close in co-located with the hot dust.

3.3 Disc modelling

In this section, I analyse the ALMA observations in the uv space and infer the mm-sized dust distribution by fitting the observed visibilities in the continuum with four different debris disc models:

1. an outer belt with a radial Gaussian surface density distribution to constrain the mean radius and width of the belt;
2. a self-stirred disc following the parametrization presented in Kennedy & Wyatt (2010) to

study if the disc is consistent with such a scenario;

3. a LHB-like density distribution, which connects the outer belt with the inner regions with a surface density proportional to $r^{1.5}$, that then I relax to a simple axisymmetric double power law distribution;

4. an eccentric outer belt to constrain the disc global eccentricity.

The models consist of a central star modelled using a Kurucz template spectrum[3] (Kurucz, 1979) with an effective temperature of 7000 K and a stellar radius of 1.75 $R_{\odot}$ to fit the stellar flux (~ 250 μJy at 0.88 mm) as I impose the luminosity of the star to be $4\pi R_{\star}^2 \sigma T_{\star}^4$. The star is surrounded by a dusty disc with grains formed by astrosilicates (Draine, 2003), amorphous carbon (Li & Greenberg, 1997) and water ice (Li & Greenberg, 1998), with mass fractions of 70%, 15% and 15%, respectively, with an internal density of 2.9 g cm^{-3} and mixed using the Bruggeman's rule (Bohren & Huffman, 1983) to match the composition used in Duchêne et al. (2014). I assume a Dohnanyi-like grain size distribution with a power law index of -3.5, with minimum and maximum grain size of 1.0 μm and 1.0 cm, respectively. This leads to a mass-weighted absorption opacity $\kappa_{\rm abs} = 3.8$ cm^2 g^{-1} at 0.88 mm, computed using the Mie theory code of Bohren & Huffman (1983). While $(a_{\rm min}, a_{\rm max})$, $\kappa_{\rm abs}$ and the derived total dust mass are highly dependent on the choice of the grain composition and size distribution, these assumptions have very little effect on the derived disc structure. Finally, I assume a Gaussian vertical mass distribution parametrized by a scale height H that scales linearly with radius as $H = hr$.

Using RADMC-3D[4] (Dullemond et al., 2015) I solve the thermal equilibrium of the mean dust species defined above, obtaining a temperature field that varies with radius as $42(r/150 \text{ au})^{-0.5}$ K, that then is used to produce synthetic images of the system at 0.88 mm. Finally, models are compared with the observations simulating model visibilities with the same uv-coverage and pointing offsets.

A Bayesian approach is used to constrain the different parameters of the disc models (details below), sampling the parameter space to recover the posterior distribution using an MCMC sampler as in Chapter 2. The posterior distribution is defined as the product of the likelihood function and the prior probability distribution functions for each parameter, which I assume are uniform. The likelihood function is defined proportional to $\exp(-\chi^2/2)$, with χ^2 defined as in Equation 2.2. The estimated error $\delta V_{\rm data,i}$ is calculated based on the intrinsic dispersion of the visibilities over one scan with the task *statwt* from CASA 4.4. In my priors, I impose a lower limit to the vertical aspect ratio, h, equivalent to 0.03. The different models are detailed below and compared in §3.3.5 using the Bayesian information criterion (BIC, Schwarz, 1978).

[3] http://www.stsci.edu/hst/observatory/crds/k93models.html
[4] http://www.ita.uni-heidelberg.de/~dullemond/software/radmc-3d/

Table 3.1: Belt model best fit values. Median ± uncertainty based on the 16th and 84th percentile of the marginalised distributions. For parameters with distributions extending out to the minimum or maximum allowed values, a 1σ upper or lower limit is specified based on the 68th or 32nd percentile, respectively.

Parameter	Best fit value
M_d [$M_\oplus$]	0.014 ± 0.001
r_0 [au]	152 ± 3
Δr [au]	46 ± 5
h	< 0.13 (1σ)
PA [°]	117 ± 4
i [°]	35 ± 2

3.3.1 A radially symmetric belt

In order to estimate the mean radius and radial width of the outer belt, the first model consists of a belt with a surface density distribution that is parametrized with a Gaussian centered at r_0 and with a radial full width half maximum (FWHM) Δr as

$$\rho(r, z) = \rho_0 \exp\left[-\frac{4\ln(2)(r - r_0)^2}{\Delta r^2} - \frac{z^2}{2H^2}\right], \tag{3.1}$$

where ρ_0 is defined to match the total dust mass, M_d, and $H = \mathrm{h}r$ is the scale height. Then, the dust density distribution is defined by M_d, r_0, Δr and h that I leave as free parameters. Two extra free parameters were defined to fit the disc inclination, i, and position angle, PA, in sky. In Table 3.1 I summarise the best fit values and uncertainties. I find the disc mean radius is 152 ± 3 au and a radial FWHM of 46 ± 5 au, consistent with the previous estimate in §3.2.1.

I derive an inclination and PA of $35 \pm 2°$ and $117 \pm 4°$, respectively, that match previous estimates by Lebreton et al. (2016) ($i = 38.2 \pm 3.6°$ and PA$= 116.2 \pm 1.1°$). The inferred disc mean radius and radial width are also consistent with their derived dust distribution, with differences due to the different disc model that they assumed. The total flux of the best fit model is 13.3 ± 1.0 mJy (excluding calibration uncertainties), consistent with the measured flux from the Clean image (13.7 ± 0.5 mJy). I also find that the posterior distribution of the aspect ratio h peaks at 0.10, $\sim 2\sigma$ above the lower limit in the prior distribution (0.03), but still consistent with 0.

A synthetic image, simulated ALMA image, and dirty map of the residuals of the best fit model are presented in Figure 3.6a, d and g, respectively (left column). Despite the model being axisymmetric, the simulated ALMA image shows asymmetric structure along the belt, similar to the observed features in the ALMA image (see Fig. 3.1), thus the observed asymmetries are likely an artefact of the image reconstruction caused by a low S/N in the visibilities and the uv-sampling. After subtracting the model visibilities, the dirty map of the residuals shows no excess above 3σ that could be attributed to an overdensity in the belt or emission inside the

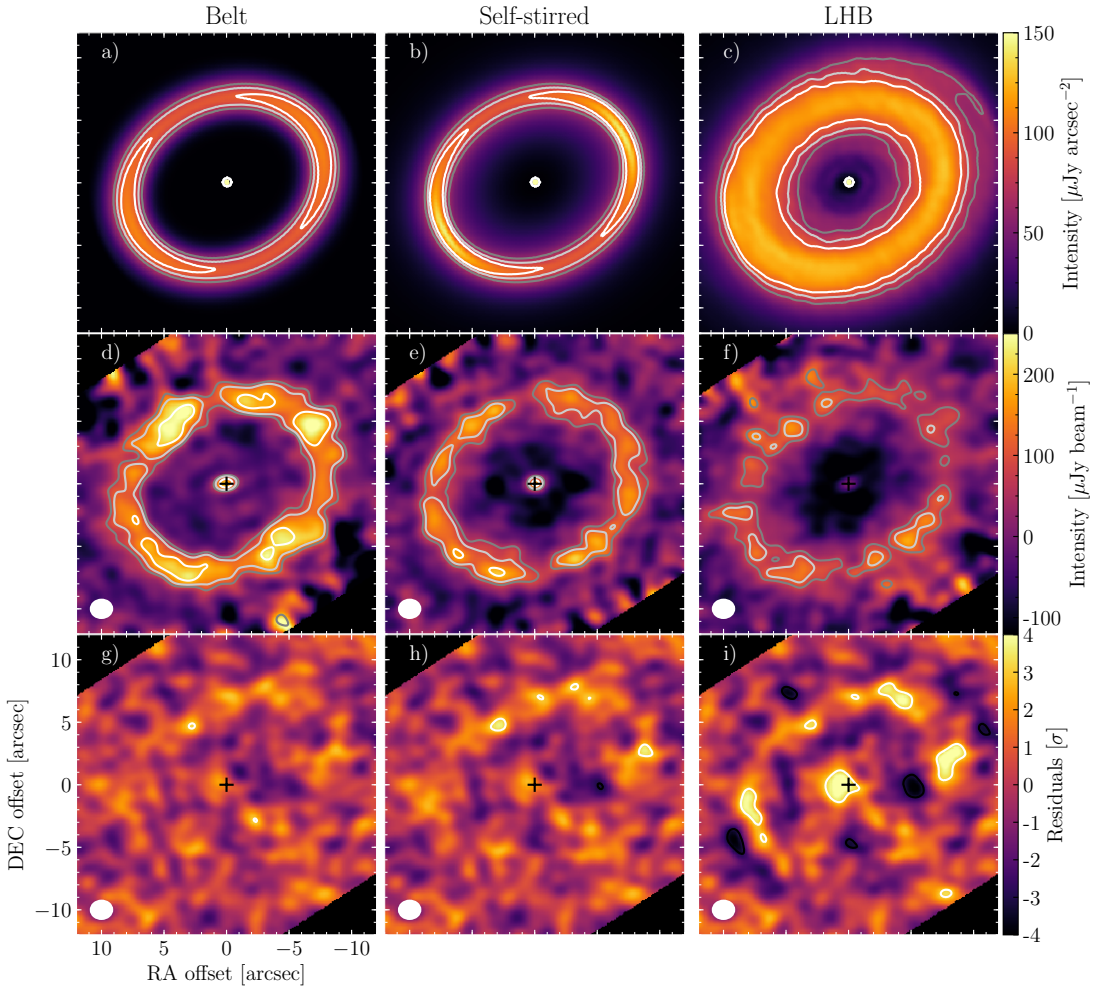

Figure 3.6: Simulated images at 0.88 mm. The first, second and third column correspond to the best-fit belt model (§3.3.1), best-fit self-stirred disc model (§3.3.2) and Late Heavy Bombardment model (§3.3.3), respectively. ***First row:*** synthetic images of the disc. Contours represent 65, 80 and 95 μJy arcsec^{-2}. ***Second row:*** primary beam corrected simulated Clean images using the same uv-sampling, adding Gaussian noise to the visibilities according to the variance of the observations, and uv-tapering the visibilities with a Gaussian of FWHM of $1\farcs2$ in sky. Contours represent 2, 3 and 5 times the local noise level. ***Third row:*** dirty map of the residuals after subtracting the model visibilities from the ALMA observations. The noise level on the residuals is uniform and equal to 30 μJy beam^{-1} as they are not corrected by the primary beam. The black and white contours represent $\pm3\sigma$. The beam size is represented by a white ellipse in the bottom left corner. The x- and y-axes indicate the offset from the stellar position in R.A. and decl. in arcsec, i.e. north is up and east is left. The stellar position is marked with a black "+".

cavity.

Similar to the analysis in §3.2.1, in Figure 3.7 I compute the azimuthal profile of the residuals along the outer belt averaging between 130 and 175 au. The integrated flux of the residuals around the outer belt is 1.2 ± 0.3 mJy (correcting by the primary beam), an excess which is within the uncertainty of the flux in the model (1 mJy). At a PA of 290° the residuals show an excess of 20 μJy beam^{-1} (3σ). Moreover, the excess on the north-west half of the disc is 0.8 ± 0.2 mJy, while 0.4 ± 0.2 mJy on the opposite side of the disc. This is consistent with what I found

in §3.2.1 and the 70 μm PACS image of the disc, and points to a slight excess of emission in the north-west side of the disc. The best fit model has a reduced chi-squared $\chi^2_{\rm red} = 1.0037898$, with 6.54×10^6 different visibility measurements before averaging. This is used later to compare the goodness of fit of different models.

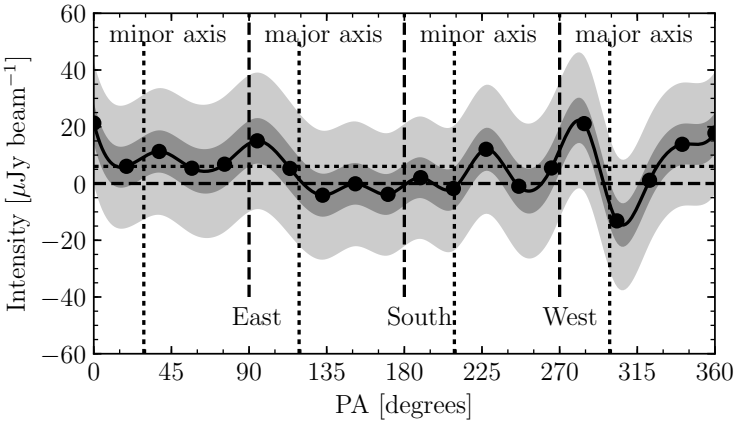

Figure 3.7: Intensity azimuthal profiles of the dirty map of the residuals of the best fit belt model, obtained averaging over elliptic annuli of semi-major axes between $6\farcs8$ and $9\farcs8$ (equivalent to 125 and 180 au) and over 18° wide wedges (centered at the black dots). The horizontal dotted line represents the mean intensity around the residuals in the outer belt. The light and dark grey areas represent the 68% and 99.7% confidence region.

3.3.2 Self-stirred disc

The cavity and outer belt and in η Corvi could be the result of a primordial depletion of solids from a few au's up to 110 au, followed by an overdensity or belt of planetesimals with a peak at 150 au, like in a transitional protoplanetary disc (e.g., Espaillat et al., 2014). Alternatively, the current disc structure could just be the result of the collisional evolution of a broad primordial disc of planetesimals being self-stirred as Pluto-sized objects are being formed at different epochs at different radii. In order to test the latter scenario and see if the disc morphology can be explained by self-stirring, I considered a second model that consists of a parametric self-stirred disc based on the work by Kennedy & Wyatt (2010). In this scenario, the surface density of solids evolves from a primordial disc of planetesimals to a stirred disc in collisional equilibrium as

$$\Sigma(r,t) = \begin{cases} \Sigma(r,0)\ x_{\rm delay} & t < t_{\rm stir}(r) \\ \Sigma(r,0) / \left[1 + \frac{t - t_{\rm stir}(r)}{t_c(r)}\right] & t > t_{\rm stir}(r) \end{cases} \tag{3.2}$$

where $\Sigma(r,0)$ is the primordial surface density of solids assumed here to follow a power law, i.e. $\Sigma_0 (r/r_0)^{-\gamma}$, and t is the age of the system (assumed to be 1.4 Gyr here). At each radius

the disc is stirred at epoch $t_{\rm stir}(r)$ after which it is assumed to be in collisional equilibrium, with a collisional lifetime of the biggest planetesimals $t_c(r)$ at the initial epoch of the collisional cascade (i.e. after being stirred). Similar to Kennedy & Wyatt (2010), I also introduce a factor $x_{\rm delay} \leq 1$ in Eq. 3.2 when $t < t_{\rm stir}$ because the collisional cascade has not yet begun, thus the amount of mass in grains that contribute to the millimetre emission could be lower (different size distributions).

The timescale at which Pluto-sized objects are formed depends both on the distance to the star and the surface density of solids at that distance. Generally speaking, this timescale will be proportional to the orbital period and inversely proportional to the primordial surface density of solids (e.g. Lissauer, 1987), i.e. $t_{\rm stir}(r) \propto r^{3/2}/\Sigma(r,0)$. Because I aim to fit the observations, in the self-stirred model I use the following empirical relation

$$t_{\rm stir}(r) = t_{\rm age}(r/r_{\rm stir})^{3/2+\gamma}, \tag{3.3}$$

where $r_{\rm stir}$ is defined as a reference radius where stirring is happening at the present epoch ($t_{\rm age}$). With this parametrization the peak of the disc emission is at $r_{\rm stir}$ which is comparable to r_0 in the belt model. It is possible to make an order of magnitude estimation of this timescale extrapolating the timescale at which Pluto formed (~ 40 Myr, see Brown, 2002, and references therein) to 150 au using $\gamma = 1$. I find $t_{\rm stir}(150{\rm au}) = 1.5$ Gyr, consistent with simulations by Kenyon & Bromley (2008) (see their Eq. 41), and of the same order as the age of the system; therefore, I consider that the self-stirring scenario is plausible.

On the other hand, the collisional lifetime of the biggest planetesimals in the disc is (Equation 1.7 and substituting $M_{\rm tot}$ by $2\pi r dr$)

$$t_c(r) \ \propto \ r^{7/3}\, D_c\, Q_{\rm D}^{\star 5/6}\, \Sigma(r,0)^{-1}, \tag{3.4}$$

where D_c is diameter of the biggest planetesimal, and $Q^\star_{\rm D}$ is the disruption threshold of planetesimals, here assumed to be independent of size. The expression above can be rewritten as

$$t_c(r) = t_0(r/r_{\rm stir})^{7/3+\gamma}, \tag{3.5}$$

where t_0 is defined as the collisional lifetime of the biggest objects at $r_{\rm stir}$. The net result is that the surface density is proportional to $r^{7/3}$ when $r \ll r_{\rm stir}$ and $r^{-\gamma}$ when $r > r_{\rm stir}$, while its shape close to $r_{\rm stir}$ is determined by the ratio $t_c/t_{\rm stir}$ which is $\approx t_0/t_{\rm age}$.

Then, the free parameters are the total mass of dust M_d, h, γ, $x_{\rm delay}$, $r_{\rm stir}$, t_0, PA and i. The posterior distributions of the most relevant parameters are presented in Figure 3.8 and in Table 3.2 I summarise the best fit parameter values and uncertainties. The total flux of the best fit model is 16.7 ± 2.3 mJy. From the best fit values of the self-stirred model, I find that $\gamma = 6.4\pm1.4$,

$x_{\rm delay} = 0.3 - 1.0$ (95.0% confidence, with a marginalised posterior distribution that peaks at 1), and $t_0 < t_{\rm age}$, i.e. $t_c < t_{\rm stir}$ (99.7% confidence). This means that the disc has a sharp inner and outer edge (see Figure 2 in Kennedy & Wyatt (2010)). The disc model image, simulated ALMA image and dirty map of the residuals are presented in Figure 3.6b, e and h, respectively (middle column). Negative and positive emission at 3σ levels appear close to the stellar position in the simulated ALMA image and dirty map of the residuals, respectively. If the emission were really there, then it should appear brighter in the residuals of the belt model since it does not have any dust in between the star and outer belt. I find the best fit model has a $\chi^2_{\rm red} = 1.0037958$, with 6.54×10^6 different visibility measurements.

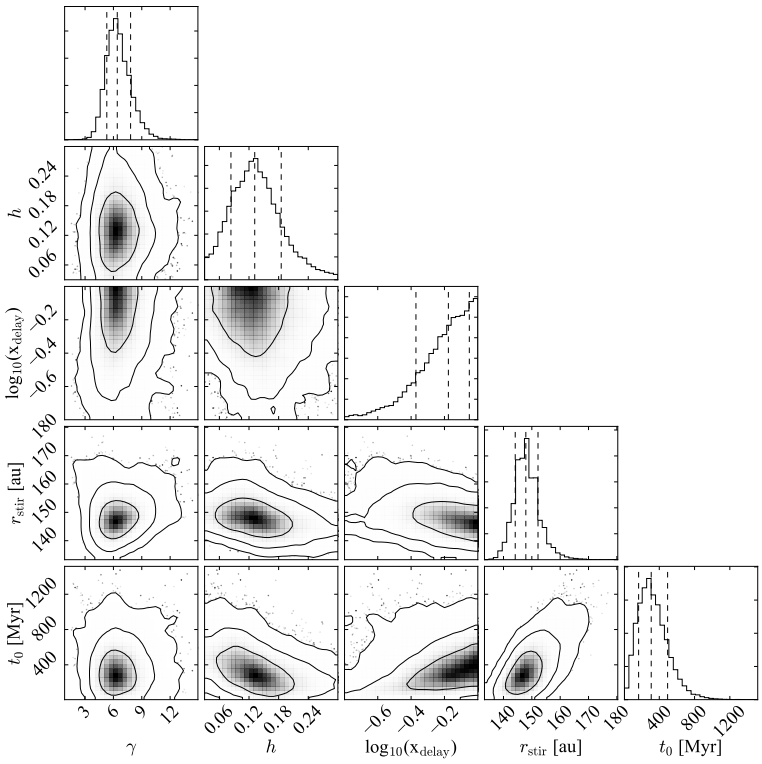

Figure 3.8: Posterior distribution of $h = H/r$, $\log_{10}(x_{\rm delay})$, $r_{\rm stir}$ and t_0 from the self-stirred model. The vertical dashed lines represent the 16th, 50th and 84th percentiles. Contours correspond to 68%, 95% and 99.7% confidence regions. This plot was generated using the python module *corner* (Foreman-Mackey et al., 2014).

Using Equation 1.7 and the derived values of $r_{\rm stir}$ and t_0 I can estimate the mean surface density ($\Sigma = M_{\rm tot}/2\pi r dr$) or total mass in planetesimals ($M_{\rm tot}$), assuming a maximum planetesimal size $D_{\rm c}$ of 1000 km and a power law size distribution of solids with an exponent of -3.5. I find

$$\Sigma_{r_{\rm stir},t=0} = 0.7 \left(\frac{r_{\rm stir}}{150\ {\rm au}}\right)^{7/3} \left(\frac{D_{\rm c}}{1000\ {\rm km}}\right) \left(\frac{Q^\star_{\rm D}}{200\ {\rm J\ Kg^{-1}}}\right)^{5/6} e^{-5/3} \left(\frac{M_\star}{1.4\ {\rm M_\odot}}\right)^{-4/3} \left(\frac{t_0}{300\ {\rm Myr}}\right)^{-1} {\rm M_\oplus\ au^{-2}}. \quad (3.6)$$

Table 3.2: Self-stirred model best fit values. Median $\pm$ uncertainty based on the 16th and 84th percentile of the marginalised distributions. For parameters with distributions extending out to the minimum or maximum allowed values, a 1σ upper or lower limit is specified based on the 68th or 32nd percentile, respectively.

M_d [$M_\oplus$]	0.019 ± 0.003
h	< 0.16 (1σ)
$\log_{10}(x_{\rm delay})$	> -0.26 (1σ)
$r_{\rm stir}$ [au]	148 ± 4
t_0 [Myr]	300^{+180}_{-140}
γ	6.4 ± 1.4
PA [°]	118 ± 4
i [°]	34 ± 3

This corresponds to a total mass of 3×10^4 $M_\oplus$ in the outer belt, which is too massive to be consistent with the self-stirred scenario. Considering only the mass on solids, this is equivalent to a Toomre Q parameter (Toomre, 1964) of 1 assuming a vertical aspect ratio of 0.1; however, if I include the gas mass present during the protoplanetary disc phase ($\Sigma_{\rm gas} \approx 100\Sigma_{\rm solids}$) I find that the disc would have been highly unstable under gravitational perturbations. The high value of $M_{\rm tot}$ is due to t_c at $r_{\rm stir}$, i.e. t_0, which is too short for 1000 km sized bodies. This is because the model fits better the data if the outer belt is narrow, i.e. $t_0 \lesssim t_{\rm age}$.

Combining the mass derived above as a function of the maximum planetesimal size, i.e. $M_{\rm solids} = 3 \times 10^4 (D_c/1000\ {\rm km})\ M_\oplus$, with dust mass on grains smaller than 1 cm, i.e. $M_{\rm solids} = 0.02 (D_c/1\ {\rm cm})\ M_\oplus$, I find a maximum planetesimal size of $D_{\rm c} \sim 40$ m and a total disc mass of 13 $M_\oplus$, but this contradicts the hypothesis that the disc is stirred by the growth of planetesimals up to Pluto-sized bodies. The collisional timescale could be longer (and so allow a larger maximum planetesimal size) if the age of the system is greater than 1.4 Gyr as it is the ratio between both that determines the shape of the surface density. However, to reconcile the maximum planetesimal size (~ 1000 km) and the disc mass in millimetre grains, the age of the system should be ~ 100 times longer, which is impossible. Therefore, I conclude that self-stirring is unlikely to have produced the observed disc morphology in η Corvi. However, I cannot rule out that all the solids are smaller than 40 m (leading to a total mass of ~ 1.3 $M_\oplus$) if the disc is externally stirred, a possibility that is discussed in §3.4.1.

3.3.3 Late Heavy Bombardment

As the hot dust around η Corvi cannot be sustained by a collisional cascade in situ, Lisse et al. (2012) suggested that this system could be undergoing an instability similar to the Late heavy bombardment (LHB) in the Solar System. The outward migration of Neptune after Jupiter and Saturn crossed the 1:2 resonance caused a massive delivery of planetesimals to the inner Solar System, high frequency collisions with the Earth and Moon, and a population of eccentric and

highly inclined objects in the Kuiper Belt (Gomes et al., 2005). During such instability the disc could have specific observable features different from a scenario in which planets are in stable orbits for long timescales. For example, Booth et al. (2009) showed that the Kuiper belt should be broad during the LHB (see Figure 1 therein) with a surface density profile approximated by a power law proportional to $r^{1.5}$ between 1 and 27 au and $r^{-4.8}$ between 38 and 106 au. Moreover, the disc could display asymmetries such as spiral arms or disc offsets with respect to the stellar position produced by a planet put on an eccentric orbit after the instability (see Figure 7 in Pearce & Wyatt, 2014).

Figure 3.9 shows the surface density of planetesimals during the LHB in the Solar System (at $t = 880$ Myr after the start of the simulation), obtained from N-body simulations from one of the Nice model runs (Gomes et al., 2005). As a first approximation I linearly scale the semi-major axis of the planetesimals orbits to match the location of the mean radius of η Corvi, which maintains unchanged the surface density proportional to $r^{1.5}$. This approximation is not necessarily correct given the large size ratio between the Kuiper belt and the η Corvi debris disc (40/150) and the different ways the timescales involved depend on the semi-major axis of particles in the simulation. Therefore, N-body simulations tailored to η Corvi might be necessary; however, this first approximation can be used to compare the observations with an LHB-like event in which an outer belt is perturbed after a dynamical instability in the system, producing a shallow surface density distribution of $r^{1.5}$ extending from the outer belt down to the inner most regions (see Figure 3.10). To smooth the derived surface density, I also randomly spread each particle around its orbit according to the velocity they have at each location. This is only valid if the collisional timescales of the solids are longer than the orbital period, which is probably true for mm-sized grains given the low surface density of the disc. This technique also washes out any resonant structure that relies on the correlation between the mean longitudes and the longitude of pericentre of a particle, although resonances may not be a strong feature at this stage of the evolution. Finally, I simulate images of the disc assuming that mm-sized grains, which dominate the continuum emission at millimetre wavelengths, have the same distribution as their parent bodies because they are not affected by radiation pressure. I vary the disc flux to fit to the visibilities finding a best fit with a total disc flux of 39 ± 2 mJy (0.048 ± 0.002 $M_\oplus$ of dust, assuming the same optical properties as the models described above). This is much higher and inconsistent with the total flux measured by SCUBA-2/JCMT and is required to fit the ALMA data because most of the emission is on large scales, and thus, resolved out. In figure 3.6 c, f and i I present the synthetic continuum image at 0.88 mm, ALMA simulation and dirty map of the residuals after subtracting it to the observed visibilities. Despite the fact that the model surface density displays asymmetric features such as spiral arms, I find that the simulated observations are not sensitive enough to recover this structure, and thus, they are roughly consistent with an axisymmetric disc. However, the LHB best fit model fails to reproduce the observed surface

brightness observed by ALMA as it is broader and fainter in the reconstructed image, despite requiring three times the flux measured by SCUBA-2/JCMT.

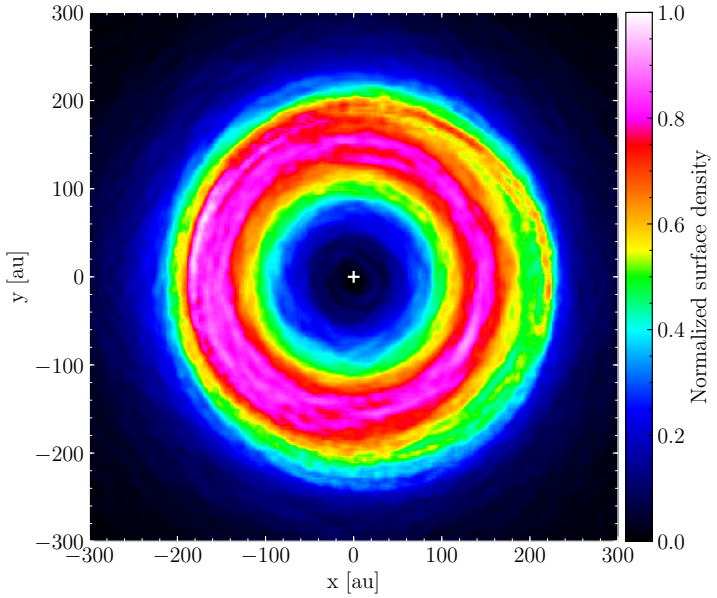

Figure 3.9: Normalized surface density of particles during the LHB computed from N-body simulations of one of the Nice models runs (Gomes et al., 2005). The particles from the simulation were duplicated assigning to each one a random anomaly in order to spread them around their orbits. Finally the particle's semi-major axes were scaled by 3.75 to match the size of the outer disc in η Corvi. The stellar position is marked with a white "+".

In order to place better constraints on the surface density exponent of a possible extended disc, I fit an axisymmetric model with a surface density defined as a double power law

$$\Sigma(r) = \begin{cases} \Sigma_0 \left(r/r_c\right)^{\alpha_{\rm in}} & r < r_c \\ \Sigma_0 \left(r/r_c\right)^{\alpha_{\rm out}} & r > r_c, \end{cases} \tag{3.7}$$

where r_c, $\alpha_{\rm in}$ and $\alpha_{\rm out}$ are free parameters, together with the total mass of dust in the disc, M_d, the vertical aspect ratio, h, and the PA and inclination of the disc in sky. In Table 3.3 I summarise the best fit values and uncertainties. I find $\alpha_{\rm in} = 6.2^{+2.0}_{-1.3}$, with a 3σ lower limit of 3.3. Therefore, I conclude that the surface density of solids in the disc has to rise considerably steeper than $r^{1.5}$ in the cavity towards the outer belt, discarding a LHB-like surface density and a highly scattered outer belt. The best fit model has a $\chi^2_{\rm red} = 1.0037906$, with 6.54×10^6 different visibility measurements.

Table 3.3: Double power law model best fit values. Median ± uncertainty based on the 16th and 84th percentile of the marginalised distributions. For parameters with distributions extending out to the minimum or maximum allowed values, a 1σ upper or lower limit is specified based on the 68th or 32nd percentile, respectively.

M_d [$M_\oplus$]	0.016 ± 0.002
h	< 0.15 (1σ)
r_c [au]	151 ± 4
$\alpha_{\rm in}$	$6.2^{+2.0}_{-1.3}$
$\alpha_{\rm out}$	$-7.5^{+1.3}_{-2.2}$
PA [°]	119 ± 4
i [°]	35 ± 2

3.3.4 Eccentric belt

I also study the possibility of the belt being eccentric. This has two main effects: the center of the belt is offset from the stellar position, and the azimuthal density profile changes as particles spend more time at the apocentre increasing its density relative to the pericentre. This is known as apocentre glow (Pan et al., 2016). Therefore, I fit a modified belt model in which I replace ρ_0 and r_0 in Eq. 3.1 by

$$\rho_c = \rho_0[1 - e\cos(f)], \tag{3.8}$$

$$r_c = \frac{r_0(1-e^2)}{1+e\cos(f)}, \tag{3.9}$$

where e is the eccentricity of the belt and f is the true anomaly, i.e. the azimuthal angle in the plane of the disc measured from the direction of pericentre as seen from the stellar position. I maintain fixed the scale height to the best fit values presented above and I added as free parameters e and the position angle of the pericenter, w, i.e. the angle in the plane of the sky between the north direction and that of the pericentre as seen from the stellar position, to have a total of 7 free parameters. I find that the disc is consistent with being circular and from the posterior distribution of e I derive a 99.7% upper limit of 0.05 (see §3.4.1 for implications of this upper limit). I find that the marginalised distribution of w is not uniform and constrained between $-80°$ and $60°$ (99.7% confidence), i.e. if eccentric the pericentre is more likely to be on the northern half of the disc. However, e still peaks at zero even for these values of w.

3.3.5 Model comparison

In Figure 3.10 I compare the surface density and surface brightness profiles of the belt and self-stirred model using the best fit parameters defined above. They display strong differences in their surface density and brightness profiles, with the self-stirred and LHB models extending significantly inside 100 au and beyond 200 au. Figure 3.11 shows intensity radial

profiles obtained by averaging azimuthally simulated Clean images of the best fit models without noise, and from the dirty maps of their respective residuals when comparing with the observations. The self-stirred and LHB models suffer from strong negative artefacts inside the cavity and appear dimmer on the simulated observation than it should based on the model images (peak of 85 and 95 μJy beam^{-1} at 8″ or 150 au, respectively). This is probably due to an insufficient number of short baselines to capture the broad emission.

With the belt model I obtain the best χ^2, followed by the double power law model. In addition, to compare the goodness of fit of the three best fit models, it is useful to compute the Bayesian information criterion (BIC, Schwarz, 1978) for each one, which penalises for the number of free parameters. It is defined as $\chi^2 + k\log(N)$, where k is the number of free parameters (6 for the belt model, 8 for the self-stirred model and 7 for the double power law model) and N is the number of data points or visibilities. A model is more preferred when its BIC is lower, with a difference larger than 10 considered to be strong evidence (Kass & Raftery, 1995). I find that the belt model's BIC is lower by ~ 40 compared to the self-stirred best model's BIC, and lower by 20 compared to the double power law model. Thus, I conclude the simple Gaussian belt model gives a better fit to the observations, even with a lower number of free parameters.

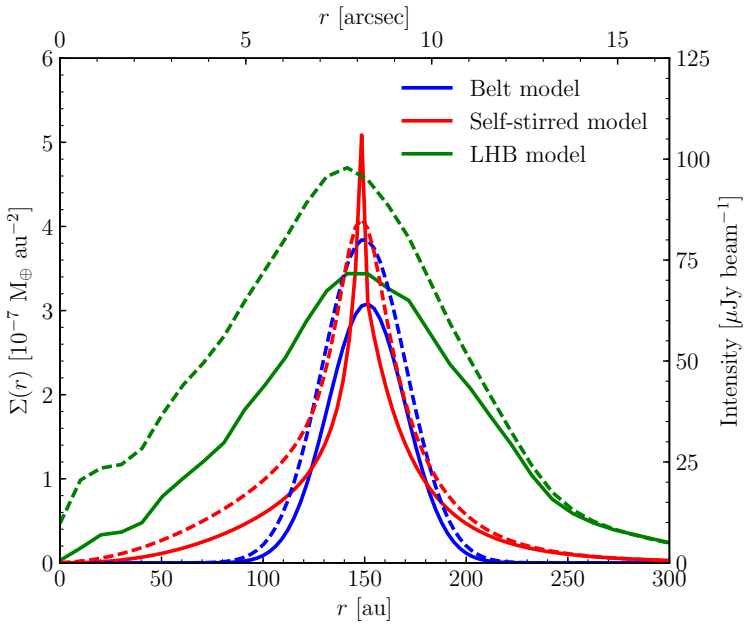

Figure 3.10: Dust surface density (continuous line) and surface brightness profiles convolved with a beam of 1″ (dashed line) of the best fit belt, self-stirred and LHB models, represented in blue, red and green, respectively.

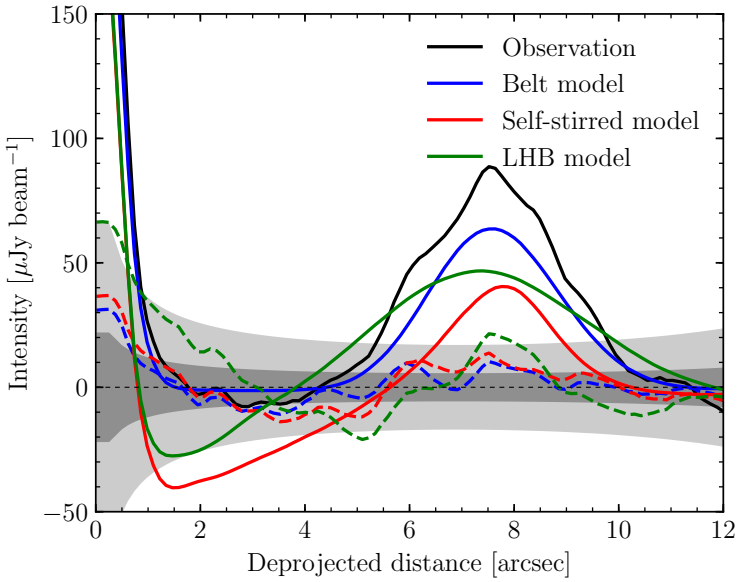

Figure 3.11: Azimuthally averaged intensity profiles obtained from Clean non tapered images of simulated observations without noise using the best fit models (continuous lines) and from the non tapered dirty map of the residuals after subtracting the best fit models (dashed). The blue, red and green lines represent the belt, self-stirred and LHB models, respectively. The η Corvi Clean azimuthally averaged profile is represented with a continuous black line. The light and dark grey areas represent the 68% and 99.7% confidence region.

3.3.6 Missed extended emission inside the belt

It is possible that there could be emission in the cavity missed by ALMA due to a low surface brightness or even due to an insufficient number of short baselines to recover more extended emission. Assuming a constant dust opacity with radius, I can estimate how much dust mass could be hidden at an undetectable level between the star and the belt at 150 au. The maximum surface density (3σ upper limit) can be defined as

$$\Sigma(r) = \frac{\delta I(r)}{\kappa_{\rm abs} B_\nu(T(r))} \tag{3.10}$$

where $\kappa_{\rm abs} = 3.8$ cm^2 g^{-1} is the absorption opacity of grains and $\delta I(r)$ is the 3σ uncertainty of the azimuthally averaged intensity profile, computed considering the noise in the image space, as well as the apodization by the primary beam. I also assume $T(r) = 42(r/150\ {\rm au})^{-0.5}$ K, derived from the dust temperature in the models described above (assuming a uniform grain size distribution and composition in the disc). Integrating $\delta I(r)$ or $\Sigma(r)$ I find a total missing flux ≤ 3.4 mJy or a possible hidden dust mass $\leq 2.4 \times 10^{-3}$ M$_\oplus$ in the cavity (3σ limits).

However, this approach does not take into account the uv-filtering that could be present due to missing short baselines, as the maximum recoverable scale is $\sim 7''$. These observations are blind to structure of that size or bigger. To study this effect and get a more reliable constraint

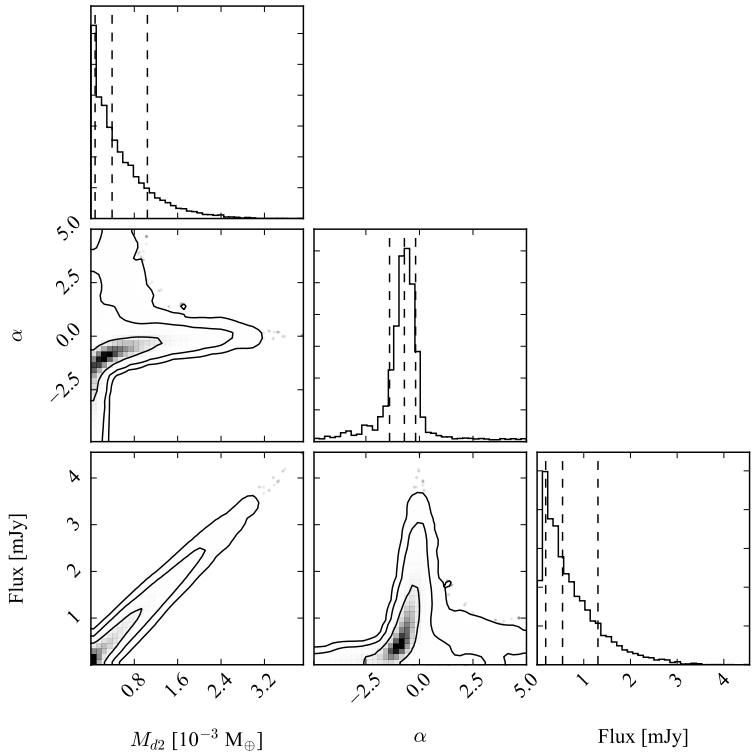

Figure 3.12: Posterior distribution of α, M_{d2} and the total disc flux of the second inner component. The vertical dashed lines represent the 16th, 50th and 84th percentiles. Contours correspond to 68%, 95% and 99.7% confidence regions. This plot was generated using the python module *corner* (Foreman-Mackey et al., 2014).

on the possible hidden emission inside the cavity I added a second component to the simple belt model described in §3.3.1 and I fit this to the observed visibilities. The second component is defined with a surface density proportional to r^{α} between 1 au and 150 au (inside the belt mean radius), where I leave α as a free parameter that can vary between -5 and 5, together with the total dust mass of the second component, $M_{\rm d2}$. In Figure 3.12 I present the distribution of α, the total dust mass $M_{\rm d2}$ and flux of the second component. I find a 3σ upper limit of 2.7×10^{-3} $M_\oplus$ for M_{d2} and 3.2 mJy for the flux of the second component. This is similar to the previous analytic estimate, which rejects the hypothesis of extended disc emission in the cavity at detectable levels, but filtered out by missing short baselines. It is worth noting that this parametric method to constrain the flux from the cavity assumes a power law surface density distribution.

3.3.7 CO mass constraints

As shown by Matrà et al. (2015) local thermodynamic equilibrium (LTE) does not necessarily apply to the low density environments of debris discs. Thus, when deriving gas masses from observed CO emission or even upper limits from non detections, it is necessary to consider

non-LTE effects when the densities of the main collisional partners, which I assume to be electrons, are not high enough. This choice is justified because if CO gas of secondary origin is present, electrons should be released from carbon ionization after the photodissociation of CO, dominating the collisional excitations and de-excitations of the CO rotational levels. However, I stress that the mass limits derived in the radiation dominated regime (low electron densities) and in LTE (high electron densities) are independent of the specific collisional partner. Similar to Fomalhaut (Matrà et al., 2015), the radiation at 345 GHz in the disc is dominated by the CMB photons ($J_\nu = 1.4 \times 10^8$ Jy sr^{-1}) as the mean dust intensity inside the belt is $\lesssim 8 \times 10^7$ Jy sr^{-1} (calculated from the best fit model in §3.3.1) and the stellar flux is $\sim 10^8$ Jy sr^{-1} at 5 au, which decreases steeply as r^{-2} and becomes negligible at 20 au. I also neglect the flux from the hot dust, as it is highly unconstrained at this wavelength. I use the code developed by Matrà et al. (2015) that computes the population of the rotational levels in the non-LTE regime to derive CO total fluxes and gas masses for different electron densities (n_{e^-}) and gas kinetic temperatures (T_k), assuming the emission is optically thin.

From the total flux of 38 ± 9 mJy km s^{-1}measured between 15 au and 37 au (see §3.2.2), I estimate the CO gas mass located around 20 au considering different n_{e^-} and T_k (20-300 K). This is shown in Figure 3.13. As expected from the work by Matrà et al. (2015), the mass of CO is highly unconstrained without any knowledge of n_{e^-}. M_{CO} could easily be between $\sim 10^{-3}$ $M_\oplus$, in the radiation dominated regime (low n_{e^-}), and 10^{-7} $M_\oplus$, in LTE (high n_{e^-}). On the other hand, different gas kinetic temperatures can change M_{CO} by a factor of a few when close to LTE.

However, in the secondary origin scenario electrons are a byproduct of CO photodissociation and carbon ionization, therefore n_{e^-} can be linked to M_{CO}. In fact, Eq. 14 in Matrà et al. (2015) shows that

$$M_{CO} = \frac{n_C}{n_{C^+}} \frac{n_{CO}}{n_C} m_{CO} V_{disc} n_{e^-} \approx 0.01 \, m_{CO} V_{disc} n_{e^-}, \tag{3.11}$$

where m_{CO} is the mass of the CO molecule and V_{disc} is the volume of the disc from 15 to 37 au assuming a vertical aspect ratio of 0.1. Based on previous studies of the β Pictoris disc, I assume $n_C/n_{C^+} = 1$ (Cataldi et al., 2014) and $n_{CO}/n_C = 1/100$ (Roberge et al., 2000) as first approximation. Therefore, if the CO gas is of secondary origin, its mass is defined roughly by the intersection of the dashed and continuous lines in Figure 3.13, i.e. $M_{CO} \sim 3 \times 10^{-7}$ $M_\oplus$. This could vary by a factor of a few given the flux uncertainty and the assumptions on V_{disc}, the carbon ionization and CO/C abundance ratio. These uncertainties are represented by the grey shaded region defined between $0.1 - 10 \, M_{CO}$. I also find a CO mass loss rate of $\sim 3 \times 10^{-9}$ $M_\oplus$ yr^{-1}, as CO photodissociates in a timescale of 120 yr due to the interstellar UV radiation field (Visser et al., 2009), which is of the same order as the hot dust mass loss rate ($\sim 3 \times 10^{-9}$ $M_\oplus$ yr^{-1}, Wyatt et al., 2010). Possible origins of the CO gas are discussed in §3.4.2.

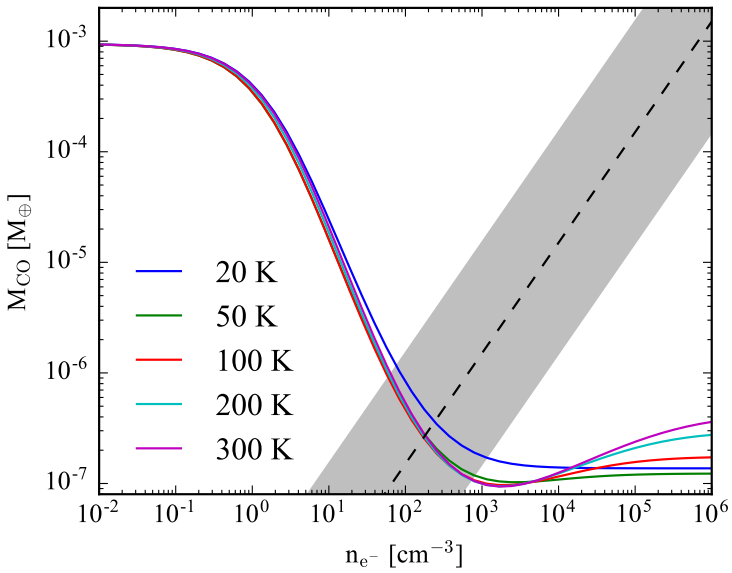

Figure 3.13: CO gas mass estimate of the detection at $\sim$ 20 au for different gas kinetic temperatures and electron densities (n_{e^-} , main collisional partner). The dashed line corresponds to the CO gas mass assuming an abundance ratio of neutral carbon and CO of 100 and a carbon ionization fraction of 0.5. The shaded grey region represents a factor of 10 of uncertainty on the CO and electron abundance ratio.

Based on the flux upper limits derived in §3.2.2, I also estimate mass upper limits on the CO gas mass that could be in the outer belt or co-located with the hot dust. In Figure 3.14 I present the 3σ mass upper limits for the CO in the outer belt, considering different $T_{\rm k}$ (10-150 K, a more appropiate range for $T_{\rm k}$ at 150 au) and electron densities. Similar to the derived mass above, the CO gas mass upper limit is not well constrained and strongly depends on the density of electrons in the disc varying by 4 orders of magnitude from 10^{-7} to 10^{-3} $M_\oplus$. Using Eq. 3.11 and the volume of the best fit belt model I can estimate the expected density of electrons for a given CO gas mass assuming the same carbon ionization and C/CO abundance ratio observed in β Pic. This is represented with a dashed line. As the C/CO abundance and carbon ionization ratio could be different than in β Pic, I represent these uncertainties with a the grey shaded region defined between $0.1 - 10$ $M_{\rm CO}$. The intersection between the dashed line and the continuous lines in Figure 3.14 gives the best mass upper limit in the secondary origin scenario, which is 4×10^{-6} $M_\oplus$ for $T_{\rm k} = 50$ K. The CO mass could be higher than this limit, but this requires a low abundance of e^-, which would be unlikely given the derived mass of CO, which would photodissociate producing carbon that would get ionised releasing further e^- (Kral et al., 2016).

Similarly, I calculate mass upper limits for the CO co-located with the hot dust using the 3σ flux upper limit (3×11 mJy km s^{-1}), considering different $T_{\rm k}$ (100-2000 K, a more appropiate range for $T_{\rm k}$ at a few au) and including the stellar flux at 345 GHz and at a radius of 1 au (important

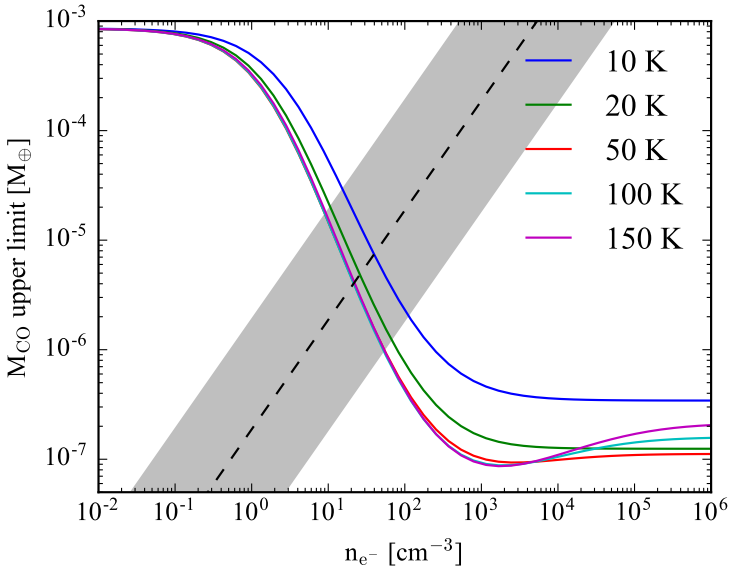

Figure 3.14: CO gas mass upper limits in the outer belt for different gas kinetic temperatures and electron densities (n_{e^-} , main collisional partner). The dashed line corresponds to the mass upper limit of CO gas assuming an abundance ratio of neutral carbon and CO of 100 and a carbon ionization fraction of 0.5. The shaded grey region represents a factor of 10 of uncertainty on the CO and electron abundance ratio.

for the radiation dominated regime). This is shown in Figure 3.15. I also overlay in dashed and dotted black lines the mass of CO gas as a function of the electron density assuming the same carbon ionization fraction and C/CO abundance ratio as in β Pic. The dashed line corresponds to a disc with uniform surface density that extends from 1 au to 10 au in radius, while the dotted line represents a scenario in which most of the emission comes from a narrow ring between 0.9 to 1.1 au. Moreover, as the C/CO abundance and carbon ionization ratio could be different than in β Pic, I represent these uncertainties with a grey shaded region defined between $0.1 M_{\rm CO}^{\rm narrow} - 10\ M_{\rm CO}^{\rm broad}$. The intersections between the dashed and dotted lines with the continuous line give the best estimate of the CO mass upper limit assuming a secondary origin as in β Pic. These two cases can be thought as extremes cases, with the narrow ring scenario having the most conservative upper limit of $\sim 5 \times 10^{-7}$ M$_\oplus$ for $T_{\rm k} = 500$ K, roughly the equilibrium temperature at 1 au. This limit is of the order of the CO gas mass derived before located at ~ 20 au. However, more CO gas could be hidden if it were distributed in an optically thick narrow ring. In the same figure I added the mass of CO at which the CO line becomes optically thick (mean τ_ν=1 across the line width), which is represented in red dotted and green dashed lines for the two scenarios detailed above. I find that the upper limits are optically thin in the regime I am interested (secondary origin), unless the electron density is very low and the CO in the disc is far from LTE.

If CO is released in collisions of icy planetesimals, e.g. releasing CO gas trapped inside them

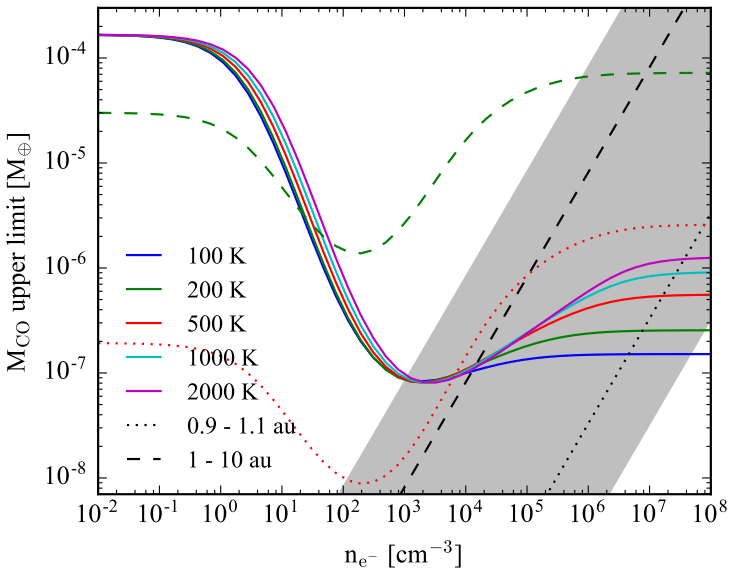

Figure 3.15: Mass upper limits of CO gas co-located with the hot dust for different gas kinetic temperatures and electron densities (n_{e^-}, main collisional partner). The dashed and dotted black lines correspond to the mass upper limit of CO gas assuming a narrow ring and a broad inner disc, respectively, and an abundance ratio of neutral carbon and CO of 100 and a carbon ionization fraction of 0.5. The dashed and dotted curves represent the mass of CO gas at which the line (3-2) becomes optically thick ($\tau = 1$) for a thin ring with $T_K = 500$ K (red) and a broad inner disc with $T_K = 200$ K (green). The shaded grey region represents a factor of 10 of uncertainty on the CO and electron abundance ratio, considering a range of volumes from a narrow to a broad inner disc.

or by exposing icy surfaces that can sublimate via thermal or photodesorption, then the rate at which CO gas is produced in the disc is given by the mass loss rate of planetesimals, and must be equal to the rate at which it photodissociates (120 yr, given by the interstellar UV radiation field, Visser et al., 2009). Using Equations 1.7 and 1.8, the fractional luminosity of the outer disc ($\sim 2 \times 10^{-5}$ Duchêne et al., 2014), its mean radius and width derived in §3.3.1, and assuming mean planetesimal eccentricities of 0.05 and a uniform planetesimal disruption threshold ($Q^\star_{\rm D}$) of 200 J kg^{-1}, I can estimate the outer disc mass loss rate and what would be the CO gas mass in the outer belt for CO mass fractions of planetesimal of 16% (maximum fraction derived in solar system comets, Mumma & Charnley, 2011). I find that for these parameters, $\dot{\rm M} \sim 10^{-3}$ M$_\oplus$ Myr^{-1} (or $\sim 4\times10^{-5}$ M$_\oplus$ Myr^{-1} for $Q^\star_{\rm D} \sim 10^4$ J kg^{-1}) and M$_{\rm CO} \sim 3\times10^{-8}$ M$_\oplus$ or much lower if I consider higher disruption thresholds or lower abundances of CO in planetesimals. This mass of CO gas is much lower than the upper limit of 5×10^{-6} M$_\oplus$ derived above. The non-detection in the outer belt is therefore consistent with Solar System comet compositions.

On the other hand, the hot dust possess a fractional luminosity of $\sim 3 \times 10^{-4}$ (Duchêne et al., 2014). Under the same assumptions detailed above and including the stellar radiation, I find that for a narrow ring $\dot{\rm M} \sim 2$ M$_\oplus$ Myr^{-1} and there should be 2×10^{-5} M$_\oplus$ of CO gas, far above

the upper limit derived for the hot dust. In fact, such a massive CO ring would be optically thick ($\tau_\nu \sim 7$). If I consider a broad inner disc spanning from 1 to 10 au, this limit decreases to 2×10^{-6} $M_\oplus$ ($\dot{M} \sim 0.1$ $M_\oplus$ Myr^{-1}), but still above the upper limit on the broad inner disc scenario. However, this prediction can be pushed down by increasing the disruption threshold or decreasing the abundance of CO trapped in planetesimals below 4% (still consistent with Solar System comets, f_{CO}=0.3-16%, Mumma & Charnley, 2011). In fact, a low fraction of CO gas trapped in planetesimals is expected if volatiles have been lost at ∼20 au on their way in from the outer belt (see §3.4.2).

3.4 Discussion

3.4.1 Hidden planet(s)

Belt or self-stirred disc

In §3.3 I found that the disc continuum emission is consistent with a belt at 150 au and given the visibility uncertainties and insufficient short baselines in the ALMA data, the Gaussian belt model with three free parameters to describe the surface density, gives the best fit and it is not necessary to invoke a more complex model such as the self-stirred disc with two more free parameters. Moreover, I found that the derived collisional timescale of the biggest bodies in the self-stirred scenario, which controls the width of the observed disc, is too short for a Pluto-sized body. However, it could be that the primordial disc of planetesimals was narrow. Then, it is no longer necessary that the stirring timescale at 150 au (i.e. the age of the system) is longer than the collisional lifetime of the largest planetesimal, i.e. $t_0 \lesssim t_{\rm age}$, to produce a narrow debris belt as the primordial disc was already narrow; therefore, the outer belt could still be self-stirred. A narrow distribution of planetesimals in the outer belt, however it is stirred, could be due to a local enhancement of solids at ~ 150 au caused by the presence of a snow line of a specific volatile species that enhanced dust growth, or due to the presence of a nearby planet truncating the inner edge of the outer disc. In the latter scenario the planet could have stirred the disc before self-stirring takes place (Mustill & Wyatt, 2012). It could also be the case that the outer belt formed narrow without being truncated by a nearby planet, but that a massive planet closer in stirred the outer belt before self-stirring could take place.

Alternatively, the morphology could be due to radial dust trapping of solids in pressure maxima at the edge of a gap or cavity during the protoplanetary disc phase (i.e. when this would have been classified as a transitional disc), where planetesimals could have grown. This can be produced by the presence of a massive planet that opens a gap in the disc (e.g., Pinilla et al., 2012), located around 100 au in the case of η Corvi. For example HD 142527 has

both an inner and outer disc, with a cavity in both dust and gas extending from 10 au out to $\sim$140 au (Fukagawa et al., 2006; Casassus et al., 2012). Although that system has a low mass companion close in, it cannot have truncated the inner edge of the outer disc (Lacour et al., 2016). Thus, a single or multiple planets have been proposed to explain both the large cavity and the transport of gas from the outer to the inner disc (as suggested by ALMA observations, Casassus et al., 2013, 2015), necessary to maintain the accretion rate that otherwise would deplete the inner disc in less than a year (Verhoeff et al., 2011). Similarly, to explain the hot dust in η Corvi a planetary system is required passing in material from its outer belt. Such a planetary system would probably stir the disc before self-stirring or the formation of a Pluto-sized object takes place (see §3.4.1).

From the outer to the inner disc

The two component debris disc around η Corvi presents a challenge to any theoretical predictions of debris discs as its hot dust cannot be explained by a collisional cascade in situ since the system is too old ($\gtrsim$ 1 Gyr). Moreover, spectroscopic features of the hot dust suggests that it was formed farther out, probably in the outer belt. P-R drag alone is incapable of transporting enough dust from the outer belt to the inner regions; therefore, a planetary system scattering material from the outer belt is required. In §3.1 I identified three possible scenarios to explain the hot dust in this system: 1) LHB-like instability, 2) a stable planetary system scattering material and feeding a collisional cascade closer in, and 3) a stable planetary system scattering planetesimals that colliding with a planet within a few au. These new ALMA observations have shown that it is unlikely that the system is going through an instability such as the LHB (scenario 1). Such a scenario should leave asymmetric signatures, e.g spiral arms or stellar-disc offsets (similar to the secular effect of an eccentric planet, Pearce & Wyatt, 2014), and a broad outer belt during the evolution of the system (see Figure 3.9 from this work and Figure 1 in Booth et al., 2009). Given the rms achieved per beam in these ALMA observations, I cannot discard asymmetric features of the size of a few beams as they would not appear at a significant level (compare Figures 3.6c and 3.6f). However, I found that the outer belt is narrower compared with the LHB scenario (See §3.3.3) or it has a much steeper surface density slope within 150 au, and that it has a small global eccentricity, below 0.05. Thus, it seems unlikely that a dynamical instability in the system similar to the LHB is responsible for the hot dust excess. The outer belt has more likely retained a stable configuration over Gyr timescales where icy material from the outer belt is being passed in to the inner regions (scenarios 2 and 3).

Bonsor & Wyatt (2012) and Bonsor et al. (2012) explored the limits at which multiple planets on circular orbits within 150 au can scatter particles inwards from the outer belt. The second study

showed that it is difficult for planets more massive than Neptune to transport high levels of material to the inner planetary system, particularly after Gyr's. This is based on the clearing of the planet's chaotic zone of material. However, if this material is replenished, planet scattering can sustain the hot dust. This can be done if the putative planet is migrating outwards into the outer belt (e.g. by planetesimal scattering, Bonsor et al., 2014).

Alternatively, solids could migrate inwards from the outer belt, e.g via scattering with a low mass planet located in the middle of the outer belt, through secular interactions with planets in the system, or by chaotic diffusion. The planet in the middle of the belt should have a mass small enough such that the clearing timescale of its chaotic zone is significantly longer than the age of the system, i.e. $\lesssim 7M_{\oplus}$ (see Eq. 3 in Shannon et al., 2016), as the observed outer belt shows no evidence of a gap or being cleared. Then, the icy material scattered from the outer belt to the inner regions could feed the hot dust via mutual destructive collisions of dust and planetesimals (scenario 2), or as a product of giant impacts on a planet close in which would release large amounts of dusty debris (scenario 3). Although the exact rate at which this material is transported and, thus, its radial distribution is unknown, in §3.3.6 I studied the possibility of a shallow component in the disc with different surface density distributions, connecting the outer belt with the hot dust region. I constrained the surface density distribution as a function of its slope and total dust mass. These limits can be used in the future to test hypotheses of planet configurations that can deliver material inward from the outer belt to the inner regions (see Chapter 6). For example, for a surface density increasing with radius as r^2 in the cavity, it cannot contain more dust mass than 8×10^{-4} M$_{\oplus}$ (assuming $\kappa_{\rm abs}$=3.8 cm^2 g^{-1}) or a total flux of 1 mJy.

Moreover, if the transport of material is in steady state, I can place a lower limit on the rate at which solids are migrating inwards by equating the hot dust mass loss rate with the inward flux of solids. The first was estimated to be $\sim 3 \times 10^{-9}$ M$_{\oplus}$ yr^{-1} (Wyatt et al., 2010). This implies that if fed from the outer belt, this has lost at least ~ 4 M$_{\oplus}$ in the last 1.4 Gyr. On the other hand, the inward flux of solids can be expressed as

$$\dot{M}^{+}_{\rm hot} = 2\,\pi\,r\,\Sigma(r)\,v_r(r), \tag{3.12}$$

where $\Sigma(r)$ is the surface density of dust in the cavity and v_r is the migration rate from the outer belt to the hot dust location. Here I assume $\Sigma(r) \propto r^{-1}$ and equal to $10^{-8}(r/100\,{\rm au})^{-1}$ M$_{\oplus}$ au^{-2}, equivalent to the upper limit of the total dust mass in the cavity (10^{-3} M$_{\oplus}$, see §3.3.6). Using the lower limit on M$_{\rm hot}$ and upper limit on $\Sigma(r)$, I find that $v_r \gtrsim 5 \times 10^{-4}$ au yr^{-1}, i.e. a total migration time of 0.25 Myr from 100 to 1 au, assuming a surface density distribution proportional to r^{-1}. This lower limit (and others for different $\Sigma(r)$) can be tested by N-body simulations to assess scenarios 2 and 3 that could transport material from the outer belt to the

inner regions producing the hot dust.

Constraints on a hidden planet at the disc inner edge

Although the depletion of dust interior to the outer belt and the high hot dust excess in η Corvi hint at the presence of stellar companions or planets, searches for them have not been successful. Radial velocity studies have discarded close in companions down to the mass of a 6 Jupiter masses with a period shorter than 2000 days or with a semi-major axis less than 3 au (Lagrange et al., 2009a; Borgniet et al., 2017). Chandra and *Spitzer* IRAC observations have also discarded the presence of a sub-stellar companion that could explain the unusually high X-ray luminosity of this old system (Marengo et al., in prep). However, given the new constraints on the disc eccentricity, mean radius and width, I can put new constraints on a hidden planet. Assuming there is a single planet inside the η Corvi cavity, it cannot have a large eccentricity, $e_{\rm plt}$, as an eccentric planet would impose a forced eccentricity, $e_{\rm f}$, on the disc through secular interactions. This forced eccentricity must be lower than 0.05, the upper limit derived in §3.3.1 for the disc eccentricity. The relation between both eccentricities can be obtained from the disturbing function. Here I adopt the expression with no restriction in $e_{\rm plt}$, based on Eq. 8 in Mustill & Wyatt (2009)

$$e_{\rm plt} = -\frac{5\alpha}{8e_{\rm f}} + \sqrt{\left(\frac{5\alpha}{8e_{\rm f}}\right)^2 + 1}, \tag{3.13}$$

where α is equal to the ratio of the semi-major axis of the planet, $a_{\rm plt}$, and the disc, $a_{\rm disc} = 152$ au.

I further assume that this planet is also responsible for truncating the outer disc and defining its inner edge, $a_{\rm in}$, e.g. through direct scattering and overlap of mean motion resonance in the so-called chaotic zone. The width of this zone has been estimated analytically for both small (Eq. 56 in Wisdom, 1980) and high eccentricities (Eq. 10 in Mustill & Wyatt, 2012), which I can use to relate the mass of the planet ($M_{\rm plt}$) and its semi-major axis

$$M_{\rm plt}(a_{\rm plt}, e_{\rm f}) = \begin{cases} \left(\frac{\frac{a_{\rm in}}{a_{\rm plt}}-1}{1.3}\right)^{7/2} M_\star & e_{\rm plt} < e_{\rm crit} \\ \left(\frac{\frac{a_{\rm in}}{a_{\rm plt}}-1}{1.8}\right)^{5} e_{\rm plt}\, M_\star & e_{\rm plt} > e_{\rm crit} \end{cases} \tag{3.14}$$

where $a_{\rm in} = r_0 - \Delta r = 106$ au, $M_\star \sim 1.4\ M_\odot$ and $e_{\rm crit}$ is the critical eccentricity at which $e_{\rm plt}$ needs to be considered for the size of the chaotic zone (Eq. 11 in Mustill & Wyatt, 2012), which for a Neptune mass planet is ~ 0.002. Eqs. 3.13 and 3.14 define a surface in ($e_{\rm f}$, $a_{\rm plt}$, $M_{\rm plt}$) space where this planet could reside. In Figure 3.16 I present $M_{\rm plt}$ as a function of $a_{\rm plt}$ for $e_{\rm f} = 0$

and 0.05 in continuous blue and red lines, respectively. With red dots I indicate the eccentricity of the putative planet along the $M_{\rm plt}(a_{\rm plt})$ curve. Both lines are nearly vertical and the region between them defines where a planet defining the outer belt's inner edge could lie.

However, a low mass planet would clear its chaotic zone on timescales of the order or even longer than the age of the system. I can use Eq. 3 in Shannon et al. (2016) which defines the clearing timescale of the chaotic zone as a function of the planet mass and semi-major axis, to estimate the minimum mass of the planet sculpting the inner edge

$$M_{\rm plt}(a_{\rm plt}) = 4 \left(\frac{t_\star}{1.4{\rm Gyr}}\right)^{-1} \left(\frac{a_{\rm plt}}{100\ {\rm au}}\right)^{1.6} \left(\frac{M_\star}{1.4\ {\rm M}_\odot}\right)^{-1/2} {\rm M}_\oplus. \tag{3.15}$$

A planet below this mass limit will not clear its chaotic zone fast enough to truncate the inner edge of the outer belt. Therefore, the planet sculpting the outer belt should lie between 60 and 110 au and have a mass higher than 3 $\rm M_\oplus$.

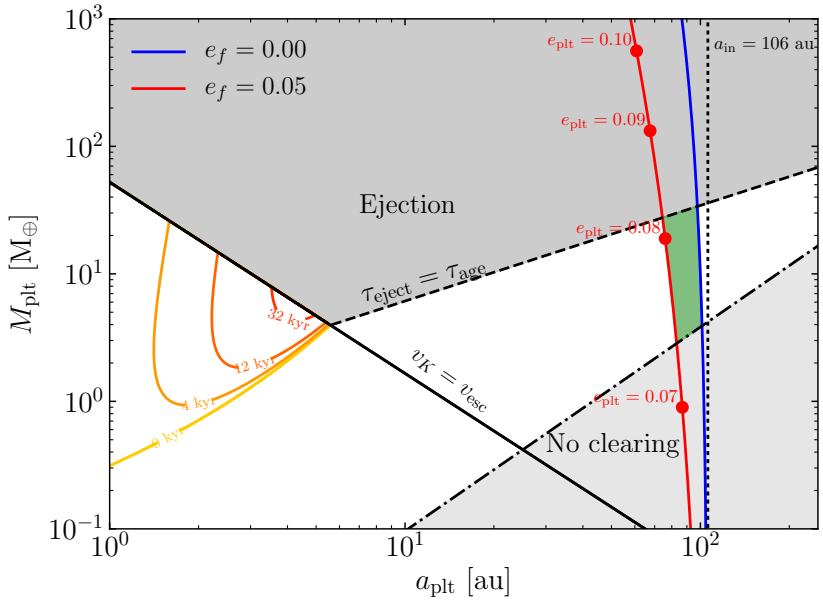

Figure 3.16: Constraints of the mass and semi-major axis of a perturbing planet in η Corvi. The blue and red lines are defined by Eq. 3.14 using a forced eccentricity of 0 and 0.05, respectively. Eq. 3.16 is represented by a continuous black line, while Eq. 3.17 is represented by a dashed black line. The mass of the planet to clear its chaotic zone on a timescale equal to the age of the system ($\sim$ 1.4 Gyr) is represented by a dashed dotted line. The red dots display the eccentricity of the planet that varies along the red curve, increasing with $M_{\rm plt}$. The inner edge of the disc is also shown with a dotted vertical line at 106 au. The grey regions show excluded regions where the planet would be too massive ejecting most of the material it encounters or not massive enough to stir the disc. In green I highlight the region where $M_{\rm plt}$ and $a_{\rm plt}$ meet all the conditions above. The yellow, orange and red contours represent different combinations of $M_{\rm plt}$ and $a_{\rm plt}$ in which a giant impact would produce debris that can remain above a fractional excess of 0.5 at 20 μm for a certain timescale.

Maximising the inward flow

As commented before, if material from the outer belt can migrate inwards, it could fall in the chaotic zone of the putative planet sculpting the outer belt, possibly continuing its inward migration and feeding the hot dust before being ejected or accreted. Assuming that the hot dust is fed by planet scattering in this manner, I can place constraints on the planet masses required, and thus, further constrain the orbital parameters of any interior planet. As the maximum kick a particle can experience when encountering a planet is of the order of the planet's escape velocity, $v_{\rm esc}$, planets with $v_{\rm esc}$ much larger than the Keplerian velocity, $v_{\rm K}$, will most likely eject particles after multiple kicks. On the other hand, if $v_{\rm esc} \ll v_{\rm K}$ then accretion will likely be the final outcome before the particle gets enough kicks to put it on an unbound orbit. As shown in Wyatt et al. (2017), by equating $v_{\rm esc}$ and $v_{\rm K}$ I can find roughly the planet mass that divides the two scenarios

$$M_{\rm plt} = 40 \left(\frac{M_\star}{M_\odot}\right)^{3/2} \left(\frac{a_{\rm plt}}{1\ {\rm au}}\right)^{-3/2} \left(\frac{\rho_{\rm plt}}{1\ {\rm g\ cm^{-3}}}\right)^{-1/2} M_\oplus, \tag{3.16}$$

where $\rho_{\rm plt}$ is the bulk mass of the planet, hereafter assumed to be 1.6 g cm^{-3} (Neptune's bulk density). This line is represented in Figure 3.16 by a continuous black line. However, ejection might only happen after several encounters, thus, material can remain in the system for timescales shorter than the ejection timescale, which I take as the cometary diffusion timescale derived empirically by Tremaine (1993). Using Eq. 2 from Wyatt et al. (2017) I find

$$M_{\rm plt} = \left(\frac{M_\star}{M_\odot}\right)^{3/4} \left(\frac{a_{\rm plt}}{1\ {\rm au}}\right)^{3/4} \left(\frac{t_\star}{1{\rm Gyr}}\right)^{-1} M_\oplus. \tag{3.17}$$

In Figure 3.16 this is represented by a dashed black line (using $t_\star$=1.4 Gyr). Therefore, particles encountering a planet with a mass above the one defined by Eq. 3.16 and below Eq. 3.17 will likely remain in the system without being ejected or accreted for timescales longer than the age of the system. Thus, a planet that both truncated the disc (red and blue lines) and does not eject particles within 1.4 Gyr must have a mass $\lesssim 30$ M$_\oplus$. However, material formed farther out, e.g. in the outer belt, could fall in this region at late epochs and thus remain in the system until the present epoch even if the putative planet is more massive than 30 M$_\oplus$.

Combining the four equations above I can define a region in $M_{\rm plt}$ vs $a_{\rm plt}$ space where the putative planet is most likely to be found. This is represented by a green region in Figure 3.16, and roughly defined by $a_{\rm plt}$ in the range $\sim$ 75-100 au and $M_{\rm plt}$ between 3-30 $M_\oplus$. Planets in this region will have a semi-major axis such that they can truncate the disc by clearing their chaotic zone on a timescale shorter than the age of the system. They will not force an eccentricity on the disc higher than 0.05, and they will not eject particles within 1.4 Gyr. Given the uncertainty on the age of the system (1-2 Gyr), the range of masses given above could change by 40%. The mass upper limit is also consistent with the limits of a few Jupiter masses

placed by direct imaging planet searches in this system.

Moreover, the planets in the green region have higher masses than the minimum mass to stir the outer belt on a timescale equal to the age of the system. Assuming a forced eccentricity of 0.05, i.e. $e_{\rm plt} \lesssim 0.08$, and using Eq. 15 from Mustill & Wyatt (2009) I find this mass is 1 $M_{\oplus}$. Therefore, self-stirring is not necessary as a planet in this region would be able to stir the disc on a timescale shorter than 1.4 Gyr.

Multiple planets

It is important to stress that the analysis above is only valid for a single planet. The planet truncating the disc could have a higher mass if other planets are present with smaller $a_{\rm plt}$, such that particles initially scattered by the outermost planet get scattered inward by the inner planets before being ejected. In a chain of planets this can be achieved consecutively if each planet on the chain has a scattering timescale shorter than the next planet with larger semi-major axis, such that particles get scattered faster by the inner planets, increasing the probability of migrating inwards. In other words, the scattering timescale of the planets in the system has to increase with distance in order to maximise the inward torque. This could be done by a flat distribution of planet mass with $a_{\rm plt}$ as the scattering timescale scales with orbital period. However, a chain of planets with uniform mass above 30 $M_{\oplus}$ would scatter material inwards until reaching the innermost planet which will eject particles in only a few encounters without feeding the hot dust.

Therefore, as discussed in Wyatt et al. (2017) I can hypothesise how a chain of planets should be distributed in mass and semi-major axis to maximise the influx from the outer to the inner most regions. The two basic requirements are:

1. the innermost planet within a few au should reside below the ejection region of Figure 3.16, such that particles can remain in the inner regions for longer timescales or produce giant impacts releasing large amounts of dusty debris as accretion is more likely;
2. the mass of planets should be close to a flat distribution or decrease with radius, maximising the inward torque.

Based on Figure 3.16 and the two conditions above, I find that a chain of planets with uniform mass between $3 - 30$ $M_{\oplus}$ would satisfy the two conditions above, e.g. a chain of less than 10 planets separated by $\gtrsim$15 mutual Hill radii with a mass of $\sim$ 10 $M_{\oplus}$. Such a system would scatter particles from the outer regions until they encounter the innermost planet in the chain which would lie below the ejection region. Then, the hot dust excess observed in η Corvi could

be the product of giant impacts releasing debris or the product of collisions between larger grains or planetesimals within a few au where collisions are more frequent and destructive.

The η Corvi sweet spot

In the scenario 3, the hot dust in η Corvi is the result of a giant collision of an embryo scattered from the outer disc with a planet at separations $\lesssim 3$ au. Based on the work by Wyatt et al. (2017) I can place some constraints on this planet or others within a few au. In their work they estimated how long debris produced from a giant collision can remain at detectable levels before being accreted or collisionally depleted (see their Eq. 22 and Figure 5). In Figure 3.16 I plot contours of the timescales at which debris produced by a giant collision can remain above the current levels in η Corvi. I assume that the giant impact puts in orbit a fraction $f_{\rm esc} = 0.05$ of the mass of the planet, that evolves through mutual collision or it gets accreted by the planet. The debris is characterised by a maximum particle size of 100 km and a planetesimal threshold $Q^{\star}_{\rm D} = 200$ J kg^{-1}. SED modelling showed that the peak of the hot dust is around 20 μm with a fractional excess (R_{20}) of about 0.5 (Duchêne et al., 2014), thus I am interested in the timescale at which the hot dust emission can stay above R_{20}, $t_{>R_{\lambda}}$. These timescales are shown in Figure 3.16 with yellow, orange and red contours.

From Figure 3.16 I find that if giant collisions are uniformly likely in the log($a_{\rm plt}$)-log($M_{\rm plt}$) space, an excess at 20 μm is more likely to be produced around 3-5 au by a collision on a planet of 4-10 M$_{\oplus}$. This excess would last around 10^4 years or a few thousands orbits. Throughout this time the debris would remain in an asymmetric distribution (Jackson et al., 2014). Such asymmetry would naturally explain why the emission is seen at a projected separation in the range 0.5-1 au by the LBTI (Defrère et al., 2015), but its temperature suggests a physical separation of ~ 3 au where the collision would have happened. Otherwise, this is hard to reconcile if the hot dust is produced in an axisymmetric disc, where a collisional cascade is fed from the outer belt (scenario 2). For scenario 2 to work this requires a very high albedo and a grain size distribution steeper than the expected from a collisional cascade (Lebreton et al., 2016), which thus means that scenario 3 may be favoured.

3.4.2 CO origin

Given the old age of η Corvi ($\gtrsim 1$ Gyr) any gas present in the system has to be of secondary origin, i.e. released from icy bodies present in the system. This could happen either in the outer belt or in the inner disc if CO is released as a consequence of collisions between icy bodies; however, the tentative detection of CO is not co-located with either of the two. Recently Kral et al. (2016) studied the evolution of secondary gas in a debris disc when

produced from a narrow ring. The gas can viscously spread forming an accretion disc, with a surface density that depends on the gas production rate and on the viscosity of the disc, expected to be higher than in a protoplanetary disc as the disc should be highly ionised (Kral & Latter, 2016). Depending on the viscous timescale and lifetime, different molecules or atomic species would have different distributions in the disc. For example, in the case of β Pic, CO gas is released at ~ 85 au from icy bodies and photodissociates in C+O, which then spread to form an atomic accretion disc. Atomic gas species such as HI, CI, CII and OI, products of the photodissociation of H_2O and CO can viscously spread in the disc before being accreted into the host star (Kral et al., 2016). On the other hand, CO has a photodissociation timescale of ~ 300 yr (longer than 120 yr as it is slightly self-shielded, Matrà et al., 2017a), which is only a fraction of an orbit, and then too short to be able to spread in the disc. This is why CO is found to be co-located with the millimetre-sized dust in the β Pic disc, where it is released (Dent et al., 2014; Matrà et al., 2017a).

However, if gas is released closer in, e.g. at ~ 1 au where the hot dust is located in η Corvi, then CO could spread significantly outwards in the disc as both the orbital and viscous timescale increase with radius. In order to assess if the CO could spread up to 20 au, I can estimate the viscous timescale, t_ν, for it assuming an α-parametrization for the viscosity (Shakura & Sunyaev, 1973), i.e. $\nu = \alpha_\nu c_s H r$, where c_s and H are the sound speed and the local disc scale height. Assuming $\alpha_\nu = 1.5$ (best fit model for β Pic, Kral et al., 2016) I find that $t_\nu \sim \frac{\Delta r^2}{\nu(r'_c)}$ is $\sim 10^4 - 10^5$ yr for $\Delta r = 20$ au and r'_c=1-20 au. This is longer by at least two orders of magnitude than the photodissociation timescale, and thus, CO would not be able to spread fast enough to reach 20 au before being photodissociated. If the CO production rate were high enough, CO could be self-shielded; however, the upper limit I found in §3.3.7 for a broad inner disc implies that the vertical column density of CO is $\lesssim 10^{14}$ cm^{-2}, not enough to be considerably self-shielded (Visser et al., 2009). Note that carbon ionization can also shield the CO, yet in β Pic this was found to be a minor effect compared to the CO self-shielding (Matrà et al., 2017a). Assuming a carbon to CO abundance ratio of 100, carbon ionization would shield the CO only by a factor of 1.2, increasing its photodissociation timescale to 140 yr (Rollins & Rawlings, 2012). Another important issue with this scenario is that within a few au solids should be depleted of icy volatiles as the temperatures are significantly higher than 140 K, the maximum temperature at which CO or CO_2 can be trapped by amorphous H_2O ice (Collings et al., 2003). In η Corvi this temperature corresponds to the equilibrium temperature at 9 au. Therefore, icy material would have to pass very quickly this ice line to reach $\sim$1 au to release the CO in destructive collisions of planetesimals or be large enough as the sublimation rate depends on their area, e.g. comets in Solar System that cross the water ice line can retain significant amounts of ices for several orbits.

Alternatively, the tentative CO detection at 22 ± 6 au could be explained by gas released in

situ. Icy material formed in the outer belt and transported from cold regions, should start to sublimate at a high rate when crossing a specific ice line or reaching specific temperatures. At 22 ± 6 au, the equilibrium temperature is 88 ± 12 K. Desorption experiments have studied in detail the desorption rate of volatiles in isolation or with the presence of water ice, as a function of the temperature. For example, in isolation the CO_2 desorption rate peaks at around 80 K (Collings et al., 2004), thus CO gas trapped in CO_2 ice could be released when crossing the CO_2 ice line; alternatively, as CO_2 photodissociates in about 30 yr into CO and O due to the interstellar UV radiation field (Hudson, 1971; Lewis & Carver, 1983), the observed CO could all come from CO_2 being photodissociated. For example, the coma activity of comet C/2012 S1 (ISON) on its last passage was likely controlled by CO_2 ice sublimation beyond the water ice line (Meech et al., 2013). Another possibility is that if the volatile content in planetesimals is dominated by water ice, the desorption rates of other molecules can be modified as they get trapped by amorphous water ice. This is true for trapped CO and CO_2 reaching a maximum desorption rate at $\sim$ 140 K during water crystallisation and at 160 K when water starts to sublimate, allowing trapped volatiles to desorb (Collings et al., 2003, 2004). In fact, this is observed in Solar System comets, where the composition of their coma changes from CO- to H_2O-driven near 2.5 au, where the comet surface temperatures reach $\sim$ 150 K (e.g., Comet Hale-Bopp (C/1995 O1) and others, Biver et al., 1997; Ootsubo et al., 2012). Therefore, CO could be released in situ explaining the tentative detection without the need of being released in collisions and viscously expand from close in regions where the hot dust is. It is also worth noting that the location at which these temperatures are reached, depend also on the surface physical properties of the icy material, e.g. if it is covered by ice or dust, on the rotation rates and if volatiles are being released from small grains or not, and they can even vary significantly across the surface of big comets (Choukroun et al., 2015, e.g., comet 67P/Churyumov-Gerasimenko,). Numerical simulations by Marboeuf et al. (2016) have explored the thermo-physical evolution of comets and production rates of H_2O gas and dust from their surface, finding for example that the H_2O gas and dust production rates increase exponentially from tens of au down to 6 au for $L_\star = 5L_\odot$. Therefore, the CO location and radial distribution, together with thermo-physical models of comets including other molecule species such as CO and CO_2, can give clues about the nature of these exocomets and composition.

The latter scenario fits with the hypothesis of icy material being passed from the outer belt to the inner regions. The non detection of CO closer in could be explained if the icy material gets depleted of volatiles before reaching the inner regions where the hot dust is. This would imply that the timescale at which material loses its volatile content is shorter than the timescale at which material migrates from $\sim$ 20 to $\sim$ 10 au, i.e. $\lesssim 2 \times 10^4$ yr (using the lower limit on the migration rate for a surface density of solids proportional to r^{-1} derived in §3.4.1).

Alternatively, the non-detection could be also explained by the CO lifetime getting shorter for smaller radii as the UV stellar radiation starts to dominate in the photodissociation process, reducing the amount of CO gas. Moreover, I find that the CO destruction rate, which is $\sim 3 \times 10^{-9}$ $M_\oplus$ yr^{-1}, is of the same order as the hot dust mass loss rate. This implies that the material passed in from the outer belt is highly rich in CO or CO_2 ($\sim$50% of mass in CO) or that only a fraction of the material that reaches 20 au continues its way in to collide where the hot dust is.

One potential problem with this scenario is that if the CO present in the disc is produced in steady state, i.e. constantly released at a rate of $\sim 3 \times 10^{-9}$ $M_\oplus$ yr^{-1}, it would imply that over a timescale of 1.4 Gyr the outer belt has lost $\sim$4 $M_\oplus$ of CO or 40 $M_\oplus$ in planetesimals assuming a CO mass fraction of 10% in solids. This value is of the order of the total amount of solids initially present at the outer belt location if I extrapolate the minimum mass solar nebula (Weidenschilling, 1977b) surface density profile (30 $M_\oplus$), and similar to the initial Kuiper belt mass in the Nice model (35 $M_\oplus$, Gomes et al., 2005). However, this assumes that the amount of CO gas present at 20 au is in steady state, which is not necessarily the case. For example, if the hot dust is fed by particles with a wide size distribution, small grains would be fed continuously, whereas bigger particles which contain most of the mass would behave stochastically as the number is much lower. Therefore, we could be witnessing a rare event in this system. This is similar to the stochastic accretion proposed to explain the pollution on white dwarfs (Wyatt et al., 2014). If the tentative CO detection is confirmed and its distribution resolved, it would help to constrain better how the hot dust is being fed from material originated in the outer belt.

3.5 Conclusions

In this chapter I have presented the first ALMA observations of the debris disc around η Corvi at 0.88 mm, obtaining the most detailed image of its outer belt up to date. I detected the outer disc at all azimuths, with a peak radius of 150 au and radially spanning over 90, consistent with being axisymmetric and with previous observations.

In order to obtain estimates of different disc parameters with uncertainties, I model the emission using a number of four disc models and compared them with the observed visibilities. The first model consists of a simple belt with radial and vertical Gaussian mass distributions. I found the outer belt density distribution peaks at 150 ± 3 au, with a radial FWHM of 44 ± 6 au. This model gives the best fit to the observations with a total flux of 13 ± 1 mJy. The second model consists of the expected profile from a self-stirred disc. I found that the derived disc parameters in the self-stirred scenario imply an unphysically high range

of surface density of solids in the primordial disc. However, self-stirring could still be the case if the outer belt was initially narrow or truncated by a planet.

Because of the comet-like composition of the hot dust and its short lifetime, it has been suggested that it is being fed from the outer belt. Several mechanisms could be responsible of such delivery. Previous observations ruled out all except three, one of which proposes that the system is going through LHB-like instability. I compared simulated observations using as input one of the LHB models, scaled to the size of the η Corvi outer belt, finding that the surface density radial profile from LHB simulations is too broad compared to the η Corvi outer belt. Moreover, a double power-law fit to the disc surface density indicates that it must increase steeply from the inner regions to the outer belt, in contradiction with a highly scattered belt produced after an instability. I also fit an eccentric disc model, finding that the disc is consistent with being circular and with a 3σ upper limit for the belt eccentricity of 0.05. Therefore, I conclude that the outer belt is probably in a stable configuration on Gyr timescales, where a chain of planets is scattering in material from the outer belt.

Although the exact mechanism or planetary configuration scattering material inwards is unknown, I placed upper limits on any millimetre extended emission from dust inside the cavity based on the measured visibilities. These limits can be used in the future to place constraints on the distribution of solids if material is indeed being transported from the outer belt to the inner most regions of the system.

I searched for any CO gas that could be present in the disc. Although I did not detect gas in the outer belt or co-located with the hot dust, I present a tentative detection of CO gas around ~ 20 au. Considering non-LTE effects, I derived a CO gas mass estimate based on a tentative CO detection at ~ 20 au and 3σ upper limits according to the non-detections in the outer belt and inner regions. Regarding the origin of the putative CO gas, I find that it could be released in situ from icy bodies when crossing an ice line, e.g. CO_2 sublimates at ~ 80 K, which could then release trapped CO or produce it via photodissociation. Alternatively, CO gas trapped in porous H_2O ice could be released following the crystallisation of water or its sublimation when reaching 140 K or 150 K, respectively. This scenario is consistent with the hypothesis that material being transported from the outer belt to the location of the hot dust and suggests that we could be observing the system with a particularly high activity after a recent event. It is unlikely that the observed CO gas is being produced within a few au and viscously expanding outwards up to 20 au, as timescales for photodissociation are shorter than viscous evolution.

Finally, based on the estimates of the disc inner edge and eccentricity, I constrain the mass and semi-major axis of any planet that could be responsible for truncating the disc at $\sim$106 au in a timescale shorter than the age of the system, inducing a forced eccentricity lower than 0.05, and with a mass and semi-major axis such that it scatters material from the outer disc that can

move inwards without being ejected from the system on timescales of the order of the age of the system. Under these restrictions, I find that such planet should have a semi-major axis around 75-100 au, a mass between 3-30 $M_{\oplus}$ and an eccentricity lower than 0.08.

Therefore, I proposed the following global scenario: volatile-rich solid material formed in the outer belt is being passed in via scattering with a chain of planets in the system. This icy material starts to sublimate and loses part of its volatiles when crossing specific ice line(s), explaining the CO at $\sim$20 au. The chain of planets should have a mass distribution close to flat between 3-30 $M_{\oplus}$ to maximise the mass flux into the inner regions where the hot dust lies. Finally, the inflowing material feeds an in situ collisional cascade or collides with a planet with a mass of 4-10 $M_{\oplus}$ located at $\sim$ 3 au (sweet spot of the system) releasing large amounts of debris and resulting in an asymmetric structure, consistent with LBTI observations and the observed spectroscopic features. This can be tested by: 1) confirming the CO detection and resolving both in radius and azimuth the distribution of gas in the disc with deeper ALMA observations; 2) detecting any extended dust emission inside the cavity combining ALMA and ACA or with SMA observations reaching a higher sensitivity on large scales; 3) follow up LBTI observations to constrain the hot dust distribution which should remain constant and asymmetric in a giant impact scenario; 4) RV upper limits of planets that discard the presence of an ejector within 3 au ($\gtrsim$ 0.1 $M_{\rm Jup}$); 4) direct imaging to search for outer planets, which at 10 $M_{\oplus}$ would be challenging to detect directly, but could have an enhanced brightness if surrounded by dust (Kennedy & Wyatt, 2011); 5) N-body simulations tailored to the system (see Chapter 6).

4

ALMA observations of the multiplanet system 61 Vir: What lies outside super-Earth systems?

4.1 Introduction

A few systems are known to host both a planet(s) and a debris disc. Among the best studied are β Pic (e.g., Smith & Terrile, 1984; Lagrange et al., 2009b; Dent et al., 2014), HR 8799 (e.g., Marois et al., 2008, 2010; Matthews et al., 2014a; Booth et al., 2016) and Fomalhaut (e.g., Kalas et al., 2008), all with planets directly imaged that lie between the star and the disc. However, these systems are outliers in terms of their planets and disc properties since neither represents the bulk of the known planetary systems, nor debris discs.

Thanks to unbiased debris disc surveys of FGK stars within 45 pc (e.g., DUNES and DEBRIS, Eiroa et al., 2013; Matthews et al., 2014b), it has been possible to study the frequency of circumstellar material around stars hosting high- and low-mass planets detected by radial velocity surveys. Studies focused on high-mass planets found no evidence of a different debris disc incidence rate in these planet hosting stars compared to normal field stars (Greaves et al., 2004; Moro-Martín et al., 2007; Bryden et al., 2009). On the other hand, two studies focused on planetary systems with planet masses below $\sim$ 95 $M_{\oplus}$ found debris disc incidence rates of: 4/6 (Wyatt et al., 2012), significantly higher compared to field stars; and

2/6 (Moro-Martín et al., 2015), consistent with field stars. Combining both samples, at least four out of eight systems with low-mass planets also have a debris disc, which suggests that there might be a difference in the occurrence of bright debris discs in systems with low-mass planets, as predicted by planet formation models (e.g., Raymond et al., 2011).

One of these planetary systems hosting a debris disc is 61 Vir. This system located at 8.6 pc (van Leeuwen, 2007) is composed of

1. a G5 4.6 ± 0.9 Gyr old star (Wright et al., 2011; Vican, 2012);
2. three RV planets with minimum masses of 5, 18 and 23 $M_{\oplus}$ and semi-major axes of 0.05, 0.22 and 0.49 au, respectively (Vogt et al., 2010), although the third one was not confirmed in the HARPS data, Wyatt et al. 2012;
3. a debris disc discovered by Spitzer with a fractional luminosity of 2×10^{-5} (Bryden et al., 2006).

The disc was later imaged by Herschel showing that the dust density peaks between 30 and 100 au and it is inclined by $\sim 77^{\circ}$ with respect to the plane of the sky (Wyatt et al., 2012). Assuming that the disc and orbits of these planets are co-planar, then the planet masses quoted above would be only underestimated by 3%. This system is particularly interesting as the fraction of stars with super-Earths, similar to 61 Vir, could be up to 30-50% (e.g., Fressin et al., 2013), which makes 61 Vir a good case to study the formation of such abundant planets by analysing its debris disc.

Due to a low 50 au resolution, Herschel could not constrain the exact morphology and dust distribution at the inner regions of the disc, but by fitting both images and SED, Wyatt et al. (2012) found three best fit models: 1) an extended disc with a sharp inner edge at $\sim$30 au, extending at least out to 100 au, and a surface density or optical depth radial profile with an exponent of -1.1; 2) similar to the first model, but adding an inner component where the surface density increases with radius as $r^{7/3}$ (inspired by collisional evolution models, see Chapter 3) from 1 au to the disc inner edge now placed at 43 au; 3) a two belt model consisting of two 10 au wide dusty belts centered at 40 and 90 au. These three models could well fit the previous observations, but the low 50 au resolution hindered determining the exact dust distribution. Moreover, because the disc emission at Herschel wavelengths is dominated by small grains that are subject to radiation forces, the derived distribution does not necessarily trace the location of the parent planetesimal belt, as they can extend to larger radii beyond that belt (e.g., Krivov et al., 2006; Thébault & Augereau, 2007).

In this chapter I present the first observations of 61 Vir with ALMA at 0.86 mm, obtained with the aim of studying its debris disc to reveal the location of the parent planetesimals, and place

constraints on the presence of planets at large separations that can shape the mass distribution in the disc. In order to obtain the best disc constraints, in my analysis I combine new ALMA band 7 observations and new data at 0.85 mm from the submillimetre Common-User Bolometer Array 2 (SCUBA2) installed in the James Clerk Maxwell Telescope (JCMT), thus, incorporating information from small and large angular scale structure.

In addition, I implement a simple numerical collisional evolution model that simulates the evolution of a broad disc, taking into account the disruption threshold of planetesimals as a function of size, how relative velocities vary with radii, and the different features in the size distribution of solids, e.g. the ripples close to the blow-out size. I use this to constrain the initial solid mass or surface density in the disc and the maximum planetesimal size.

This chapter is organised as follows. In §4.2 I present new SCUBA2/JCMT data. In §4.3 I describe the ALMA observations, studying the dust continuum and how it compares with previous Herschel observations, and I search for CO line emission. In §4.4 I fit the SCUBA and ALMA data using a parametric disc model to study the distribution of millimetre dust in the disc. §4.5 describes a numerical model to calculate the collisional evolution of a disc at different radii that can be used to compare with observations determining the maximum planetesimal size in a disc and the initial sold mass. In §4.6 I discuss the observations and possible scenarios than could explain the low initial solid mass and maximum planetesimal size. Moreover, I constrain the mass, semi-major axis and eccentricity of a hypothetical planet stirring the disc. Finally, In §4.7 I summarise and present the main conclusions of this chapter.

4.2 SCUBA2 observations

As part of the SCUBA-2 Observations of Nearby Stars (SONS) survey (Panić et al., 2013; Holland et al., 2017), 61 Vir was observed at 0.85 mm with SCUBA2/JCMT (Holland et al., 2013) to constrain the millimetre flux and extent of its debris disc. 61 Vir was observed for 7.5 h and the data was reduced using the Dynamic Iterative Map-Maker within the Starlink SMURF package (Chapin et al., 2013), which was called from the automated pipeline ORAC-DR (Cavanagh et al., 2008). More details on the SCUBA2 data reduction of the SONS survey can be found in Holland et al. (2017).

Herschel and VLA observations previously found three background sources close to 61 Vir which could affect the analysis of the SCUBA2 data. To obtain a non-contaminated large scale image and photometry of 61 Vir I subtract these as point sources, using as PSF the SCUBA2 reduced observation of Uranus obtained in the same run. As two of these sources are detected in the ALMA data (see §4.3.1), I can derive their fluxes and astrometric positions at 0.86 mm, and accurately subtract these from the SCUBA2 reduced image, correcting for the proper

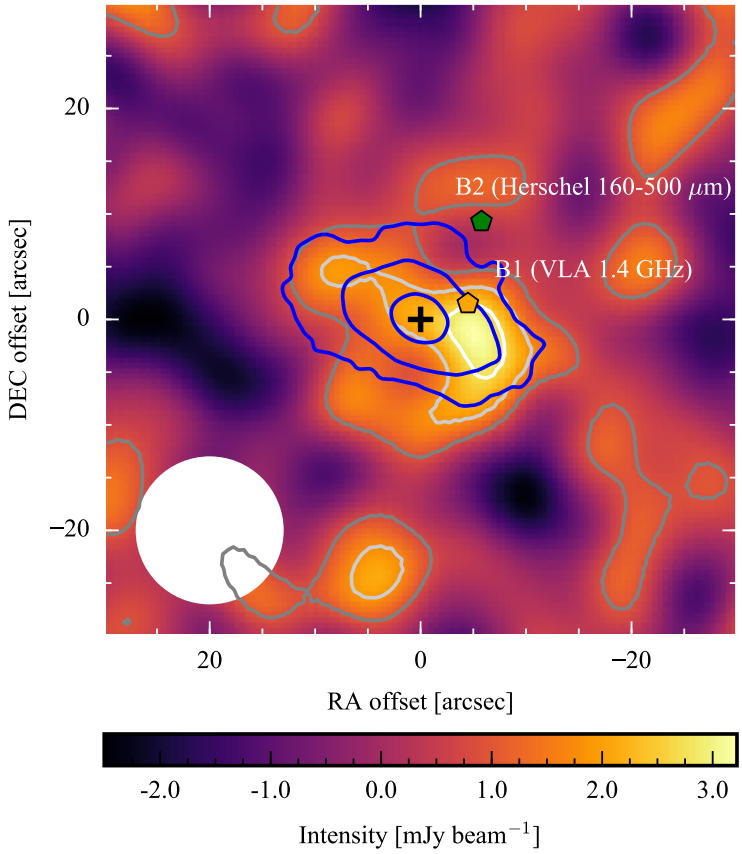

Figure 4.1: SCUBA2 0.85 mm continuum image of 61 Vir after subtracting two point sources from background emission. The beam size is 13″ and is represented with a white ellipse at the bottom left corner of the image. The grey and white contours represent emission above 1, 2 and 3 times the noise level. Blue contours at arbitrary levels from the Herschel 70 μm image are overlayed and are corrected for proper motion. The green and yellow pentagon symbols indicate the position of the background sources that were subtracted from this image. The x- and y-axes indicate the offset from the stellar position in R.A. and decl. in arcsec, i.e. north is up and east is left. The stellar position is marked with a black "+".

motion of 61 Vir μ=(1.07, -1.06) $''$ yr^{-1} (van Leeuwen, 2007). The third background and more distant source from 61 Vir is not detected with SCUBA2, and lies outside the field of view of the ALMA observations. In Figure 4.1 I present the SCUBA2 image smoothed with a Gaussian kernel of FWHM $6\farcs5$ after subtracting the two background sources. Integrating all the emission inside a circumference of $15''$ radius I find a total flux of 5.0 ± 1.2 mJy (including the stellar emission and calibration uncertainty), slightly lower but consistent within errors with the previous data presented in Panić et al. (2013).

4.3 ALMA Observations

ALMA band 7 (0.86 mm) observations of 61 Vir were carried out on 2015 April, split into 4 scheduling blocks (one on April 9 and three on April 22) as part of the project 2013.1.00359.S (PI: M.C. Wyatt). The total number of antennas was 44, with baselines ranging from 29 to 228 m (5th and 95th percentiles). This allows us to recover angular scales of $0\farcs6$ up to $6''$ on the sky. The correlator was set up with three spectral windows to image the continuum centered at 333.84, 335.78 and 347.74 GHz, each with 128 channels and a total bandwidth of 1.88 GHz; and a fourth one to search for CO (v=0, 3-2) emission in the disc centered at 344.85 GHz, with 3840 channels, a channel width of 0.42 km s^{-1} (effective spectral resolution of 0.82 km s^{-1}) and a total bandwidth of 2 GHz. Calibrations were applied using the pipeline provided by ALMA. The total time on source excluding overheads was 178 min.

4.3.1 Continuum emission

To study the continuum emission, I use the four spectral windows to reach the highest sensitivity as no CO emission is present in the data (this is discussed below). Figure 4.2 shows the continuum image using the task CLEAN in CASA 4.4 (McMullin et al., 2007a) with natural weights and correcting for the primary beam — note that the noise increases towards the edges of the image as the primary beam sensitivity decreases. At the center of the image the rms noise level is 16 μJy beam^{-1}, which increases to 32 μJy beam^{-1} at $7\farcs5$. The beam size is $1\farcs1 \times 0\farcs7$ with a position angle (PA) of $-70°$. In the image three compact sources are detected: 61 Vir's stellar emission at the center with a total flux of 374 ± 16 μJy, which is 2.4σ higher than the 320 ± 16 μJy predicted photospheric emission assuming a spectral index of -2, thus, which could be due to chromospheric emission at this wavelength (e.g., Loukitcheva et al., 2004; Fontenla et al., 2007); and two other sources to the north of the star with offsets of $4\farcs5$ and $12\farcs5$, and peak fluxes of 360 ± 20 μJy and 850 ± 70 μJy, respectively. The latter is resolved with a total flux of 2.2 ± 0.3 mJy within a $2''$ radius circumference. These two sources are almost certainly the background galaxies previously reported in Wyatt et al. (2012) and

their position is overlayed with pentagon markers and labelled as B1 and B2. I also overlay the position of a third background source (B3) detected at 5 GHz with the VLA and not present in the ALMA data. The latter is the southern component of a double-lobed structure with the northern component outside the ALMA primary beam. At 1.4 GHz, B1 was marginally resolved and found to be extended in the north-south direction with a fitted FWHM of 33″, therefore, consistent as being the two lobes resolved at 5 GHz.

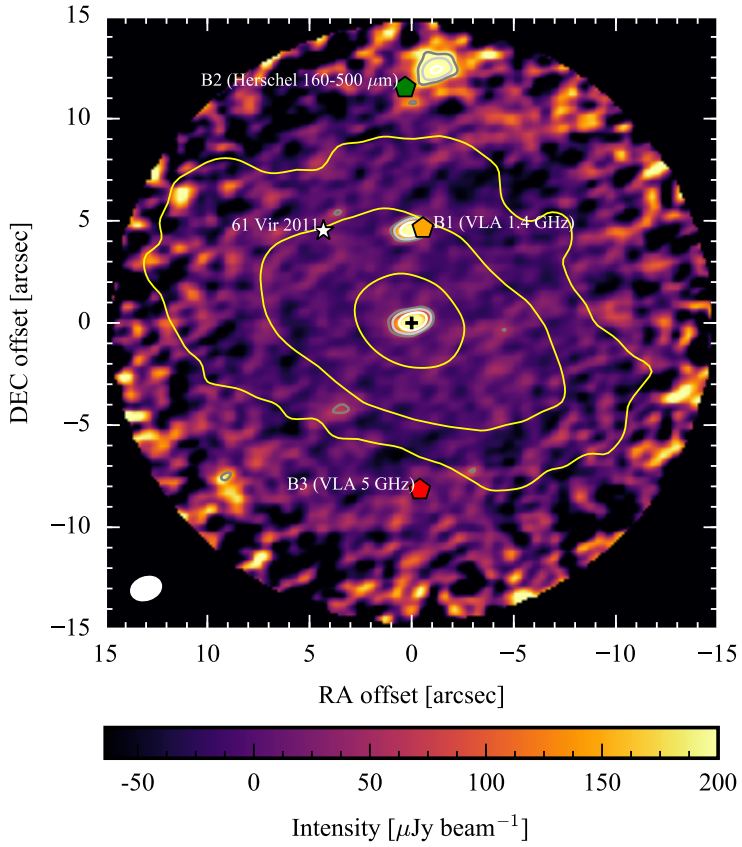

Figure 4.2: ALMA band 7 (0.86 mm) continuum image of 61 Vir with natural weights and corrected by the primary beam response (FWHM$\sim$ 17″). The beam size is $1\farcs1 \times 0\farcs7$ and is represented with a white ellipse at the bottom left corner of the image. The grey and white contours represent emission above 3, 5 and 10 times the local noise level. Yellow contours from the Herschel 70 μm image at arbitrary levels are overlayed correcting by the stellar proper motion. The x- and y-axes indicate the offset from the stellar position in R.A. and decl. in arcsec, i.e. north is up and east is left. The stellar position is marked with a black "+" and the position of background sources previously detected are represented with pentagons. The black masked region indicates a primary beam response below 10%

Although there is no disc emission above 3σ in the ALMA Clean image, significant signal is present in the real component of the visibilities after subtracting the three compact sources. By de-projecting the observed visibilities assuming a disc PA and inclination of 65° and 77°, respectively (consistent with the Herschel observations, Wyatt et al., 2012), I recover disc emission in the short baselines ($\lesssim$ 10 kλ, see Figure 4.3), corresponding to extended emission

($\gtrsim$ 20″ or 150 au). I also overlay the model visibilities of a disc with a flux of 4 mJy and extending from 30 to 140 au, consistent with the data (see §4.4). The imaginary part of the visibilities is consistent with pure noise around zero, which is expected for an axisymmetric centered disc.

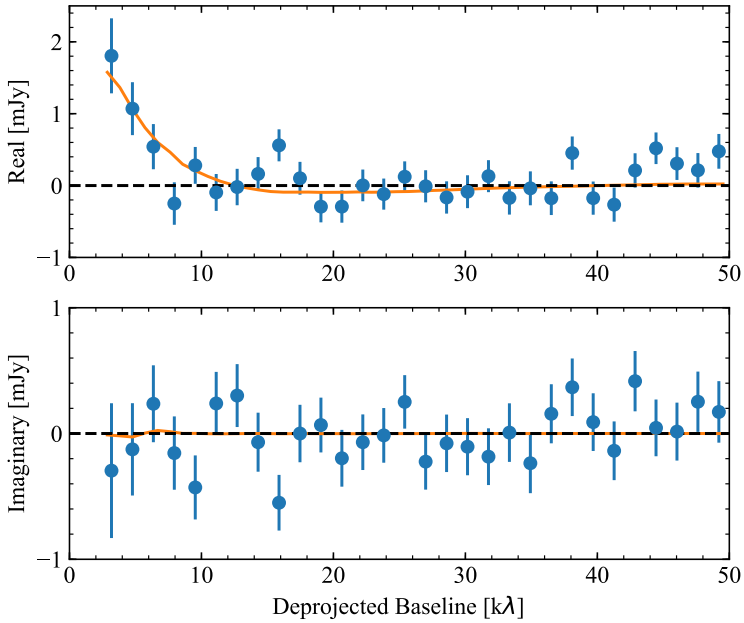

Figure 4.3: Deprojected visibility profile of the ALMA band 7 (0.86 mm) continuum after subtracting the emission from the three compact sources. The blue points represent averaged and binned visibilities with 1σ errorbars. Overlayed is a best fit disc model (orange line).

I can also recover the disc emission in the image space by integrating the flux inside ellipses of different semi-major axes (with the same PA and aspect ratio or inclination as the disc resolved by Herschel). In this integration I exclude a 30° wide wedge in the direction of B1. The resulting radial profile is presented in the top panel of Figure 4.4. Within 10″ the total disc and stellar emission is only 0.8 ± 0.2 mJy, 2.2 σ lower than the derived flux from SCUBA2. If I subtract the stellar emission, the disc is marginally detected at 2.2σ with a total flux of 0.43 ± 0.2 mJy. The lower ALMA disc flux could be produced by spatial filtering in the ALMA data due to a lack of short baselines, as the maximum recoverable scale is 6″ given the range of baselines in the data. This is illustrated in Figure 4.3 and demonstrated in §4.4, where I fit and simulate the observed visibilities and the SCUBA2 image using a parametric disc model that I use to constrain the disc flux and disc surface density.

I search for any spatially resolved disc emission by azimuthally averaging a Clean ALMA image, which was smoothed by tapering the visibilities with the Fourier transform of a Gaussian of FWHM of 1.″5. This process degrades the Clean beam to a size of $1.''8 \times 1.''5$, increasing the S/N for extended emission. The azimuthal averaging method also takes into account the disc inclination and PA and is done in wedges of $\pm 30°$ along the major axis of the

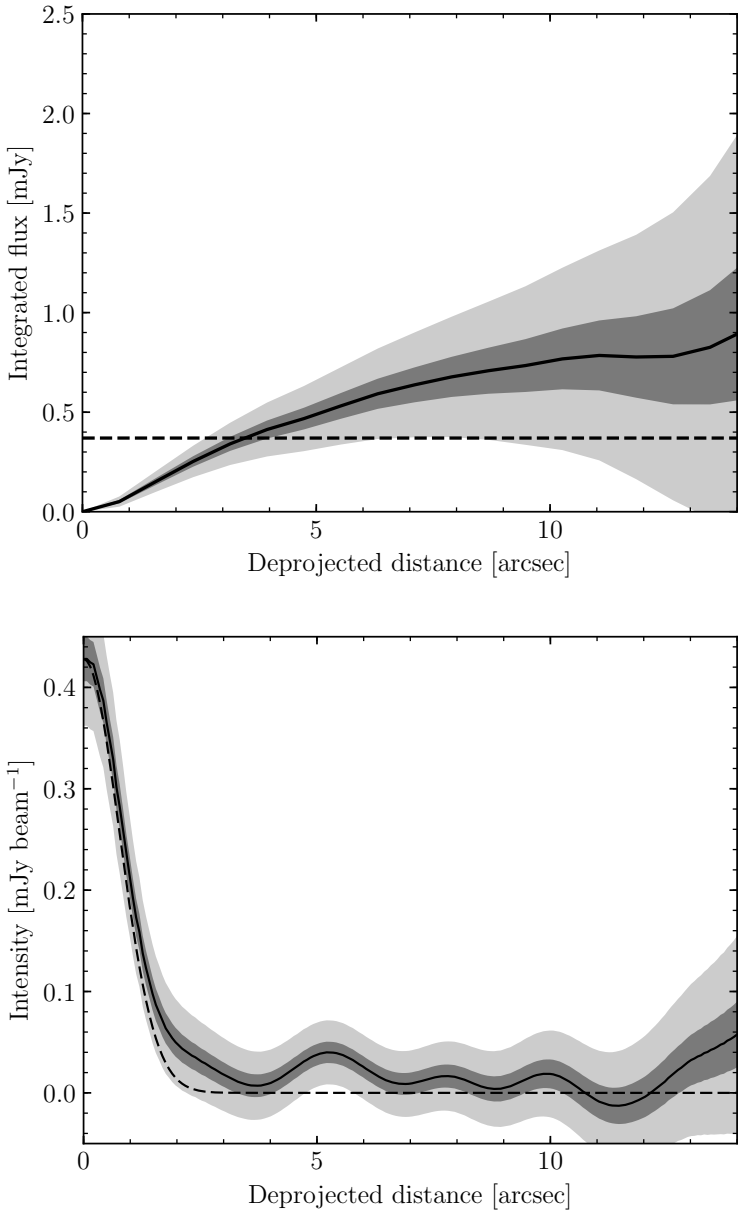

Figure 4.4: ***Top:*** Integrated flux vs semi-major axis of elliptic regions over which the flux is integrated. The dashed line represents the stellar flux. ***Bottom:*** Average intensity radial profile computed in wedges of $\pm 30°$ along the major axis of the disc, using the reconstructed Clean image tapered with the Fourier transform of a Gaussian of FWHM of $1\farcs5$. The dashed line represents the PSF. The grey shaded areas in both panels represent 68% and 99.7% confidence regions.

disc. At each radius, the uncertainty is computed based on the uncertainty on each pixel and the number of independent measurements, estimated to be equal to the length of the arc over which I am averaging, divided by the beam's semi-major axis. The azimuthally averaged intensity is presented in the bottom panel of Figure 4.4. This shows a marginal disc detection of 0.04 ± 0.01 mJy beam^{-1} at $5\farcs5 \pm 0\farcs9$ (where the positional uncertainty is roughly estimated as $\sim$beam semi-major axis$/\sqrt{S/N}$), equivalent to 47 ± 8 au, consistent with the inner disc

radius constrained to be between $30 - 40$ au, depending on the disc model assumed to fit the Herschel observations (Wyatt et al., 2012). Moreover, positive emission is present from the stellar position to a distance of $11''$, but not at a significant level apart from the peak at $5\farcs5$. This is consistent with the positive total flux described before, in other words, with the 2.2σ detection integrating over all radii.

4.3.2 CO

Although CO gas of secondary origin has been found in a few young bright debris discs, probably released in collisions of icy solids as shown in Chapter 2, no CO (v=0, J=3-2) emission was detected in 61 Vir ALMA data. However, given the short photodissociation timescale of 120 yr, together with the low dust optical depth, and thus, low collisional rates of solids in the disc, I do not expect to detect CO gas being released in collisions of icy planetesimals in this system. Therefore, planetesimals in this system could still be as rich in volatiles as Solar System comets.

4.4 Disc modelling

In order to place better constraints on the total disc flux, disc size, inclination and position angle, I fit a parametric disc model to the SCUBA2 image and ALMA visibility data simultaneously. The model consists of a central star surrounded by a dusty disc and two background point sources (B1 and B2) at the position of the maxima in the ALMA image. The fluxes of the star, B1 and B2 are held fixed at their observed values of 0.37, 0.36 and 0.85 mJy, respectively. Note that the B2 is apparently resolved and could be modelled with an extended component, but this has no effect on the fitted parameters and best fit models.

The dusty disc is assumed to have the same dust size distribution and composition as the disc models in Chapter 3. The central star is modelled using a stellar template spectrum with a effective temperature of 5500 K[1] (Kurucz, 1979) and a radius of 1.1 $R_{\odot}$ to fit the stellar emission at 0.86 mm. Then, the dust equilibrium temperature at different radii is computed using RADMC-3D[2] (Dullemond et al., 2016). The disc surface density varies with radius and is parametrized with a power law function as r^{α} from a minimum radius of 30 au, extending to $R_{\rm max}$, which is a free parameter as well as α and the total disc flux, $F_{\rm disc}$. I maintain $R_{\rm min}$ fixed at 30 au (best fit value for a model with a sharp inner edge when fitting the Herschel observations and SED, Wyatt et al., 2012). The vertical mass distribution is assumed to be Gaussian with a standard deviation or scale height H that scales linearly with radius as

[1] http://www.stsci.edu/hst/observatory/crds/k93models.html
[2] http://www.ita.uni-heidelberg.de/~dullemond/software/radmc-3d/

$H = 0.1r$. Synthetic images at 0.86 mm are then produced using RADMC-3D with an inclination, i, and PA that are also left as free parameters. In total there are 5 free parameters that I vary to fit the observations.

Model visibilities are computed at the same uv points as the ALMA observations (as in the previous chapters). On the other hand, the SCUBA2 observation are simulated by convolving the model image with a two dimensional Gaussian with a FWHM of $13''$ (SCUBA2 PSF).

To find the best fit I use a Bayesian approach, sampling the parameter space using an MCMC sampler as in the previous chapters. The posterior distribution is defined as the product between the likelihood function and the prior distributions. The first is defined as $\exp(-\chi^2/2)$, with $\chi^2 = \chi^2_{\rm ALMA} + \chi^2_{\rm SCUBA2}$, with $\chi^2_{\rm ALMA}$ defined as in Equation 2.2. $\chi^2_{\rm SCUBA2}$ is defined as the sum over every pixel of the squared difference between the SCUBA2 real and model images, divided by the pixel rms. The pixel rms is empirically estimated by measuring the dispersion on the unsmoothed SCUBA image (which has uncorrelated pixel noise). The prior probabilities of the parameters are assumed to be uniform. I restrict $R_{\rm max}$ to be between 30 and 250 au, α from -5 to 5, $F_{\rm disc}$ >0, PA from 0° to 90° and i from 45° to 90° (priors based on the previous Herschel observations).

To demonstrate that there is disc emission in the ALMA data that can be better constrained by adding the SCUBA2 image to the fitting process, in Figure 4.5 I present the marginalised distributions of i and PA when fitting only the ALMA data and constraining $R_{\rm max}$ to values below 140 au as any disc emission beyond that would lie outside the ALMA primary beam. Even though disc emission above 3σ is not present in the reconstructed ALMA image (see Figure 4.2), but only when integrating the emission, I find that the disc orientation can still be constrained and matches with the previous estimates from Herschel observations (blue lines).

Table 4.1 summarises the best fit values and Figure 4.6 displays the marginalised distributions of $R_{\rm max}$, α and $F_{\rm disc}$, when ALMA visibilities and the SCUBA2 image are combined in the analysis. The disc orientation is better constrained, with PA $= 59 \pm 5$ and $i = 82 \pm 4^\circ$, consistent with the Herschel observations (PA $= 65^\circ$ and $i = 77^\circ$), and within the limits obtained from fitting the ALMA data alone (see Figure 4.5). Regarding the disc structure, I find that α peaks at zero on its marginalised posterior distribution and is constrained between -0.2 and 3.5 (68% confidence), but still consistent within the 95% confidence region with the value of -1 (see Figure 4.6) found by fitting the Herschel observations, which was also poorly constrained (Wyatt et al., 2012). If I restrict i between $70 - 80^\circ$ (using the prior information from Herschel images), I can improve the constraints on the slope, finding $\alpha = 0.1^{+1.1}_{-0.8}$. Therefore, I conclude that the surface density distribution is not very centrally concentrated.

For example, I can discard a scattered disc that has an initial characteristic surface density proportional to $r^{-3.5}$ (e.g., Duncan & Levison, 1997). The collisional evolution of such an

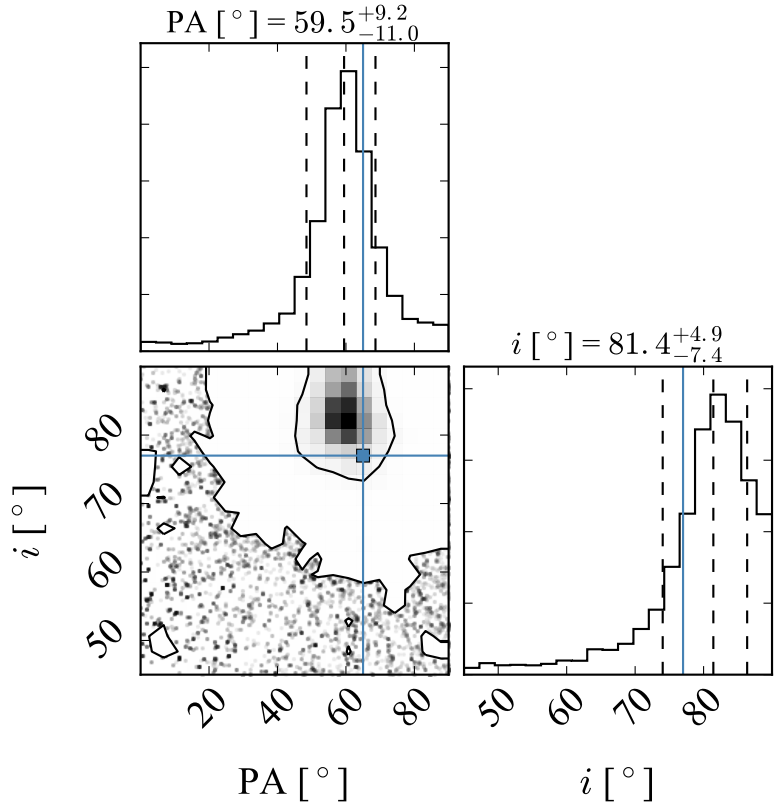

Figure 4.5: Posterior distributions of PA and i when fitting the ALMA data only. The vertical dashed lines represent the 16th, 50th and 84th percentiles. Contours correspond to 68% and 95% confidence regions. The blue lines represent the previous estimates of i and PA from Herschel observations. This plot was generated using the python module CORNER (Foreman-Mackey et al., 2014).

scattered disc has been studied analytically by Wyatt et al. (2010). I find that for 61 Vir parameters, i.e. assuming $t = 4.6$ Gyr, $\Sigma(t = 0) \propto r^{-3.5}$, pericentre at 30 au and $M_{\rm disc} \sim 10^{-2} - 10^{2}$ M$_{\oplus}$, the resulting surface density should be significantly peaked at 30 au (pericentre) and decrease steeply with radii, inconsistent with the observations (see their Figure 5). Although the analytic model used by Wyatt et al. (2010) could overestimate the surface density of dust at low radii as it is the case for low eccentricities. On the other hand, a flat radial distribution could be expected in the context of an extended disc with a wide range of semi-major axes and small eccentricities, collisionally evolved after being stirred (e.g., Schüppler et al., 2016; Geiler & Krivov, 2017, see §4.5).

I also find that $R_{\rm max}$ is peaked at ~ 150 au, consistent with the maximum radius of at least 100 au derived with Herschel. However, if $\alpha < 0.5$ then the maximum radius is not well constrained as the surface brightness decreases with radius as $r^{\alpha-0.5}$. $F_{\rm disc}$ peaks above zero (3.4σ), and is constrained to be $3.7^{+1.2}_{-1.1}$ mJy; however, this is highly dependent on $R_{\rm max}$ and α. For example, if $\alpha \sim -1$ then $F_{\rm disc} < 4$ mJy (95% confidence).

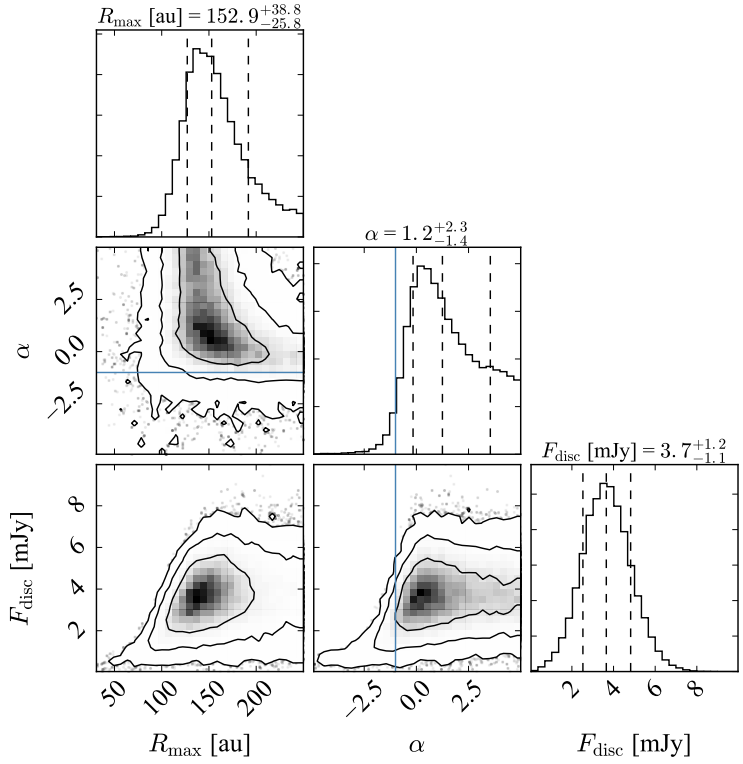

Figure 4.6: Posterior distribution of $R_{\rm max}$, α and $F_{\rm disc}$. The vertical dashed lines represent the 16th, 50th and 84th percentiles. Contours correspond to 68%, 95% and 99.7% confidence regions. The blue lines represent the previous estimate of α from Herschel observations. This plot was generated using the python module CORNER (Foreman-Mackey et al., 2014).

I try to leave $R_{\rm min}$ as a free parameter, but I find that it is not well constrained in these observations. The posterior marginalised distribution of $R_{\rm min}$ is close to flat with a peak at 5 au (the inner boundary of the model). With a smaller $R_{\rm min}$ the disc surface brightness decreases which fits best the ALMA visibilities, while conserving the total flux to fit the SCUBA observations. Therefore, I decide to leave $R_{\rm min}$ fixed based on the previous Herschel and SED information that are inconsistent with $R_{\rm min} \ll 30$ au.

In Figure 4.7 I compare simulated observations of different models and their residuals when subtracted from the real observations. The first column shows the best fit model from the

Table 4.1: Best fit values of the ALMA and SCUBA2 data combined. Median $\pm$ uncertainty based on the 16th and 84th percentile of the marginalised distributions.

Parameter	Best fit value
$R_{\rm max}$ [au]	153^{+39}_{-26}
α	$1.2^{+2.3}_{-1.4}$
$F_{\rm disc}$ [mJy]	$3.7^{+1.2}_{-1.1}$
PA [°]	59 ± 5
i [°]	82 ± 4

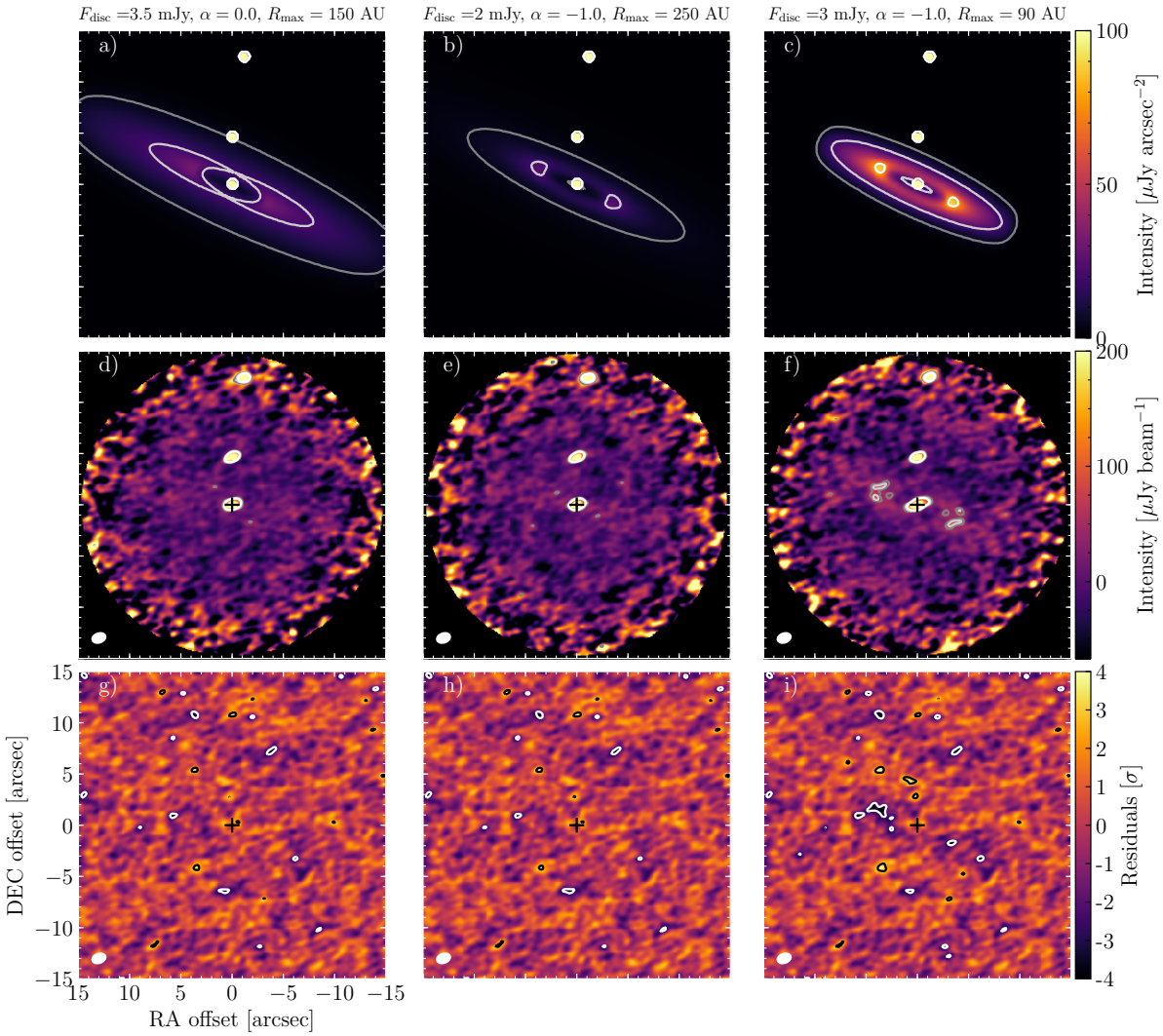

Figure 4.7: Simulated model images and residuals at 0.86 mm. ***First column:*** $F_{\rm disc}$ =3 mJy and $\alpha = 0$. ***Second column:*** $F_{\rm disc}$ =3.5 mJy and $\alpha = -1$. ***Third column:*** $F_{\rm disc}$ =6 mJy and $\alpha = -1$. All disc model images are computed assuming PA $= 65°$ and $i = 77°$. ***First row:*** synthetic images of the disc. Contours represent 5, 20 and 80 μJy arcsec^{-2}. ***Second row:*** primary beam corrected simulated ALMA Clean images using the same uv-sampling and adding Gaussian noise to the visibilities, according to their variance in the observations. Contours represent 3, 4 and 5 times the local noise level. ***Third row:*** Dirty map of the ALMA residuals after subtracting the model visibilities from the ALMA observations. The noise level on the residuals is uniform and equal to 16 μJy beam^{-1} as they are not corrected by the primary beam. The black and white contours represent $\pm 3\sigma$. The beam size is represented by a white ellipse in the bottom left corner. The x- and y-axes indicate the offset from the stellar position in R.A. and decl. in arcsec, i.e. north is up and east is left. The stellar position is marked with a black "+".

posterior distribution presented above with a total flux of 3.5 mJy, $\alpha = 0$, $R_{\rm max} = 150$ au, PA $= 65°$ and $i = 77°$, which has a reduced chi-squared $\chi^2_{\rm red}$=1.0028838 ($N \sim 6 \times 10^6$). The second column shows a model with $\alpha = -1.0$, $R_{\rm max} = 250$ au and $F_{\rm disc} = 2$ mJy, i.e. the most likely disc flux for this α. This model is still consistent with having no disc emission above 3σ in the reconstructed image and has $\chi^2_{\rm red}$=1.0028840 (1.4σ difference with the first model). The third column corresponds to a model similar to the second, but with a less extended disc with

$R_{\rm max} = 90$ au and $F_{\rm disc} = 3$ mJy, increasing the surface brightness of the disc to levels above 3σ in the simulated observation (Figure 4.7f), which translates to significant negative residuals (Figure 4.7i) and $\chi^2_{\rm red}$=1.0028897 (35σ difference with the previous model). I also find that the image reconstruction suffers from flux loss due to an insufficient number of short baselines and the size of the primary beam ($17''$). For the models in the 1st, 2nd and 3rd columns, I recover integrated fluxes of 0.6, 1.0 and 2.3 ± 0.2 mJy, respectively. From the best fit values of the parameters (i.e. $R_{\rm max} \gtrsim 150$ au), the SCUBA2 measured flux (5.0 ± 1.2 mJy) and the simulated observations which show that a compact disc would be detectable, I conclude that the disc of planetesimals must be broad and not concentrated in a single or a few narrow rings, which could not have been resolved by Herschel (model 3 in §4.1).

4.5 Steady state collisionally evolved disc model

It is generally assumed in debris discs that the surface density of millimetre-sized grains can be simply scaled to derive the distribution of the total solid mass in discs. This is true under the assumption that the size distribution from big to small bodies remains fixed. However, using detailed numerical simulations with the Analysis of Collisional Evolution (ACE) code (Krivov et al., 2006), Schüppler et al. (2016) recently showed that the radial profile of the vertical optical depth can deviate considerably from the distribution of planetesimals, when considering this more realistic model of how the grain size distribution evolves at different radii. For example, when assuming a maximum planetesimal size of 100 and 200 km in diameter, they found that the optical depth (dominated by the smallest grains in the disc) stays roughly constant as a function of radius between 10 and 100 au, even though the total surface density decreases with radius. This effect is not due to radiation pressure affecting small dust grains, but due to the evolution of the size distribution at different radii. Specifically, the difference arises when the largest planetesimals in the disc (that dominate the disc mass) are not collisionally evolved, but the smallest grains are already in collisional equilibrium. Using a three phase analytic model for the size distribution, Geiler & Krivov (2017) confirmed this effect and explored how it changes depending on the primordial conditions of the disc.

This implies that even assuming that the primordial distribution of solids in a debris disc is close to a standard Minimum Mass Solar Nebula (MMSN) with a radial distribution with an exponent of -1.5 after the protoplanetary disc disperses (Weidenschilling, 1977b; Hayashi, 1981), or any model for the initial surface density profile of an accreting protoplanetary disc (e.g., Kuchner, 2004; Raymond et al., 2005; Chiang & Laughlin, 2013), the radial distribution of dust grains with lifetimes shorter than the age of the system could have a significantly different radial dependence. Therefore, the surface density exponent for millimetre grains derived in §4.4 cannot be simply extrapolated to the total surface density of solids in 61 Vir.

Here, I aim to study the expected surface density of millimetre grains in a broad debris disc undergoing collisional evolution, and how that depends on the choice of maximum planetesimal size. I do this by using a simple numerical prescription that simulates the size distribution using size bins and assuming that the size distribution is in quasi steady state. This means that the mass loss rate due to catastrophic collisions in each size bin is balanced by the input from fragmentation of larger bodies in destructive collisions, which inputs mass into the bin. The maximum size in collisional equilibrium, D_c, corresponds to the one having a collisional lifetime equal to the age of the system. This method is described in detail in (Wyatt et al., 2011, see §2.4.2, 2.5 and 2.9 therein) and can reproduce the morphology (slope and wiggles) seen in more detailed numerical simulations (e.g. using the ACE code, Löhne et al., 2008).

The model is composed of a 1 $M_\odot$ star at the center and a debris disc spanning 1 to 300 au. The primordial mass surface density of solids is assumed to be that of a MMSN: $\Sigma_0(r) = (r/1\text{ au})^{-1.5}\ M_\oplus\ \text{au}^{-2}$, with an initial size distribution of solids proportional to $D^{-3.7}$, though the main results presented below are independent of this choice. The minimum size of solids in the cascade is set to 0.8 μm, which is the blow-out size assuming a star of 1 $L_\odot$ and 1 $M_\odot$, and an internal density of solids of 2.7 g cm^{-3}. Grains smaller than this are immediately lost from the disc. I explore different maximum diameters ($D_{\max}$) between 1-100 km. The disc is assumed to be pre-stirred or stirred on a timescale much shorter than the age of the system, i.e. initially having velocities high enough so collisions between planetesimals are destructive and result in a collisional cascade. This is accounted by setting the mean eccentricity (e) and inclination (I) of the particles to be 0.05 and 1.4° ($e/2$), respectively, which defines the relative velocities of the particles. These velocities are calculated as $v_{\rm rel} = v_{\rm K}(1.25e^2 + I^2)^{1/2}$ (valid for Rayleigh distributions of e and I, Lissauer & Stewart, 1993; Wetherill & Stewart, 1993), where $v_{\rm K}$ is the Keplerian velocity on a circular orbit. Hence, the relative or impact velocities are a 6% of $v_{\rm K}$.

Furthermore, in this model destructive collision are only caused by impactors with specific energies greater than the disruption threshold or planetesimal strength ($Q^\star_{\rm D}$), which depends both on the size and impact velocity. The disruption threshold has been studied in laboratory experiments (e.g., Fujiwara et al., 1989; Davis & Ryan, 1990; Ryan et al., 1991) and with numerical simulations of colliding basalt and icy bodies (e.g., Benz & Asphaug, 1999). It is well known that for small bodies bound by cohesive binding forces, $Q^\star_{\rm D}$ decreases with size and thus larger bodies are weaker, unless they are large enough such that self-gravity becomes important. For the latter case, $Q^\star_{\rm D}$ increases with size. Therefore, I assume the following prescription

$$Q^\star_{\rm D} = \left[Q_{\rm D,s} \left(\frac{\rm D}{1\text{ m}} \right)^{b_{\rm s}} + Q_{\rm D,g} \left(\frac{\rm D}{1\text{ m}} \right)^{b_{\rm g}} \right] \left(\frac{v_{\rm rel}}{v_0} \right)^{1/2}, \tag{4.1}$$

where $Q_{\rm D,s}$, $Q_{\rm D,g}$, $b_{\rm s}$ and $b_{\rm g}$ are parameters that depend on the specific composition of solids in the disc. The dependence on the relative or impact velocity is inspired by the results from Stewart & Leinhardt (2009). I use $Q_{\rm D,s} = 500$ J kg^{-1}, $Q_{\rm D,g} = 0.03$ J kg^{-1}, $b_{\rm s} = -0.37$, $b_{\rm g} = 1.36$ and $v_0 = 3$ km s^{-1} values consistent with basalt in simulations from Benz & Asphaug (1999). Note that the choice of basalt is not important and similar results are obtained assuming, for example, icy planetesimals. Finally, I assume a "redistribution function" for the fragments created in a destructive collision proportional to $D^{-3.5}$, with the largest fragment having half the mass of the original disrupted body. The specific dependence on D does not change the results presented below.

I divide the disc in different independent annuli, each one with a total mass of $2\pi r \Delta r \Sigma_0(r)$, with $\Delta r = 2er$, which fixes the initial total mass in each radial bin. At a given radius, I solve for the steady state size distribution by equating the mass loss rate and gain in each size bin that is smaller than D_c, the largest object that is in collisional equilibrium. The mass in size bins larger than D_c is held fixed to the primordial distribution as they have lifetimes or collisional timescales longer than the age of the system and have not had enough time to significantly evolve. The timescale to reach quasi steady state or damp perturbations is the same as the collisional timescale (Wyatt et al., 2011); therefore, the quasi steady state assumption is valid for sizes smaller than D_c. To find the specific D_c I solve for the steady state size distribution varying D_c, until finding the specific size bin with a lifetime equal to the age of the system (or with a difference smaller than a 10%). In the resulting size distribution bins for planetesimals larger than D_c retain their original masses, while the masses in all smaller bins are anchored to D_c and their size distribution set by the collisional equilibrium condition. As the system age increases, D_c increases, and the size distribution evolves, and thus, the total and mm-sized dust mass too.

If $D_c > D_{\rm max}$, i.e. the lifetime of the biggest planetesimal is shorter than the age of the system ($t_{\rm age}$), the mass in every bin is scaled as

$$M(r,t,D) = M'_0(D)\frac{t_{\rm c}(0)}{t_{\rm age}}, \tag{4.2}$$

where $t_{\rm age}$ is the age of the system, and M'_0 is the mass distribution in collisional equilibrium when $D_c = D_{\rm max}$, or when the system had an age equal to the lifetime of the biggest planetesimal, $t_{\rm c}(0)$. Equation 4.2 is approximately valid if $t_{\rm age} > t_{\rm c}(0)$ and the mass loss rate is proportional to M^2, which is the case in my models as the collisional lifetime is inversely proportional to the mass in the cascade. The evolution of the surface density of solids at 10 au is illustrated in the top panel of Figure 4.8. The main relevant feature of this evolution is that when $D_c < D_{\rm max}$, the mass in the small size bins decreases more slowly than it would when the entire size distribution is in equilibrium ($D_c = D_{\rm max}$).

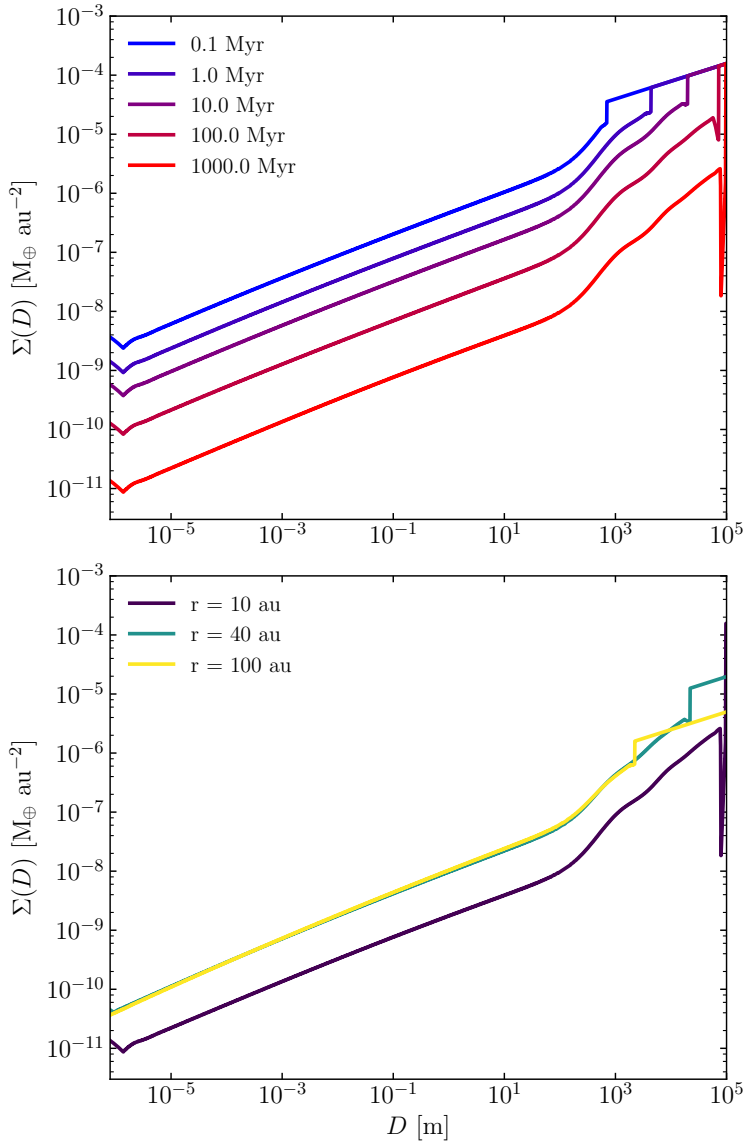

Figure 4.8: Mass surface density in each of the 3000 size bins spaced logarithmically, with $D_{\max} =$ 100 km and Σ_0 =MMSN. ***Top:*** Size distribution at 10 au for a system age ranging from 0.1 Myr to 1 Gyr. ***Bottom:*** Size distribution at 10, 40 and 100 au (purple, green and yellow lines, respectively) for a system age of 1 Gyr.

In Figure 4.9 I present the evolution of three discs varying $D_{\max}$ from 1 to 100 km (top and middle), and changing the stellar mass and luminosity together with Σ_0 and $D_{\max}$ to fit 61 Vir disc properties (bottom panel), i.e. the surface density of mm-sized grains and disc inner edge (see §4.5.1). The surface density of the total mass in solids (Σ, left column) evolves with time similarly to analytic models (e.g., Wyatt et al., 2007b), increasing with distance as expected up to the characteristic radius, r_c, at which the largest planetesimal in the disc has a lifetime equal to the age of the system, i.e. $t_{\rm c}(0) = t_{\rm age}$, and from there decreasing with radius as $\Sigma_0(r)$. This radius depends on the initial total solid mass and on $D_{\max}$ as the three panels in the left column show, with r_c being smaller for larger $D_{\max}$ or lower initial mass as the rate of collisions

is reduced. The surface density of mass in mm-sized grains ($\Sigma_{\rm mm}$, right column) behaves in a way similar to the optical depth described in Schüppler et al. (2016) and fractional luminosity in Geiler & Krivov (2017), mimicking $\Sigma(r)$ for $r < r_c$, but considerably flatter compared to $\Sigma(r)$ at $r > r_c$. This is because $D_c < D_{\rm max}$ and D_c decreases with r outside r_c, so $\Sigma_{\rm mm}$ is less depleted for larger r. The net effect is that $\Sigma_{\rm mm}(r)$ is almost constant, even though $\Sigma(r)$ decreases with r.

To illustrate the differences in the evolved size distribution at different radii, in the bottom panel of Figure 4.8 I compare the size distribution at 1 Gyr with $D_{\rm max} = 100$ km and $r = 10$, 40 and 100 au. At 10 au (red line) the disc evolves fast as relative velocities are higher and all the size bins are in collisional equilibrium. At 40 au (purple line) relative velocities are slower, hence $D_c \sim 20$ km and only smaller bodies are in collisional equilibrium; therefore, the mass in small bodies is highly depleted compared to the primordial, while the total mass in solids has not decreased significantly. At 100 au (blue line) relative velocities are even slower, $D_c \sim 2$ km and the mass in small bodies is less depleted compared to the primordial than at 40 au. Even though the surface density of the total mass in solids at $t = 0$ and 1 Gyr is higher at 40 au than at 100 au, the mass surface density in solids smaller than 1 km is approximately the same at both radii after 1 Gyr. This causes the slope of $\Sigma_{\rm mm}$ to flatten out and be almost constant at large radii where $t_{\rm c}(0) > t_{\rm age}$ as mentioned above. I also observe a very similar evolution for the vertical optical depth in the disc, consistent with Schüppler et al. (2016).

This behaviour that makes $\Sigma_{\rm mm}$ to be almost flat can be understood analytically if I consider a planetesimal strength approximated by two broken power laws and a continuous size distribution with three regimes: i) small bodies in collisional equilibrium with a size distribution proportional to D^{-q_1}; ii) large bodies with gravity dominated strengths in collisional equilibrium with a size distribution proportional to D^{-q_2}; and iii) largest planetesimals with lifetimes longer than the age of the system that conserve their primordial size distribution proportional to D^{-q_3}. The value of q_1 and q_2 are strictly related to the dependence on D for $Q^{\star}_{\rm D}$, with (Durda & Dermott, 1997; O'Brien & Greenberg, 2003)

$$q_i = \frac{21 + b_i}{6 + b_i}, \tag{4.3}$$

where b_i is the slope or exponent of $Q^{\star}_d$ in the strength or gravity-dominated regime. Therefore, assuming reasonable values for b_s, b_g and q_3 I can find an analytic expression for the size distribution at different radii (e.g., Löhne et al., 2008). Moreover, assuming an initial surface density or mass distribution in the disc, I can derive an expression for the fractional luminosity as a function of radius, as shown by Shannon & Wu (2011) (Equation A10 therein) and Geiler & Krivov (2017) (Equation A11 therein). As the fractional luminosity is proportional to the surface density of small grains, I can rewrite Equation A10 in Shannon &

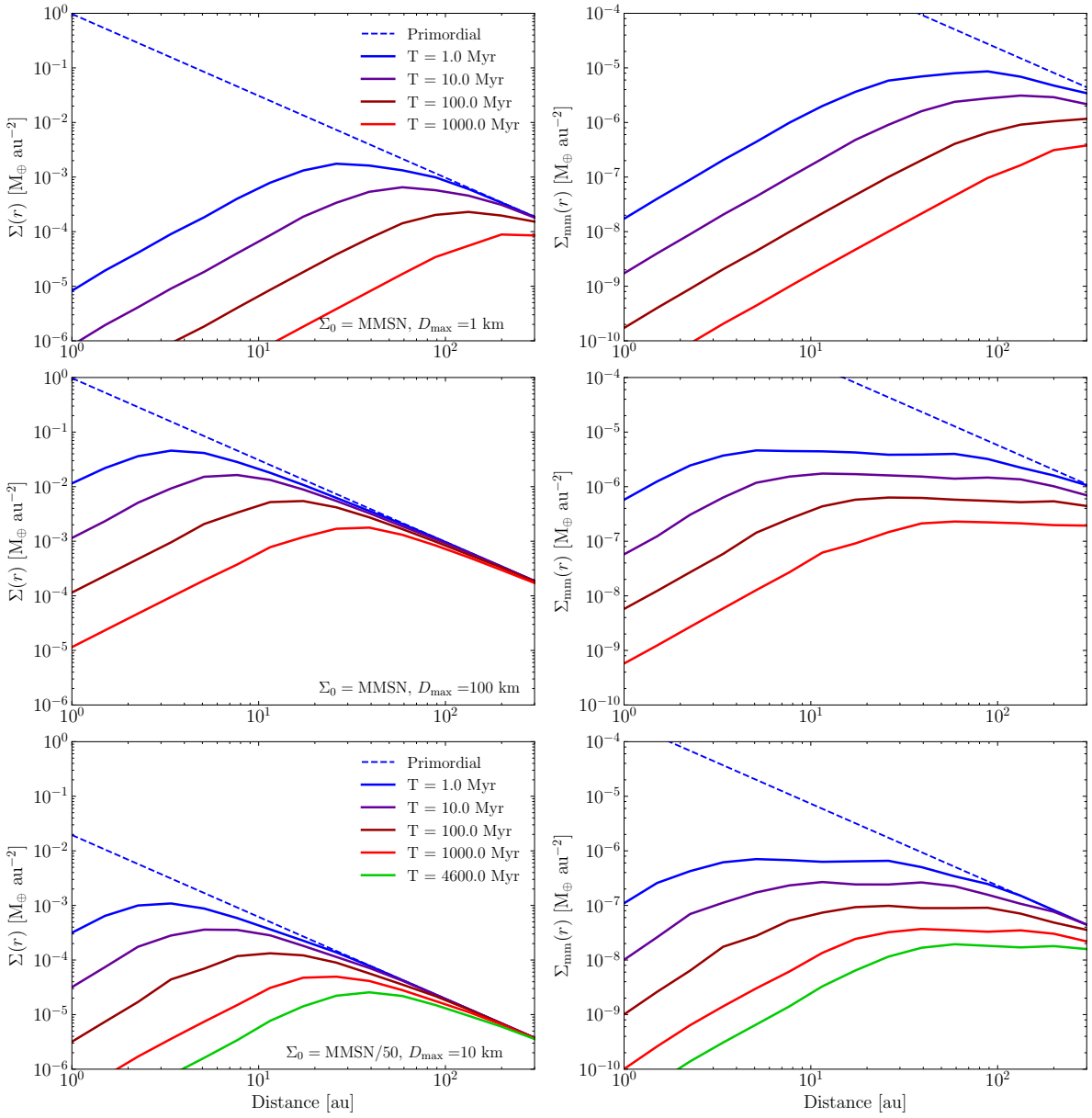

Figure 4.9: Total (left column) and millimetre-sized dust mass (right column) evolution of a disc from 1 to 300 au. The different rows represent the evolution of a disc with the following parameters. ***Top:*** solar type star with a primordial surface density equal to a MMSN and a maximum planetesimal size of 1 km. ***Middle:*** solar type star with a primordial surface density equal to a MMSN and a maximum planetesimal size of 100 km. ***Bottom*** central star of 0.88 $M_\odot$ and 0.84 $L_\odot$ with a primordial surface density equal to 0.02 MMSN and a maximum planetesimal size of 5 km. The colours represent 5 different ages: 1, 10, 100, 1000 and 4600 Myr, varying from blue to red and green as time evolves.

Wu (2011) to find

$$\Sigma_{\rm mm}(r) \propto \left[r^2\Sigma_0(r)\right]^{\frac{2+k_2-k_2q_2}{2+q_2-q_3+k_2-k_2q_2}} r^{-2+\frac{(19+2q_2)(q_2-q_3)}{6(2+q_2-q_3+k_2-k_2q_2)}}, \tag{4.4}$$

where $\Sigma_0(r)$ is the primordial total surface density of solids, and k_2 is equal to $\frac{6-q_2}{q_2-1}$ and

represents the size scaling of the minimum impactor size to cause a catastrophic collision. The expression above is only valid when D_c is less than $D_{\max}$, but large enough so it is in the gravity dominated regime ($D_c \gtrsim 100$ m). Assuming q_1=3.6, q_2=3.0, $k_2 = 1.5$ (values consistent with b_s and b_g used above), q_3=3.7 and $\Sigma_0(r) = \Sigma_0(r/1\text{ au})^\alpha$ I find

$$\Sigma_{\rm mm}(r) \propto r^{0.6\alpha+0.9}. \tag{4.5}$$

Therefore, for $\alpha = -1.5$, $\Sigma_{\rm mm}$ is independent of radius, which matches with my more detailed numerical simulation. Moreover, the flatter $\Sigma_{\rm mm}$ in the evolved size distribution compared to the primordial distribution is independent of α as Equation 4.5 shows; although a steeper primordial surface density of solids decreasing with radius would result in a steeper surface density of millimetre sized grains with a slope of $0.6\alpha+0.9$. For $q_3 = 3.5$ and 3.9 I still find a flat slope for $\Sigma_{\rm mm}$ of -0.3 and 0.2, respectively. From the results in my simulations I can estimate the dependence of $\Sigma_{\rm mm}$ on $t, D_{\max}$ and Σ_0, by assuming a power law dependence and fitting it to the numerical results. Coupling these with the dependence on r from Equation 4.5 (only valid for q_1=3.6, q_2=3.0 and q_3=3.7), I find

$$\Sigma_{\rm mm}(r > r_c) \approx 2 \times 10^{-7} \left(\frac{r}{1\text{ au}}\right)^{0.6\alpha+0.9} \left(\frac{t}{1\text{ Gyr}}\right)^{-0.4} \left(\frac{D_{\max}}{100\text{ km}}\right)^{-0.1} \left(\frac{\Sigma_0}{1\text{ MMSN}}\right)^{0.6} \text{M}_\oplus\text{ au}^{-2}, \tag{4.6}$$

where Σ_0 is the initial surface density of solids at 1 au in units of the MMSN. The factor 2 and the exponents of -0.4, -0.1 and 0.6 are the results from a fit to the numerical simulations. Equation 4.6 is only valid for $r > r_c$ and $D_c \gtrsim 100$ m. Using Equation A5 in Shannon & Wu (2011) I can also estimate how r_c varies with time and Σ_0. Moreover, from my simulations I can derive a dependence on $D_{\max}$ fitting a power law. I find

$$r_c \approx 4 \left(\frac{t}{1\text{ Myr}}\right)^{\frac{1}{-\alpha+1.5}} \left(\frac{\Sigma_0}{1\text{ MMSN}}\right)^{\frac{1}{-\alpha+1.5}} \left(\frac{D_{\max}}{100\text{ km}}\right)^{-0.5} \text{au}, \tag{4.7}$$

Assuming a specific dependence of planetesimal strength on size, equations A10 from Shannon & Wu (2011), and 4.6 and 4.7 from this work, together with the disc model presented above, can be used to retrieve the primordial radial distribution of solids from ALMA observations of extended discs if the biggest planetesimals in the disc still conserve their primordial size distribution. Moreover, they can be used to constrain the initial total mass in the disc and maximum planetesimal size. So far there is no evidence of extended debris discs at millimetre wavelengths with a steep slope decreasing with radius (or non consistent with being flat, e.g., Booth et al., 2016); however, even with ALMA (the most sensitive instrument at millimetre wavelengths) the detection and study of extended debris discs is only possible around a few of the brightest systems.

It is worth noting that the maximum planetesimal size in a disc could vary with radius by orders of magnitude as the growth timescales for planetesimals are a steep function of radius and the surface density in solids (e.g., Kenyon & Bromley, 2008). Moreover, stirring could have stopped the growth at different epochs for different radii. Although in my models I assume that the maximum planetesimal size is independent of radius, the prediction for $\Sigma_{\rm mm}(r > r_c)$ in Equation 4.6 is not very sensitive to $D_{\rm max}$. Therefore, these predictions are reasonably valid even if the maximum planetesimal size decreases with radius (as expected in planet formation models). This is already illustrated in Figure 4.9. If I consider a disc with $D_{\rm max}$ decreasing from 100 to 1 km between 40-300 au, then the resulting $\Sigma_{\rm mm}(r)$ at 1 Gyr would be almost the same as the red line in the middle right panel on that Figure, because $\Sigma_{\rm mm}(300\ {\rm au})$ increases only by a factor of 2 when decreasing $D_{\rm max}$ from 100 to 1 km. This is due to two opposite effects: 1) for a constant total mass in solids, reducing $D_{\rm max}$ increases the mass in millimetre sized dust; and 2) reducing $D_{\rm max}$ makes the collisional evolution faster which reduces the mass in every bin in collisional equilibrium. A similar effect would be present at $r < r_c$ making the surface density slope flatter. The maximum planetesimal size is only significantly important to determine r_c. The opposite scenario, and less likely, in which $D_{\rm max}$ increases with radius would result in a slightly steeper slope for both $r < r_c$ and $r > r_c$.

Other differences relative to the assumptions could also change the slope of the millimetre surface density, such as the epoch of stirring (in my simulations I consider a pre-stirred disc), or the mean eccentricity and inclination of particles in the disc, or even the disruption threshold of planetesimals and dust if their composition varies with radius. For example, a different $Q^{\star}_{\rm D}$ would modify the size distribution, changing the slope of the predicted millimetre surface density as Equation 4.4 shows.

4.5.1 Application to 61 Vir

In §4.4 I find that the observations in the millimetre are best fitted with a disc extending to ~ 150 au, an integrated flux of 3.7 ± 1.2 mJy and a flat surface density distribution, equivalent to a dust mass of $\sim 2\times10^{-8}$ M$_\oplus$ au^{-2}. In addition, the minimum radius derived from a best fit model of a collisionally evolved disc to the Herschel observations is ~ 40 au. Using the same model for the collisional evolution of a disc described above (replacing the stellar mass and luminosity with 0.88 M$_\odot$ and 0.84 L$_\odot$, Sousa et al., 2008; Wyatt et al., 2012) I find a best match with a primordial surface density between 20-100 times less dense than the MMSN and a maximum planetesimal size between $5-20$ km. These two parameters determine that $t_c(0) = 4.6$ Gyr at ~ 40 au and $\Sigma_{\rm mm}(r) \sim 2\times10^{-8}$ M$_\oplus$ au^{-2} for $r > 40$ au.

The need for a low primordial surface density and a maximum planetesimal size of 10 km is due to the low mass in millimetre grains, which scales roughly as $D_{\rm max}^{-0.1}\Sigma_0^{0.6}$ (see Equation 4.6),

together with a large r_c, that scales roughly as $D_{\max}^{-0.5}\Sigma_0^{0.33}$ (see Equation 4.7). Therefore, I need a very low Σ_0 to fit the millimetre surface density and a low $D_{\max}$ to have $r_c \sim 40$ au given the low Σ_0. From the size distribution I can also determine a vertical optical depth of 2×10^{-4}, a few times higher than the optical depth from Herschel observations and SED fitting, but still consistent considering all the assumptions made in both modelling efforts. For example, a more detailed treatment of radiation pressure could change the value of the optical depth by a factor of a few. The derived maximum planetesimal size and primordial surface density go in the same direction as the ones from Wyatt et al. (2012): the primordial surface density of solids in the disc was much lower compared to the MMSN and with a maximum planetesimal size not much larger than 10 km.

4.6 Discussion

4.6.1 A depleted broad disc of planetesimals

In §4.4 I found that the debris disc in 61 Vir is broad, extending from 30 to 150 au or larger radii. If the emission were concentrated in a few $\lesssim$20 au wide rings of planetesimals the disc would have been detected above 3 sigma in the ALMA map. Moreover, the 2.2σ difference between the flux measured by SCUBA2 and ALMA is indicative that there is flux loss in the reconstructed ALMA image due to the disc emission being mostly in structures on scales larger than 6″ (50 au); and thus not recoverable by the range of baselines in the ALMA data. This was corroborated using simulated observations of different broad disc models. Therefore, I conclude that the planetesimal disc must be extended with a wide range of semi-major axes. A different scenario with a population of highly eccentric planetesimals with a small range of semi-major axes is discarded as the derived surface density is flatter than expected in a scattered disc scenario (e.g., Duncan & Levison, 1997) and while collisional erosion can flatten this distribution by preferentially eroding the inner regions this cannot completely erase the density enhancement at the inner edge of the disc (Wyatt et al., 2010).

The inner edge of the disc could be defined by the collisional evolution that has been ongoing for 4.6 Gyr as assumed in §4.5, or instead the disc could have been truncated by a yet unseen planet. In the first scenario, the observed inner edge of the disc (30-40 au) can be explained by a maximum planetesimal size of only about 10 km and primordial surface density of solids 50 times lower than a MMSN. One explanation for why the planetesimals did not grow to larger sizes could be the low surface density of solids which slows down the growth timescales (Kenyon & Bromley, 2008), but could also be because the planetesimals were stirred by a planet closer in hindering their growth.

In the second scenario, in which the inner edge of the disc has been truncated by a planet, the maximum planetesimal size is no longer constrained to be of the order of ~ 10 km. However, even if I consider a maximum planetesimal size of 1000 km, the mass of the primordial disc still needs to be a factor of ~ 10 lower compared to a MMSN in order to fit the flat surface density of millimetre grains derived in this chapter and the Herschel observations (Wyatt et al., 2012). This depletion could arise from the protoplanetary disc phase if the disc had a low mass, or a low efficiency of planetesimal formation, or due to radial drift of solid particles during that gas rich phase which concentrated most of the solid mass in the inner regions (Whipple, 1973; Weidenschilling, 1977a). The radial drift of solids could have also contributed to an in situ formation of the 2-3 planets found within 1 au of the Star (e.g., Hansen & Murray, 2012).

A variant on the second scenario involves the 30 au truncation radius being caused by a planet which is no longer present. For example, if the close-in planets formed further out (just inside 30au) and then migrated to their current location accreting and scattering planetesimals on their way in, the early evolution of these close-in planets could be responsible for both the truncation of the outer disc and its stirring (e.g., Alibert et al., 2006; Terquem & Papaloizou, 2007; Kennedy & Kenyon, 2008; Payne et al., 2009; Ida & Lin, 2010).

4.6.2 Stirring by a yet unseen planet

If 61 Vir b and c formed in situ, then something else must have stirred the disc as these are too far in and not massive enough to have stirred the disc at large radii within 4.6 Gyr (Wyatt et al., 2012). Hence, I propose that an unseen planet at a larger distance and within the 30 au disc inner edge stirred the disc. Similar to Moór et al. (2015b), using Eq. 6 from Mustill & Wyatt (2009) (valid for planets with eccentricities $\lesssim 0.3$) I can derive lower limits on the eccentricity of such a planet depending on its semi-major axis and mass so the timescale of stirring is shorter than the age of the system. Moreover, the eccentricity imposed on the planetesimals (e_f) must be higher than a certain value so that their relatives velocities are high enough to cause destructive collisions ($v_{\rm rel,max} \sim 2e_{\rm f}v_{\rm K}$). Here I impose that the forced eccentricity (Equation 8 in Mustill & Wyatt, 2009) must be higher than 0.01 so planetesimals of 5 km diameter undergo destructive collisions with planetesimals of the same size at 150 au. This is illustrated in Figure 4.10. The minimum planet eccentricity decreases with increasing planet semi-major axis and mass as the timescale for stirring is held fixed at 4.6 Gyr. The forced eccentricity must be > 0.01, which results in a kink in the 0.1 contour (because e_f is independent of mass). All other contours are set by the stirring time set equal to the age of the system.

I can add additional constrains if I require planets with a pericenter that does not get closer than 5 mutual Hill radii (see Eq. 9 in Pearce & Wyatt, 2014) from the apocentre of 61 Vir c

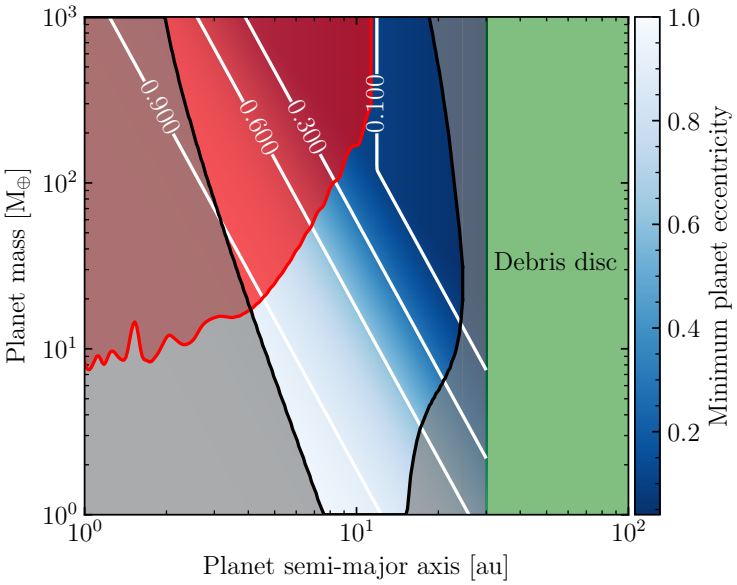

Figure 4.10: Allowed masses and semi-major axes for a putative planet that stirred the 61 Vir debris disc out to 150 au, in a timescale shorter than 4.6 Gyr, and forcing an eccentricity higher than 0.01. The blue colour map and white contours represent the minimum eccentricity for a given planet mass and semi-major axis. The green shaded region on the right is excluded as the planet would overlay with the inner edge of the disc at 30 au. The grey shaded region is excluded as those planets would get closer than 5 Hill radii to 61 Vir c or to the inner edge of the disc. Finally the red region in the top left corner is excluded from upper limits based on RV data.

(a=0.22 au, e=0.14), i.e

$$a_{\rm plt}(1-e) - 5R_{\rm H,q} > a_{\rm c}(1+e_{\rm c}), \tag{4.8}$$

where $R_{\rm H,q}$ is the Hill radii at pericentre and $a_{\rm c}$ and $e_{\rm c}$ are the semi-major axis and eccentricity of 61 Vir c. In addition, the apocentre of the hypothetical planet d has to be such that it does not get closer than 5 Hill radii to the disc inner edge at $\sim$ 30 au. These two constraints exclude the grey shaded area. Because lower mass planets have higher eccentricity, the maximum semi-major axis decreases with decreasing planet mass for $\rm M_{plt} \lesssim 10\ M_{\oplus}$, but also decreases with increasing planet mass as the $R_{\rm H,q}$ gets larger. Finally, using upper limits from RV data from HARPS I can exclude planets more massive than the red line (Wyatt et al., 2012; Kennedy et al., 2015a).

With these limits on $\rm M_{plt}$ and $a_{\rm plt}$ I can conclude that if an unseen planet interior to the debris disc is responsible for stirring the planetesimals up to 150 au, and has an eccentricity lower than 0.1, then it must be more massive than 10 $\rm M_{\oplus}$ and have a semi-major axis between 10-20 au. Less massive planets and closer in ($a_{\rm plt} = 4 - 20$ au) could have stirred the disc, but with $e \gg 0.1$. For the allowed combinations of $M_{\rm plt}$ and $a_{\rm plt}$ even a highly eccentric planet will not induce an eccentricity higher than the observed on 61 Vir b and c or cause close encounters (see Figure 5 in Read & Wyatt, 2016). Moreover, an eccentric planet will impose an eccentricity on

the disc which may be detectable by imaging of the disc (Wyatt et al., 1999). While there is no evidence of any asymmetry, the constraints are weak, both because the imaging is in the far-IR where the transition from pericentre to apocentre glow occurs (Pan et al., 2016), and because the disc would look symmetric if the pericentre is aligned with the minor axis of the disc projected in the sky.

The equations used to derive the minimum eccentricity are only valid for $e_{\rm plt} \lesssim 0.3$. Planet eccentricities higher than 0.3 could be overestimated as the predicted stirring timescales are longer than expected for $e > 0.3$ (see Figure 1 in Mustill & Wyatt, 2009). Therefore, the lower limits presented in Figure 4.10 are only representative of the constraints expected for $e_{\rm plt} \lesssim 0.3$.

4.7 Summary and Conclusions

I have presented the first resolved millimetre study of 61 Vir, a planetary system with two confirmed RV planets within 1 au and a debris disc at tens of au. Combining ALMA and SCUBA2/JCMT observations I found that at 0.86 mm the total disc emission is 3.7 ± 1.2 mJy, the disc extends from ~ 30 to at least 150 au, and has surface density exponent of millimetre grains of $0.1^{+1.1}_{-0.8}$. This implies that the parent planetesimal disc is broad with a wide range of semi-major axes. The alternative scenario of a highly scattered disc with planetesimals with a common pericentre is discarded given the constraints on the surface brightness of the disc. No CO gas emission was detected in the disc, although even if planetesimals are rich in CO and releasing gas through collisions, any emission should be below the detection limit of these observations.

I developed a full disc collisional evolution model based on previous numerical work that can reproduce some of the results obtained in more detailed simulations, but in a much more computationally efficient approach. These models predict that the surface density of millimetre grains and optical depth radial profiles do not necessary match with the surface density of the parent bodies, tending to be flatter in regions of the disc where the age of the system is shorter than the collisional lifetime of the biggest planetesimals. This can be used to constrain the primordial surface density distribution of solids and maximum planetesimal size for extended discs for reasonable assumptions on the eccentricity, inclination and strength of planetesimals. For example, with this model I can reproduce the observations if 61 Vir debris disc started with a surface density ~ 50 times more depleted in solids compared to a MMSN, and with planetesimals that did not grow more than 5-20 km in size so the disc is collisionally depleted at $r < 40$ au. However, these conclusions are based on the assumption that the inner edge of the observed disc is set by the collisional evolution of the disc. If instead the inner edge is set by other mechanism, e.g. planet-disc interaction, then the maximum planetesimal size is

no longer constrained, but the primordial surface density would still need to be depleted by a factor of ~ 10 compared to the MMSN.

Finally I discussed and constrained the mass, semi-major axis and eccentricity of a planet stirring the disc located between the known RV planets and the inner edge of the disc. I found that in order to have stirred the disc out to 150 au, the planet must be more massive than 10 $M_{\oplus}$ and have a semi-major axis between 10 and 20 au if it has an eccentricity lower than 0.1. Otherwise, for higher eccentricities it could have a lower mass and a semi-major axis between 4 and 20 au.

5

A gap in the planetesimal disc around HD 107146 and asymmetric warm dust emission revealed by ALMA

5.1 Introduction

While exoplanet campaigns have discovered thousands of close in planets in the last decade, at separations greater than 10 au it has only been possible to detect a few gas giants, mainly through direct imaging (see Figure 1.1 and Marois et al., 2008; Lagrange et al., 2009b; Rameau et al., 2013). On the other hand, the ubiquity of debris discs shows that massive planetesimal belts can and do form at tens and hundreds of au in extrasolar systems.

It is natural then to wonder *how far out can planets form?* In situ formation of the imaged distant gas giants is challenging as the growth timescale of their cores can easily take longer than the protoplanetary gas-rich phase (Pollack et al., 1996; Rafikov, 2004; Levison et al., 2010). Gravitational instability was thought to be the only potential pathway towards in-situ formation at tens of au (Boss, 1997; Boley, 2009), but the revisited growth timescale of embryos through pebble accretion could be fast enough to form ice giants or the core of gas giants during the disc lifetime (Johansen & Lacerda, 2010; Ormel & Klahr, 2010; Lambrechts &

Johansen, 2012; Morbidelli & Nesvorny, 2012; Bitsch et al., 2015; Johansen & Lambrechts, 2017). Alternatively, the observed giant planets at tens of au may have formed closer in and evolved to their current orbits by migrating outward (Crida et al., 2009), as could be the case for HR 8799 with four gas giants in mean motion resonances (Marois et al., 2008, 2010) surrounded by an outer debris disc (Su et al., 2009; Matthews et al., 2014a; Booth et al., 2016); or may have been scattered from closer in onto a highly eccentric orbit (Ford & Rasio, 2008; Chatterjee et al., 2008; Jurić & Tremaine, 2008), as has been suggested for Fomalhaut b (Kalas et al., 2008, 2013; Faramaz et al., 2015). On the other hand, after the dispersal of gas and dust, planetesimals could continue growing to form icy planets at tens of au over 100 Myr timescales; however, numerical studies show that once a Pluto size object is formed at 30-150 au within a disc of planetesimals, these are inevitably stirred, stopping growth and the formation of higher mass planets through oligarchic growth (Kenyon & Bromley, 2002, 2008, 2010). Thus, it is not yet clear how far from their stars planets can form. Moreover, the existence of hybrid discs with vast amounts of gas in systems with low debris-like levels of dust (e.g. Moór et al., 2017) has opened the possibility for long lived gaseous discs that could facilitate the formation of both ice and gas giant planets at tens of au.

Broad debris discs provide a unique tool to investigate planet formation at tens of au. Planets formed at large radii or evolved onto a wide orbit should leave an imprint in the parent planetesimal belt, and thus in the dust distribution around the system. Gaps have been tentatively identified in a few young debris discs using scattered light observations suggesting the presence of planets at large orbital radii clearing their orbits from debris, e.g. HD 92945 (Golimowski et al., 2011) and HD 131835 (Feldt et al., 2017). However, alternative scenarios without planets that could also reproduce the observed structure have not been ruled out yet in these systems. For example, multiple ring structures can arise from gas-dust interactions if gas and dust densities are similar (Lyra & Kuchner, 2013; Richert et al., 2018), which might explain HD 131835's rings since large amounts of CO gas have been found in this system (of likely primordial origin, Moór et al., 2017). Moreover, the double ring structure around HD 92945 and HD 131835 has only been identified in scattered light images, tracing small dust grains whose distribution can be highly affected by radiation forces (Burns et al., 1979), therefore not necessarily tracing the distribution of planetesimals (e.g. Wyatt, 2006).

Only HD 107146, an $\sim 80-200$ Myr old G2V star (Williams et al., 2004, and references therein) at a distance of 27.5 ± 0.3 pc (Gaia Collaboration et al., 2016b,a), has a double debris ring structure tentatively identified at longer wavelengths thanks to ALMA observations (Ricci et al., 2015a), therefore indicating that the double ring structure is imprinted in the planetesimal distribution as well. Moreover, these observations ruled out the presence of gas at densities high enough to be responsible for such structure. The debris disc surrounding HD 107146 was first discovered by its infrared (IR) excess using IRAS data (Silverstone, 2000), but it was not until recently

that the disc was resolved by the HST in scattered light, revealing a nearly face on disc with a surface brightness peak at 120 au and extending out to ~ 160 au (Ardila et al., 2004; Ertel et al., 2011; Schneider et al., 2014). Despite HST's high resolution, limitations in subtracting the stellar emission or a smooth distribution of small dust likely kept the double ring structure hidden. Using ALMA's unprecedented sensitivity and resolution, Ricci et al. (2015a) showed that this broad disc extended from about 30 to 150 au, but that it had a decrease in the dust density at intermediate radii, which could correspond to a gap produced by a planet of a few Earth masses clearing its orbit at 80 au through scattering. Finally, analysis of *Spitzer* spectroscopic and photometric data revealed the presence of an additional unresolved warm dust component in the system, at a temperature of $\sim$120 K and thus inferred to be located between 5-15 au from the star (Morales et al., 2011; Kennedy & Wyatt, 2014).

Despite the tentative evidence of planets producing these gaps around their orbits, neither the HD 107146 ALMA observations, nor the scattered light observations of HD 92945 and HD 131835, ruled out alternative scenarios in which planets are not orbiting within these gaps, but similar structure is created in the dust distribution through different mechanisms. These different scenarios have important implications for the inferred dynamical history of the system and planet formation. While a planet formed in situ could explain the data reasonably well, questions arise regarding how a planet of a few Earth masses could have formed at such large separations, where coagulation and planetesimal growth timescales are significantly longer. Alternative scenarios such as the one suggested by Pearce & Wyatt (2015) to explain HD 107146's gap, could avoid these issues. In that scenario a broad gap is produced by secular interactions between a planetesimal disc and a similar mass planet on an eccentric orbit, which formed closer in and was scattered out by an additional massive planet. That scenario also predicts that the planet's orbit should become nearly circular and the planet would be located at the inner edge of the disc at the current epoch. The model also predicts the presence of asymmetries in the disc such as spiral features that would be detectable in deeper ALMA observations.

A second alternative scenario was proposed by Golimowski et al. (2011) to explain the double-ring structure around HD 92945 seen in scattered light. As shown by Wyatt (2003), planet migration can trap planetesimals in mean motion resonances; resulting in overdensities that are stationary in the reference frame co-rotating with the planet. Small dust released from these trapped planetesimals can exit the resonances due to radiation pressure, forming a double-ring structure that could be observable in scattered light (Wyatt, 2006). On the other hand, in this planet migration scenario the distribution of mm-sized dust should match the planetesimal distribution, with prominent clumps that could be seen in millimetre observations.

Finally, secular resonances produced by a single eccentric planet in a massive gaseous disc (Zheng et al., 2017) or by two planets formed interior to the disc could also explain some of the

wide gaps (Yelverton et al., submitted), but possibly also leaving asymmetric features. Hence debris disc observations at multiple wavelengths can disentangle these different scenarios, and provide insights into the dynamical history of the outer regions of planetary systems, testing the existence and origin of planets at tens of au, which otherwise would remain invisible.

In this chapter I present new ALMA observations of HD 107146 in both band 6 and 7 (1.1 and 0.86 mm). These observations resolve the broad debris disc around this system at higher sensitivity and resolution than the data presented by Ricci et al. (2015a), which showed tentative evidence of a gap as commented above. This chapter is outlined as follows. In §5.2 I present the new ALMA observations of the dust continuum and line emission of HD 107146. Then in §5.3 I model the data using both parametric models and the output of N-body simulations to quantify the disc structure and assess whether a single planet could explain the observations. In §5.4 I discuss the results, the origin of the gap and implications for planet formation; the total mass of HD 107146's outer disc; the detection of an inner component that could be warm dust; and gas non-detection. Finally the main conclusions of this chapter are summarised in §5.5.

5.2 Observations

HD 107146 was observed both in band 7 (0.86mm, project 2016.1.00104.S, PI: S. Marino) and band 6 (1.1mm, project 2016.1.00195.S, PI: J. Carpenter). Band 7 observations were carried out between October and December 2016 (see Table 5.1) both using the 12m array and the Atacama Compact Array (ACA) to recover small and large scale structures. The total number of antennas for the 12m array was 42, with baselines ranging from 48 to 410 m (5th and 95th percentiles), and between 9 to 11 ACA 7m antennas with baselines ranging from 9 to 44 m. The correlator was set up with two spectral windows centered at 343.13 and 357.04 GHz with 2 GHz bandwidths and 15.625 MHz spectral resolution; and other two centered at 345.03 and 355.14 GHz with 1.875 GHz bandwidths and 0.976 MHz spectral resolution. The four windows are used together to study the dust continuum emission, while the latter two are also used specifically to search for line emission from CO and HCN molecules in the disc (see §5.2.2).

Table 5.1: Summary of band 6 and band 7 (12m and ACA) observations. The image rms and beam size reported corresponds to briggs weighting using robust=0.5.

Observation	Dates	t_{sci} [min]	Image rms [μJy]	beam size (PA)	Min & max baselines [m] (5^{th} & 95^{th} percentiles)
Band 6 - 12m	24, 27-30 Apr 2017	236.4	6.8	$0\farcs67 \times 0\farcs66$ ($-3°$)	41 and 312
Band 7 - 12m	11 Dec 2016	48.8	30.0	$0\farcs46 \times 0\farcs37$ ($21°$)	48 and 410
Band 7 - ACA	20 Oct & 2 Nov 2016 22 Mar & 13 Apr 2017	135.1	245	$4\farcs3 \times 3\farcs4$ ($-76°$)	9 and 44
Band 7 - 12m+ACA	-	-	31.1	$0\farcs47 \times 0\farcs38$ ($20.8°$)	-

Band 6 observations were carried out in April 2017 (see Table 5.1) using the 12m array only. The total number of 12m antennas varied between 41-42, with baselines ranging from 41 to 312 m (5th and 95th percentiles). The correlator was set up with four spectral windows centered at 253.60, 255.60, 269.61 and 271.61 GHz with 2 GHz bandwidths and 15.625 MHz spectral resolution. The four are used together to study the dust continuum emission only. Calibrations were applied using the pipeline provided by ALMA. The total time on source for band 6 was 236 min, and 184 min for band 7 (49 and 135 min for the 12m array and ACA, respectively). Below I present the image analysis of continuum and line observations.

5.2.1 Continuum

Continuum maps at band 6 and 7 are created using the CLEAN task in CASA 4.7 (McMullin et al., 2007b) and are presented in Figure 5.1. I adopt natural weighting for band 6 and 7 (12m+ACA combined) for a higher signal to noise. These maps have a rms of 6.3 and 27 μJy beam^{-1} at the center, which increases towards the edges as the maps are corrected by the primary beam, reaching values of 7.0 and 34 μJy beam^{-1} at $5''$ (140 au) for band 6 and 7, respectively. The band 6 and band 7 synthesised beams have dimensions of $0\farcs80 \times 0\farcs79$ and $0\farcs58 \times 0\farcs47$[1], respectively, reaching an approximate resolution of 22 au for band 6 and 15 au for band 7. The higher resolution and sensitivity of these new data reveal a nearly axisymmetric broad disc with a large decrease or gap in the surface brightness centered at a radius of $\sim$ 80 au as suggested by Ricci et al. (2015a). The disc extends from nearly 40 to 180 au, being one of the widest discs resolved at millimetre wavelengths (Matrà et al., 2018). I compute the total flux by integrating the disc emission inside an elliptical mask with a 180 au semi-major axis and the same aspect ratio as the disc (see §5.3.1). I find a total flux of 16.1 ± 1.6 and 34.4 ± 3.5 mJy at 1.1 and 0.86 mm (including 10% absolute flux uncertainties), leading to a spatially unresolved millimetre spectral index of 2.64 ± 0.48, consistent with results from Ricci et al. (2015b) which combined ALMA and ATCA observations. The total flux in band 6 is consistent with that measured by Ricci et al. (2015a) at similar wavelengths and using a more compact ALMA configuration, thus proving that the band 6 observations do not suffer from flux loss or miss large scale structure.

In order to study in more detail the disc radial structure, the top panel of Figure 5.2 shows the radial intensity profile, computed by azimuthally averaging the disc emission over ellipses as in the previous chapters. Both in band 6 and 7, I find that the disc surface brightness peaks near the disc inner edge at $\sim$ 45 au, from which it decreases reaching a minimum at 80 au that is deeper in the band 7 profile likely due to the higher resolution. Beyond this minimum, the surface brightness increases until 120 au where it peaks and then decreases steeply with

[1]Note that the rms and beam sizes are different to the one reported in Table 5.1 as the imaging is done with natural weights to increase the S/N

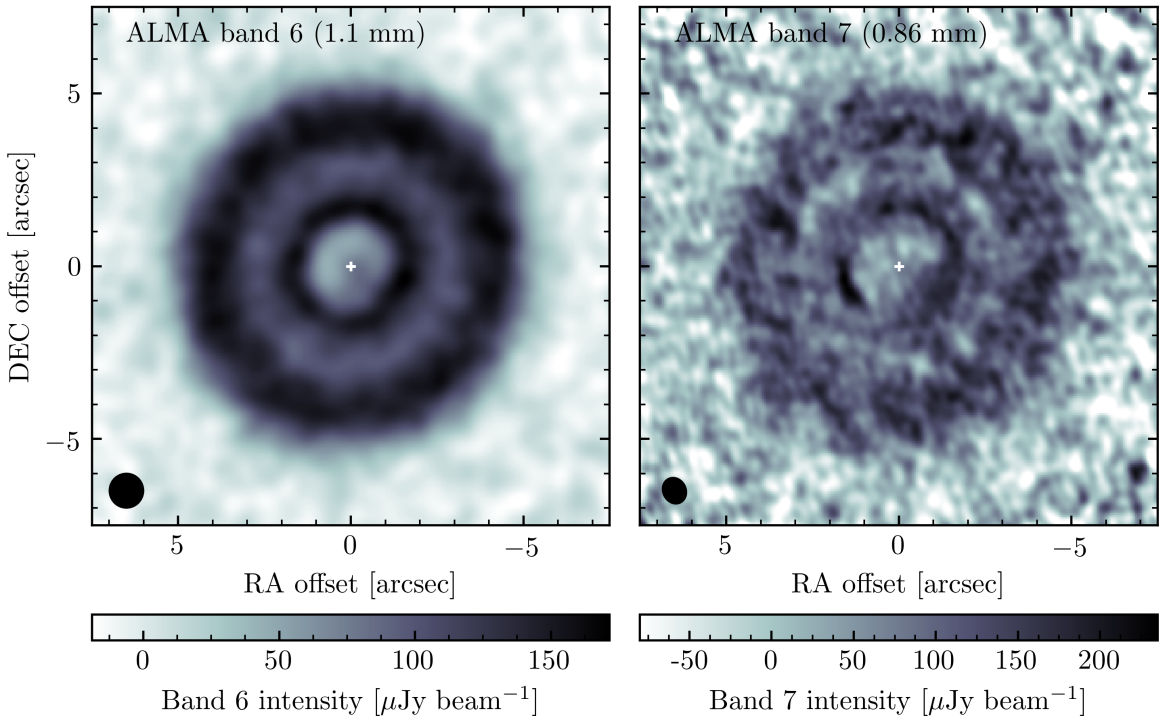

Figure 5.1: Clean images of HD 107146 at 1.1 (left) and 0.86 mm (right) using natural weights and primary beam corrected. The band 7 image is obtained after combining the 12m array and ACA data. The stellar position is marked with a white cross at the center of the image, while the beams of band 6 ($0\farcs80 \times 0\farcs79$) and band 7 ($0\farcs58 \times 0\farcs47$) are represented by black ellipses in the bottom left corners. The image rms at the center is 6.3 and 27 μJy beam^{-1} increasing with distance from the center and reaching values of 7.0 and 34 μJy beam^{-1} at $5''$ from the center.

radius. No significant positive emission is recovered beyond 180 au. Within the gap, I find that the radial profile is not symmetric with respect to the minimum, with the outer section (80-100 au) having a steeper slope than the inner part (60-80 au), a feature that is present both in band 6 and 7 data. This is also visible in Figure 5.1 and is an important feature that could shed light on the origin of this gap. I also compute a spectral index map using multi-frequency clean (NTERMS=2) and natural weights. The bottom panel of Figure 5.2 shows the azimuthally averaged radial profile of the spectral index ($\alpha_{\rm mm}$). From 40 to 150 au the disc has spectral index of roughly 2.7 ± 0.1 (assuming $\alpha_{\rm mm}$ is constant over radii), consistent with the overall spectral index estimated above. Note that uncertainties on $\alpha_{\rm mm}(r)$ do not include the 10% absolute flux uncertainties as I am only interested in relative differences as a function of radius.

In addition to the outer disc, I detect emission from within 30 au that peaks near the stellar position in the azimuthally averaged profile. However, it has a much higher level than the photospheric emission if I extrapolate this from available photometry at wavelengths shorter than 10μm using a Rayleigh-Jeans spectral index ($F_{\nu\star} = 32 \pm 1$ and 18 ± 1 μJy at 0.86 and

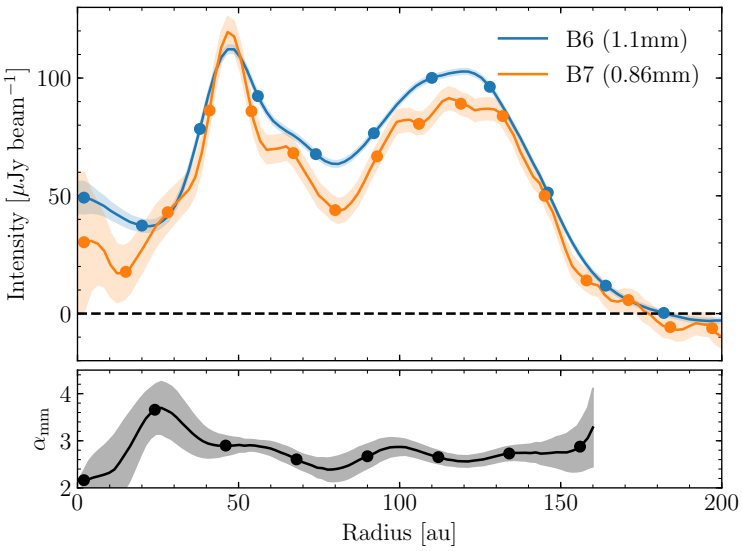

Figure 5.2: Average intensity (top) and spectral index (bottom) profile computed azimuthally averaging the Clean and spectral index maps over ellipses oriented as the disc in the sky. The blue and orange lines are obtained from the band 6 and band 7 Clean images, using Briggs (robust=0.5) weights, while the spectral index is computed using natural weights. The shaded areas represent the 68% confidence region over a resolution element (represented by circles spaced by 18 au for band 6, 13 au for band 7 and 22 au for the spectral index).

1.1 mm, respectively). Moreover, between 20 and 30 au I also find that $\alpha_{\rm mm}$ has a peak of $\sim$ 3.7, although still within 2σ from the average spectral index. In §5.3.1 I recover this inner component in more detail after subtracting the disc emission using a parametric model and I find that it is inconsistent with point source emission, significantly offset from the stellar position, and unlikely to be a background submillimetre galaxy.

The fact that the disc emission is consistent with being axisymmetric disfavours the scenario in which a planet is scattered out from the inner regions opening a gap through secular interactions with the disc (Pearce & Wyatt, 2015, see their figure 6). In their model, spiral density features are present in the planetesimal disc for hundreds of Myr, which should be imprinted in the mm-sized dust distribution as well, thus being detectable by the observations. In §5.3.1 I fit parametric models to the data to study with more detail the level of axisymmetry of HD 107146's disc. Moreover, in §5.3.2 I compare the observations with N-body simulations of a planet on a circular orbit clearing a gap in a planetesimal disc.

5.2.2 CO J=3-2 and HCN J=4-3

Despite the increasing number of CO gas detections in nearby debris discs, neither CO v=0 J=3-2 nor HCN v=0 J=4-3 emission is detected around HD 107146 in the dirty continuum-subtracted data cube. This non detection is, however, not surprising since HD 107146 is significantly older

and fainter than the other systems in which primordial gas has been found (i.e. the hybrid discs). Furthermore, the sensitivity of these observations is expected to be insufficient to detect gas if being released through collisions of volatile-rich planetesimals (Kral et al., 2017b). Using a similar method as in Chapters 2-4 I derive an upper limit of 74 mJy km s^{-1} for CO 3-2, which combined with the previous upper limit for the 2-1 transition of 40 mJy km s^{-1}, leads to an overall CO upper mass limit of 5×10^{-6} M$_\oplus$ (considering non-LTE effects, Matrà et al., 2017b). I then use Equation 1.10 and the estimated photodissociation timescale of 120 yr to estimate an upper limit on the CO+CO_2 mass fraction of planetesimals in the disc, but I find no meaningful constraint because this CO gas mass upper limit is much higher than the predicted 5×10^{-7} M$_\oplus$ if gas were released in collisions of comet-like bodies (see Chapter 2 and Marino et al., 2016; Kral et al., 2017b; Matrà et al., 2017a,b).

Similarly, I search for HCN emission, finding no significant emission. Based on this non detection I place a 3σ upper limit of 91 mJy km s^{-1}. In the absence of a tool to calculate the population of rotational levels for HCN, I estimate a mass upper limit assuming LTE. For temperatures ranging between 30-50 K, I find an upper limit of 3×10^{-9} M$_\oplus$, which translates to an upper limit on the mass fraction of HCN in planetesimals of 3%, an order of magnitude higher than the observed abundance in Solar System comets (0.1-0.5% in mass, Mumma & Charnley, 2011). Note that this HCN upper limit could be much higher due to non-LTE effects, thus this 3% limit must be taken with caution.

5.3 Modelling

In this section I model the data using parametric models to constrain the density distribution of solids in the system (§5.3.1); and N-body simulations of a planet embedded in a planetesimal disc tailored to HD 107146, to constrain the mass and orbit of a putative planet carving the observed gap (§5.3.2). In both approaches I model the central star as a G2V type star with a mass of 1 $M_\odot$, an effective temperature of 5750 K and a radius of 1 $R_\odot$.

5.3.1 Parametric model

I first use a set of parametric models to study the underlying density distribution of mm-sized dust in the system, which I fit directly to the observed visibilities as in previous chapters. Inspired by the radial profile of the dust emission (Figure 5.2), I first choose as a disc model an axisymmetric disc with a surface density that is parametrized as a triple power law that divides the disc into an inner edge, an intermediate section (where the bulk of the dust mass is) and an outer edge. On top of this, the triple power law surface density distribution has a gap, which I parametrise with a Gaussian profile, to reproduce the depression seen in the

ALMA data. This parametrization introduces a total of 9 parameters that define the surface density as follows,

$$\Sigma(r) = \Sigma_0 f_{\rm gap}(r) \begin{cases} \left(\frac{r}{r_{\rm min}}\right)^{\gamma_1} & r < r_{\rm min}, \\ \left(\frac{r}{r_{\rm min}}\right)^{\gamma_2} & r_{\rm min} < r < r_{\rm max}, \\ \left(\frac{r}{r_{\rm max}}\right)^{\gamma_3} \left(\frac{r_{\rm max}}{r_{\rm min}}\right)^{\gamma_2} & r > r_{\rm max}, \end{cases} \tag{5.1}$$

$$f_{\rm gap}(r) = 1 - \delta_{\rm g} \exp\left[-\frac{(r-r_{\rm g})^2}{2\sigma_{\rm g}^2}\right], \tag{5.2}$$

where $r_{\rm min}$ and $r_{\rm max}$ are the inner and outer radii of the disc, and $\gamma_{1,2,3}$ determine how the surface density varies interior to the disc inner radius, within the disc and beyond the disc outer radius. The gap is parametrized with a fractional depth $\delta_{\rm g}$, a center $r_{\rm g}$ and a full width half maximum (FWHM) $w_{\rm g} = 2\sqrt{2\ln(2)}\sigma_{\rm g}$. I leave as a free parameter the total dust mass $M_{\rm d}$, which is the surface integral of $\Sigma(r)$. Although the disc is close to face on, I still model the dust distribution in three dimensions adding the scale height h as an extra parameter (i.e. vertical standard deviation of hr), and imposing a prior of $h > 0.03$.

I solve for the dust equilibrium temperature and compute images at 0.86 and 1.13 mm using RADMC-3D[2]. I assume a weighted mean dust opacity corresponding to dust grains made of a mix of astrosilicates (Draine, 2003), amorphous carbon and water ice (Li & Greenberg, 1998), with mass fractions of 70%, 15% and 15%, respectively, and assuming a size distribution with an exponent of -3.5 and minimum and maximum sizes of 1μm and 1cm. This translates to a dust opacity of 1.5 cm^2 g^{-1} at 1.1 mm. I note that these choices in dust composition and size distribution have no significant effect on the modeling apart from the derived total dust mass. I then use these images to compute model visibilities at the same *uv* points as the 12m band 6, 12m band 7 and ACA band 7 observations by taking the Fast Fourier Transform after multiplying the images by the corresponding primary beam. Additionally, I leave as free parameters the disc inclination (i), position angle (PA), RA and Dec offsets for the three observation sets, and a disc spectral index ($\alpha_{\rm mm}$) that sets the flux at 0.86 mm given the dust mass and opacity at 1.1 mm, i.e. the size distribution is assumed to be the same throughout the disc. In total, the model has 19 parameters, 10 for the density distribution and 9 for the disc centre, orientation, and spectral index.

To find the best fit parameters I sample the parameter space using an MCMC approach as in previous chapters. The posterior probability distribution is defined as the product of the likelihood function (proportional to $\exp[-\chi^2/2]$) and prior distributions which I assume uniform. In computing the χ^2 over the three visibility sets I applied three constant re-weighting factors for band 6, 12m band 7 and for ACA band 7 that ensures that the final reduced χ^2 of each of the three sets is approximately 1 without affecting the relative weights

[2]http://www.ita.uni-heidelberg.de/ dullemond/software/radmc-3d/

within each of these data sets that are provided by ALMA. The re-scaling is necessary as the absolute uncertainty of ALMA visibilities can be offset by a factor of a few, even after re-weighting the visibilities with the task STATWT in CASA. These factors could be alternatively left as free parameters by adding an extra term to the likelihood function, however I find no differences in the results compared to leaving them fixed during multiple tries. Therefore I opt for leaving them fixed.

In Table 5.2 I present the best fit parameters of the 3-power law model with a Gaussian gap. I find a disc inner radius of 47 au that is significantly larger than the inner edge of $\sim 25-30$ au derived by Ricci et al. (2015a). This is because in their model they considered a sharp inner edge, while in mine I allow for the presence of dust within this inner radius, but decreasing towards smaller radii. I find that $r_{\rm min}$ matches well the radius at which the surface density peaks as seen in Figure 5.2. Similarly, the new estimate of the outer radius (136 au) is significantly smaller than their outer edge (150 au). I find that the disc inner edge has a power law index (slope hereafter) of ~ 2.6, while the outer edge is much steeper with a slope of -11. The intermediate component has a very flat slope of ~ 0.3, 2.7σ flatter than the previous estimate (0.59), although the difference could as well be simply due to different parametrizations, i.e. considering a three vs a single power law parametrization or leaving the gap's depth as a free parameter vs fixed to 1. Note that the slope derived from the intermediate component does not imply that the mass surface density of planetesimals is flat. In fact, from collisional evolution models I expect the surface density of mm-sized dust and optical depth to have a flatter slope than the total mass surface density in regions of the disc where the largest planetesimals are not yet in collisional equilibrium (i.e. have a lifetime longer than the age of the system, as shown in Chapter 4). Moreover, I also expect that in the inner regions where the largest planetesimals are in collisional equilibrium, the surface density of material should have a slope close to $7/3$ (Wyatt et al., 2007a; Kennedy & Wyatt, 2010), as I find interior to $r_{\rm min}$. This suggests that the regions interior to 47 au might be relatively depleted of solids simply due to collisional evolution rather than clearing by planets or inefficient planetesimal formation. I compare the derived inner radius and surface density of millimetre grains ($\sim 3\times10^{-6}$ $M_\oplus$ au^{-2} at 50 au) with collisional evolution models presented in Chapter 4, which include how the size distribution evolves at different radii, to estimate the maximum planetesimal size and initial total surface density of solids. I find that the best match has a maximum planetesimal size of ~ 10 km and an initial disc surface density of 0.015 $M_\oplus$ au^{-2} at 50 au, i.e. 5 times the surface density of the Minimum Mass Solar Nebula (Weidenschilling, 1977b; Hayashi, 1981) extrapolated to large radii, or a total solid disc mass of ~ 300 $M_\oplus$. This implies a very massive initial disc and efficient planetesimal formation at large radii. These conclusions assume, however, that the observed structure in the surface brightness profile arise from collisional evolution neglecting alternative origins.

Table 5.2: Best fit parameters of the ALMA data for the different parametric models. The quoted values correspond to the median, with uncertainties based on the 16th and 84th percentiles of the marginalised distributions or upper limits based on 95th percentile.

Parameter	best fit value	description
3-power law + Gaussian gap		
$M_{\rm d}$ [$M_\oplus$]	0.250 ± 0.004	total dust mass
$r_{\rm min}$ [au]	$46.6^{+1.4}_{-1.5}$	disc inner radius
$r_{\rm max}$ [au]	$135.6^{+1.1}_{-1.2}$	disc outer radius
γ_1	$2.6^{+0.3}_{-0.2}$	inner edge's slope
γ_2	$0.26^{+0.08}_{-0.10}$	disc slope
γ_3	$-10.5^{+0.9}_{-1.0}$	outer edge's slope
$r_{\rm g}$ [au]	$75.5^{+1.1}_{-1.2}$	gap mid radius
$w_{\rm g}$ [au]	$38.6^{+4.5}_{-3.6}$	gap's FWHM
$\delta_{\rm g}$	$0.52^{+0.03}_{-0.02}$	gap's fractional depth
h	$0.12^{+0.04}_{-0.05}$	scale height
PA [°]	153 ± 3	disc PA
i [°]	19.3 ± 1.0	disc inclination from face-on
$\alpha_{\rm mm}$	2.57 ± 0.11	millimetre spectral index
Step gap		
$r_{\rm g}$ [au]	$75.4^{+0.8}_{-0.7}$	gap mid radius
$w_{\rm g}$ [au]	$42.2^{+1.7}_{-2.2}$	gap's width
$\delta_{\rm g}$	0.43 ± 0.02	gap's fractional depth
Eccentric disc		
$e_{\rm d}$	¡0.03	disc global eccentricity
Inner component		
$r_{\rm min}$ [au]	$41.9^{+1.2}_{-1.4}$	disc inner radius
γ_1	$11.6^{+3.0}_{-2.7}$	inner edge's slope
γ_2	$0.03^{+0.19}_{-0.26}$	disc slope
$r_{\rm g}$ [au]	$72.1^{+2.2}_{-2.9}$	gap mid radius
$w_{\rm g}$ [au]	51^{+12}_{-8}	gap's FWHM
$\delta_{\rm g}$	$0.58^{+0.08}_{-0.06}$	gap's fractional depth
$M_{\rm c}$ [$M_\oplus$]	$3.0^{+0.9}_{-0.6} \times 10^{-3}$	dust mass inner component
$r_{\rm c}$ [au]	$19.3^{+2.8}_{-2.8}$	radius of inner component
$\Delta r_{\rm c}$ [au]	$35.8^{+9.1}_{-6.7}$	radial width of inner component
$\omega_{\rm c}$ [°]	85^{+9}_{-9}	PA of inner component south of disc PA, and in the disc plane
σ_ϕ [°]	94^{+15}_{-12}	azimuthal width of inner component

Finally, regarding the disc orientation, I find values that are consistent with previous estimates, but with tighter constraints (see Table 5.2).

These results show that the gap is centered at $75.5^{+1.1}_{-1.2}$ au, consistent with the previous estimate. However, I find a FWHM of $\sim$40 au that is much larger than the previous estimate of 9 au, likely due to Ricci et al. (2015a) assuming a gap depth of 100%. Instead, I fit the gap's depth finding a best fit value of 0.5. I also fit an alternative model in which the gap is a step function with a constant depth, finding best fit values that are similar to the model with the Gaussian gap (see Table 5.2). The difference in widths between the previous study and this work is interesting as Ricci et al. (2015a) derived the mass of a putative planet clearing a gap in the disc based on the gap's width and assuming that it should be roughly equal to the planet's chaotic zone. A 3-4 times wider gap would imply a much higher planet mass as the width of the chaotic zone scales as $m_{\rm p}^{2/7}$ (Wisdom, 1980; Duncan et al., 1989). Such planet mass estimates assume that the system is in steady state, that the gap is devoid of material, and that the gap's width is simply equal to the chaotic zone's width. However, given the age of the system ($\sim$80-200 Myr), and that any planet may be younger, it is reasonable to consider that the distribution of particles in the planet's vicinity could still be evolving. Therefore, instead of using the gap's width to estimate a planet mass, in §5.3.2 I estimate this by comparing with N-body simulations tailored to HD 107146.

Using the best fit PA and i, I deproject the observed visibilities and bin them to compare them with the axisymmetric model in Figure 5.3 (continuous line). The 12m and ACA band 7 observations are consistent with each other within errors, with some systematic differences due to the different primary beams. I find that the best fit model fits well both the real and imaginary components, with the imaginary part being consistent with zero as expected for an axisymmetric disc. However, I find a significant deviation between the real components of the 12m band 7 data and model at around 50 kλ (corresponding to an angular scale of $4''$), with the model visibility predicting a slightly lower value than the data. This could be due to large scale variations in the spectral index as the same model fits well those baselines in the band 6 data. This deviation is the same when comparing the model with a step gap, which has an indistinguishable visibility profile for baselines shorter than 200 kλ. Beyond 150 kλ I also find deviations between the data and model, expected since as shown in Figure 5.2 the radial profile seems to have structure that is more complex than a simple Gaussian gap.

A more intuitive way to study the goodness of fit of the model is to look at the dirty map of the residuals. The left column of Figure 5.4 shows the dirty maps of the residuals after subtracting the best fit model from the data (in visibility space). These are computed using natural weights, plus an outer taper of $0\farcs8$ for band 7 to obtain a synthesised beam of similar size compared to the band 6 beam. Both band 6 and 7 residual images show significant residuals (with peaks of 9 and 5 times the rms) within the disc inner edge and with a peak that

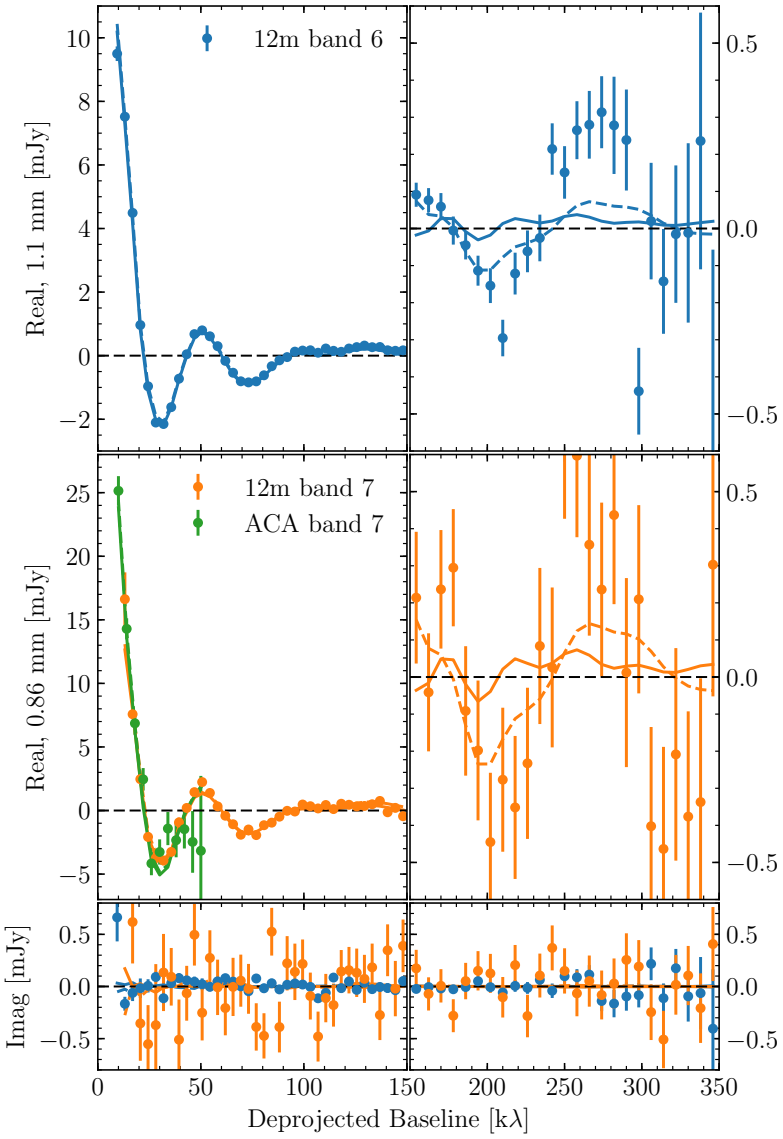

Figure 5.3: Deprojected and binned visibilities assuming a disc position angle of 153° and inclination of 19°. The real components of the band 6 and band 7 data are presented in the top and middle panels, respectively. The imaginary components of the 12m data are displayed in the lower panels. The errorbars represent the binned data with their uncertainty estimated as the standard deviation in each bin divided by the square root of the number of independent points. The continuous line shows the triple power law best fit model with a Gaussian gap. The dashed line represents the best fit model with the same parametrization, but with an additional inner component. Note that the scale in the left and right panels is different.

is significantly offset from the stellar position by $\sim 0\farcs5$, corresponding to a projected distance of ~ 15 au. Moreover, the emission is marginally resolved, extending radially by more than a beam (i.e. larger than 10 au) and with an integrated flux significantly higher than the predicted photospheric emission at these wavelengths assuming a Rayleigh-Jeans spectral index (18 and 32 μJy at 1.1 and 0.86 mm). I estimate the flux of these components by integrating the dirty maps over a circular region of $2''$ diameter, finding an integrated flux of

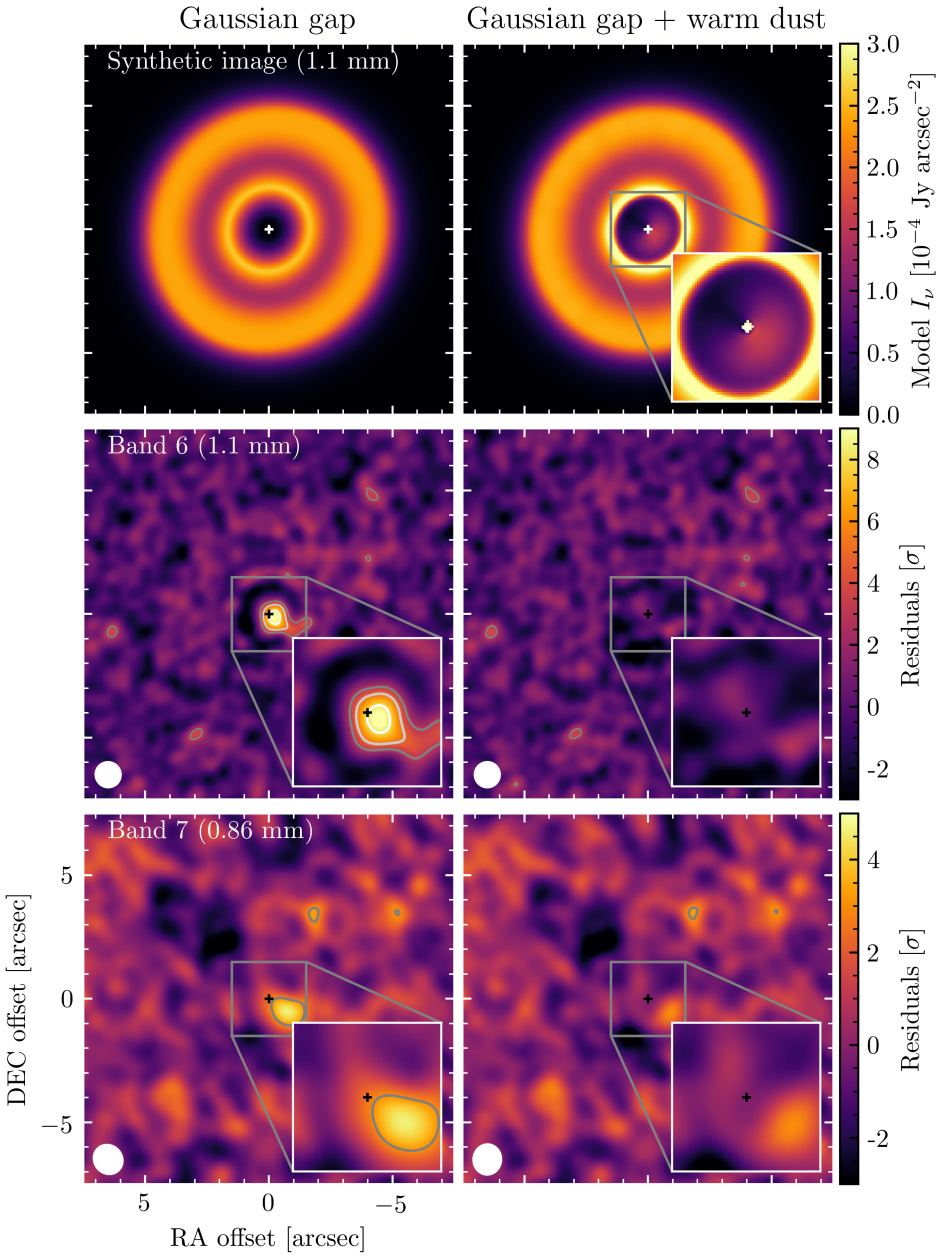

Figure 5.4: Best fit model images (1.1 mm) and dirty map of residuals. ***Left column:*** 3-power law model with a Gaussian gap. ***Right column:*** 3-power law model with a Gaussian gap and a warm inner component. The residuals of band 6 (middle row) and band 7 (12m+ACA, bottom row) are computed using natural weights and with an outer taper of $0\farcs8$, leading to a synthesised beam of $0\farcs80 \times 0\farcs79$ and $1\farcs0 \times 0\farcs9$ and an rms of 6.1 and 41 μJy beam^{-1}, respectively. Contours represent 3, 5 and 8σ.

85 ± 13 μJy and 290 ± 70 μJy at 1.1 and 0.86 mm, respectively (without including 10% absolute flux uncertainties). Because this inner emission is resolved, it cannot arise from a compact source such as a planet or circumplanetary material. I identify two plausible origins for this inner component. It could be the same warm dust that was inferred based on Spitzer data

(Morales et al., 2011), as the clump is at a radial distance that is consistent with the inferred black body radius (5-15 au) from its spectral energy distribution (SED), although the detection would imply that the warm component has an asymmetric distribution (see discussion in §5.4.4). On the other hand, the residual could be also due to a background submillimetre galaxy that are often detected incidentally as part of ALMA deep observations (see Simpson et al., 2015; Carniani et al., 2015; Marino et al., 2017a; Su et al., 2017). Submillimetre galaxies have typical sizes of the order of $1''$ and spectral indices ranging between $\sim\ 3-5$ at mm-wavelengths, thus consistent with the observed clump. However, I estimate a very low probability of 0.6% and 1% of finding a submillimetre galaxy as bright as 0.3 mJy at 0.86 mm or 0.1 mJy at 1.1 mm, respectively, and within $1''$ from the star (Simpson et al., 2015; Carniani et al., 2015), i.e. at the expected warm dust location, and therefore favouring the warm dust scenario. In fact, I do not detect any other compact emission above 5σ within the band 7 and 6 primary beams, which is consistent with the number counts of submillimetre galaxies.

Disc global eccentricity

As shown by Pearce & Wyatt (2014, 2015), a planet on an eccentric orbit can force an eccentricity in a disc of planetesimals through secular interactions. Here I aim to assess whether HD 107146's debris disc could have a global eccentricity and pericentre, using the same parametrization as in Chapter 3, i.e. taking into account the expected apocentre glow (Pan et al., 2016). I find that the disc is consistent with being axisymmetric, with a 2σ upper limit of 0.03 for the forced eccentricity. I find though that the marginalised distribution of $e_{\rm d}$ peaks at 0.02 with a pericentre that is opposite to the residual inner clump. This peak is likely produced as the residuals are lower when the disc is eccentric and with an apocentre oriented towards the clump's position angle due to apocentre glow. I therefore conclude that the fit is biased by the inner clump and that the disc is most probably not truly eccentric.

Inner component

In order to constrain the geometry or distribution of the inner emission found in the residuals, I add an extra inner component by introducing five additional parameters to the reference parametric model (3-power law surface density with a Gaussian gap). I parametrise its surface density as a 2D Gaussian in polar coordinates, with a total dust mass $M_{\rm c}$ and centered at a radius $r_{\rm c}$ and azimuthal angle $\omega_{\rm c}$ (measured in the plane of the disc from the disc PA and increasing in an anti-clockwise direction). The width of this Gaussian is parametrized with a radial FWHM $\Delta r_{\rm c}$ and an azimuthal standard deviation σ_ϕ. Best fit values are presented in Table 5.2. I find that this inner component is extended both radially and azimuthally, but concentrated around 19 ± 3 au and orthogonal to the disc PA ($\omega_{\rm c} \sim 90°$), as I found in the

residuals of the axisymmetric model. In the right panel of Figure 5.4 I present a synthetic image of the best fit model and its residuals, which are below 3σ in both band 6 and 7 within the disc inner edge. I also find that the total dust mass of this inner component is $3.0^{+0.9}_{-0.6} \times 10^{-3}$ $M_\oplus$ ($\sim$1% of the outer disc mass).

When adding this extra inner component I find that the slope of the inner edge is steeper and the inner radius smaller compared with the previous model (symmetric disc model hereafter). This difference is due to the previous model compensating for the emission within 30 au with a less steep inner edge. I also find a slightly smaller gap radius of 72 au, a larger and deeper gap (51 au wide and 0.58 deep), and a flatter surface density slope of 0.0 ± 0.2. These differences in the gap's structure and disc slope are overall consistent within 3σ with the previous estimates, but significantly improve the fit at large baselines as Figure 5.3 shows (dashed blue and orange lines). These improvements in the fit at large baselines are not due to the addition of the clump, but due to the different best fit surface density profile of the outer disc. In fact, the visibilities of the inner component are negligible beyond 200 kλ. The rest of the parameters are consistent within 1σ with the values presented for the symmetric disc model. To have a better estimate of the flux of this inner component, I subtract the new best fit of the outer component (its inner edge is steeper), finding an integrated flux over a circular region of $3''$ diameter of 0.82 ± 0.14 and 0.31 ± 0.04 mJy at 0.86 and 1.1 mm, respectively (including 10% absolute flux uncertainties). Note that this flux is a factor two higher than that estimated from the residuals of the symmetric disc model, as without the inner component the model tries to compensate for the emission interior to 40 au. From these fluxes I estimate a spectral index of 3.3 ± 0.6, thus still consistent with the typical observed spectral indices of debris discs. Based on this new flux estimate at 0.86 mm, I find an even lower probability of 0.1% and 0.3% of finding a submillimetre galaxy as bright as this inner emission at 0.86 and 1.1 mm, respectively, and within $1''$ from the star (Simpson et al., 2015; Carniani et al., 2015). These results also confirm that the peak of the inner component is significantly offset from the star and it is incompatible with an axisymmetric inner component. If this emission is produced by warm dust, then it could bring valuable insights into the origin of warm dust emission in general, as it is inconsistent with an axisymmetric asteroid belt (see §5.4.4).

Because the new estimate of the inner edge slope is too steep to be consistent with being set by collisional evolution, the maximum planetesimal size is only constrained to be $\gtrsim 10$ km. Despite this, the relative brightness between the inner and outer components can still be explained simply by collisional evolution. This has also been found for other systems with warm dust components, e.g. q^1 Eridani (Schüppler et al., 2016), suggesting the presence of planets clearing the material in between (Shannon et al., 2016).

5.3.2 N-body simulations

In this section I compare the observations with dynamical N-body simulations of a planet embedded in a planetesimal disc. To simulate the gravitational interactions between the planet and particles I use the N-body software package REBOUND (Rein & Liu, 2012), using the hybrid integrator MERCURIUS[3] that switches from a fixed to a variable time-step when a particle is within a given distance from the planet (here chosen to be 8 Hill radii). The fixed time step is chosen to be 4% of the planet's period, which is lower than 17% of the orbital period of all particles in the simulation. Although the total mass of the disc could be tens of $M_\oplus$, and thus comparable with the mass of the simulated planets, I assume particles have zero or a negligible mass. In §5.4.3 I discuss the effect of considering a massive planetesimal disc on planet disc interactions.

Particles are initially randomly distributed in the system with a uniform distribution in semi-major axis (a) between 20 and 170 au (i.e. with a surface density proportional to r^{-1}), with an eccentricity and inclination uniformly distributed between 0-0.02 and 0-0.01 radians, respectively. I use a total number of 10^4 particles, sufficient to sample the 150 au span in semi-major axes and recover smooth images of the disc density distribution. The planet is placed on a circular orbit at 80 au and assumed to have a bulk density of 1.64 g cm^{-3} (Neptune's density). I run a set of simulations with planet masses varying from 10 to 100 $M_\oplus$ with a 5 $M_\oplus$ spacing, and integrate their evolution up to 200 Myr, roughly the upper limit for the age of HD 107146.

In order to translate the outcome of these simulations to density distributions used to produce synthetic images, I populate the orbits of each particle with 200 points randomly distributed in mean anomaly as in Pearce & Wyatt (2014), but in the frame co-rotating with the planet in order to see if there are resonant structures (e.g. loops or Trojan regions). I find however no significant azimuthal structures due to first or second order resonances in the derived surface density of particles. I weight the mass of each particle based on its initial semi-major axis to impose an initial surface density proportional to r^γ between a minimum and maximum semi-major axis ($a_{\rm min}, a_{\rm max}$). Finally, because I only run simulations with a fixed planet semi-major axis of 80 au to save computational time, I scale all the distances in the output of the simulation and leave $a_{\rm p}$ as a free parameter (only varying roughly between 75-80 au). This linear scaling is motivated by the fact that some of the features that I am interested in should scale with semi-major axis (e.g. Hill radius, mean-motion resonances, chaotic zone), although some other important quantities, such as the scattering diffusion timescale (Tremaine, 1993), have a dependency on a that is

[3]I also used Hermes in several trial runs; however, I decided to use Mercurius instead because with Hermes I obtained results that differ significantly from other integrators such as ias15, whfast and the hybrid integrator within Mercury. I found that some particles outside the chaotic zone were driven to unstable orbits and did not conserve their Tisserand parameter. The possibility of a potential bug in Hermes was confirmed by private communication with Hanno Rein.

different from linear. I test the validity of the scaling approximation for the narrow range of planet semi-major axis that I explore (70-80 au), finding it reproduces well the expected surface density when compared to the results obtained running an scaled simulation instead.

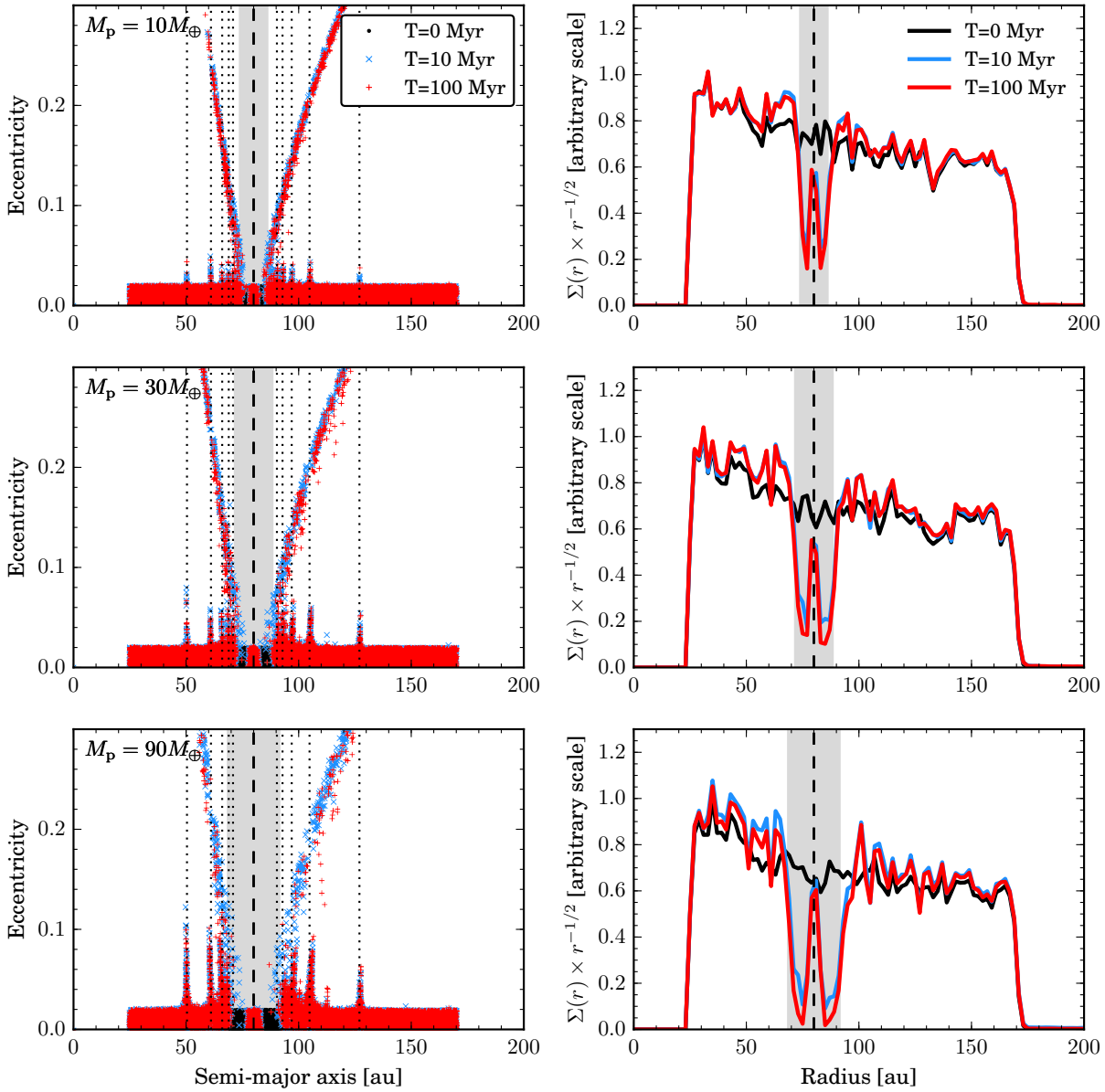

Figure 5.5: Evolution of massless particles in a system with a single planet on a circular orbit at 80 au. ***Left column:*** eccentricity and semi-major axis of particles after 0, 10 and 100 Myr of evolution. The dotted and dashed vertical lines represent first order mean motion resonances and the semi-major axis of the planet. ***Right column:*** Surface brightness of particles assuming an initial surface density proportional to $r^{1/4}$ and a dust temperature profile decreasing with radius as $r^{-1/2}$. The grey shaded region represents the chaotic zone approximated by $a_p \pm 1.5 a_p (m_p/M_\star)^{2/7}$. The top, middle and bottom panels show systems with planet masses of 10, 30 and 90 $M_\oplus$, respectively.

In Figure 5.5 I present, as an example, the evolution of a, e and the surface density of particles for planet masses of 10, 30 and 90 $M_\oplus$. The width of the chaotic zone is overlayed in grey to compare with the gap in the surface density cleared by the planet — note that the chaotic zone

is a region in semi-major axis rather than radius. Although by 100 Myr the chaotic zone is almost empty of material (except for particles in the co-rotation zone) the surface density is not zero inside the gap as some particles have apocentres or pericentres within this region while being scattered by the planet. Some particles also remain on stable tadpole or Trojan orbits until the end of the simulation, creating an overdensity within the gap at 80 au. Interior and exterior to the planet, a small fraction of particles are in mean motion resonance with the planet and have their eccentricities increased. In agreement with previous work, I find that the gap's width approximates to the chaotic zone, and its width does not vary after 10 Myr for the planet masses explored.

To compare with observations, I use snapshots of the simulations at 50, 100 and 200 Myr since the age of the system is uncertain and could vary roughly within this range. These ages assume that the putative planet formed (or grew to its current mass) early during the evolution of this system, rather than recently, or that this is the time since the planet formed. For each assumed epoch, I explore the parameter space using the same MCMC technique as in §5.3.1, varying $a_{\rm min}$ and $a_{\rm max}$, the surface density exponent γ, the semi-major axis of the planet, and its mass by interpolating the resulting surface density between two neighbouring simulations. I also leave as a free parameters the disc orientation, pointing offsets and spectral index, and instead of varying the disc scale height I assume a flat disc. I find a best fit mass of 30 ± 5 $M_\oplus$ and semi-major axis of 77 ± 1 au, independently of the assumed age since after 10 Myr there is no significant evolution in the orbits of particles near the planet (see Figure 5.5). I find, however, that the best fit cannot reproduce well the gap's width and depth. This is illustrated in the top and middle panels in Figure 5.6, where the model has a narrower gap compared with the band 6 radial profile, and thus overall larger residuals. Although larger planet masses could produce wider gaps, these would also be significantly deeper and thus inconsistent with the observations. Moreover, the planet gap could be even deeper if, for example, I assume a different starting condition with a depleted surface density within the planet's feeding zone as it accreted a large fraction of that material while growing. To test this, I repeat the fitting procedure, but removing those particles that start the simulation within two Hill radii from the planet's orbit (planet's feeding zone). I find a slightly lower best fit planet mass of 26 ± 3 $M_\oplus$, but overall the fit is worse with a difference of ~ 300 in the total χ^2, strongly preferring the model with particles starting near the planet. Therefore, I conclude that a single planet on a circular orbit that was born within the outer disc is unable to explain the ALMA observations.

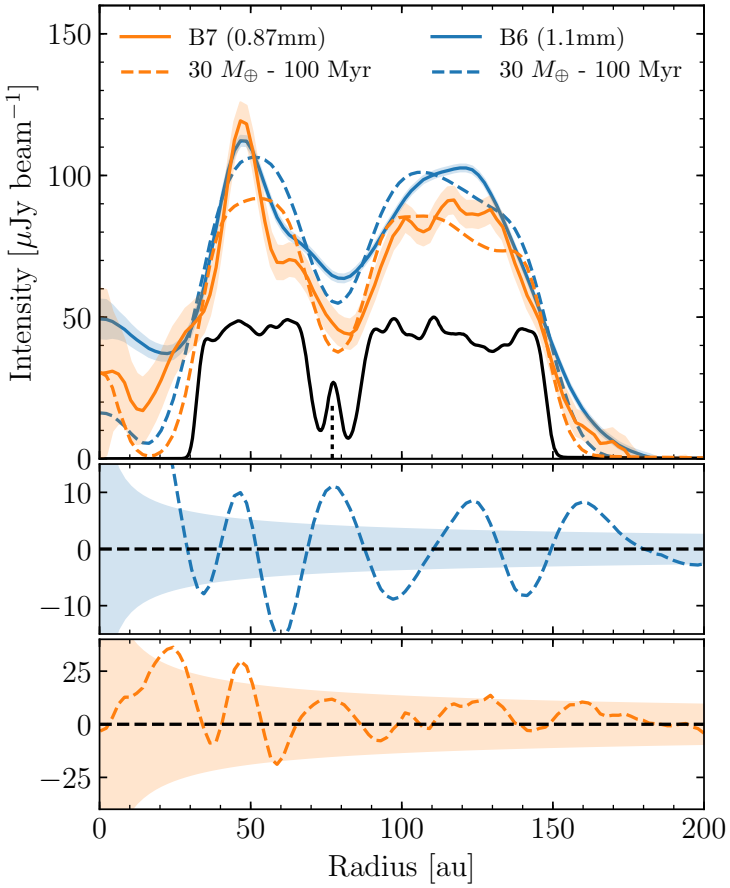

Figure 5.6: ***Top:*** Average intensity profile computed azimuthally averaging the disc emission over ellipses oriented as the disc in the sky. The blue and orange lines are obtain from the band 6 and band 7 Clean images (continuous lines) and simulated Clean images based on an N-body simulation of one 30 $M_\oplus$planet (dashed lines), using Briggs (robust=0.5) weights. The black continuous line represents the surface brightness profile with a 1 au resolution and displayed at an arbitrary scale. The vertical dotted line represents the orbital radius of the planet. ***Middle:*** Azimuthally averaged residuals in band 6. ***Bottom:*** Azimuthally averaged residuals in band 7. The shaded areas represent the 68% confidence region in the top panel and 99.7% confidence region in the middle and bottom panel, over a resolution element (18 au for band 6 and 13 au for band 7).

5.4 Discussion

5.4.1 The gap's origin

As mentioned in §5.1, there are multiple scenarios where a single planet may open a gap in a planetesimal disc. Below I discuss these and how well they could fit the data.

Single planet on a circular orbit

As I showed in §5.3.2, a single planet on a circular orbit and formed inside the gap could clear its orbit of debris through scattering, opening a gap with a width similar to the chaotic zone. Such a planet, however, needs to be very massive to produce a ~ 40 au wide gap ($\gtrsim 3$ M_{Jup}), which, on the other hand, results in a gap that is significantly deeper than the observations suggest. Based on these constraints I find that a 30 $M_\oplus$ planet is the best trade-of between the gap's width and depth.

If, however, the planet could migrate (inwards or outwards) then these two observables could become compatible. A low mass planet that migrated through the disc could carve a sufficiently wide gap to explain the ~ 40 au gap's width. Migration could also explain the relative depth of $\sim 50\%$ that is observed as after migrating, the planet would also leave behind debris that was scattered onto excited orbits, but that no longer cross the planet's orbit (e.g. Kirsh et al., 2009), therefore the gap would still contain a significant fraction of the original material. Planet migration could be induced by planetesimal scattering, which is discussed in §5.4.3.

Multiple planets on circular orbits

If I assume planet migration is negligible (e.g. disc mass around the planet's orbit is much lower than its mass), then multiple planets would need to be present to carve such a wide and shallow gap. Let us assume that the gap was carved by multiple equal mass planets orbiting between 60 and 90 au. As shown by Shannon et al. (2016) and in §5.3.2, the gap's width and age of the system place tight constraints on the minimum mass of a planet to clear the region surrounding its orbit, and on the maximum number of planets that could be orbiting within the gap based on a stability criterion. Given HD 107146's age range of $\sim 50-200$ Myr, only planets with masses greater than 10 $M_\oplus$ would have enough time to clear their orbits via scattering. On the other hand, only planet masses $\lesssim 30$ $M_\oplus$ can create a gap that is not too deep compared with the observations. Given this range of planet masses, I estimate that a maximum of three 10 $M_\oplus$ planets could orbit between 60 and 90 au spaced by 8 mutual Hill radii at the limits of long term stability (Chambers et al., 1996; Smith & Lissauer, 2009). If I require planets to be spaced

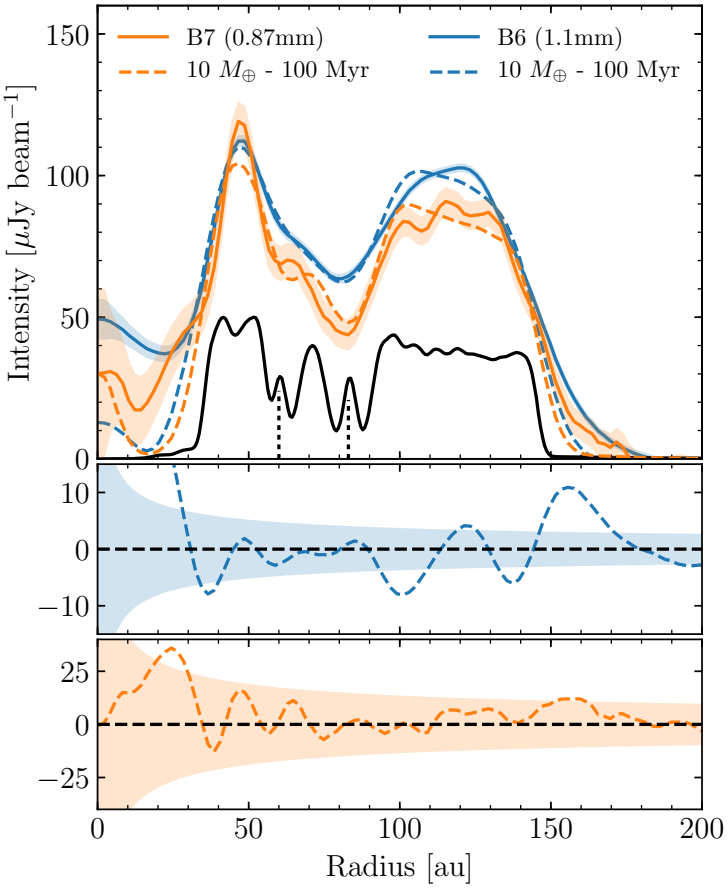

Figure 5.7: ***Top:*** Average intensity profile computed azimuthally averaging the disc emission over ellipses oriented as the disc in the sky. The blue and orange lines are obtain from the band 6 and band 7 Clean images (continuous lines) and simulated Clean images based on an N-body simulation of two 10 $M_\oplus$planets (dashed lines), using Briggs (robust=0.5) weights. The black continuous line represents the surface brightness profile with a 1 au resolution and displayed at an arbitrary scale. The vertical dotted line represents the orbital radii of the planets. ***Middle:*** Azimuthally averaged residuals in band 6. ***Bottom:*** Azimuthally averaged residuals in band 7. The shaded areas represent the 68% confidence region in the top panel and 99.7% confidence region in the middle and bottom panel, over a resolution element (18 au for band 6 and 13 au for band 7).

by more than 8 mutual Hill radii, this multiplicity reduces considerably to two or only one planet if planet masses are slightly higher. I tested this by running new simulations with the same parameters as in §5.3.2, but instead with a pair of 30 or 10 $M_\oplus$ planets and semi-major axes ranging between 60 to 90 au. After a few iterations I found a good fit using two 10 $M_\oplus$ planets with semi-major axes of 60 and 83 au (i.e. spaced by 12 Mutual Hill radii). Figure 5.7 shows the radial profile for this model reproducing the gap's width and depth. The gap's relative depth is similar to the one observed since there are still particles on stable orbits at around 70 au and trapped in the co-orbital regions of the two planets — note that there are residuals above 3σ at the inner and outer edge of the disc because this model has sharp boundaries in semi-major

axis. If I assumed that no particles were present near the planet at the start of the simulation as commented in §5.3.2, then even lower mass planets creating narrower gaps would be needed in order to achieve an overall gap depth of 50%.

Planet(s) on eccentric orbits

Although a single or multiple low mass planets might explain the observed gap, the formation of an ice giant planet at $\sim$ 80 au encounters significant difficulties compared to within a few tens of au (see §5.4.2). The scenario proposed by Pearce & Wyatt (2015), where a planet opens a broad gap through secular interactions, circumvents some of these problems as the planet is formed closer in at 10-20 au, and scattered out by a more massive planet onto an eccentric orbit with a larger semi-major axis. This scenario was able to fit the mean radial profile derived by Ricci et al. (2015a) and predicted the presence of asymmetries in the form of spiral features and a small offset between the inner and outer regions of the disc due to secular interactions with the planet. However, no significant offset between the inner and outer regions is present in the observations. By fitting an ellipse to the inner and outer bright arcs in the band 6 image (roughly at 50 and 110 au), I constrain the offset to be $0\farcs05 \pm 0\farcs02$, (i.e. consistent with zero and lower than 1.6 au). This translates to a maximum eccentricity of 0.03 if I assume that the outer bright arc is circular while the inner arc is eccentric and thus offset from the star. Moreover, the observations suggest that the disc inner edge is much steeper than predicted by Pearce & Wyatt (2015), thus inconsistent with their model. A last recently proposed scenario involves two interior planets with low but non-zero eccentricity, which open a gap in the outer regions due to secular resonances (Yelverton et al., submitted). Although this scenario can produce an observable gap, in its simplest form the model produces a gap that is narrower than seen for HD 107146.

Dust-gas interactions

There are other scenarios that might not require the presence of planets to produce a gap or multiple ring structures in the dust distribution. Photoelectric instability (Klahr & Lin, 2005; Besla & Wu, 2007; Lyra & Kuchner, 2013; Richert et al., 2018) is one of those scenarios and has received particular attention lately as the presence of vast amounts of gas around a few debris discs suggests that this mechanism could be common. However, this mechanism is only important when dust-to-gas ratios are comparable and it is not yet clear if relevant for the dust distribution of large millimetre-sized grains that are not well coupled to the gas. Assuming some residual primordial gas could still be present in the disc, I convert the CO gas mass upper limit of 5×10^{-6} $M_\oplus$ (see §5.2.2 below) to a total gas mass upper limit of ~ 0.05 $M_\oplus$ (assuming a CO/H_2 ratio of 10^{-4}) or a surface density of $\sim 10^{-5}$ g cm^{-2}. This upper limit is comparable

to the total dust mass in millimetre grains, thus photoelectric instability could occur. However, using this gas surface density upper limit I estimate a Stokes number of 10^5 for millimetre grains, thus the stopping time is much longer than the collisional lifetime of millimetre dust and of the order of the age of the system. Therefore, I conclude that photoelectric instability does not play an important role in the formation of the structure observed by ALMA around HD 107146.

5.4.2 Planet formation at tens of au

Based on these new ALMA observations, if the gap was cleared by a single or multiple planets, these must have a low mass ($\lesssim$30 $M_\oplus$) and formed between 50 and 100 au. Otherwise, if the planets were formed closer in and scattered out onto an eccentric orbit, the disc would appear asymmetric (Pearce & Wyatt, 2015). Such low planet masses and orbits at tens of au resemble the ice giant planets in the Solar System, but with a semi-major axis 2-3 times larger than Neptune's. *Could such planets have formed in situ as these observations suggest?* HD 107146's broad and massive debris disc indicates that planetesimals efficiently formed at a large range of radii from 40 to 140 au. Moreover, the mass of these putative planets ($\lesssim$ 30 $M_\oplus$) is consistent with the solid mass available in their feeding zones ($\sim$ 4 Hill radii wide), based on the dust surface density derived in §5.3.1 and extrapolating it to the total mass surface density (assuming a size distribution $dN \propto D^{-3.5}dD$ and planetesimals up to sizes of 10 km). Nevertheless, in situ formation encounters the two following problems. First, although a planet at $\sim$ 80 au might grow through pebble accretion fast enough to form an ice giant before gas dispersal (Johansen & Lacerda, 2010; Ormel & Klahr, 2010; Lambrechts & Johansen, 2012; Morbidelli & Nesvorny, 2012; Bitsch et al., 2015), it requires the previous formation of a massive planetesimal (or protoplanet) of $10^{-2} - 10^{-1}$ $M_\oplus$ (so-called transition mass). However, newly born planetesimals through streaming instability (Youdin & Goodman, 2005) have characteristic masses of rather $10^{-6} - 10^{-4}$ $M_\oplus$ (Johansen et al., 2015; Simon et al., 2016). These planetesimals can grow through the accretion of pebbles and smaller planetesimals, but this growth (so-called Bondi accretion) is very slow for low mass bodies at large stellocentric distances (Johansen et al., 2015). A possible solution to this problem is that the protoplanetary disc around HD 107146 was unusually massive and long-lived, which would increase the chances of forming protoplanets. Alternatively, the low mass protoplanet(s) could have formed closer in and been scattered out and circularised during the protoplanetary disc phase. The second problem that in-situ formation faces is related to planet migration. A protoplanet growing to form an ice giant is expected to migrate inwards through type-I migration (Tanaka et al., 2002). While this might imply that the single or multiple putative planets might have formed at larger radii, the observations suggest that they would have attained most of their mass within the observed gap, i.e. within 100 au. If pebble accretion is fast enough, the

planet(s) could grow fast and migrate only slightly before disc dispersal.

Why would planets form only between 60-90 au within this 100 au wide disc of planetesimals? While no planets might have formed beyond 90 au as planetesimal accretion was too slow for a planetesimal to reach the transition mass and efficiently accrete pebbles, this is not the case for planetesimals formed at smaller radii between the inner edge of the disc and the orbit of the innermost putative planet. *Why did only planetesimals form between 40-60 au?* Planetesimal growth might have been hindered there if the orbits of large solids were stirred by inner planets, making their accretion rate slower. Alternatively, planetesimal growth between 60-90 au could have been more efficient due to a local enhancement in the available solid mass. As stated before, it is also possible that the low mass protoplanet(s) did not form in situ, but was (were) scattered out from further in.

5.4.3 Massive planetesimal disc

Here I discuss the effect that a massive planetesimal disc could have on the conclusions stated above where I assumed a disc of negligible mass ($\ll 10$ M$_\oplus$). As shown in §5.3, this debris disc is likely very massive and thus affects the dynamics of this system, e.g. because of the gravitational force on the planet(s) and disc self-gravity. A massive disc can induce planetesimal driven migration where the planet migrates through a planetesimal disc due to the angular momentum exchange in close encounters (e.g. Fernandez & Ip, 1984; Ida et al., 2000; Gomes et al., 2004). This type of migration has been well studied in the context of the outer Solar System, as it could have driven an initially compact orbital configuration to a more extended and current configuration (Hahn & Malhotra, 1999, 2005), or towards an orbital instability (e.g. Tsiganis et al., 2005). In all these models the outer planets scatter material in to Jupiter which ejects most of it, leading to an outward migration of the outer planets and a small inward migration of Jupiter. However, Ida et al. (2000) showed that even in the absence of interior planets self-sustained migration could have led Neptune's orbit to expand due to the asymmetric planetesimal distribution around it. A more recent work by Kirsh et al. (2009), however, showed that a single planet embedded in a planetesimal disc migrates preferentially inwards due to the timescale difference between the inner and outer feeding zones (see also Ormel et al., 2012). Therefore, I expect that any putative planet at ∼80 au around HD 107146 is likely migrating or has migrated inwards since it formed.

Simple scaling relations from Ida et al. (2000) predict that the migration rate should be of the order of

$$\left|\frac{da}{dt}\right| \approx \frac{4\pi\Sigma a^2}{M_\star}\frac{a}{T}, \tag{5.3}$$

where T is the planet's orbital period, which agrees roughly with numerical simulations (e.g.

Kirsh et al., 2009). Given the expected surface density of planetesimals at 80 au around HD 107146 ($\Sigma \gtrsim 10^{-2}$ $M_\oplus$ au^{-2} for a maximum planetesimal size of 10 km), Equation 5.3 predicts that the migration rate is such that the planet would have crossed the whole disc reaching its inner edge in only a few Myr. Kirsh et al. (2009) found, however, that when the planet mass exceeds that of the planetesimals within a few Hill radii, the migration rate decreases strongly with planet mass. Assuming that the gap is indeed caused by a single or multiple planets between 60-90 au, given the 30 $M_\oplus$ upper limit for the planet mass I conclude that the surface density of planetesimals must be much lower than 0.01 $M_\oplus$ au^{-2} to hinder planetesimal driven migration, i.e. a total disc mass $\lesssim 430$ $M_\oplus$. If not the surface density profile would probably be significantly different without a well defined gap. This dynamical upper limit together with the lower limit derived from collisional models constrain the total disc mass to be between $\sim 300 - 400$ $M_\oplus$, which is close to the maximum solid mass available in a protoplanetary disc under standard assumptions (e.g. disc-to-stellar mass ratio of 0.1 and gas-to-dust mass ratio of 100). This particularly high disc mass at the limits of feasibility is not unique, but a confirmation of the so-called "disc mass problem" as many other young and bright discs need similar or even higher masses according to collisional evolution models (see discussion in Krivov et al., 2018).

Although I expect that the gap produced by a migrating planet might look significantly different compared with the no migration scenario (e.g. wider and radially and perhaps azimuthally asymmetric), none of the above studies provided a prediction for the resulting surface density of particles during planetesimal driven migration that I could compare with the observations. In experimental runs with a 10 or 30 $M_\oplus$ planet and a similar mass planetesimal disc (using massive test particles) I find that the planet migrates inward ∼5-40 au in 100 Myr depending on the planet and disc mass, and that the gap has an asymmetric radial profile that is significantly distinct from the no-migration scenario, which could explain why I find a slight asymmetry within the gap (see §5.2.1). Future comparison with numerical simulations of planetesimal-driven migration could provide evidence for inward or outward migration, and thus set tighter constraints on the disc and planet mass. Dynamical estimates of the disc mass could also shed light on the disc mass problem, confirming the high mass derived from collisional models or rather indicating that these need to be revisited.

5.4.4 Warm inner dust component

While IR excess detections can be generally explained by a single temperature black body, there is a large number of systems that show evidence for a broad range of temperatures that are hard to explain simply as due to a single dusty narrow belt, even with temperatures varying as a function of grain size (e.g. Backman et al., 2009; Morales et al., 2009; Chen et al., 2009; Ballering

et al., 2014; Kennedy & Wyatt, 2014). Although this might be explained by material distributed over a broad range of radii (like in protoplanetary discs), an alternative and very attractive explanation for these systems is the presence of a two-temperature disc, with an inner asteroid belt and an outer exo-Kuiper belt, analogous to the Solar System (e.g. Kennedy & Wyatt, 2014; Schüppler et al., 2016; Geiler & Krivov, 2017). HD 107146 is a good example of this type of system (Ertel et al., 2011; Morales et al., 2011), with a significant excess at 22 μm that cannot be reproduced by models of a single outer belt, but rather is indicative of dust located within ~ 30 au produced in an asteroid belt. These type of belts are typically hard to resolve due to the small separation to the star (hindering scattered light observations) where current instruments are not able to resolve and due to their low emissivity that peaks in the MIR.

Is the detected inner emission related to the ~ 20 μm excess? In order to test if the inner emission seen by ALMA is compatible with being warm dust, I use the parametric model developed in §5.3.1 to see if it can reproduce the available photometry of this system, including the MIR excess. I introduce, though, two changes to the model assumptions: first, I modify the size distribution index from -3.5 to -3.36 to be consistent with the derived spectral index in this work and previous studies (Ricci et al., 2015b); and second, I extend the size distribution from 1 to 5 cm. The latter is necessary to reproduce the photometry at 7 mm as the contribution from cm-sized grains is significant at these wavelengths. In Figure 5.8 I compare the model and observed SED, including the new ALMA photometric points of the inner component. Despite the simplicity of the model, it reproduces successfully both the photometry at 22 μm and at millimetre wavelengths, confirming that the detection is consistent with being warm dust emission.

These new ALMA observations provide unique information on the nature of the warm dust emission as it is marginally resolved (see Figure 5.9). The surface brightness peaks at ~ 20 au, thus roughly in agreement with the predicted location based on SED modelling. The emission, however, is far from originating in an axisymmetric asteroid belt, but is rather asymmetric with a maximum brightness towards the south west side of the disc. *What could cause such an asymmetric dust distribution?* I identify three scenarios proposed in the literature that could cause long- or short-term brightness asymmetries in a disc or belt.

First, the inner emission could correspond to an eccentric disc, which at millimetre wavelengths would be seen brightest at apocentre. This is known as apocentre glow, which is caused by the increase in dust densities at apocentre for a coherent disc (Wyatt, 2005; Pan et al., 2016; Löhne et al., 2017). Disc eccentricities can be caused by perturbing planets (e.g. Wyatt et al., 1999; Nesvold et al., 2013; Pearce & Wyatt, 2014), as it has been suggested to explain Fomalhaut's eccentric debris disc (Quillen, 2006; Chiang et al., 2009; Kalas et al., 2013; Acke et al., 2012; MacGregor et al., 2017) and HD 202628 (Krist et al., 2012; Thilliez & Maddison, 2016). At long wavelengths, the contrast between apocentre and pericentre

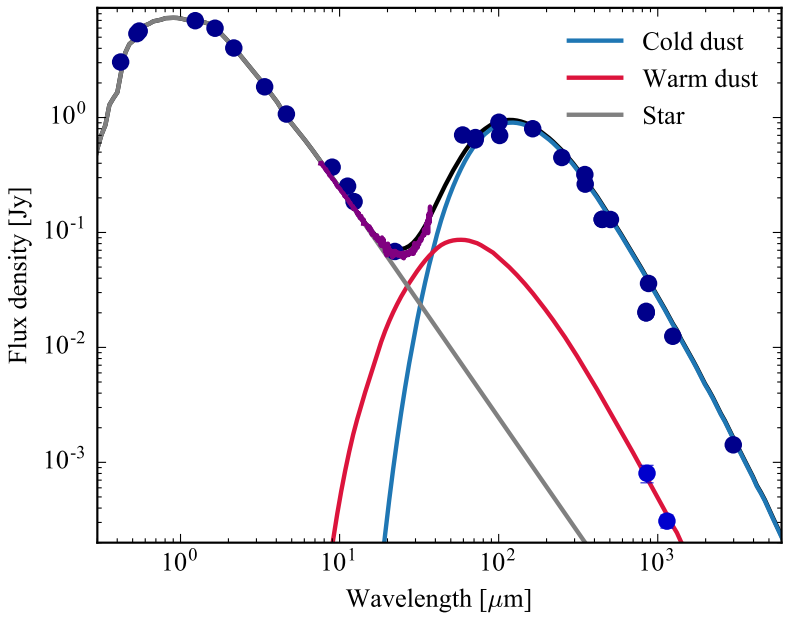

Figure 5.8: Spectral Energy Distribution of HD 107146 (dark blue points, Kennedy & Wyatt, 2014) and its inner component (light blue colours) obtained after subtracting the outer component of the model presented in §5.3.1. The grey, light blue and red lines represent the stellar, outer disc, inner component contribution to the total flux (black line), respectively.

brightness is expected to be approximately (Pan et al., 2016)

$$\left(\frac{1-e/2}{1+e/2}\right)\left(\frac{1+e}{1-e}\right),$$

thus to reach a contrast higher than 2 (as observed for HD 107146's inner disc), the disc eccentricity would need to be higher than 0.5. Assuming the disc eccentricity corresponds to the forced eccentricity (i.e. free eccentricities are much smaller), then the perturbing planet should have a very high eccentricity $\gtrsim 0.5$. One potential problem with this scenario is that the outer disc does not show any hint of being influenced by an eccentric planet. This problem could be circumvented if the true eccentricity of the inner belt is lower than derived based on the image residuals (e.g. $\lesssim 0.2$) and the inner planet has a semi-major axis of only a few au, as the forced eccentricity on the outer disc would be much smaller. Alternatively, if the disc or putative outer planet(s) are much more massive than the inner eccentric planet, the disc might remain circular as it is observed.

A second potential scenario relates to a recent collision between planetary embryos, which would release large amounts of dust at the collision point producing an asymmetric dust distribution that could last for $\sim$ 1000 orbits or $\sim$ 1 Myr at 20 au (Kral et al., 2013; Jackson et al., 2014). In such a scenario the *pinch point* would appear brightest since the orbits of the generated debris converge where the impact occurred and more debris is created from collisions. In this manner, the pinch point would also appear radially narrow. However, both

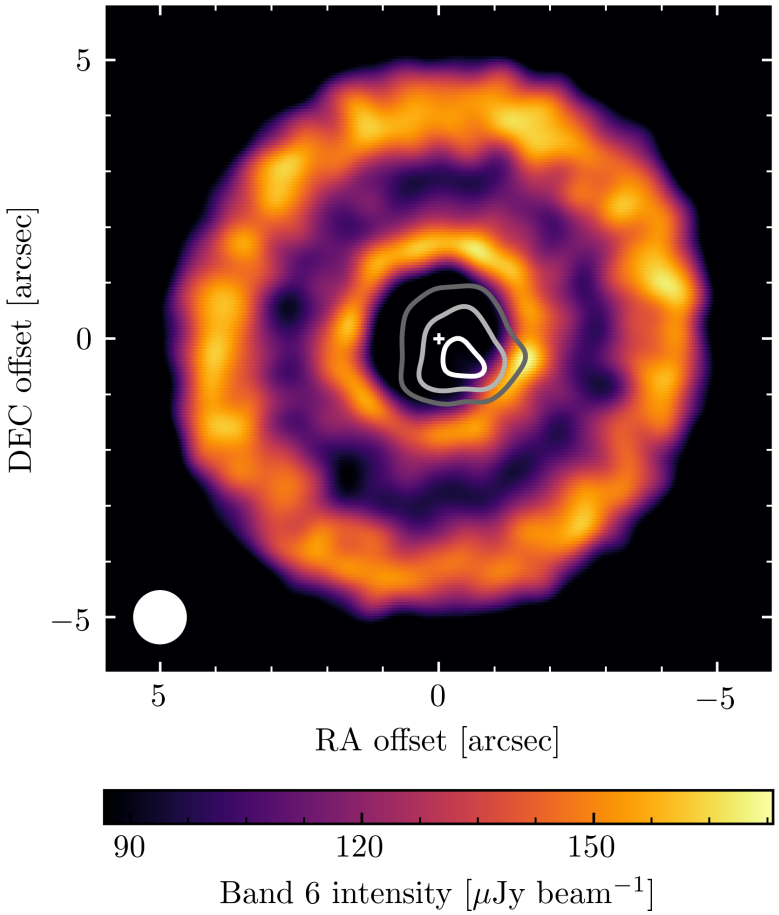

Figure 5.9: Clean image of HD 107146 at 1.1 mm (band 6) using natural weights. Overlayed in contours are the residuals after subtracting the best fit model presented in §5.3.1, but without the inner component. Contour levels are set to 4, 8 and 12 σ. The stellar position is marked with a white cross at the center of the image, while the beam ($0\farcs80 \times 0\farcs79$) is represented by a white ellipse in the bottom left corner. The image rms at the center is 6.3 μJy beam^{-1}. For a better display I have adjusted the color scale with a minimum of 50% the peak flux.

the band 6 and 7 datasets show that the emission is radially broad at its brightest point, spanning $\gtrsim$ 20 au. This could be circumvented if the collision occurred within a broad axisymmetric disc. Higher resolution observations are necessary to discard this scenario or confirm these two inner components.

Finally, a third possible scenario is that the asymmetric structure is caused by planetesimals trapped in mean motion resonances (typically 3:2 and 2:1) with an interior planet that migrated through the planetesimal disc (Wyatt & Dent, 2002; Wyatt, 2003, 2006; Reche et al., 2008). The exact dust spatial distribution depends on the planet mass, migration rate and eccentricity. The single clump inferred from the observations suggests that planetesimals would be trapped predominantly on the 2:1 resonance rather than 3:2 as the latter only creates a two clump symmetric structure. Simulations by Reche et al. (2008) showed that in order to

trap planetesimals in the 2:1 resonance, a Saturn mass planet (or higher) with a very low eccentricity was needed, therefore, placing a lower limit on the planet mass if the asymmetry is due to resonant trapping.

Future observations could readily distinguish between scenarios 1-2 and 3, as in the first two scenarios the orientation of the asymmetry should stay constant (precession timescales are orders of magnitude longer than the orbital period), while in the third scenario it should rotate at the same rate as the putative inner planet orbits the star. Moreover, higher resolution and more sensitive observations could reveal if the disc is eccentric, smooth with a radially narrow clump, or smooth with a radially broad clump (scenarios 1 to 3, respectively). Observations at shorter wavelength would also be useful. In the eccentric disc scenario I expect the disc to be eccentric and broader due to radiation pressure on small dust grains, while resonant structure would be completely absent and the disc should look axisymmetric as small grains are not trapped also due to radiation pressure. Finally, future ALMA observations should be able to definitely rule out the possibility of the inner emission arising from a submillimetre galaxy. Given HD 107146's proper motion (-174 and -148 mas yr^{-1} in RA and Dec. direction, respectively), in 2 years any background object should shift by $0\farcs23$ towards the north east with respect to HD 107146, thus enough to be measured with ALMA observations of similar sensitivity and resolution to the ones presented here.

5.5 Conclusions

In this chapter, I have analysed new ALMA observations of HD 107146's debris disc at 1.1 and 0.86 mm, to study a possible planet-induced gap suggested by Ricci et al. (2015a) with a higher resolution and sensitivity. These new observations show that HD 107146, a 80-200 Myr old G2V star, is surrounded by a broad disc of planetesimals from 40 to 140 au, that is divided by a gap $\sim$40 au wide (FWHM), centered at 80 au and 50% deep, i.e. the gap is not devoid of material. I constrained the disc morphology, mass and spectral index by fitting parametric models to the observed visibilities using an MCMC procedure. I find that the disc is consistent with being axisymmetric, and I constrain the disc eccentricity to be lower than 0.03.

The observed morphology of HD 107146's debris disc suggests the presence of a planet on a wide circular orbit opening a gap in a planetesimal disc through scattering. I run a set of N-body simulations of a planet embedded in a planetesimal disc that I compare with the observations. I find that the observed morphology is best fit with a planet mass of 30 $M_\oplus$, but significant residuals appear after subtracting the best fit model. I conclude that the observed gap cannot be reproduced by the dynamical clearing of such a planet as the gap it creates is significantly deeper and narrower than observed. I discuss that this could be circumvented by

allowing the planet to migrate (e.g. due to planetesimal driven migration) or by allowing multiple planets to be present. I discuss how a planet could have formed in situ if the primordial disc was massive and long-lived, and possibly grew to its final mass very quickly and by the end of the disc lifetime (e.g. through pebble accretion), avoiding significant inward migration and runaway gas accretion. Moreover, because the putative planet(s) could undergo very fast planetesimal driven migration, I set an upper limit on the surface density and total mass of the disc.

These ALMA observations also revealed unexpected emission near the star that is best seen when subtracting the best fit parametric model of the outer disc. This inner component has a total flux of 0.8 and 0.3 mJy at 0.86 mm and 1.1 mm, respectively, a peak intensity that is significantly offset from the star by $0\farcs5$ (15 au), and I resolve the emission both radially and azimuthally. Its radial location indicates that it could be the same warm dust that had been inferred to be between 10-15 au to explain HD 107146's excess at 22μm. Indeed, I fit this emission with an extra inner asymmetric component finding a good match with these ALMA observations and also with HD 107146's excess at 22μm. I constrain its peak density at 19 au, and a radial width of at least 20 au. I hypothesise that this asymmetric emission could arise from a disc that is eccentric due to interactions with an eccentric inner planet, asymmetric due to a recent giant collision, or clumpy due to resonance trapping with a migrating inner planet. On the other hand, I find that this inner emission is unlikely to be a background submillimetre galaxy, as the probability of finding one as bright as 0.8 mJy at 0.86 mm within the disc inner edge (i.e. co-located with the warm dust) is 0.1%.

Finally, I search for CO and HCN gas that could be released from volatile-rich solids throughout the collisional cascade in the outer disc. However, I find no gas, but I place upper limits on the total gas mass and HCN abundance inside planetesimals, being consistent with comet-like composition.

6

Inward scattering of exocomets by a planet chain: exozodi levels, impacts and the scattered disc between the planets

6.1 Introduction

In this chapter I study how the scattering of solids (e.g. planetesimals, dust, etc) varies as a function of the architecture of a planetary system. In particular, I focus on particles on unstable orbits originating from an outer belt (e.g. an exo-Kuiper belt) that get scattered by an outer planet and can continue being scattered to the inner regions of a system by a chain of planets. I use N-body simulations to investigate:

1. whether or not exozodis can be produced by the inward scattering of material from an outer planetesimal belt, and how this ability depends on the architecture of the planetary system. There are two observational constraints that must be met, the amount of material delivered to the inner regions must be able to account for the observed excess, and the amount of material in between the outer belt and exozodi must not exceed the upper limits from observations.

2. the planetary system architectures that are best suited for delivering material to inner

planets, including volatiles locked in ices and organic material.

In §6.2 I describe the general framework of the inward transport problem, and on which aspects I will focus in this chapter. In §6.3 I summarise the key factors and considerations that can increase or reduce the inward transport of material via scattering and the number of impacts on inner planets. Then in §6.4 I describe the initial conditions of a set of N-body simulations that I use to tackle the two points above. §6.5 presents the results from the simulations. In §6.6 I discuss the observability of material being scattered between the planets using current and future instruments and implications for one known system, which systems are potentially the most optimum at producing exozodis and delivering cometary material to inner planets, and I test how a different choice of simulation parameters could affect my results. Finally, §6.7 summarises my conclusions.

6.2 Framework

The process of scattering of particles by a chain of planets that feed an exozodi can be split into three parts (see sketch in Figure 6.1):

1. Planetesimals are put on unstable orbits near the outermost planet. Planetesimals could be born there or be transported from an outer belt, e.g. via chaotic diffusion (Morbidelli, 2005). I simply assume a constant input rate $R_{\rm in}$.

2. Planetesimals are scattered by the chain of planets resulting in ejections, accretion onto planets, or inward transport.

3. The solid mass in planetesimals that gets to the inner regions where the exozodi lies, is assumed to be transformed into dust and removed. This could happen through sublimation of ices or disruption events, releasing dust as Solar System comets, or through mutual collisions in a collisional cascade.

In this chapter I focus on studying the second stage (ii). I want to test analytic predictions from previous work (see §6.3 below) and investigate further the process of scattering by multiple planets on circular orbits. I assume that particles are already on unstable orbits, or equivalently, they are input near the outermost planet at a constant rate $R_{\rm in}$ (see possible scenarios in §6.6.4). I follow the different outcomes of particles being scattered and I trace the number of particles that get ejected, accreted and that reach the exozodi region. I assume that particles are lost immediately after reaching this exozodi region (or rather on a timescale much shorter than their orbital evolution). This is the most optimistic scenario as in reality only a fraction of the mass would end up as exozodiacal dust.

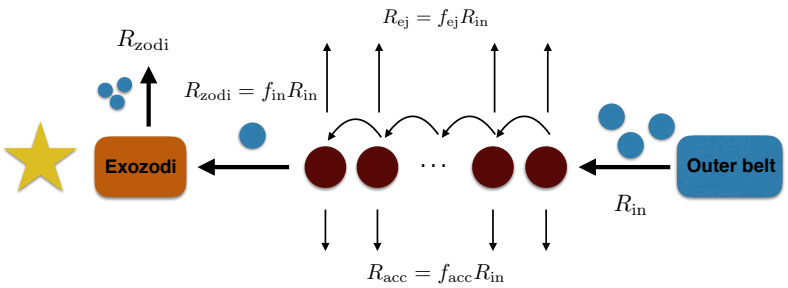

Figure 6.1: Sketch of a planetary system (planets as brown circles) scattering planetesimals (blue circles) that are input near the outermost planet at a rate $R_{\rm in}$, get ejected at a rate $R_{\rm ej}$, accreted by planets at a rate $R_{\rm acc}$ and get to the inner regions at a rate $R_{\rm zodi}$. Once in the inner regions, I assume that planetesimals are processed into small dust that is lost, e.g. via radiation pressure or P-R drag.

6.3 Scattering considerations

In this section I describe the results from previous studies that I use to make predictions regarding how the scattering process depends on the architecture of a planetary system. The basic condition for a particle to be scattered by a planet is that their orbits must cross or get sufficiently close in order to have a close encounter. For a planet on a circular orbit this translates to a condition on the planet's semi-major axis ($a_{\rm p}$) and on the semi-major axis and eccentricity of the particle (a and e, respectively), i.e.

$$a(1+e) \gtrsim a_{\rm p} - 1.5R_{\rm H} = Q_{\rm min} \text{ if } a < a_{\rm p}, \tag{6.1}$$

or

$$a(1-e) \lesssim a_{\rm p} + 1.5R_{\rm H} = q_{\rm max} \text{ if } a > a_{\rm p}, \tag{6.2}$$

where $R_{\rm H} = a_{\rm p}[M_{\rm p}/(3M_\star)]^{1/3}$ is the planet's Hill radius and $M_{\rm p}$ is the planet mass. The factor preceding $R_{\rm H}$ should be of the order of unity and is arbitrarily set to 1.5 to match the results presented below. Particles that satisfy this condition can be scattered by the planet diffusing in energy or $1/a$ (e.g., Duncan et al., 1987). Below I present the main analytic considerations and predictions from previous works that I will test with my simulations.

6.3.1 Planet spacing - multiple scattering

Particles scattered by only one planet on a circular orbit will be constrained by the Jacobi constant or Tisserand parameter ($T_{\rm p}$, Tisserand, 1896; Murray & Dermott, 1999), which is conserved in the circular restricted three-body problem when $M_{\rm p} \ll M_\star$. The Tisserand

parameter can be written as

$$T_{\rm p} = \frac{a_{\rm p}}{a} + 2\sqrt{\frac{(1-e^2)a}{a_{\rm p}}}\cos(I), \tag{6.3}$$

where I is the particle's inclination. Particles with $T_{\rm p} \lesssim 3$ can get sufficiently close to a planet (e.g. within a Hill radius) to experience a close encounter. As shown by Bonsor & Wyatt (2012), the condition for scattering together with the conservation of $T_{\rm p}$ implies that a particle being scattered by a single planet on a circular orbit will be constrained in the $a - e$ space. Specifically, given the restriction in Equation 6.1, zero inclination and assuming $2 < T_{\rm p} < 3$, there is a minimum pericentre that a particle can reach ($q_{\rm min}$) given by

$$q_{\rm min} = \frac{-a_{\rm p}Q_{\rm min}T_{\rm p}^2 + 2a_{\rm p}^2T_{\rm p} + 4Q_{\rm min}^2 - 4\sqrt{2a_{\rm p}^3Q_{\rm min} - a_{\rm p}^2Q_{\rm min}^2T_{\rm p} + Q_{\rm min}^4}}{a_{\rm p}T_{\rm p}^2 - 8Q_{\rm min}}. \tag{6.4}$$

Equation 6.4 implies that particles initially in low eccentricity orbits ($e_{\rm p} \lesssim 0.3$) cannot reach the very inner regions if their Tisserand parameter is conserved, i.e. when being scattered by a single planet.

There are multiple ways around this restriction. Particles could arrive near the scattering region of the planet with high eccentricities or inclinations, i.e. low $T_{\rm p}$, for example if originating in an exo-Oort cloud. Alternatively, the presence of additional planets could modify the initial Tisserand parameter of particles if these get scattered by multiple planets, in which case there is a constraint on the separation of the additional planets (Bonsor & Wyatt, 2012). This is the scenario considered in this chapter.

Assuming particles start with low eccentricity and inclinations near the outermost planet (which is the case for my simulations), for efficient inward scattering the next planet in the chain must have a semi-major axis larger or near $q_{\rm min,p1}$, which is the minimum pericentre that particles can reach when scattered by the outermost planet ("p1"). If not, inward scattering may still occur since particles could have their Tisserand parameter modified via secular perturbations or resonances from the additional planets, although these act on longer timescales and thus will be inefficient. Therefore, assuming particles start on orbits with low e and I, and near planet p1 ($T_{\rm p1}$ close to 3), my first consideration for a chain of planets to optimally scatter particles inwards from an outer belt, is that their two outermost planets must be in orbits near to each other. The closer they are, the higher the number of particles with $T_{\rm p1}$ small enough to reach the next planet in the chain. If particles are initially in highly eccentric or inclined orbits, e.g. Oort cloud objects, their Tisserand parameter will be low enough such that the separation between the planets is no longer a constraint.

To illustrate the scattering restriction, Figure 6.2 shows curves of constant Tisserand parameter

(solid lines) as a function of semi-major axis and eccentricity with respect to two 30 $M_\oplus$ planets on circular orbits with $a_p = 20, 50$ au (orange and blue, respectively). Assuming particles in the system are initially in the vicinity of the outermost planet (denoted as p1), their final outcome will depend on their initial Tisserand parameter with respect to p1. For example, $T_{p1} \gtrsim 3.0$ particles will form a scattered disc constrained within $a_p = 35 - 80$ au and since particles with eccentricities lower than 0.4 will never have a close encounter with the second planet (p2), these will not make it to the inner regions. Otherwise, $T_{p1} \lesssim 2.97$ particles can reach a pericentre near 20 au and be scattered by p2 (which then changes their T_{p1}). Multiple scattering can put particles on highly eccentric orbits that can reach the inner regions (in grey for those reaching with a pericentre smaller than 1 au), or get eventually ejected from the system. This condition is met in the Solar System, where Uranus is close enough to Neptune such that particles in the Kuiper belt with $T_{Nep} < 2.999$ can be scattered by Uranus after a few encounters with Neptune (e.g., Levison & Duncan, 1997). Additional planets could be present closer in which could help to increase the inward flux of scattered particles.

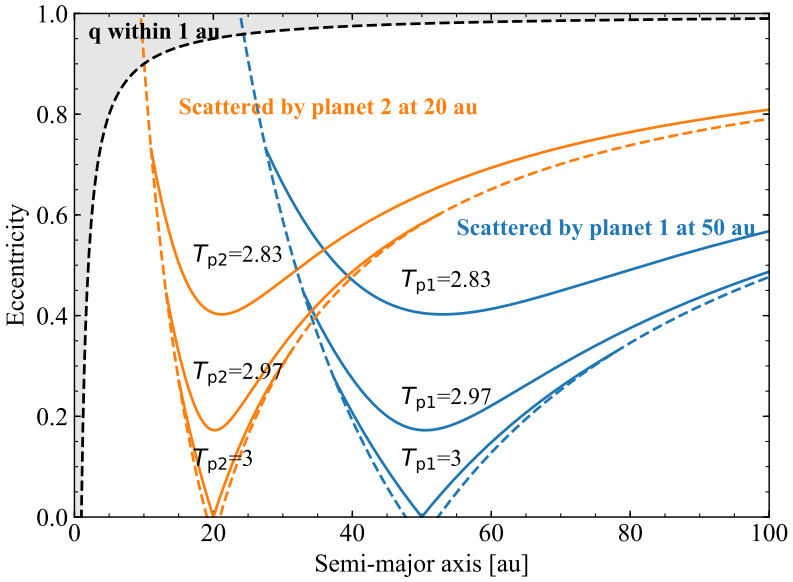

Figure 6.2: Constant Tisserand parameter curves and scattering regions for two 30 $M_\oplus$ planets in circular orbits and with semi-major axes of 50 (i, blue) and 20 au (ii, orange). The dashed lines correspond to the scattering regions, i.e. orbits crossing $a_p \pm 1.5R_H$. The continuous lines represent curves of constant Tisserand parameter with respect to planets i and ii, and assuming $I = 0$. The black dashed line shows the semi-major axes and eccentricities of particles that have a pericentre of 1 au.

6.3.2 Planet masses - timescales

The second consideration relates the mass distribution of planets as a function of semi-major axis. As stated by Wyatt et al. (2017), particles will be passed inwards more efficiently when

interior planets start dominating the scattering process, i.e. when the scattering timescale is shorter for interior planets. The scattering timescale can be approximated by the cometary diffusion time (Brasser et al., 2008)

$$t_{\rm scat} \cong \left(\frac{a_{\rm p}}{1\ {\rm au}}\right)^{3/2} \left(\frac{M_{\rm p}}{1\ {\rm M}_{\oplus}}\right)^{-2} \left(\frac{M_{\star}}{1\ {\rm M}_{\odot}}\right)^{3/2} {\rm Gyr}. \tag{6.5}$$

Since these timescales increase with orbital radius and decrease with planet mass, chains of planets with equal mass or decreasing as a function of orbital radius should be more efficient at passing particles inwards.

Because in this chapter I assume that particles are born near the outermost planet in the chain, it is the mass of the outermost planet that will determine the timescale and rate at which particles are scattered in (Bonsor et al., 2012). If this scattering timescale is longer or of the order of the age of a system, then planet scattering can sustain an exozodi at the current age of the system relying solely on planetesimals formed in its vicinity. Otherwise, the exozodi fed by scattered primordial particles would only last a fraction of the age of a system. Therefore, in order to sustain high exozodiacal dust levels for 0.1-1 Gyr from planetesimals born near the outermost planet, a massive outer belt and a chain of tightly packed low mass planets are required.

Similarly, using analytical arguments Wyatt et al. (2017) considered that in order to maximise the inward flux in a system at a given age, no planets should lie in the *ejected* region in the $a_{\rm p} - M_{\rm p}$ space. In this region planets can eject particles on a timescale (approximated by the cometary diffusion timescales) shorter than the age of the system, and thus might never get to the inner regions before being ejected, or if they do, they will be quickly removed. However, the effect of a complex multi-planet system on this simple argument has to be investigated.

An important caveat in the arguments above is that planetesimals are assumed to be born near the outermost planet. The scenario that I am considering in this chapter is that particles are continually input near the outermost planet. This means that both of the above constraints are relaxed (i.e. the scattering timescale for the outermost planet, and those closer in, can potentially be shorter than the system age and still result in material reaching the inner regions at a given age. However, for planets that are very low in mass, the orbits of particles will still evolve on timescales much longer than the age of the system, thus, being unable to scatter particles in at a high rate and setting a lower limit on the mass of the outermost planet. For example, particles scattered by a 5 $\rm M_{\oplus}$ planet at 50 au will evolve on timescales of ~ 10 Gyr.

To conclude, I expect that the best systems for scattering particles inwards from an outer belt should be the ones with equal mass planets or decreasing mass with orbital radius.

6.3.3 Planet masses and relative velocities - accretion

The third consideration relates to the possibility of particles being accreted by planets, possibly delivering volatiles to the inner planets. To quantify the number of particles that will be accreted by a planet, or the rate at which they will, it is necessary to consider the mass and radius of the planet (which define its collisional cross-section), the volume density of particles that the planet encounters, and the encounter velocities. If the system is continually fed from particles starting in the outer regions (the scenario that we are considering here), these will then form what I will call a *scattered disc*, with a density of particles that will reach a steady state. This density represents the amount of material that can potentially be accreted at any given time and orbital radius. It will depend both on the amount of material that is passed in from the outermost planet to the inner regions, and on its lifetime before being lost, e.g. via ejection or onto the rest of the planets in the system. The rate at which a planet accretes can be approximated as

$$R_{\rm acc,p} = \frac{v_{\rm rel}\Gamma\Sigma(r)}{h}, \tag{6.6}$$

where Γ, $\Sigma(r)$, $v_{\rm rel}$ and h are the collisional cross-section of the planet, the steady state surface density of particles (number per unit area), the relative velocity between a planet and particles, and the scale height of the scattered disc, respectively. The latter can be approximated by the product of r and the average inclination $< I >$ of the particles orbits. Both $\Sigma(r)$ and h are determined by the specific architecture of the planetary system. For example, particles being scattered by low mass planets are likely to survive for longer timescales against ejection, increasing $\Sigma(r)$. The collisional-cross section is defined by the mass and radius of the planet, together with the relative velocities, as

$$\Gamma = \pi R_{\rm p}^2 \left(1 + \frac{v_{\rm esc}^2}{v_{\rm rel}^2}\right), \tag{6.7}$$

where $R_{\rm p}$, $v_{\rm esc}$ and $v_{\rm rel}$ are the radius of the planet, its escape velocity, and relative velocity before the encounter, respectively. The higher Γ is, the higher the rate of impacts on that planet (Equation 6.6). For $v_{\rm esc} \gg v_{\rm rel}$ and $M_{\rm p} \propto R_{\rm p}^3$ (i.e. fixed density) I find $\Gamma \propto M_{\rm p}^{4/3}$, otherwise $\Gamma \propto M_{\rm p}^{2/3}$. Therefore, $R_{\rm acc,p}$ will be greater for more massive planets, as these have greater radii and escape velocities (i.e. greater Γ), lower relative velocities (greater Γ and lower h), and higher surface densities.

However, it is unclear how the mass distribution of planets will also affect the density of particles (determined by the inward scattering and particles lifetimes) and their relative velocities (mainly defined by the distribution of eccentricities and inclinations). I can guess that chains of more massive planets will result in lower $\Sigma(r)$ and higher relative velocities because particles are easily put on highly eccentric/inclined orbits. As shown by Wyatt et al.

(2017), the most likely outcome of particles being scattered by a planet can be understood by comparing the planet's Keplerian velocity ($v_{\rm k}$) with its escape velocity $v_{\rm esc}$. This is because the maximum kick that a particle can experience after a single scattering event is of the order of $v_{\rm esc}$, since to get a larger kick it would have to come so close that it would hit the planet. Therefore, if $v_{\rm esc} \gg v_{\rm k}$ particles are likely to be ejected in a few close encounters, decreasing the surface density of the scattered disc. Otherwise particles would need a large number of encounters before being ejected, increasing the surface density of the scattered disc and the likelihood of being accreted by a planet. Equating $v_{\rm esc}$ and $v_{\rm k}$ I find (equation 1 in Wyatt et al., 2017)

$$M_{\rm p} \cong 40 \left(\frac{a_{\rm p}}{1\ {\rm au}}\right)^{-3/2} \left(\frac{\rho_{\rm p}}{1\ {\rm g\ cm^{-3}}}\right)^{-1/2} \left(\frac{M_\star}{1\ {\rm M_\odot}}\right)^{3/2} {\rm M_\oplus}, \tag{6.8}$$

where $\rho_{\rm p}$ is the bulk density of the planet. Planets below this mass are likely to accrete particles if these are not lost on shorter timescales via other means.

6.3.4 Predictions

To summarise, assuming particles are input at a constant rate in the vicinity of the outermost planet, I predict the following based on previous studies:

1. Systems with outer planets close to each other will be better at scattering particles inwards as more particles will have a low enough Tisserand parameter to reach the second outermost planet (Equation 6.4).

2. Higher mass planets will scatter and eject particles on shorter timescales (Equation 6.5) and could result in inefficient inward scattering.

3. In order to scatter particles inwards, scattering timescales of the inner planets must be shorter than those further out, as shown by Equation 6.5. These can be achieved by planet chains of equal mass or decreasing mass with orbital radius.

4. Planets will accrete more particles if they are more massive, if the surface density of particles around their orbits is higher and if particles are on low eccentricity and low inclination orbits, i.e. low relative velocities (Equations 6.6 and 6.7).

There is no analytic prediction for how the surface density will change when varying the planet masses as it depends both on the scattering timescale and on the inward flux of material. Moreover, the inward flux, distribution of eccentricities and inclinations, and accretion onto planets could vary as a function of the spacing between the planets. N-body simulations are well suited to study these effects and test the predictions above.

6.4 N-body Simulations

In order to test my predictions presented above, and quantify how the mass distribution and orbit spacing of a chain of planets affects the inward transport of particles being scattered, I simulate such interactions using N-body simulations. I model the gravitational interactions with the N-body integrator MERCURY 6.2 (Chambers, 1999), using the hybrid symplectic/Bulirsch-Stoer integration algorithm. This allows us to speed up the simulations computing distant interactions quickly, without losing precision in close encounters. The systems are composed of a 1 $M_\odot$ star, a chain of planets and 10^3 massless particles. The simulations lasted 1 Gyr, long enough such that the majority of the particles are lost via ejections and accretion onto the star or planets. Outputs or snapshots of the simulations are saved every 10^4 or 10^5 yr, that I estimate is shorter than the scattering diffusion timescale for most of my simulations (see §6.4.1 below). I set an outer boundary of 10^3 au and an inner boundary of 0.5 au, i.e particles are removed from the simulation when their apocentre is larger than 10^3 au or their pericentre is lower than 0.5 au. The latter is set to trace the number of particles that are able to reach the innermost regions that I am interested in, and also because the time-step of 30 days is not small enough to accurately integrate the orbits within this boundary. This assumes that particles are lost as soon as they reach this boundary by being incorporated into the exozodi. Each simulation is run 20 independent times with random mean anomalies, longitudes of ascending node and pericentres, and splitting the total number of massless particles (50 test particles for each).

6.4.1 Planet mass and semi-major axis distribution

I consider a chain of planets on circular co-planar orbits, with masses varying from 1 to 200 $M_\oplus$ (0.63 $M_{\rm Jup}$) and semi-major axes between 1 and 50 au. I assume uniform planet densities of 1.6 g cm^{-3} (Neptune's density). As I am interested in studying how the scattering process depends on the mass distribution and spacing of planets, I parametrise their masses as a function of $a_{\rm p}$; and their spacings or separations as a function of $a_{\rm p}$ and their mutual Hill radius ($R_{\rm H,m}$). More specifically, I define

$$M_{\rm p}(a_{\rm p}) = M_0 \left(\frac{a_{\rm p}}{a_0}\right)^{\alpha_{\rm M}}, \tag{6.9}$$

where M_0, a_0 and $\alpha_{\rm M}$ define the planet masses in the chain. The semi-major axis of the planets is defined such that $a_{\rm p} = 50$ au for the outermost planet and the separation between their orbits

is

$$\Delta a = K(a_{\rm p1}, a_{\rm p2}) R_{\rm H,m}, \tag{6.10}$$

$$K(a_{\rm p1}, a_{\rm p2}) = K_0 \left(\frac{a_{\rm p1} + a_{\rm p2}}{2a_0} \right)^{\alpha_\Delta}, \tag{6.11}$$

where K_0 and α_Δ control the separation of the planets and their long-term stability. I add planets in the system from 50 to 1 au using Equations 6.9 and 6.11. The initial mean anomaly of every planet is chosen randomly such that each simulated system is run on 20 slightly different configurations.

The reference chain of planets has $M_0 = 30$ M$_\oplus$, $a_0 = 10$ au, $\alpha_{\rm M} = 0$, $\alpha_\Delta = 0$ and K_0=20. This defines a reference to which I compare when varying the different parameters. I vary M_0 between 10 and 90 M$_\oplus$ to study chains of low and high mass planets, $\alpha_{\rm M}$ between -1 and 1 to study the effect of decreasing or increasing planet mass as a function of $a_{\rm p}$, $\alpha_\Delta = 0.3$ and -0.3 (such that no pair of planets is closer than 10 $R_{\rm H,m}$) to study the effect of planet spacing varying with $a_{\rm p}$, and K_0 between 8 and 30 to study the differences between tightly packed systems and widely spaced. The range of spacings is inspired by the spacing distribution found for *Kepler* close in multi-planet systems, where spacings between 10-30 mutual Hill radii are the most common (Fang & Margot, 2013; Pu & Wu, 2015; Weiss et al., 2018), although this is uncertain for planets at large orbital radii. In addition, if $K < 10$ the system could go unstable on a timescale shorter than 1 Gyr (Chambers et al., 1996; Smith & Lissauer, 2009). Table 6.1 and Figure 6.3 summarises the 10 main planet configurations that I explore. In the same figure, the dashed black lines represent the mass above which planets are more likely to eject particles rather than accrete (Equation 6.8), while the continuous black lines represent the scattering diffusion timescale or the planet masses above which particles are ejected on a timescale shorter than 1 Gyr, 10 Myr and 100 kyr (Equation 6.5). In all the configurations there are planets that will eject particles on timescales shorter than or of the order of 1 Gyr, the length of the simulations.

6.4.2 Massless particles distribution

Particles are initially distributed in a cold disc, with eccentricities and inclinations uniformly distributed between $0 - 0.02$ and $0 - 10°$, respectively. [1]. As I am interested only in those particles that can be scattered, I initialise all of them in the outermost planet's chaotic zone, i.e. the unstable region of semi-major axes surrounding the planet in which mean motion resonances overlap. The size of the chaotic zone has been analytically estimated to be (Wisdom, 1980)

$$\delta_{\rm chaos} = 1.3\, a_{\rm p} \left(\frac{M_{\rm p}}{M_\star} \right)^{2/7}. \tag{6.12}$$

[1] Note that this choice is arbitrary and its effect is discussed in §6.6.5

Table 6.1: Setups of the different N-body simulations varying M_0 (planet mass at 10 au), $\alpha_{\rm M}$ (planet mass semi-major axis dependence), K_0 (planet spacing at 10 au in mutual Hill radii) and α_{Δ} (planet spacing semi-major axis dependence). $\rm N_p$ is the number of planets in each simulated system.

Number	Label	Colour	$\alpha_{\rm M}$	α_{Δ}	Masses [$\rm M_{\oplus}$]	$a_{\rm p}$ [au]	$\Delta a/R_{\rm H,m}$	$\rm N_p$
0	single planet	black			30	50.0		1
1	reference	dark blue	0.0	0.0	30	(1.8, 4.2, 9.6, 21.9, 50.0)	20	5
2	incr M	orange	1.0	0.0	(4, 6, 10, 18, 40, 150)	(1.2, 1.9, 3.2, 5.9, 13.5, 50.0)	20	6
3	decr M	green	-1.0	0.0	(180, 44, 19, 10, 6)	(1.7, 6.8, 15.8, 29.9, 50.0)	20	5
4	incr K	red	0.0	0.3	30	(1.2, 1.9, 3.2, 6.2, 14.3, 50.0)	(11, 13, 16, 20, 28)	6
5	decr K	purple	0.0	-0.3	30	(2.4, 7.1, 15.6, 29.4, 50.0)	(25, 19, 16, 13)	5
6	high M	brown	0.0	0.0	90	(1.1, 3.9, 13.9, 50.0)	20	4
7	low M	pink	0.0	0.0	10	(1.0, 1.8, 3.1, 5.4, 9.4, 16.4, 28.7, 50.0)	20	8
8	high K	yellow	0.0	0.0	30	(3.4, 13.0, 50.0)	30	3
9	low K	light blue	0.0	0.0	30	(1.1, 1.8, 2.8, 4.6, 7.4, 11.9, 19.2, 31.0, 50.0)	12	9
10	low M - low K	grey	0.0	0.0	10	(1.3, 1.9, 2.6, 3.6, 5.0, 7.0, 9.7, 13.4, 18.7, 25.9, 36.0, 50.0)	12	12
11	very low K	light blue	0.0	0.0	30	(1.1, 1.6, 2.1, 2.9, 4.0, 5.5, 7.5, 10.3, 14.1, 19.4, 26.6, 36.5, 50.0)	8	13

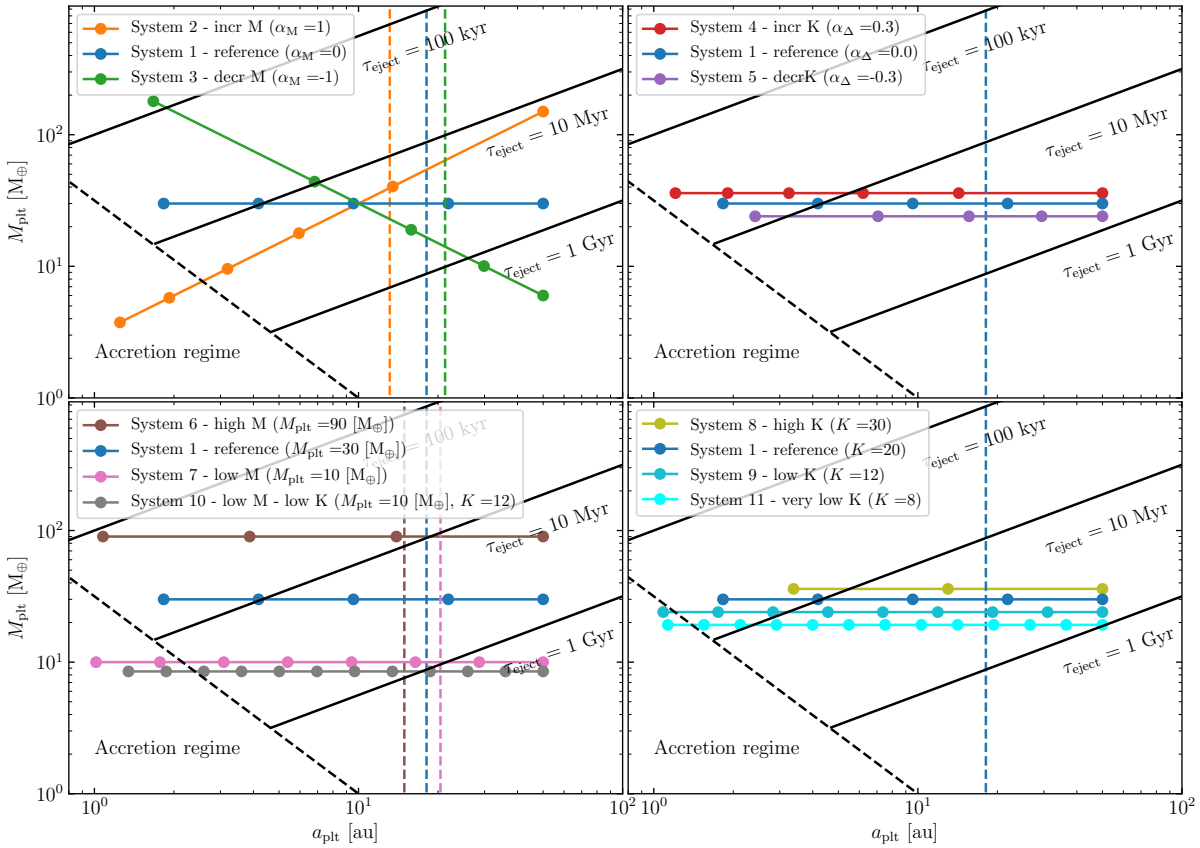

Figure 6.3: Masses and semi-major axes of planets in each simulated system. ***Upper left panel***: chains of planets with varying α_M. ***Upper right panel***: chains of planets with varying α_Δ (the mass of the planets is offset for display). ***Lower left panel***: chains of equal mass planets of 10, 30 and 90 $M_\oplus$ and separations of 20 or 12 mutual Hill radii. ***Lower right panel***: chains of equal mass planets with K_0 =12, 20 and 30. The dots represent the position of the planets. The vertical dashed lines represent the minimum pericenter of particles scattered by the outermost planet given their initial Tisserand parameter (Equation 6.4). The dashed black lines represent the mass above which planets are more likely to eject particles rather than accrete (Equation 6.8). The continuous lines represent the planet mass above which particles are ejected on a timescale shorter than 1 Gyr, 10 Myr and 100 kyr (Equation 6.5). Planet masses of systems 4, 5, 8, 9 and 10 have been scaled by 20% and 36% for a better display.

Within this zone, eccentricities are excited and initially non-crossing orbits start to cross the planet's orbit, or get sufficiently close to have close encounters and be scattered by the planet. I initialise all the particles with semi-major axes (a_p) uniformly distributed within $a^i_{plt} \pm \delta_{chaos}$ ($\sim 45 - 55$ au for a 30 $M_\oplus$ planet at 50 au). This ensures that particles will be dynamically excited and likely to be scattered early on during the simulation.

The initial distribution of orbital parameters sets the range of Tisserand parameters that the particles have with respect to the outermost planet (p1). For a 30 $M_\oplus$ planet, T_{p1} is initially distributed between 2.97 and 3.01 (in §6.6.5 I discuss the effect of varying the initial e and i). The minimum T_{p1} is the same for all the simulations as it is set approximately by the particles with semi-major axis equal to that of the planet (if e and I are small). On the other hand, the

maximum $T_{\rm p1}$ is set by particles at the inner and outer edge of the chaotic zone whose size increases with planet mass, therefore the maximum $T_{\rm p1}$ is higher for more massive planets and scales approximately as $3 + 5(M_{\rm p}/M_{\star})^{4/7}/4$. As explained in §6.3, the minimum Tisserand parameter sets the minimum pericentre ($q_{\rm min,p1}$) that scattered particles can have after multiple scattering events by the outermost planet, and thus, if they can be readily scattered by the second outermost planet. The latter enables the further inward scattering that I am interested in.

In Figure 6.3 I show $q_{\rm min,p1}$ (vertical dashed lines) as a reference to identify those configurations that I expect not to be optimal for inward scattering, i.e. those systems in which the second outermost planet has semi-major axis lower than the minimum pericentre of particles when interacting only with the outermost planet. This pericentre is calculated using Equation 6.4 and setting $a_{\rm p} = a_{\rm p1}$, $Q_{\rm min} = a_{\rm p1} - 1.5R_{\rm H}$ and $T_{\rm p} = \min(T_{\rm p1})$, where the minimum Tisserand parameter is approximately 2.97 given my initial conditions. For low planet masses and $T_{\rm p1} = 2.97$ I find $q_{\rm min,p1} \approx a_{\rm p1}/2 - 9R_{\rm H}/2$, thus lower for higher planet masses. I anticipate that planet configurations 4 and 8 from Table 6.1 (red and light green in Figure 6.3) will be inefficient at inward scattering because their outermost planets are too separated under this criterion.

While my simulations assume that particles start near the outermost planet on low eccentricity and inclination orbits, the exact distribution of eccentricities and inclinations would depend on the specific mechanism that is inputting particles near the outermost planet. Hence, a caveat in what follows is that I am assuming that the particles' initial conditions described above are a good approximation to their orbits at the start of the scattering process. The specific mechanism inputting particles and initial conditions are discussed in §6.6.4 and 6.6.5.

6.4.3 Analysis of simulations

For each simulation, I first remove those particles that were initially in stable tadpole and horseshoe orbits (hereafter called Trojans, $N_{\rm Troj}$). I identify Trojan particles as the ones that after 1 Myr of evolution lie within 1.2 Hill radii from the outermost planet and with an eccentricity lower than 0.03 (typically $20 - 30\%$ of simulated particles). Then we follow the evolution of the rest of the particles (a total number $N_{\rm tot}$) and trace the number of particles ejected ($N_{\rm ej}$), that cross the inner boundary at 0.5 au ($N_{\rm in}$), and that were accreted by planets ($N_{\rm acc}$). I compare these between the different simulations by dividing by the total number of particles that are lost during 1 Gyr of evolution ($N_{\rm lost} = N_{\rm ej} + N_{\rm in} + N_{\rm acc}$). I divide by $N_{\rm lost}$ rather than by $N_{\rm tot}$ (the total number of simulated particles) because the timescales at which particles evolve in some of the simulated systems are comparable to 1 Gyr, hence a significant number of particles have not been lost by the end of the simulation. These particles (a total of $N_{\rm tot} - N_{\rm lost}$) remain in the system in highly eccentric and inclined orbits (i.e. in the scattered

disc). Hence, I compare the fraction of particles ejected ($f_{\rm ej} = N_{\rm ej}/N_{\rm lost}$), that cross the inner boundary ($f_{\rm in} = N_{\rm in}/N_{\rm lost}$) and that are accreted by planets ($f_{\rm acc} = N_{\rm acc}/N_{\rm lost}$). I also compute the fraction of particles accreted per inner planet ($f_{\rm acc,p}$), defined as those with $a_{\rm p} < 10$ au. Comparing these relative fractions is equivalent to extrapolating to $t = \infty$ assuming that the remaining particles will be lost via ejection, accretion, or crossing the inner edge in the same proportions as the particles that are lost by 1 Gyr, i.e. this is equivalent to assuming that $f_{\rm ej}$, $f_{\rm in}$, $f_{\rm acc}$ stay constant over time. This is not necessarily the case as most of the particles remaining are typically in an outer scattered disc with large semi-major axes, where they could be more likely to be ejected than when they started near the outermost planet. However, this helps to give an idea of the absolute fractions if simulations were run for longer and is shown to be representative in one of the simulations (the one with lowest mass planets) that was run for 5 Gyr in §6.6.5. I also report uncertainties on $f_{\rm ej}$, $f_{\rm in}$, $f_{\rm acc}$, etc. based on 68% Poisson confidence intervals (16th and 84th percentiles) using analytic approximations from Gehrels (1986).

In order to quantify how fast particles are lost I also compute the half-life of ejected particles, $t_{\rm ej}$. This is defined as the time it takes to eject half of the total number of particles expected to be ejected by $t = \infty$, assuming $N_{\rm ej}$ will tend to $f_{\rm ej}N_{\rm tot}$ by the end of the simulation (i.e. assuming that $f_{\rm ej}$ is constant over time).

I am also interested in the spatial distribution or surface density distribution of scattered particles within the chain of planets, i.e from 1 to 50 au. Because the distribution of particles evolves with time (see §6.5.1 and 6.5.2) and on different timescales for each planet configuration, I focus on the steady state surface density of scattered particles, $\Sigma(r)$. This assumes that particles are input in the system at a constant rate inside the chaotic zone of the outermost planet. In order to use the simulation results to mimic a steady-state input scenario, I take each particle and randomise its initial epoch (originally t=0) to a value between 0 and 1 Gyr. Once a Gyr is reached (the initial integration time), I loop the particle's later evolution to $t = 0$. In order to minimise random effects caused by the finite number of particles used in these simulations (~ 700 excluding Trojans), I effectively mimic each particle 200 times by randomising in terms of mean anomaly at each time step. This leads to an effective ∼140,000 particles used to calculate the surface density distribution at each epoch. I then average the surface density over time to obtain the average steady state surface density distribution $\Sigma(r)$. I estimate the uncertainty on $\Sigma(r)$ by computing the variance of $\Sigma(r, t)$ averaged over 100 Myr time bins (i.e. from 10 data points at each orbital radius). Finally, because $\Sigma(r)$ is proportional to the mass input rate (the same for all the simulations), in my analysis I compare $\Sigma(r)$ divided by the mass input rate. Then the surface density can be obtained by multiplying by any mass input rate. Below, I will also use the surface density at 10 au, $\Sigma(10\ {\rm au})$, as a metric to compare different systems.

6.5 Results

In this section I present the main results from each simulation. I first describe the results of a case with a single 30 $M_\oplus$ planet at 50 au (§6.5.1) and my reference chain of equal mass planets (§6.5.2). Then, I present results for planet configurations of equal mass planets, but varying their spacing (§6.5.3), and configurations with constant spacing in mutual Hill radii, but varying their masses (§6.5.4). In §6.5.5 I discuss my results in the context of the predictions made in Sec 6.3.

6.5.1 Single planet system

In the single planet system I find that of the total number of particles lost, 85% of particles are ejected, 15% are accreted by the planet and none cross the 0.5 au inner edge. The ejection timescale is 380 Myr, consistent with the 390 Myr scattering timescale estimated with Equation 6.5. After 1 Gyr of evolution, 17% of particles remain in the system on highly eccentric orbits, most of which have semi-major axes beyond 50 au. The top panel in Figure 6.4 shows the evolution of the surface density of particles when they all start near the outermost planet at $t = 0$ (colours) and the steady state surface density when particles are input at a constant rate (black). In all cases the surface density peaks near 50 au (where particles are initially placed). Beyond 50 au, $\Sigma(r)$ decreases steeply with orbital radius $\propto r^{-\gamma}$, where γ is about -3 as expected for a scattered disc population with a common pericentre (Duncan et al., 1987). Within 50 au $\Sigma(r)$ decreases towards smaller orbital radii, but with a sharp edge at 18 au, which is the location of $q_{\rm min,p1}$, expected since no particles should be scattered interior to this.

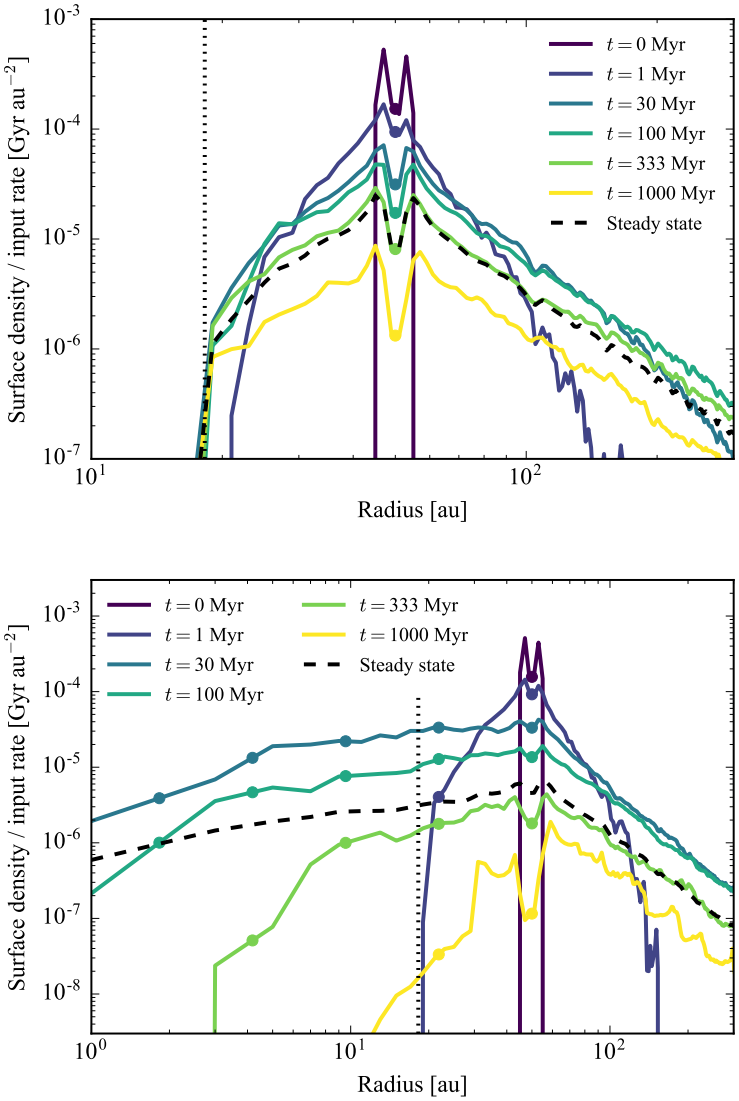

Figure 6.4: Surface density of particles as a function of time (colours) for the scenario in which particles start at $t = 0$ in the chaotic zone of a planet at 50 au in the single planet case (top) and in the reference multi-planet system (bottom). The black dashed line represents the steady state surface density when particles are input in the system at a constant rate in the chaotic zone of the outermost planet. The radial location of the dots corresponds to the semi-major axis of each planet. The black dotted vertical line represents $q_{\mathrm{min,p1}}$. At $t = 0$ the distribution of particles is double peaked near 50 au because particles that stayed as Trojans are removed. Note that the x-axis in the lower panel extends further in than in the upper panel.

6.5.2 Reference system

When considering the reference chain of equal mass 30 $M_\oplus$ planets separated by 20 mutual Hill radii, I find that the fraction of particles that are ejected increases relative to the single planet case from 85 to 93%, with a shorter ejection timescale of 120 Myr (compared with 380 Myr in the single planet case). The shorter ejection timescale is due to multiple scattering

with interior planets as well as the outermost planet, which makes particles evolve faster onto unbound orbits. After 1 Gyr of evolution, only 5% remain in the system, most of which are in a scattered disc beyond 50 au (see yellow line on the bottom panel of Figure 6.4). As predicted, the presence of multiple planets makes it easier for particles to be scattered inwards, and the fraction of particles that cross 0.5 au increases from $< 0.65\%$ to $3.7^{+0.9}_{-0.7}\%$. On the other hand, the fraction of particles that are accreted by planets decreases relative to the single planet case from 15% to 3.6% (0.4% by inner planets). This is because particles are scattered by multiple planets, thus increasing the level of stirring and reducing the number of close encounters that they have with the outermost planet (e.g. the steady state surface density near the outermost planet is lower by a factor of 2 in the reference system). Table 6.2 summarises the results for each of the planetary configurations.

The bottom panel of Figure 6.4 shows the evolution of $\Sigma(r, t)$ and its steady state form when particles are input at a constant rate. Beyond 50 au, the system has a surface density similar to the single planet case, but within 50 au it is flatter and extends within $q_{\rm min,p1}$ as particles are scattered by inner planets. Within 10 au, $\Sigma(r)$ approximates to a power law with a slope of ~ 0.7, which flattens out towards 50 au. This slope is overall steeper compared to the surface density expected in a P-R drag scenario (van Lieshout et al., 2014; Kennedy & Piette, 2015), thus if material was detected between an outer belt and exozodi, the slope could be used to discern between scattering and P-R drag scenarios. Note that the surface density within a few au could be underestimated due to the boundary condition at 0.5 au. Particles within a few au are likely to be highly eccentric after being scattered multiple times, with pericentres that could reach 0.5 au, and thus, be removed from the simulation. This is investigated further in §6.6.5 decreasing the inner boundary to 0.1 au. The short lifetime of particles in the system with multiple planets is also manifested in the surface density at $t = 1$ Gyr that is significantly lower compared to the single planet system. Note that whereas Figure 6.4 shows the evolution of the surface density, future figures will only show the steady state surface density.

6.5.3 Varying $K(a)$

Here I present results from four simulations of equal mass planets (30 $M_\oplus$), but with different spacing, measured with the number of mutual Hill radii (K) between adjacent planets. These are planet configurations 4, 5, 8, 9 and 11, for which α_Δ and K_0 vary (see Figure 6.3 upper and lower right panels). I also include results from the reference and single planet system for comparison. Figure 6.5 presents the results for $\Sigma(r)$, $f_{\rm ej}$, $t_{\rm ej}$, $f_{\rm in}$ and $f_{\rm acc,p}$.

Table 6.2: Results for each of the different planetary configurations. All the fractions are with respect to the total number of particles lost after 1 Gyr of simulation. The fraction of trojans is computed with respect to the total number of particles (1000). The uncertainties are estimated based on 68% confidence intervals and assuming a Poisson distribution. The upper limits correspond to 2σ (95% confidence upper limit).

Number	Label	Colour	$f_{\rm ej}$ (%)	$f_{\rm in}$ (%)	$f_{\rm acc}$ (%)	$f_{\rm acc,p}$ (%)	Fraction accreted per planet (%)	Fraction remaining after 1 Gyr (%)	Absolute fraction of Trojans (%)	$t_{\rm ej}$ [Myr]
0	single planet	black	$85.0^{+4.0}_{-3.9}$	¡0.65	$15.0^{+1.8}_{-1.6}$	-	(15.0)	$17.0^{+1.7}_{-1.6}$	$31.1^{+1.9}_{-1.8}$	383±21.9
1	reference	blue	$92.7^{+3.9}_{-3.7}$	$3.7^{+0.9}_{-0.7}$	$3.6^{+0.9}_{-0.7}$	$0.35^{+0.20}_{-0.13}$	(0.3, 0.4, 0.3, 0.1, 2.4)	$4.8^{+1.0}_{-0.8}$	$29.5^{+1.8}_{-1.7}$	120±7.1
2	incr M	orange	$95.1^{+3.7}_{-3.5}$	$2.9^{+0.8}_{-0.6}$	$2.0^{+0.7}_{-0.5}$	¡0.15	(0.0, 0.0, 0.0, 0.0, 0.1, 1.8)	$0.4^{+0.4}_{-0.2}$	$23.8^{+1.6}_{-1.5}$	12±0.8
3	decr M	green	$92.3^{+4.4}_{-4.2}$	$3.1^{+1.0}_{-0.8}$	$4.6^{+1.2}_{-0.9}$	$1.06^{+0.44}_{-0.31}$	(0.8, 1.3, 1.2, 0.4, 1.0)	$27.7^{+2.1}_{-2.0}$	$28.2^{+1.8}_{-1.7}$	350±29.3
4	incr K	red	$89.0^{+4.0}_{-3.8}$	$2.3^{+0.8}_{-0.6}$	$8.7^{+1.4}_{-1.2}$	$0.04^{+0.12}_{-0.03}$	(0.0, 0.0, 0.2, 0.0, 0.3, 8.3)	$11.2^{+1.4}_{-1.3}$	$30.4^{+1.8}_{-1.7}$	340±16.8
5	decr K	purple	$94.7^{+3.9}_{-3.7}$	$3.1^{+0.8}_{-0.7}$	$2.2^{+0.7}_{-0.6}$	$0.29^{+0.25}_{-0.14}$	(0.3, 0.3, 0.3, 0.3, 1.0)	$1.4^{+0.6}_{-0.4}$	$30.5^{+1.9}_{-1.7}$	79±5.8
6	high M	brown	$94.8^{+3.7}_{-3.6}$	$1.9^{+0.7}_{-0.5}$	$3.3^{+0.8}_{-0.7}$	$0.07^{+0.21}_{-0.06}$	(0.1, 0.0, 0.1, 3.0)	$0.4^{+0.4}_{-0.2}$	$26.6^{+1.7}_{-1.6}$	28±1.3
7	low M	pink	$89.7^{+4.5}_{-4.3}$	$4.5^{+1.2}_{-1.0}$	$5.8^{+1.3}_{-1.1}$	$0.45^{+0.19}_{-0.13}$	(0.4, 0.4, 0.4, 0.8, 0.2, 0.6, 0.8, 2.1)	$30.4^{+2.2}_{-2.1}$	$30.5^{+1.9}_{-1.7}$	583±36.2
8	high K	yellow	$86.9^{+4.0}_{-3.8}$	$1.4^{+0.7}_{-0.5}$	$11.7^{+1.6}_{-1.4}$	¡0.65	(0.0, 0.0, 11.7)	$15.2^{+1.6}_{-1.5}$	$30.4^{+1.8}_{-1.7}$	404±22.0
9	low K	light blue	$93.7^{+3.7}_{-3.6}$	$4.8^{+1.0}_{-0.8}$	$1.5^{+0.6}_{-0.4}$	$0.19^{+0.11}_{-0.07}$	(0.3, 0.4, 0.1, 0.0, 0.1, 0.1, 0.4, 0.0, 0.0)	$1.5^{+0.6}_{-0.4}$	$26.2^{+1.7}_{-1.6}$	62±4.2
10	low M - low K	grey	$90.6^{+4.1}_{-3.9}$	$7.3^{+1.3}_{-1.1}$	$2.0^{+0.8}_{-0.6}$	$0.12^{+0.09}_{-0.05}$	(0.0, 0.0, 0.2, 0.0, 0.3, 0.2, 0.2, 0.2, 0.0, 0.2, 0.3, 0.5)	$14.4^{+1.6}_{-1.4}$	$31.4^{+1.9}_{-1.8}$	284±19.4
11	very low K	light blue	$91.9^{+3.7}_{-3.6}$	$6.7^{+1.1}_{-1.0}$	$1.4^{+0.6}_{-0.4}$	$0.02^{+0.06}_{-0.02}$	(0.0, 0.0, 0.0, 0.0, 0.1, 0.0, 0.0, 0.0, 0.1, 0.1, 0.1, 0.4, 0.4)	$0.4^{+0.5}_{-0.2}$	$28.1^{+1.8}_{-1.7}$	40±2.5

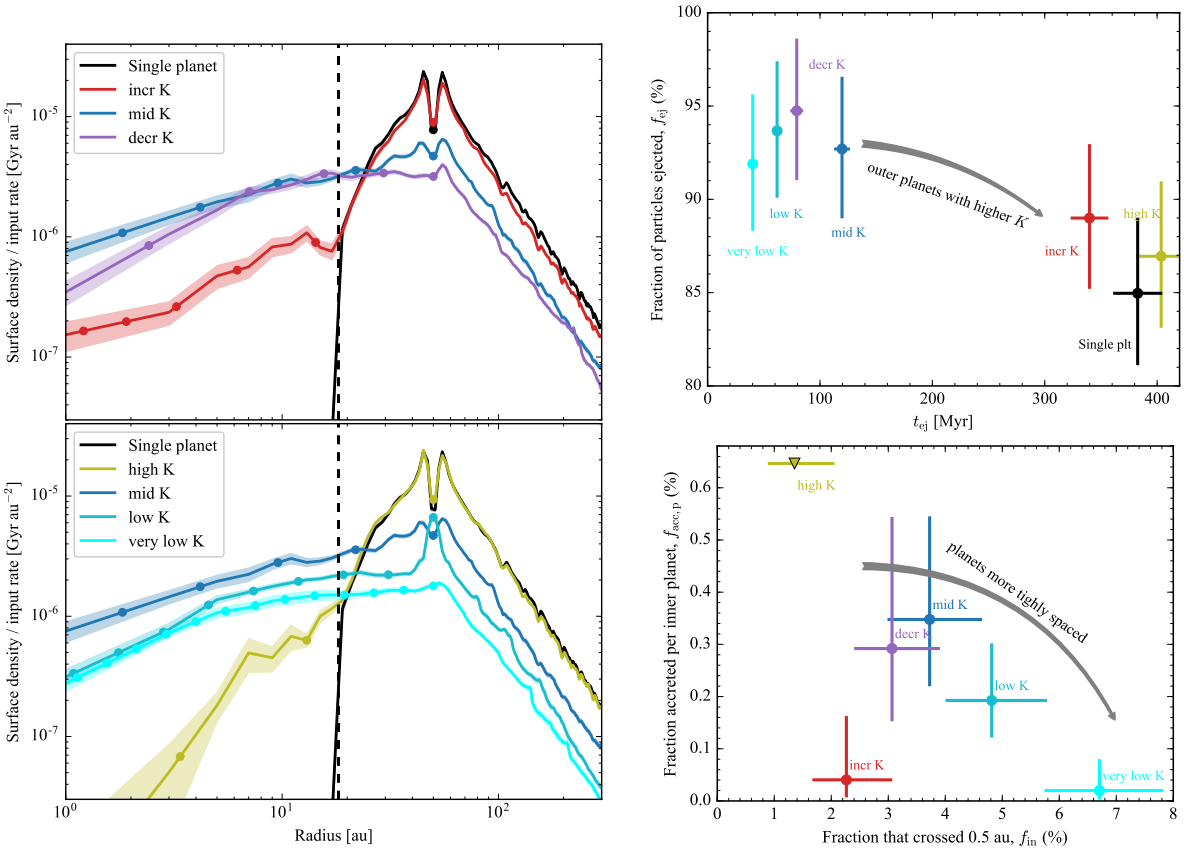

Figure 6.5: Results from N-body simulations for planet configurations with 30 $M_\oplus$ planets and varying the spacing between planets. ***Left:*** steady state surface density distribution of particles. Models varying α_Δ are shown at the top left panel, while models with constant separations in mutual Hill radii of 8, 12, 20 and 30 at the bottom left. The radial location of the dots corresponds to the semi-major axis of each planet. Particles are input in the chaotic zone of the outermost planet at a constant rate. The black dashed vertical line represents $q_{\rm min,p1}$. The black continuous line represents the surface density of a single planet system ($a_{\rm p} = 50$ au). ***Top right:*** fraction of particles ejected vs ejection timescales, calculated as the median of epochs at which particles are ejected. ***Lower right:*** fraction of particles accreted per planet within 10 au vs fraction that crosses the inner boundary at 0.5 au.

Varying K uniformly

When increasing the spacing from $K = 20$ (reference system, dark blue, called mid K in Figure 6.5) to 30 (yellow, high K) I observe the following effects:

1. The surface density of scattered particles is higher in the outer scattered disc, but much lower towards smaller orbital radii. In fact, the surface density is very similar to the single planet case beyond $q_{\rm min,p1}$. Only a very small fraction extends within 18 au as expected because the next planet in the chain is inside $q_{\rm min,p1}$.

2. The fraction of ejected particles is 87%, slightly lower than the 93% in the reference system and similar to the single planet case. This difference is due to the higher fraction

of accreted particles (12% by the outermost planet).

3. The ejection timescale is also increased from 120 to 404 Myr. The longer lifetime of particles causes the surface density to be higher beyond 50 au in the case of large planet spacing. In fact, both $f_{\rm ej}$ and $t_{\rm ej}$ are very similar compared to the single planet case. The rest of the particles that are not ejected are mostly accreted by the outermost planet (12%).

4. Only a very small fraction of particles are able to cross 0.5 au (1.4%).

5. The fraction accreted per inner planet is zero, but statistically consistent with the results of the reference system ($\lesssim 0.65\%$). This is because there is only one planet within 10 au in this system, therefore there is a large uncertainty on $f_{\rm acc,p}$.

6. After 1 Gyr of evolution 14% of particles remain in the scattered disc beyond the outermost planet.

Therefore, I find that when increasing the spacing, the results approximate to the single planet case, with the subtle difference that a few particles are able to be scattered within $q_{\rm min,p1}$. These results confirm the first prediction, that planet configurations with outer planets too widely spaced, i.e. with $a_{\rm p2} < q_{\rm min,p1}$, would be inefficient at scattering particles inwards as multiple scattering is hindered.

When K is lower, e.g. 12 or 8 (represented with light blue colours) instead of 20, I observe the following effects:

1. The surface density of the scattered disc is lower at both small and large radii compared to the reference planet configuration.

2. On the other hand, $f_{\rm in}$ increases as the planet separation (K) is decreased. This is because scattering by inner planets becomes more likely as particles do not require high eccentricities to reach the next planet in the chain. Therefore, inward scattering happens faster and before particles get a kick strong enough to be ejected from the system or get accreted by a planet. Note that although the amount of material being passed inwards is higher, $\Sigma(r)$ is lower. This is because the steady state surface density is also proportional to the lifetime of particles at a specific orbital radius. For example, at 10 au I find that $\Sigma(r)$ is lower compared to the reference system by a factor that is consistent with the ratios of ejection timescales (see Table 6.2), which is a proxy for the lifetime of particles in the scattered disc. I also rule out that the decrease in $\Sigma(r)$ is due to the increase in $f_{\rm in}$, as the removal of particles only has an effect within 4 au (see §6.6.5).

3. I also find a decrease in the fraction of particles accreted per inner planet when the planet separation becomes low ($K = 12$ and 8, light blue points in lower right panel in

Figure 6.5). This effect is also observed in §6.5.4 at a significant level. This could be due to the lower surface density as the planet masses are the same. Other factors could be at play too, such as the eccentricity and inclination distribution of particles which can change the distribution of relative velocities in close encounters (Equations 6.6 and 6.7). In fact, I do find that in systems with low spacing the distribution of eccentricities and inclinations is slightly shifted towards higher values by a few percent compared to the reference system, although this difference is not large enough to explain the lower accreted fraction. Therefore, I conclude that it is the change in surface density the main factor at decreasing the accretion onto planets. These results suggest that there is an optimum planet spacing that maximises the accretion onto inner planets for systems of equal mass planets.

Varying K as a function of $a_{\rm p}$ (α_{Δ})

When the planet spacing decreases towards larger orbital radii (purple) the surface density remains very similar to the reference scenario, although slightly lower between 30-150 au. This simulation also has a similar or consistent fraction of particles that are accreted per inner planet and that cross 0.5 au compared to the reference case. On the other hand, the ejection timescale in this simulation (79 Myr) is more similar to the low spacing case ($K = 12$), which has outermost planets at similar separations. This suggests that the ejection timescale is dominated by the separation of the two outermost planets rather than the average separation of planets in the system (for equal mass planets). However, despite the fact that the outer planets are close to each other, the fraction of particles that cross 0.5 au is lower or consistent with the reference system (dark blue).

In the system with increasing planet spacing (red) I find that the ejection timescale and surface density beyond $q_{\rm min,p1}$ are very similar to the case of high K (yellow) or single planet case. Nevertheless it has a higher surface density within $q_{\rm min,p1}$ and higher fraction of particles that get to 0.5 au. The number of accreted particles per inner planet is lower, but within the errors compared to the reference system.

Neither increasing nor decreasing the spacing as a function of orbital radius increases the fraction of particles that get into the inner regions compared to the reference system. However, if I compare planet configurations with similar spacing for their outer planets (i.e. pairs yellow-red and light blue-purple), I find that if the planet spacing decreases towards smaller orbital radii, then the fraction of particles that cross 0.5 au and the surface density within $q_{\rm min,p1}$ increases. Therefore, I predict that a system with both $a_{\rm p2} > q_{\rm min,p1}$ and $\alpha_{\Delta} \geq 0$ will be very efficient at passing material inwards.

Conclusions regarding planet spacing

Based on these results I conclude the following:

1. For efficient inward multiple scattering, outer planets must be close enough such that $a_{\rm p2} > q_{\rm min,p1}$—noting that $q_{\rm min,p1}$ depends on the initial condition of particles which could be different to that assumed here.
2. Closely spaced outer planets means that particles are ejected faster—assuming particles start in the outer regions of the system.
3. Planets in compact configurations, with either uniform spacing or decreasing towards smaller orbital radii for a fixed outermost planet separation, are most efficient at passing particles inwards.
4. The more closely packed the planets are, the lower the surface density in the scattered disc, and the fewer impacts per inner planet.

6.5.4 Varying $M_{\rm p}(a)$

In this section, I present results from four other simulations of planets separated by 20 mutual Hill radii, but varying their masses. These are planet configurations 2, 3, 6 and 7, for which $\alpha_{\rm M}$ and M_0 vary. I also include the reference system and configuration 10 which has low mass planets closely spaced to see the effect of decreasing both planet masses and spacing. Figure 6.6 presents the results for $\Sigma(r)$, $f_{\rm ej}$, $t_{\rm ej}$, $f_{\rm in}$ and $f_{\rm acc,p}$.

Varying $M_{\rm p}$ uniformly

The simulations show that at constant separation (K), the surface density, the ejection timescale, and the fractions of particles that are accreted per inner planet and that cross the inner edge, decrease when increasing planet mass (Figure 6.6, see changes from pink to dark blue and from dark blue to brown). The ejection timescale decreases in factors of $\sim 4-5$ when increasing $M_{\rm p}$ from 10 to 30 $M_\oplus$ and from 30 to 90 $M_\oplus$, as higher mass planets scatter on shorter timescales. The change in ejection timescale also results in the surface density increasing by similar factors when decreasing $M_{\rm p}$. These strong differences in surface density cause also an increment in the fraction of particles accreted per inner planet when decreasing $M_{\rm p}$. Note that although 31% of particles remain in the low mass planet system by 1 Gyr, when extending the integration to 5 Gyr I find that the fractions of particles ejected, accreted and that cross 0.5 au do not change significantly (see §6.6.5).

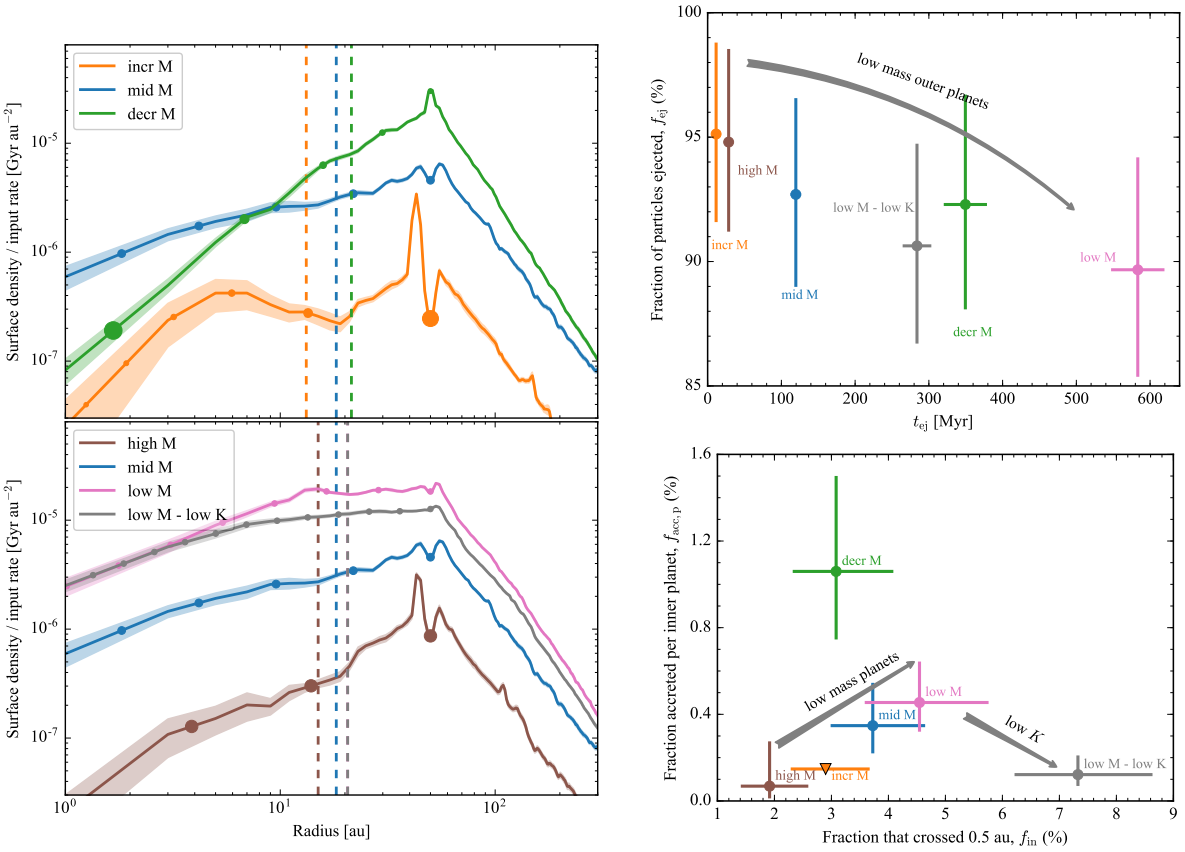

Figure 6.6: Results from N-body simulations for planet configurations with a constant planet spacing of 20 mutual Hill radii ($K = 20$) and varying their masses. ***Left:*** steady state surface density distribution of particles. Models varying $\alpha_{\rm M}$ are shown at the top left panel, while models with constant masses of 10, 30 and 90 $M_\oplus$ at the bottom left. The radial location of the dots corresponds to the semi-major axis of each planet and their size representing their masses with an arbitrary scale. Particles are input in the chaotic zone of the outermost planet at a constant rate. The dashed vertical lines represent $q_{\rm min,p1}$. ***Top right:*** fraction of particles ejected vs ejection timescales, calculated as the median of epochs at which particles are ejected. ***Lower right:*** fraction of particles accreted per planet within 10 au vs fraction that crosses the inner boundary at 0.5 au. The inverted triangle represents a 2σ upper limit. The grey line (lower left panel) and points (right panels) represent a system with 10 $M_\oplus$ planets closely separated by 12 mutual Hill radii.

I can use these results to derive an empirical relation for the fraction of particles that get into 0.5 au and surface density as a function of the planet mass, for a fixed input rate and a chain of equal mass planets separated by 20 mutual Hill radii. I find that $f_{\rm in}$ varies approximately as $M_{\rm p}^{-0.37\pm0.13}$ and the surface density at 10 au as $M_{\rm p}^{-1.6\pm0.2}$. This indicates that the surface density in the scattered disc is not directly proportional to the fraction of particles that get to 0.5 au, with the surface density being more sensitive to changes in planet mass. By combining these two empirical expressions I find $f_{\rm in} \propto \Sigma(10\ {\rm au})^{0.23\pm0.09}$ for chains of equal mass planets.

Varying $M_{\rm p}$ as a function of $a_{\rm p}$ ($\alpha_{\rm M}$)

When varying $\alpha_{\rm M}$ with a fixed planet mass of 30 $M_\oplus$ at 10 au (see top left panel of Figure 6.3 and compare orange blue and green) I find the following. For planet masses decreasing with orbital radius ($\alpha_{\rm M} = -1$, green) the ejection timescale is increased relative to the reference system. Similarly, for planet masses increasing with orbital radius ($\alpha_{\rm M} = 1$, orange) the ejection timescale is decreased. The changes in the ejection timescale are due to its strong dependence on the mass of the outermost planet as that is where particles are initiated. This is similar to what I found in §6.5.3 in which the ejection timescale is dominated by the separation of the outermost planets.

I also find that the surface density changes significantly when varying $\alpha_{\rm M}$ (Figure 6.6 top left panel). For planet masses decreasing with orbital radius (decr M, green), the surface density becomes steeper both inside and outside 50 au, with a slope of ~ 1.5 within 50 au. This causes $\Sigma(r)$ to be lower (higher) within (beyond) 10 au compared to the reference system. For planet masses increasing with orbital radius, the surface density is lower and flatter. The steep slope within 4 au and the peak at 43 au seen in the orange line are due to the inner boundary, low number statistics, and particles trapped in the 5:4 mean motion resonance with the outermost planet, respectively. The slope of the surface density within 50 au depends strongly on $\alpha_{\rm M}$ because the lifetime of particles or ejection timescale is a function of $M_{\rm p}$ and $a_{\rm p}$ (Equation 6.5), hence, more negative $\alpha_{\rm M}$'s will result in steeper positive slopes.

Regarding the efficiency of particles reaching 0.5 au ($f_{\rm in}$), the bottom right panel in Figure 6.6 shows that this is slightly lower compared to the reference system for both $\alpha_{\rm M} = -1$ and 1 (decr M and incr M, respectively), but consistent within errors. However, when comparing systems with outermost planets of similar mass (green-pink and brown-orange) I find that positive $\alpha_{\rm M}$ results in a slightly higher fraction of particles reaching 0.5 au, while slightly lower for negative $\alpha_{\rm M}$. This partially contradicts one of my prediction in §6.3, that chains of planets with mass decreasing with distance to the star (i.e. scattering timescales increasing with distance) would be better at inward scattering than the opposite. This could be due to the system with with planet masses decreasing with distance from the star (green) having inner planets in the ejection regime (see discussion in §6.5.5).

I find that the fraction of particles accreted per inner planets is the highest in the system with planet masses decreasing with orbital radius (0.8 and 1.3% for the planets at 2 and 7 au, respectively) compared to the other 11 simulated systems. This is surprising as it has one of the lowest surface densities within 10 au. On the contrary, no particles were accreted by inner planets in the system with planet masses increasing with orbital radius ($f_{\rm acc,p} \lesssim 0.1$).

To understand what drives the higher accretion fraction per inner planet in the configuration

with decreasing mass with orbital radius (green), I need to consider the density of particles around their orbits, the planet masses and radii, and the relative velocities of particles that the inner planets encounter (Equation 6.6). As seen in Figure 6.6 the surface density is not particularly high within 10 au compared, for example, to the reference configuration. Moreover, I analyse the number of close encounters per planet (those that get within 3 mutual Hill radii) finding that the surface density is a reasonable tracer of this quantity, being lower within 10 au. The higher level of accretion of the innermost planet for the simulation with decreasing mass with orbital radius (green) compared to the innermost planet in the reference simulation (dark blue) could be explained mostly by its higher planet mass (180 vs 30 $M_\oplus$) and radius. However, the second innermost planet also accretes significantly more than the inner planets in the reference system ($\gtrsim 3$ times more), but with a slightly lower $\Sigma(r)$ and a similar planet mass of 44 $M_\oplus$(remember that Γ is proportional to $M_{\rm p}^{4/3}$ for these planet masses and semi-major axes). Therefore, the fraction of accreted particles must be also enhanced by a difference in the distribution of eccentricities and inclinations of particles in these regions, which defines the relative velocities at which these planets are encountering scattered particles and the collisional cross sections (see Equation 6.7). When comparing the distribution of eccentricities and inclinations of particles having close encounters, I find that their distributions are indeed significantly shifted towards lower values for the decr M system (see Figure 6.7). Therefore encounters happen on average at lower relative velocities and in a flatter scattered disc (lower h). The lower eccentricities and inclinations, and higher collisional cross-section can increase $R_{\rm acc,plt}$ by a factor of ~ 3 for the second innermost planet of the decreasing mass system (green) compared to inner planets in the reference system, which is consistent with the higher number of impacts that I find for close-in planets. The lower eccentricities and inclinations are likely due to the fact that the outer planets scattering in the material from 50 au are lower in mass. I observe a similar effect for the system with equal low mass planets (pink) and the opposite for the incr M system, i.e higher eccentricities and inclinations are likely due to the high mass of the outermost planets..

Low planet mass and spacing

Finally, in order to test if lowering the spacing of low mass planets can increase even more $f_{\rm in}$ and possibly reduce $f_{\rm acc,p}$ as found in §6.5.3, in Figure 6.6 I overlay a system with 10 $M_\oplus$ planets spaced with $K = 12$ (grey). In accordance with my results in §6.5.3, I find that such system has a higher number of particles that get to 0.5 au (7%), but significantly lower $f_{\rm acc,p}$. This is due to two effects: the surface density of the scattered disc is lower, but also I find that the distribution of eccentricities and inclinations in close encounters is shifted towards higher values. Thus, it could be that there is an optimum separation ($> 8R_{\rm H,m}$) that maximises the amount of accretion per inner planet.

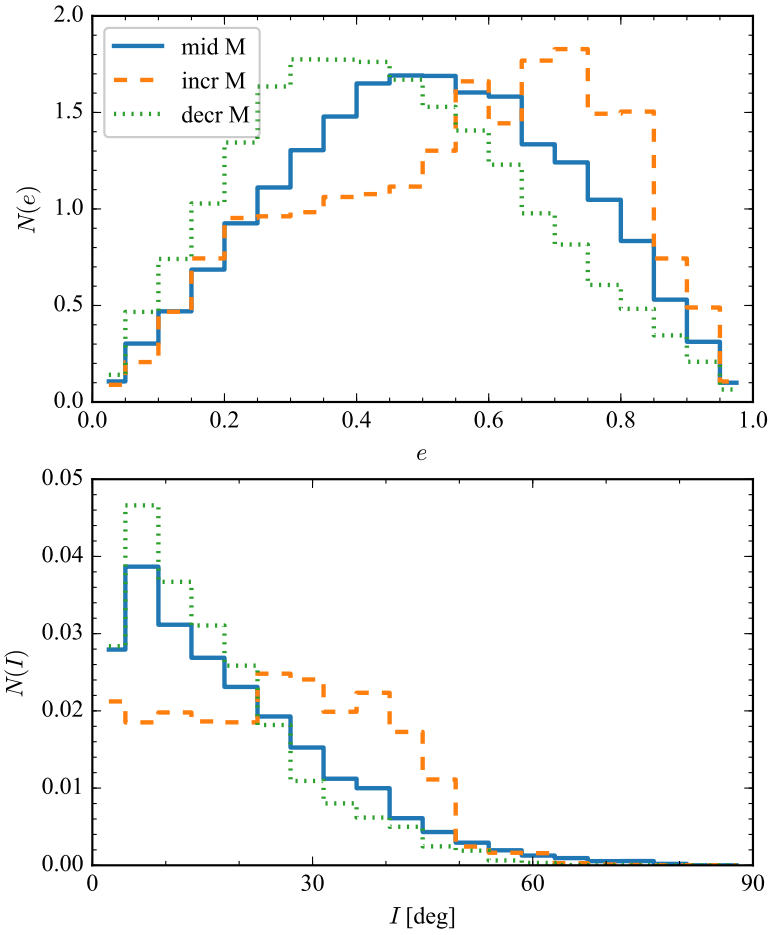

Figure 6.7: Normalized distribution of eccentricities and inclinations of particles having close encounters with planets within 10 au.

Conclusions regarding planet masses

Based on the results varying the masses of the planets I conclude that:

1. The surface density decreases with increasing $M_{\rm p}$ for fixed planet spacing K.
2. The slope of the surface density profile varies when changing the planet masses as a function of semi-major axis. For planet masses decreasing as a function of orbital radius, $\Sigma(r)$ increases steeply with orbital radius compared to the reference system.
3. The fraction of particles that get to 0.5 au increases when decreasing $M_{\rm p}$. Placing the planets closer together increases even more the fraction of particles that get to 0.5 au, but reduces the surface density and thus the fraction of particles accreted per inner planet.
4. Systems with innermost planets in the ejection regime are less efficient at transporting material within 0.5 au (green and brown).
5. The number of particles accreted per inner planet increases with decreasing $M_{\rm p}$ as the surface density is increased due the longer lifetime of particles in the disc. However, systems with $\alpha_{\rm M} < 0$ have the highest $f_{\rm acc,p}$ because of the high collisional cross-section of inner planets caused by their high mass and planet radii, and the low relative velocities of particles in the scattered disc.

6.5.5 Comparison with my predictions

In this section I compare my results with previous work from which I made some predictions in §6.3.4. First, if particles start from a cold disc near the outermost planet, then systems with widely spaced planets, or at least with outermost planets too far from each other, would have trouble scattering particles inwards. In my simulations I find that this is approximately true, since systems with wide outer planets were the ones with the least amount of material transported to 0.5 au confirming results by Bonsor et al. (2012).

The second expected outcome was that chains of high mass planets will scatter and eject particles on shorter timescales. In my simulations I find that this is true with ejection timescales varying from 580 to 30 Myr when varying $M_{\rm p}$ from 10 to 90 $M_{\oplus}$. Shorter ejection timescales lead to lower surface densities of scattered particles.

The third expected outcome regarded the mass distribution of the planets in the chain, with the best systems passing material inwards being the ones with equal mass chain of planets or decreasing with distance from the star (Wyatt et al., 2017). I find that this is true for systems of equal mass planets, being the best of the simulated systems at scattering material inwards to

within 0.5 au. Systems with decreasing mass were not as efficient at that because they encounter the following obstacle. The outermost planet must have a mass high enough that the scattering timescale is shorter than 1 Gyr (length of simulation), otherwise particles will take too long to be scattered inwards. This means that if the outermost planet is at 50 au, then it must be more massive than ~ 10 $M_{\oplus}$ for a Gyr old system. However, if the planet masses increase towards smaller orbital radii, then the innermost planet at 1 au will be in the ejected region (see Figure 6.3), hence ejecting most of the particles instead of scattering them in so that they can reach 0.5 au. This is similar to the Solar System where Jupiter ejects most of the minor bodies that are scattered in from the Kuiper belt, which thus never get into the inner Solar System.

The fourth expected outcome was that the accretion onto inner planets (which has implications for the delivery of volatile-rich material formed in an outer belt) will be higher if they are more massive, the surface density of particles around their orbits is higher, and particles are on low eccentricity and inclination orbits. I confirmed this, however, as expected I also found that these factors are not independent of each other as the planet mass and spacing affects both the surface density and the distributions of eccentricity and inclination of scattered particles. I found that systems of low mass planets have the highest accretion per inner planet as the density of particles is highest for these systems. If planet masses are allowed to vary as a function of orbital radius, the system with low mass outer planets and high mass inner planets has the highest accretion per inner planet, as it is an optimum of the different factors presented above confirming my predictions. Finally, I also found that there must be an optimum planet separation for delivering material to inner planets. While particles in systems with planets widely spaced are less likely to be scattered inwards, particles in systems of tightly packed planets are ejected on shorter timescales and have higher relative velocities, hence both wide and small planet spacing hinder accretion onto inner planets.

6.6 Discussion

In this chapter I have explored the process of inward scattering for a variety of planetary systems. Below I discuss my main findings regarding the surface density of scattered particles, inward transport to 0.5 au, and delivering material to inner planets. I also discuss some of the model assumptions and simulation parameters.

6.6.1 Is a scattered disc detectable in a system with an exozodi?

Consider a system that is observed to have an exozodi. Infrared observations of the dust emission can be used to infer the rate at which mass is lost from the exozodi, $R_{\rm zodi}$. For example, for $\sim$1 Gyr old systems with exozodis such as Vega, η Corvi and HD69830 this is

$R_{\rm zodi} \sim 10^{-11} - 10^{-9}$ M$_\oplus$ yr^{-1} (see Equation 29 in Wyatt et al., 2007a), being highest for Vega and η Corvi. Here I consider what constraints the results from §6.5 place on the possibility that an exozodi is replenished by scattering of planetesimals from an outer belt. The two conditions that we must consider are whether mass is passed in at a sufficient rate to replenish the exozodi at a rate $R_{\rm zodi}$ and whether this requires the presence of a scattered disc between the outer disc and the exozodi that is bright enough to be detectable. Below I first present some general considerations to estimate the surface density of dust in the disc of scattered particles to compare it with sensitivity limits from different telescopes (§6.6.1). Then I apply these to a specific system (§6.6.1).

General considerations

As discussed in §6.2, here I assume that solids from an outer belt of planetesimals are input near an outermost planet (located at 50 au) at a constant rate $R_{\rm in}$, and that when they cross 0.5 au their mass is incorporated in a collisional cascade where solids are ground down to dust. Then $R_{\rm zodi} = f_{\rm in} R_{\rm in}$, and if assuming that scattering has been ongoing for the system's whole lifetime, the total mass that has been scattered from the outer belt is $t_\star R_{\rm zodi}/f_{\rm in}$, where $t_\star$ is the age of the system. It is worth noting that although $f_{\rm in}$ varies as a function of the planetary system architecture, it does not change by more than an order of magnitude when varying considerably the planet masses and spacing (based on the simulations, $f_{\rm in}$ is in the range 1-7%). This means that for $\sim$ 1 Gyr old systems with a high $R_{\rm zodi}$ of $\sim 10^{-9}$ M$_\oplus$ yr^{-1} (e.g. Vega or η Corvi) the amount of material scattered from the outer belt over the lifetime of the system (assuming this is the origin of the exozodi) is probably as high as $\sim$10 M$_\oplus$ if this has been a continuous process or even higher if not all of the mass that reaches 0.5 au ends up in the exozodi. Note that this is a significant fraction of estimated masses of their outer belts assuming a size distribution with a power index of -3.5 and a maximum planetesimal size of 10-100 km (Holland et al., 2017).

Comparing the fraction of particles that get to 0.5 au with the surface density of particles (Figure 6.8), I find that there is a correlation between the two. This correlation is similar to the one that I found in §6.5.4, with $f_{\rm in} \propto \Sigma(10\ {\rm au})^{0.23\pm0.09}$. That is, while the surface density varies by two orders of magnitude, $f_{\rm in}$ only varies by a factor of a few. Moreover, although there is a correlation for systems with equal planet spacing ($K = 20$) and different planet masses (high M, reference and low M), there is an important dispersion for the rest of the architectures explored. This means that bright exozodis (i.e. high $f_{\rm in}$) do not necessarily require a bright scattered disc between the exozodi and outer belts (i.e. large $\Sigma(10\ {\rm au})$) if, for example, massive planets or tightly packed medium mass planets are present. Therefore, for a given exozodi, upper limits on the amount of material between these regions can help us to constrain the mass

and separations of intervening planets (see §6.6.1).

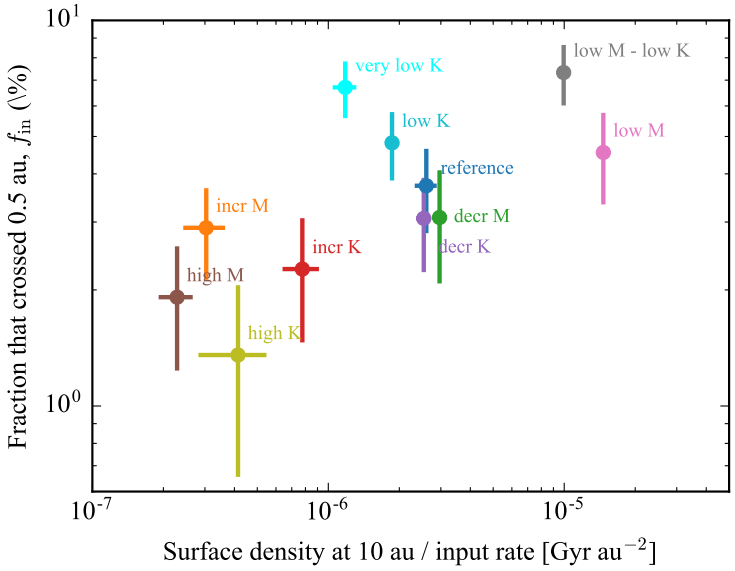

Figure 6.8: Fraction of particles that cross 0.5 au vs mass surface density at 10 au divided by the mass input rate for the simulated systems presented in Table 6.1.

To estimate if the scattered disc between the outer belt and the exozodi could be detected, I assume that the distribution of mass shown in figures 6.5 and 6.6 is also representative of the distribution of dust (i.e neglecting radiation forces acting on small grains). Although collisions can deplete dust densities through collisions before being lost from the system (ejected, accreted or transported within 0.5 au), dust should also be replenished by collisions of bigger bodies that are also scattered and have lifetimes longer than the scattering timescales. I first obtain the total surface density of solids by scaling the surface density to the necessary input rate ($R_{\rm in}$) that can sustain a given exozodi ($R_{\rm zodi} = f_{\rm in} R_{\rm in}$). Then, I scale the surface density of solids to consider only the mass in dust grains smaller than 1 cm (as infrared observations at wavelengths shorter than 1 mm are only sensitive to emission from dust grains smaller than $\sim$ 1 cm). In the scenario that I am considering solids originate in an outer debris belt, thus I assume a standard -3.5 power law size distribution of solids with a maximum size of 100 km and a minimum size of 1 μm, roughly the blow-out size for a Sun-like star. Then the scaling factor to transform the total mass into the mass of dust grains smaller than 1 cm is $\sim 3 \times 10^{-4}$. This factor is approximately the same when using the resulting size distribution of solids at 50 au after 1 Gyr of evolution, and taking into account a size dependent disruption threshold of solids (see middle panel of Figure 4.9).

In Figure 6.9 I show the predicted mass surface density of dust smaller than 1 cm for a system inferred to have $R_{\rm zodi} = 10^{-9}$ and 10^{-11} M$_\oplus$ yr^{-1}, assuming these exozodis are fed by the reference chain of planets ($f_{\rm in} = 3.7\%$). The resulting surface densities are

$\sim 10^{-8} - 10^{-10}$ $M_\oplus$ au^{-2} within 50 au. Figure 6.9 also compares these with typical sensitivities (3σ for 1h observations) of ALMA at 880 μm (0.1 mJy and $1''$ resolution), Herschel at 70 μm (3.0 mJy and $5''.6$ resolution), JWST at 20 μm (8.6 μJy and $1''$ resolution) and a possible future 3-meter far-IR (FIR) space telescope similar to SPICA at 47 μm (15 μJy and $3''.4$ resolution). I assume a system at a distance of 10 pc with a 1 $L_\odot$ central star. To translate the above sensitivities to dust masses, I assume black body temperatures and dust opacities corresponding to dust grains with a -3.5 size distribution and composed of a mix of amorphous carbon, astrosilicates and water ice. Moreover, assuming a face-on disc orientation sensitivities are also improved by azimuthally averaging the emission over 10 au ($1''$) wide disc annuli. Figure 6.9 shows that although ALMA has one of the highest resolutions, it is not very sensitive to the dust emission within an outer belt at $\sim$ 50 au. JWST is more sensitive than ALMA within $\sim$ 30 au where dust is expected to be warmer and therefore emits significantly more at MIR wavelengths. In the FIR Herschel does better than ALMA within $\sim$ 100 au and could detect the scattered disc in systems with extreme exozodis; however, it is limited by its low resolution. A future FIR mission could do much better, being able to detect much fainter emission at 47 μm and resolve structure down to 20 au. I conclude that current or previous instruments like ALMA or Herschel could only constrain the architecture of systems with the highest mass loss rates (see example below).

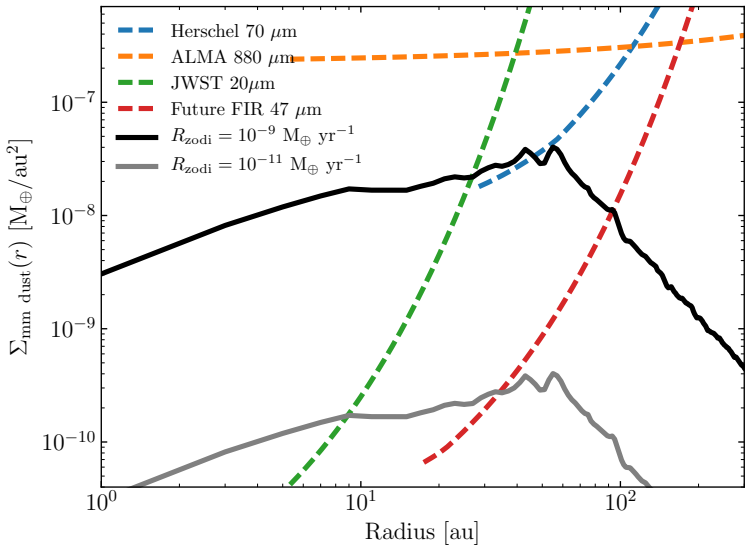

Figure 6.9: Steady state surface density distribution of dust grains smaller than 1 cm for the reference system. The dashed lines represent the 1 h integration sensitivities (3σ) from different instruments, assuming a distance of 10 pc, a face-on disc orientation, and azimuthally averaging the emission over 10 au wide annuli. The estimated sensitivities only extend inwards to half of the resolution. Note that for the ALMA sensitivity we have not considered the size of its primary beam as this can be overcome by multiple pointings (mosaic mode).

η Corvi

η Corvi is one of the best studied systems with hot/warm dust (~ 400 K, Stencel & Backman, 1991; Smith et al., 2009). Its hot component has a fractional luminosity of $\sim 3 \times 10^{-4}$ and its location was constrained to be between $\sim 0.2 - 1.4$ au (Defrère et al., 2015; Kennedy et al., 2015b; Lebreton et al., 2016). This implies that it can only be explained if material is resupplied from further out (e.g. an outer belt of planetesimals) at a rate of $\sim 10^{-9}$ $M_\oplus$ yr^{-1} (Wyatt et al., 2007a). In fact, this system is known to host a massive cold debris disc located at around 150 au and resolved in the submillimetre and FIR (see Chapter 3). Despite the presence of this massive outer belt which could feed an exozodi through small dust migrating due to P-R drag, this scenario has been discarded as an explanation for the large exozodi levels observed since it is not efficient enough (Kennedy & Piette, 2015). Moreover, observations found no dust located between its hot and cold components. However, in Chapter 3 I found evidence for CO gas at ~ 20 au using ALMA observations. The short-lived CO gas hints at the possibility of volatile-rich material being passed inwards from the outer belt and outgassing, consistent with spectroscopic features of the hot dust (Lisse et al., 2012). An outstanding question though is whether this can be achieved without requiring scattered disc densities that exceed the detection limits of FIR and submillimetre observations.

I run two new models with 30 and 90 $M_\oplus$ planets spaced with $K = 12$ (tightly packed) to achieve a high inward scattering efficiency, but now extending the chain of planets up to 100 au — the maximum semi-major axis of a planet sculpting the inner edge of the outer belt (see Chapter 3). In the first case, when extending the chain up to 100 au I find that $f_{\rm in}$ decreases from 4.8% to 2.8%, $t_{\rm ej}$ increases from 62 to 120 Myr and $f_{\rm ej}$ increases from 94% to 97%. For the more massive planets, I find $f_{\rm in} = 2.1\%$, $t_{\rm ej} = 20$ Myr and $f_{\rm ej} = 97\%$. I compute the expected total surface density for a mass input rate such that $R_{\rm zodi} = 10^{-9}$ $M_\oplus$ yr^{-1}. Under the same assumption stated in the previous section, I extrapolate $\Sigma(r)$ to the surface density of dust grains smaller than 1 cm ($\Sigma_{\rm mm\ dust}$) assuming a -3.5 size distribution between the largest planetesimals and the cm-sized grains and an opacity of 1.7 cm^2 g^{-1} at 880 μm. However, given the existing constraints from image and spectral energy distribution modelling, I adopt a grain opacity index $\beta = 0.2$ (i.e a ~ -3.1 grain size distribution) between FIR and sub-mm wavelengths. I also assume a dust temperature of 50 K at 100 au which increases towards smaller orbital radii as $r^{-0.5}$, consistent with radiative transfer modelling of this system. In Figure 6.10 I compare $\Sigma_{\rm mm\ dust}$ from my simulations with the upper limits from ALMA and Herschel observations (see Chapter 3 and Duchêne et al., 2014). I find that for both type of systems, the sensitivity curves of ALMA and Herschel are above the predicted surface densities. The surface density of a 30 $M_\oplus$ chain barely reaches the 3σ limit imposed by Herschel. The total mass in dust smaller than 1 cm in the scattered disc within 80 au is 3×10^{-4} and 9×10^{-5} $M_\oplus$ for the systems with 30 and 90 $M_\oplus$ planets, respectively. These dust

masses are well below the mass upper limit of 2.7×10^{-3} $M_\oplus$ from ALMA observations derived in Chapter 3.

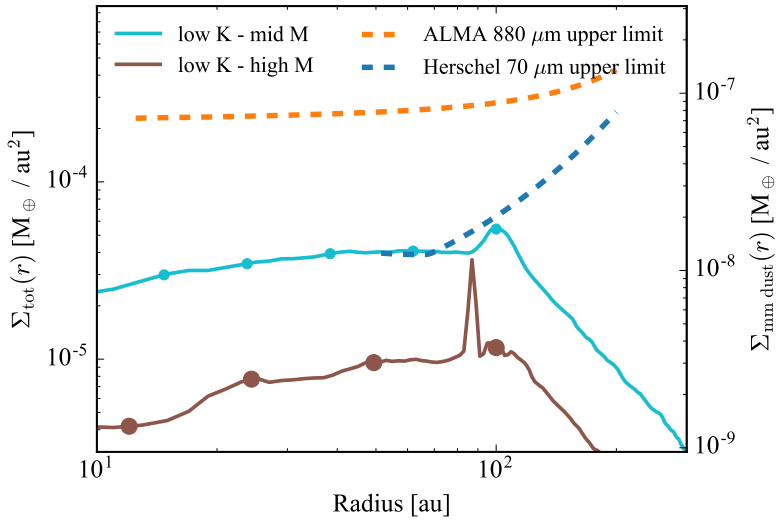

Figure 6.10: Steady state surface density distribution of particles for a model tailored to η Corvi. Particles are input in the chaotic zone of the outermost planet ($a_{\rm p1} = 100$ au) at a constant rate of $10^{-9}/f_{\rm in}$ $M_\oplus$ yr^{-1}. All planets are spaced with $K = 12$ and have masses of 30 (light blue) and 90 $M_\oplus$ (brown). The dashed lines represent the upper limits on the amount of mm-sized dust from ALMA at 0.88 mm (blue) and Herschel at 70 μm (orange).

It is also possible to compare these dust densities with alternative scenarios such as the P-R drag scenario. Although it is not efficient enough to explain η Corvi's exozodi, P-R drag is inevitable and small dust will be dragged inwards and be present in between its exozodi and outer belt with a surface density distribution close to flat. I find that the two simulated systems presented in this section have optical depths of $10^{-6}-10^{-5}$, estimated as the product of the surface density and a standard dust opacity at optical wavelengths (assuming a -3.5 grain size distribution with a minimum and maximum size of 1 μm and 1 cm). These optical depths are similar or slightly greater than for small dust migrating in due to P-R drag in the absence of planets (see Figure 1 in Kennedy & Piette, 2015). Therefore it is worth noting that observations looking for an intermediate component within a few au in between bright exozodis and outer belts (e.g. using the Large Binocular Telescope Interferometer) should consider the possibility that any detected emission could correspond to a scattered disc rather than P-R dragged dust. Constraints on the radial profile of the surface density of dust could help to disentangle between these two scenarios as a scattered disc would have a steeper slope.

Now, I can go one step further and use these results to constrain the planet masses assuming that the exozodi in η Corvi is fed by scattering within a chain of equal mass planets. In §6.5.4 I found that in systems of equal mass planets and uniform spacing (20 mutual Hill radii) the surface density scales with planet mass approximately as $M_{\rm p}^{-1.6\pm0.2}$, while the fraction of particles that get to 0.5 au scales as $M_{\rm p}^{-0.37\pm0.13}$. Assuming these relations stay the same for planet chains out to 100 au and with low spacing (12 mutual Hill radii), I can approximate $f_{\rm in}$

and the surface density of dust smaller than 1 cm at 60 au ($\Sigma_{\rm mm,60\ au}$) by

$$f_{\rm in} = 0.028 \left(\frac{M_{\rm p}}{30\ {\rm M}_\oplus}\right)^{-0.37}, \tag{6.13}$$

$$\Sigma_{\rm mm,60\ au} = 1.3 \times 10^{-8} \left(\frac{M_{\rm p}}{30\ {\rm M}_\oplus}\right)^{-1.6} \left(\frac{R_{\rm in}}{40\ {\rm M}_\oplus\ {\rm Gyr}^{-1}}\right) {\rm M}_\oplus\ {\rm au}^{-2}, \tag{6.14}$$

where I have assumed a maximum planetesimal size of 100 km and fixed the values of $f_{\rm in}$ and $\Sigma_{\rm mm,60\ au}$ to the ones presented above, only valid for chains of equal mass 30 $M_\oplus$ planets spaced by 12 mutual Hill radii. By equating Equation 6.14 to the Herschel upper limit of $1.3 \times 10^{-8} {\rm M}_\oplus\ {\rm au}^{-2}$ at 60 au I can infer a maximum planet mass as a function of the mass input rate (orange solid line in Figure 6.11). This limit assumes a maximum planetesimal size ($D_{\rm max}$) of 100 km and a -3.5 power law size distribution. A smaller $D_{\rm max}$ would make $\Sigma_{\rm mm,60\ au}$ greater (dashed line), while a larger maximum planetesimal size would decrease the surface density of dust (dotted line). Larger planet spacing would also have an effect on the surface density, being increased for larger planet spacing as found in §6.5.3 (e.g. $K = 20$).

I also expect that there is a limit on the mass input rate from an outer belt if it has been ongoing for 1-2 Gyr (the age of η Corvi) at a constant rate. This limit is chosen such that the total mass scattered from the outer regions is $\lesssim 100\ {\rm M}_\oplus$(close to the solid mass available in a protoplanetary disc at this location) which is equivalent to a rate of $\lesssim 100\ {\rm M}_\oplus\ {\rm Gyr}^{-1}$. This upper limit for the mass input rate is represented as a red region in Figure 6.11, although the exact value is uncertain. This upper limit of ∼1% sets a lower limit for the fraction of scattered particles that get to 0.5 au to resupply the exozodi. A caveat in this argument is that it assumes that mass has been continuously scattered in over $\sim$ 1 Gyr at a steady state. However, this could be significantly different if ongoing only for a fraction of the age of the system or if stochastic processes are at play, making $R_{\rm zodi}$ vary significantly over short periods of time (e.g. as explored in the context of white dwarf pollution, Wyatt et al., 2014).

In addition, because the fraction of particles that get to 0.5 au depends on the planet mass (Equation 6.13), for a given mass input rate there is a maximum planet mass. This upper limit is represented as a blue region in Figure 6.11 assuming chains of equal mass planets spaced by 12 mutual Hill radii. Planet chains with lower spacing would have a larger $f_{\rm in}$ therefore the maximum mass could be pushed up, although planet chains with spacing smaller than 10 mutual Hill radii are likely to go unstable on Gyr timescales. Wider planet spacing would result in a lower $f_{\rm in}$, thus a smaller mass upper limit. It is important to note that these limits are conservative, as $f_{\rm in}$ is the maximum fraction of the material that could be incorporated into the exozodi, since some of that material that makes it to 0.5 au will end up being ejected, which would narrow the allowed white region in Figure 6.11.

Based on these excluded regions I can constrain the mass of the planets scattering material

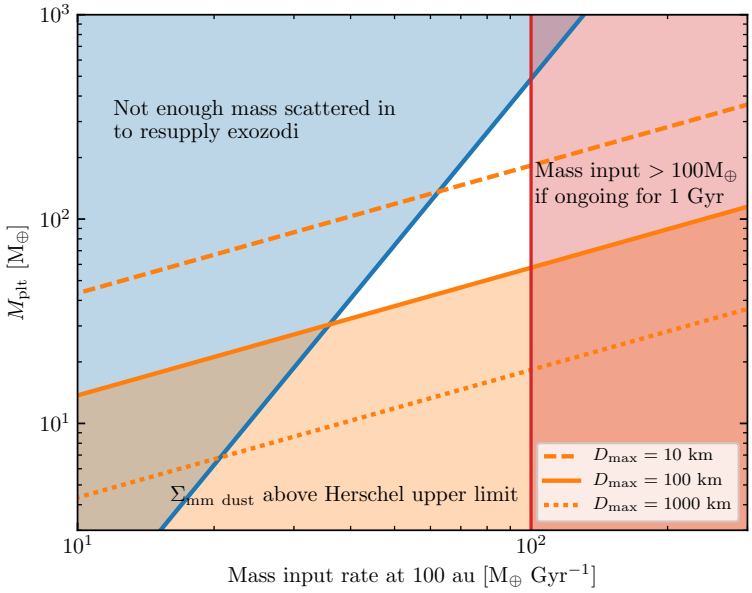

Figure 6.11: The planetary system that could orbit η Corvi and supply the exozodi, whilst not contradicting observational limits for the scattered disc, and assuming a constant mass input rate at 100 au and a system composed of equal mass tightly packed planets ($K = 12$). The lower limit for the planet mass (orange) is estimated based on the results for the surface density as a function of the planet masses, the Herschel 70 μm upper limit for dust between η Corvi's outer belt and exozodi, and assuming a size distribution of solids up to a size of 10, 100 and 1000 km (dashed, continuous and dotted orange lines). The mass upper limit is estimated by setting the rate at which mass is transported into 0.5 au equal to the exozodi mass loss rate. The red region is discarded as it would lead to unphysically large total solid mass beyond 100 au being scattered in for 1-2 Gyr, although the exact upper limit for the mass input rate is uncertain. The white region represents the planet masses and mass input rate that are roughly consistent with the observational constraints and exozodi estimated mass loss rate.

inwards and resupplying the exozodi. Assuming planets are of equal mass, spaced by 12 mutual Hill radii and a maximum planetesimal size of 100 km, I find that the mass input rate and planet mass must be greater than 36 $M_\oplus$ Gyr^{-1} and 30 $M_\oplus$, respectively. If the maximum planetesimal size is larger (smaller), then the planet mass and mass input rate could be smaller (larger). In addition, assuming a maximum mass input rate of $\sim$ 100 $M_\oplus$ Gyr^{-1}, I find a maximum planet mass of 300 $M_\oplus$. Planets much more massive than that are not efficient enough at scattering particles into 0.5 au. Future observations by JWST or FIR space missions could provide important constraints for the models explored here. A detection of dust between the outer belt and exozodi together with further modelling considering a wider variety of planetary system architectures and P-R drag, could be used to constrain the planet masses in this planet scattering scenario.

6.6.2 Best system at transporting material within 0.5 au

I have found that the systems best suited for transporting material inwards are those with lower mass planets and that are tightly packed (at the limit of stability). Varying the planet spacing and mass as a function of orbital radius did not result in a higher fraction that reached 0.5 au. Moreover, although I varied to extremes the architecture of these planetary systems to study how the inward scattering efficiency changes, the fraction that reached 0.5 au did not change by more than a factor of ~ 7, while the surface density of the scattered disc varied by two orders of magnitude. This could imply that in order to explain the short-lived hot dust observed in many systems, no fine tuning is necessary, and a vast range of architectures could explain this frequent phenomenon.

6.6.3 Best system at delivering material to inner planets

I found that the best systems at delivering material to inner planets were those with low mass outer planets and either with uniform mass or increasing towards smaller semi-major axis. This is a consequence of two factors. First, particles being scattered by low mass planets can stay in the system for longer, increasing the density of particles near the planets, and so the probability of being accreted by a planet before being ejected. Second, particles scattered by lower mass planets tend to have lower eccentricities and inclinations, thus lower relative velocities which increases the collisional cross-section of the planets. The latter is important as it also implies that the best systems at creating exozodis are not necessarily the best at delivering material to the inner planets (compare green, pink and grey points in bottom right panel of Figure 6.6). For example, a system with low mass tightly packed planets scatters twice the amount of particles into 0.5 au compared to the reference system, but with a similar fraction of accreted material per inner planet.

Similar to the fraction of material transported into 0.5 au, the efficiency of delivery to inner planets does not vary by more than an order of magnitude when comparing the different systems that I simulated. I find typical values between 0.1% to 1% for the fraction of scattered particles that are accreted per inner planet. These could be even higher for lower mass planets (e.g. Earth or super-Earths) if I extrapolate my results. Note that these fractions can be understood as collision probabilities, which are considerably higher than the 10^{-6} collision probability of cometesimals with Earth in the early Solar System (Morbidelli et al., 2000; Levison et al., 2000). It is unclear though how these results extrapolate to close-in planetary systems of chains of super-Earths, or close-in Earth-sized planets around low mass stars (e.g. Trappist-1, Gillon et al., 2017). Most of these planets are in a different regime where they are much more likely to accrete particles rather than to eject them (Wyatt et al., 2017), and thus the

accretion efficiencies and relative velocities could be very different (Kral et al., 2018).

The low collision probability of comets has been used as an argument for the unlikely cometary origin for the water on Earth. However, my results show that this conclusion cannot be simply extrapolated to extrasolar systems. The low probabilities might be heavily determined by the presence of Jupiter and Saturn in the Solar System which eject most of the minor bodies that are scattered in from the outer regions, never getting into the inner regions. I have shown that comet delivery can be much more efficient for other architectures and so could represent a significant source of water and volatiles for close in planets, although it is not clear yet how common are the architectures that I assumed in this chapter. For example, assuming a total mass of 1 $M_\oplus$ of icy exocomets being scattered with an ice mass fraction of 0.5 dominated by water (roughly what is found in Solar System comets, see review by Mumma & Charnley, 2011), the total amount of volatiles accreted could be higher than 10^{-4} $M_\oplus$ per inner planet, and if extrapolated to systems of 1 $M_\oplus$ planets, this could be enough to deliver the mass of Earth's oceans and atmosphere (2×10^{-4} $M_\oplus$) to Earth-like planets.

An important caveat in my results regarding planet accretion is the uncertain fraction of volatiles (including water) that a planet is able to retain from an impact. This strongly depends on the impact velocities, mass of the planets, volatile fraction of planetesimals, presence of primordial atmospheres and size of impactors (e.g., de Niem et al., 2012). These considerations are beyond the scope of this chapter and require a statistical analysis of the impact velocities with a larger number of test particles than considered here.

6.6.4 Migrating from exo-Kuiper belt to outermost planet

What could drive particles on stable orbits in the outer regions towards the outer planets? In this chapter I have assumed this happens at a constant rate and for long timescales. I now discuss possible mechanisms that could make these particles migrate in. Particles could be slowly exited onto orbits with higher eccentricities and pericentres near the outermost planet by: chaotic diffusion produced by high order or three-body resonances acting on long timescales (Duncan et al., 1995; Nesvorný & Roig, 2001; Morbidelli, 2005); secular resonances if multiple planets are present (Levison et al., 1994); mean-motion resonances with an exterior massive planet on a low eccentric orbit (Beust & Morbidelli, 1996; Faramaz et al., 2017); dwarf planets embedded in the outer belt dynamically exciting smaller bodies (Muñoz-Gutiérrez et al., 2015); or Kozai oscillations induced by an outer companion. Alternatively, if the outer belt is massive enough the outermost planet could migrate outwards instead, while scattering material inwards and continually replenishing its chaotic zone (Bonsor et al., 2014). In these scenarios, particles that were initially near the outermost planet in the chain would start interacting with it with similar orbital parameters to those assumed here, thus we expect that

the assumed initial conditions in this chapter are representative of the scenarios stated above. A fourth possibility is that exocomets are fed from a massive exo-Oort cloud where they are perturbed by Galactic tides or stellar passages, decreasing their pericentres enough to have planet-crossing orbits (e.g., Veras & Evans, 2013; Wyatt et al., 2017). In this last scenario, I expect that particles will start interacting with the planets at high eccentricities and inclinations, and the detailed origin might affect conclusions that rely on the Tisserand parameter (such as about the spacing of the outermost planets). All these scenarios could act on long-timescales feeding material into the vicinity of the outermost planet in the chain. Although in this chapter I have focused purely on the process of scattering (see §6.2), my results are independent of the rate at which these mechanisms can feed material into the vicinity of the outermost planet. Understanding how these different mechanisms can be coupled with the process of inward scattering by a chain of planets is the subject of future work.

6.6.5 Simulation parameters

Here I discuss the effect of changing some of the chosen simulation parameters. Throughout this chapter I have assumed planets with a uniform bulk density of 1.6 g cm^{-3} (Neptune's density), although planet densities could vary as a function of planet mass as suggested by Solar System and extrasolar planets (e.g. Chen & Kipping, 2017, and references therein). For the range of planet masses used in this chapter ($\sim 4-180$ M$_\oplus$), planet densities are expected to vary roughly as $\sim M_{\rm p}^{-0.8}$ (Chen & Kipping, 2017), thus the uniform density assumption could underestimate and overestimate the planet densities by a factor of 2.4 for 10 and 90 M$_\oplus$ planets, respectively. This translates to a factor of 1.3 in planet radius. For high mass planets, the collisional cross section is proportional to both mass and radius (due to gravitational focusing), thus the fraction of accreted particles could be underestimated by 30%. On the other hand, the collisional cross section of low mass planets orbiting within 10 au could be either proportional to $R_{\rm p}^2$ (if the relative velocities are greater than the escape velocity) or $R_{\rm p}M_{\rm p}$ (if gravitational focusing is important). Hence, the fraction of accreted particles could be overestimated by 25-45% for low mass planets. Therefore, the trend seen in §6.5.4 could become flatter if I considered planet densities varying as a function of planet mass.

I also tested the effect of changing some other parameters by: varying the initial distribution of eccentricities and inclinations, extending the length of my simulations, and varying the inner boundary to shorter orbital radii. Depending on the specific mechanism inputting material near the outermost planet, particles will have different distributions of eccentricities and inclinations. When varying their initial eccentricity and inclination distributions in the reference system, I found that $t_{\rm ej}$, $f_{\rm in}$, $f_{\rm acc,p}$ and $\Sigma(r)$ do not change significantly, except when

the eccentricities or inclinations are initially very high (e.g. $e \gtrsim 0.2$). Higher initial eccentricities led to slightly higher fractions of particles reaching 0.5 au and being accreted by inner planets. This is due to a larger fraction of particles having a Tisserand parameter low enough to reach the second outermost planet.

To test if my results are robust against extending my simulations in time, I continued the simulation of low mass planets (pink), which is the one with the slowest evolution, to 5 Gyr. I found that the new values of $t_{\rm ej}$, $f_{\rm in}$, $f_{\rm acc,p}$ and $\Sigma(r)$ are consistent with the ones obtained before (remember that these had been extrapolated to $t = \infty$ on the assumption that the different outcomes occurred in the same proportions as they had up to 1 Gyr), confirming that 1 Gyr of simulation is enough to understand the behaviour of such systems.

Finally, I moved the inner boundary from 0.5 to 0.1 au finding no significant changes in $t_{\rm ej}$, $f_{\rm acc,p}$. As expected $f_{\rm in}$ is decreased and $\Sigma(r)$ becomes flatter, but only within 4 au as predicted in §6.5.2.

6.7 Conclusions

In this chapter I have studied the evolution of exocomets in exoplanetary systems using a set of N-body simulations. I focused specifically on how the scattering process varies as a function of the architecture of the planetary system when exocomets originate in the outer region of a system (50 au), e.g. in an outer belt, and start being scattered in by the outermost planet. I was interested in the delivery of material to the terrestrial region, either as exozodiacal dust or cometary material (including volatiles) onto planets themselves.

This chapter aimed to assess whether exocomets scattered by planets could provide a plausible explanation for exozodiacal dust commonly observed in exoplanetary systems. I found that the systems of tightly packed low mass planets lead to the highest fraction ($\sim 7\%$) of scattered comets reaching the inner regions, where they could resupply exozodis. Moreover, for a given pair of outermost planets, systems with decreasing (increasing) planet spacing and mass towards the star lead to higher (lower) levels of exozodis. I also found that systems with a very high mass innermost planet (e.g. 150 $M_\oplus$) are inefficient at producing exozodis. However, although tightly packed low mass planets are the most efficient at feeding exozodis, the fraction of comets scattered within 0.5 au does not change by more than a factor of ~ 7 (1-7%) when varying the architecture of the planetary systems that I tested, noting that my simulations were generally devoid of planets more massive than 0.3 $M_{\rm Jup}$. The fact that this fraction does not change by orders of magnitude suggests that many different types of planetary architectures could be efficient at feeding exozodis, possibly explaining the high frequency of exozodis around nearby stars.

In addition, I characterised the surface density of scattered comets between the exozodi region and an outer belt of exocomets. The surface density can be used as a test for the scattering scenario to resupply exozodis since feeding an exozodi could require the presence of a scattered disc that is bright enough to be detectable. First, I found that the surface density radial profile of the scattered disc between the planets typically increases with distance to the star instead of being flat as in a purely P-R drag scenario.

Second, unlike the fraction of scattered comets into 0.5 au ($f_{\rm in}$), the surface density of comets can vary by two orders of magnitude and is not directly proportional to the fraction scattered inwards. For example, systems of tightly packed planets have a higher $f_{\rm in}$, but a lower surface density compared to a system of planets with medium spacing. This implies that for a given exozodi, the amount of scattered material present between the planets can vary depending on the specific planetary architecture, with systems of low mass planets and medium spacing having the highest surface density of material between the planets. Future space missions like JWST or a FIR space telescope should be able to detect and characterize scattered discs in thermal emission around nearby systems with exozodis, setting tight constraints for the comet scattering scenario. For some systems, current observational limits already allow me to set some constraints. For example, the current Herschel and ALMA limits on the dust emission in between η Corvi's exozodi (< 1 au) and outer belt (100-200 au) can be used to rule out some planetary architectures. For chains of equal mass planets and tightly spaced (12 mutual Hill radii), I find that only planet masses between 30 and 300 $M_\oplus$ could feed the exozodi at a high enough rate and hide an scattered disc below current upper limits, assuming the exozodi levels have stayed roughly constant and planetesimals/comets have a maximum size of about 100 km.

Finally, I have studied the delivery of volatiles by exocomets to the inner planets via impacts. I found that for a variety of architectures the delivery of material is relatively efficient. For every thousand comets scattered, between 1-10 are delivered to each inner planet. This is efficient enough to deliver the mass in Earth's oceans if ~ 1 $M_\oplus$ of icy exocomets were being scattered, which is reasonable considering the expected initial mass of exo-Kuiper belts. Of the planetary architectures explored in this chapter, I found that chains of low mass planets with medium spacing (~ 20 mutual Hill radii) are one of the most efficient at delivering comets to inner planets. If the spacing is reduced below ~ 20 mutual Hill radii, the fraction of particles scattered to the exozodi region increases, but the number of impacts per inner planet decreases. This is because particles scattered by tightly spaced planets evolve faster and are lost before they can be accreted by a planet. This results in a lower surface density of the scattered disc for these systems. The systems that lead to the most planetary impacts have low mass outer planets and high mass inner planets. This configuration maximises the collisional cross-section of inner planets as they have high masses and the particles scattered in by low

mass planets have lower relative velocities. Hence, low mass outer planets are best suited for delivering material to the inner planets. My results show that exoplanetary systems could potentially deliver volatiles to inner planets at a similar level to Earth, and if chains of low mass planets are common, they may not lack the volatiles necessary to sustain life.

7

Conclusions

7.1 Summary

This thesis has studied debris discs through the analysis of ALMA observations and the use of numerical simulations. I showed how these observations can be used to constrain the distribution and volatile content of planetesimals; how numerical simulations can be used to infer the initial distribution of solids in an evolved debris disc; how the scattering of exocomets could lead to observable levels of hot dust and volatile delivery to inner planets; and how debris disc observations can place tight constraints on the presence of planets at tens of au. Below I summarise the main conclusions.

- **Chapter 2**. I analysed ALMA observations of the debris disc around the star HD 181327. I found that the disc of planetesimals is consistent with an axisymmetric narrow belt with a mean radius and width of 86 and 23 au, respectively. Additionally, I detected an extended component that is consistent with a dusty halo or secondary belt.

  I also detected CO gas emission in this system, which represents the first gas detection in a debris disc around a solar-type star. Because the CO gas has very low densities and is co-located with the belt of planetesimals, the observed gas must be of secondary origin and released in collisions of volatile-rich planetesimals, i.e. exocomets. The derived

CO+CO_2 abundances in planetesimals are consistent with the composition observed in Solar System comets.

- **Chapter 3**. I analysed ALMA observations of the debris disc around the star η Corvi. This system is particularly interesting as it presents both an exozodi that must be replenished from material formed further out, and an outer belt of planetesimals. I found that its outer belt has a mean radius and width of 150 and 44 au, respectively; is consistent with being axisymmetric; and is too narrow compared with models of a LHB-like instability, in which vast amounts of material from an outer belt are delivered to the inner regions, and thus explaining its exozodi. Moreover, I constrained the eccentricity of the outer belt to be lower than 0.05, finally concluding that the outer belt is likely in a stable configuration on Gyr timescales, where a chain of planets is scattering material from the outer belt into the inner regions.

  I searched for CO gas emission and I found a tentative detection at around 20 au, i.e. between the exozodi and outer belt. The level of CO detected is so low that the gas must be of secondary origin and possibly continually released by volatile-rich bodies. I found that a possible explanation for the gas not being co-located with the dust is that the observed CO is released in situ when icy bodies being scattered from the outer belt cross an ice line, e.g. CO_2 or water iceline, as outgassing comets do in the Solar System. This scenario is consistent with the big picture of the system, in which material is transported in from the outer belt resupplying the exozodi. This tentative detection could represent the first observation of outgassing exocomets as we observe them in the Solar System.

  Based on the structure of the outer belt and scattering analytic considerations I placed constraints on the semi-major axis, mass and eccentricity of the outermost planet in the system (interior to the outer belt) that is scattering material to the inner regions of the system.

- **Chapter 4** I studied the multiplanet system 61 Vir using ALMA observations of its debris disc and numerical simulations of its collisional evolution. I found that the disc extends from 30 to at least 150 au and has a surface density of dust that is consistent with being constant as a function of radius. By modelling the collisional evolution of a broad debris disc I concluded that the surface density of dust does not necessarily match the surface density profile of the parent bodies, tending to be flatter in regions of the disc where the collisional lifetime of the largest planetesimals is longer than the age of the system. Moreover, using the same models I found that 61 Vir's disc is consistent with a broad debris disc that started its collisional evolution $\sim$50 times more depleted in solids compared to a MMSN, and with planetesimals up to a size of 5-20 km. Finally, based on the disc inner edge, planetesimal stirring up to 150 au and known RV planets, I

constrained the semi-major axis, eccentricity and mass of an unseen planet responsible of planetesimals being stirred up to 150 au.

- **Chapter 5** I studied the solar analogue HD 107146 using ALMA observations that reveal the radial structure of its exo-Kuiper belt at wavelengths of 1.1 and 0.86 mm. I found that the planetesimal disc is broad, extending from 40 to 140 au, and it is characterised by a circular gap extending from 60 to 100 au in which the continuum emission drops by about 50%. To date, HD 107146 is the only gas-poor system showing multiple rings in the distribution of millimetre sized particles. These rings suggest a similar distribution of the planetesimals producing small dust grains that could be explained invoking the presence of one or more perturbing planets. Because the disc appears axisymmetric, such planets should be on circular orbits. By comparing N-body simulations with the observed visibilities I found that to explain the radial extent and depth of the gap, it would require the presence of multiple low mass planets or a single planet that migrated through the disc. Interior to HD 107146's exo-Kuiper belt I also found extended emission with a peak at $\sim$ 20 au and consistent with the inner warm belt that was previously predicted based on 22μm excess as in many other systems. This warm belt is the first to be imaged, although unexpectedly suggesting that it is asymmetric. This could be due to a large belt eccentricity or due to clumpy structure produced by resonant trapping with an additional inner planet.

- **Chapter 6** I investigated how the process of inward scattering of comets originating in an outer belt, is affected by the architecture of a planetary system, to determine whether this could lead to observable exozodi levels or deliver volatiles to inner planets. Using N-body simulations, I modelled systems with different planet mass and orbital spacing distributions in the 1-50 au region. I found that tightly packed ($\Delta a_{\rm p} < 20 R_{\rm H,m}$) low mass planets are the most efficient at delivering material to exozodi regions (5-7% of scattered exocomets end up within 0.5 au at some point), although the exozodi levels do not vary by more than a factor of ~ 7 for the architectures studied here. I suggested that emission from scattered dusty material in between the planets could provide a potential test for this delivery mechanism. I showed that the surface density of scattered material can vary by two orders of magnitude (being highest for systems of low mass planets with medium spacing), whilst the exozodi delivery rate stays roughly constant, and that future instruments such as JWST could detect it. In fact for η Corvi, the current Herschel upper limit rules out the scattering scenario by a chain of $\lesssim$30 M$_\oplus$ planets. Finally, we show that exocomets could be efficient at delivering cometary material to inner planets (0.1-1% of scattered comets are accreted per inner planet). Overall, the best systems at delivering comets to inner planets are the ones that have low mass outer planets and medium spacing ($\sim 20 R_{\rm H,m}$).

7.2 Future

Debris disc studies have been revolutionised in the last decade by the development of new observatories such as Herschel and ALMA, which with an unprecedented sensitivity and resolution in the far-IR and millimetre have allowed detailed characterisation of exo-Kuiper belts. Despite the great progress, fundamental questions remain open which could be answered in the next 10 years. Below I describe some of the most promising avenues of debris disc research for answering these questions.

7.2.1 The volatile composition of exocomets, beyond CO

Although we know of ∼20 debris disc systems with gas and this number has been steadily increasing in the last few years, only in four systems it is certain that the observed CO gas is of secondary origin, i.e. released by exocomets. This is because in most of debris disc observations with ALMA in which CO has been targeted the sensitivities have only been sufficient to detect high levels of CO, i.e. primordial gas. In the four systems where secondary origin gas has been detected, it was required an hour or more of integration with ALMA (the most sensitive instrument at submillimetre wavelengths). It is possible that all debris discs have gas that is released in collisions of icy planetesimals (Kral et al., 2017b), however, in order to test this hypothesis it is necessary to do deep CO surveys that can either detect low levels of CO or place meaningful upper limits.

Debris disc gas studies need to be expanded to other molecular species. So far, all the volatile species detected in gaseous debris discs can be understood as products of CO or CO_2 released by icy planetesimals and the products of its photodissociation (CO, CI, CII and OI). This is problematic because it means that when comparing the nature of these exocomets with Solar System comets we do so by inferring the CO+CO_2 absolute abundances in exocometary ices which have large uncertainties (Chapter 2). However, if we were able to measure other molecular species we could compare relative abundances with much greater precision. One of the most promising molecules is HCN and CN, which have lifetimes similar to CO (∼10-100 yr) and are strong emitters at submillimetre wavelengths. Similar to CO, HCN is abundant in Solar System comets and could be directly released from planetesimals and CN a product of HCN photodissociation. HCN is of particular interest as together with water could be a key molecule for the emergence of life via prebiotic chemistry (Patel et al., 2015)

7.2.2 Outgassing exocomets

It is known that at least 20-30% of nearby stars present exozodis that need to be resupplied by material formed further out in those systems, that somehow is transported in. As shown in Chapter 6, comets scattered in by planets could transport material from the outer regions into within a few au to resupply exozodis. In Chapter 3 I showed strong evidence to support such scenario, where I detected CO gas likely being released from outgassing exocomets when being scattered in by planets around η Corvi. However, the search for volatiles originated from outgassing exocomets has not been expanded to other systems.

I plan to to do the first survey to search for gas being released from outgassing exocomets around systems with exozodis using ALMA. CO and HCN are the most promising molecules to detect as stated above. Although the CO around η Corvi was barely detected with deep observations, the level of cometary activity could be two orders of magnitude higher around other systems with similar or even lower exozodi levels. This is because the density distribution of comets being scattered depends strongly on the planetary system architecture and is not strictly correlated with exozodi levels (Chapter 6, see Fig. 7.1). I have selected systems within 18 pc (η Corvi's distance) and with F or G type central stars (i.e. $L_\star < 5L_\odot$), resulting in a sample of 7 systems: τ Ceti, HD22484, HD131156, HD222368, HD14412, e Eri, HD69830. Four of these systems have detected outer discs, although it is possible that the other three also have exo-Kuiper belts that are not massive enough to be detected yet (note that our Kuiper belt is not massive enough to be detectable in another system with current instrumentation). Higher stellar luminosities would significantly shorten the lifetime of CO and HCN near the outgassing region, and thus their densities and observed flux.

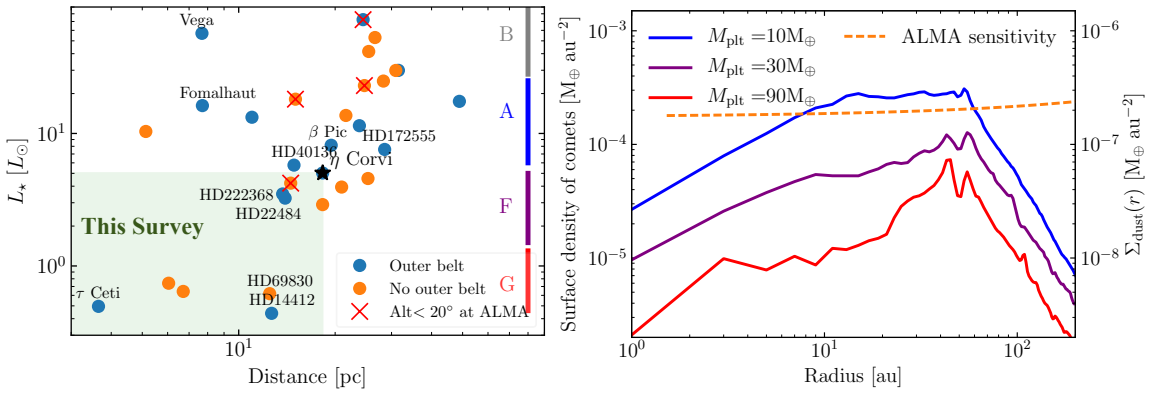

Figure 7.1: ***Left:*** Luminosity vs distance of nearby stars with exozodis (Absil et al., 2013; Ertel et al., 2014). ***Right:*** Surface density of scattered comets for different planet masses (color lines). The lower the planet mass and stellar luminosity the greater the comet density and CO lifetime, and thus CO flux.

Alternatively, the study of exocomets could also be expanded by looking for comets in transit surveys. It was only recently that Rappaport et al. (2018) reported the presence of a comet-like

transits in two systems monitored by the Kepler mission. Future transit missions could detect a larger population of systems exhibiting this behaviour at lower levels, opening a new window for exocomet studies.

7.2.3 Debris discs around low-mass stars

While thousands of planets have been discovered around Solar type stars, only a few tens have been detected around low mass stars (Astudillo-Defru et al., 2017). However, their occurrence rate could be as high as 30-50% for both groups (Fressin et al., 2013; Dressing & Charbonneau, 2013; He et al., 2017). This is relevant as most of the discovered planets around FGKs are too close to their host star, and thus uninhabitable. On the other hand, planets around lower mass/luminosity stars, e.g. ultra cool dwarfs (UCDs), in similar close in orbits could be temperate and sustain liquid water. It was only recently that Gillon et al. (2017) found seven terrestrial planets within 0.06 au around TRAPPIST-1, a nearby UCD (M8), with three of them in the habitable zone. While low-mass planets in compact orbits are known to be common around FGK stars, this was the first indication that such systems could also be common around lower mass stars and thus the majority of habitable planets could be in fact around low mass stars. However, since UCD undergo significant evolution of the habitable zone, this could mean that the three transiting planets that are currently in the habitable zone may not have any water if formed in situ.

I have been awarded ALMA time to observe Trappist-1 (8h cycle 5, ranked A) for the first time, data that I will analyse to determine if Trappist-1 hosts a debris disc. This is the key to understand the habitability of these type of exoplanets, since planetesimals discs can provide bombardment and delivery of volatiles. Moreover, if a disc is detected based on its structure I will constrain the formation history of inner planets, e.g. if formed further out and migrated in, providing unique constraints on planet formation around low-mass stars and indicating if these habitable planets could have formed water rich. Finally, I will also use these observations to investigate the presence of additional planets beyond 1 au where transit probabilities are zero.

Bibliography

Absil, O., Defrère, D., Coudé du Foresto, V., et al. 2013, A&A, 555, A104

Absil, O., di Folco, E., Mérand, A., et al. 2006, A&A, 452, 237

Acke, B., Min, M., Dominik, C., et al. 2012, A&A, 540, A125

Alexander, R. D., Clarke, C. J., & Pringle, J. E. 2006, Monthly Notices of the Royal Astronomical Society, 369, 216

Alibert, Y., Baraffe, I., Benz, W., et al. 2006, A&A, 455, L25

ALMA Partnership, Brogan, C. L., Pérez, L. M., et al. 2015, ApJ, 808, L3

Andrews, S. M., Rosenfeld, K. A., Kraus, A. L., & Wilner, D. J. 2013, ApJ, 771, 129

Andrews, S. M., Wilner, D. J., Espaillat, C., et al. 2011, ApJ, 732, 42

Andrews, S. M., Wilner, D. J., Zhu, Z., et al. 2016, ApJ, 820, L40

Ansdell, M., Williams, J. P., van der Marel, N., et al. 2016, ApJ, 828, 46

Ardila, D. R., Golimowski, D. A., Krist, J. E., et al. 2004, ApJ, 617, L147

Astudillo-Defru, N., Forveille, T., Bonfils, X., et al. 2017, A&A, 602, A88

Aumann, H. H., Beichman, C. A., Gillett, F. C., et al. 1984, ApJ, 278, L23

Backman, D., Marengo, M., Stapelfeldt, K., et al. 2009, ApJ, 690, 1522

Backman, D. E., & Paresce, F. 1993, in Protostars and Planets III, ed. E. H. Levy & J. I. Lunine, 1253–1304

Ballering, N. P., Rieke, G. H., & Gáspár, A. 2014, ApJ, 793, 57

Batalha, N. M., Rowe, J. F., Bryson, S. T., et al. 2013, ApJS, 204, 24

Benz, W., & Asphaug, E. 1999, Icarus, 142, 5

Besla, G., & Wu, Y. 2007, ApJ, 655, 528

Beust, H., & Morbidelli, A. 1996, Icarus, 120, 358

Beust, H., Vidal-Madjar, A., Ferlet, R., & Lagrange-Henri, A. M. 1990, A&A, 236, 202

Birnstiel, T., Dullemond, C. P., & Brauer, F. 2010, A&A, 513, A79

Bitsch, B., Lambrechts, M., & Johansen, A. 2015, A&A, 582, A112

Biver, N., Bockelee-Morvan, D., Colom, P., et al. 1997, Science, 275, 1915

Blum, J. 2018, Space Sci. Rev., 214, 52

Blum, J., & Wurm, G. 2008, Annual Review of Astronomy and Astrophysics, 46, 21

Boccaletti, A., Thalmann, C., Lagrange, A.-M., et al. 2015, Nature, 526, 230

Bohren, C. F., & Huffman, D. 1983, Absorption and scattering of light by small particles, Wiley science paperback series (Wiley)

Boley, A. C. 2009, ApJ, 695, L53

Boley, A. C., Payne, M. J., Corder, S., et al. 2012, ApJ, 750, L21

Bonsor, A., Augereau, J.-C., & Thébault, P. 2012, A&A, 548, A104

Bonsor, A., Raymond, S. N., & Augereau, J.-C. 2013, MNRAS, 433, 2938

Bonsor, A., Raymond, S. N., Augereau, J.-C., & Ormel, C. W. 2014, MNRAS, 441, 2380

Bonsor, A., & Wyatt, M. C. 2012, MNRAS, 420, 2990

Booth, M., Jordán, A., Casassus, S., et al. 2016, MNRAS, 460, L10

Booth, M., Wyatt, M. C., Morbidelli, A., Moro-Martín, A., & Levison, H. F. 2009, MNRAS, 399, 385

Borgniet, S., Lagrange, A.-M., Meunier, N., & Galland, F. 2017, A&A, 599, A57

Boss, A. P. 1997, Science, 276, 1836

Brasser, R., Duncan, M. J., & Levison, H. F. 2008, Icarus, 196, 274

Brown, M. E. 2002, Annual Review of Earth and Planetary Sciences, 30, 307

Bryden, G., Beichman, C. A., Carpenter, J. M., et al. 2009, ApJ, 705, 1226

Bryden, G., Beichman, C. A., Trilling, D. E., et al. 2006, ApJ, 636, 1098

Burns, J. A., Lamy, P. L., & Soter, S. 1979, Icarus, 40, 1

Carniani, S., Maiolino, R., De Zotti, G., et al. 2015, A&A, 584, A78

Carpenter, J. M., Bouwman, J., Mamajek, E. E., et al. 2009a, ApJS, 181, 197

Carpenter, J. M., Mamajek, E. E., Hillenbrand, L. A., & Meyer, M. R. 2009b, ApJ, 705, 1646

Casassus, S., Cabrera, G. F., Förster, F., et al. 2006, ApJ, 639, 951

Casassus, S., Marino, S., Pérez, S., et al. 2015, ApJ, 811, 92

Casassus, S., Perez M., S., Jordán, A., et al. 2012, ApJ, 754, L31

Casassus, S., van der Plas, G., Perez, S. M., et al. 2013, Nature, 493, 191

Cassan, A., Kubas, D., Beaulieu, J.-P., et al. 2012, Nature, 481, 167

Cataldi, G., Brandeker, A., Olofsson, G., et al. 2014, A&A, 563, A66

Cavanagh, B., Jenness, T., Economou, F., & Currie, M. J. 2008, Astronomische Nachrichten, 329, 295

Chambers, J. E. 1999, MNRAS, 304, 793

Chambers, J. E., & Wetherill, G. W. 1998, Icarus, 136, 304

Chambers, J. E., Wetherill, G. W., & Boss, A. P. 1996, Icarus, 119, 261

Chapin, E. L., Berry, D. S., Gibb, A. G., et al. 2013, MNRAS, 430, 2545

Chatterjee, S., Ford, E. B., Matsumura, S., & Rasio, F. A. 2008, ApJ, 686, 580

Chen, C. H., Fitzgerald, M. P., & Smith, P. S. 2008, ApJ, 689, 539

Chen, C. H., Mittal, T., Kuchner, M., et al. 2014, ApJS, 211, 25

Chen, C. H., Sargent, B. A., Bohac, C., et al. 2006, ApJS, 166, 351

Chen, C. H., Sheehan, P., Watson, D. M., Manoj, P., & Najita, J. R. 2009, ApJ, 701, 1367

Chen, J., & Kipping, D. 2017, ApJ, 834, 17

Chiang, E., Kite, E., Kalas, P., Graham, J. R., & Clampin, M. 2009, ApJ, 693, 734

Chiang, E., & Laughlin, G. 2013, MNRAS, 431, 3444

Choukroun, M., Keihm, S., Schloerb, F. P., et al. 2015, A&A, 583, A28

Cieza, L. A., Casassus, S., Tobin, J., et al. 2016, Nature, 535, 258

Civs, S., Juha, L., Babnkov, D., et al. 2004, Chemical Physics Letters, 386, 169

Clarke, C. J. 2007, MNRAS, 376, 1350

Collings, M. P., Anderson, M. A., Chen, R., et al. 2004, MNRAS, 354, 1133

Collings, M. P., Dever, J. W., Fraser, H. J., McCoustra, M. R. S., & Williams, D. A. 2003, ApJ, 583, 1058

Coughlan, C. P., & Gabuzda, D. C. 2013, in European Physical Journal Web of Conferences, Vol. 61, European Physical Journal Web of Conferences, 7009

Crida, A., Masset, F., & Morbidelli, A. 2009, ApJ, 705, L148

Crifo, F., Vidal-Madjar, A., Lallement, R., Ferlet, R., & Gerbaldi, M. 1997, A&A, 320, L29

Davis, D. R., & Ryan, E. V. 1990, Icarus, 83, 156

de Niem, D., Kührt, E., Morbidelli, A., & Motschmann, U. 2012, Icarus, 221, 495

Defrère, D., Absil, O., Augereau, J.-C., et al. 2011, A&A, 534, A5

Defrère, D., Hinz, P. M., Skemer, A. J., et al. 2015, ApJ, 799, 42

Dent, W. R. F., Greaves, J. S., & Coulson, I. M. 2005, MNRAS, 359, 663

Dent, W. R. F., Wyatt, M. C., Roberge, A., et al. 2014, Science, 343, 1490

Dickinson, A. S., & Richards, D. 1975, Journal of Physics B Atomic Molecular Physics, 8, 2846

Dipierro, G., Price, D., Laibe, G., et al. 2015, MNRAS, 453, L73

Dohnanyi, J. S. 1969, J. Geophys. Res., 74, 2531

Dominik, C., & Decin, G. 2003, ApJ, 598, 626

Donaldson, J. K., Lebreton, J., Roberge, A., Augereau, J.-C., & Krivov, A. V. 2013, ApJ, 772, 17

Draine, B. T. 2003, ApJ, 598, 1017

Dressing, C. D., & Charbonneau, D. 2013, ApJ, 767, 95

Duchêne, G., Arriaga, P., Wyatt, M., et al. 2014, ApJ, 784, 148

Dullemond, C., Juhasz, A., Pohl, A., et al. 2015, RADMC3D v0.39 http://www.ita.uni-heidelberg.de/ dullemond/software/radmc-3d/

—. 2016, RADMC3D v0.40 http://www.ita.uni-heidelberg.de/ dullemond/software/radmc-3d/

Duncan, M., Quinn, T., & Tremaine, S. 1987, AJ, 94, 1330

—. 1989, Icarus, 82, 402

Duncan, M. J., & Levison, H. F. 1997, Science, 276, 1670

Duncan, M. J., Levison, H. F., & Budd, S. M. 1995, AJ, 110, 3073

Durda, D. D., & Dermott, S. F. 1997, Icarus, 130, 140

Dutrey, A., Lecavelier Des Etangs, A., & Augereau, J.-C. 2004, The observation of circumstellar

disks: dust and gas components, ed. M. C. Festou, H. U. Keller, & H. A. Weaver, 81–95
Eiroa, C., Marshall, J. P., Mora, A., et al. 2013, A&A, 555, A11
Eiroa, C., Rebollido, I., Montesinos, B., et al. 2016, A&A, 594, L1
Ercolano, B., & Pascucci, I. 2017, Royal Society Open Science, 4, 170114
Ertel, S., Absil, O., Defrère, D., et al. 2014, A&A, 570, A128
Ertel, S., Wolf, S., Metchev, S., et al. 2011, A&A, 533, A132
Espaillat, C., Muzerolle, J., Najita, J., et al. 2014, Protostars and Planets VI, 497
Fang, J., & Margot, J.-L. 2013, ApJ, 767, 115
Faramaz, V., Beust, H., Augereau, J.-C., Kalas, P., & Graham, J. R. 2015, A&A, 573, A87
Faramaz, V., Ertel, S., Booth, M., Cuadra, J., & Simmonds, C. 2017, MNRAS, 465, 2352
Feldt, M., Olofsson, J., Boccaletti, A., et al. 2017, A&A, 601, A7
Ferlet, R., Vidal-Madjar, A., & Hobbs, L. M. 1987, A&A, 185, 267
Fernandez, J. A., & Ip, W.-H. 1984, Icarus, 58, 109
Fontenla, J. M., Balasubramaniam, K. S., & Harder, J. 2007, ApJ, 667, 1243
Ford, E. B., & Rasio, F. A. 2008, ApJ, 686, 621
Foreman-Mackey, D., Hogg, D. W., Lang, D., & Goodman, J. 2013, PASP, 125, 306
Foreman-Mackey, D., Price-Whelan, A., Ryan, G., et al. 2014, triangle.py v0.1.1
Fressin, F., Torres, G., Charbonneau, D., et al. 2013, ApJ, 766, 81
Fujiwara, A., Cerroni, P., Davis, D., Ryan, E., & di Martino, M. 1989, in Asteroids II, ed. R. P. Binzel, T. Gehrels, & M. S. Matthews, 240–265
Fukagawa, M., Tamura, M., Itoh, Y., et al. 2006, ApJ, 636, L153
Gagné, J., Faherty, J. K., Cruz, K., et al. 2014, ApJ, 785, L14
Gaia Collaboration, Brown, A. G. A., Vallenari, A., et al. 2018, ArXiv e-prints
—. 2016a, A&A, 595, A2
Gaia Collaboration, Prusti, T., de Bruijne, J. H. J., et al. 2016b, A&A, 595, A1
Gehrels, N. 1986, ApJ, 303, 336
Geiler, F., & Krivov, A. V. 2017, MNRAS, 468, 959
Gillon, M., Triaud, A. H. M. J., Demory, B.-O., et al. 2017, Nature, 542, 456
Golimowski, D. A., Krist, J. E., Stapelfeldt, K. R., et al. 2011, AJ, 142, 30
Gomes, R., Levison, H. F., Tsiganis, K., & Morbidelli, A. 2005, Nature, 435, 466
Gomes, R. S., Morbidelli, A., & Levison, H. F. 2004, Icarus, 170, 492
Gontcharov, G. A. 2006, Astronomy Letters, 32, 759
Greaves, J. S., Holland, W. S., Jayawardhana, R., Wyatt, M. C., & Dent, W. R. F. 2004, MNRAS, 348, 1097
Greaves, J. S., Holland, W. S., Matthews, B. C., et al. 2016, MNRAS, 461, 3910
Hahn, J. M., & Malhotra, R. 1999, AJ, 117, 3041
—. 2005, AJ, 130, 2392
Hales, A. S., Barlow, M. J., Crawford, I. A., & Casassus, S. 2017, MNRAS, 466, 3582

Hansen, B. M. S., & Murray, N. 2012, ApJ, 751, 158
Hayashi, C. 1981, Progress of Theoretical Physics Supplement, 70, 35
He, M. Y., Triaud, A. H. M. J., & Gillon, M. 2017, MNRAS, 464, 2687
Heap, S. R., Lindler, D. J., Lanz, T. M., et al. 2000, ApJ, 539, 435
Hillenbrand, L. A., Carpenter, J. M., Kim, J. S., et al. 2008, ApJ, 677, 630
Holland, W. S., Bintley, D., Chapin, E. L., et al. 2013, MNRAS, 430, 2513
Holland, W. S., Matthews, B. C., Kennedy, G. M., et al. 2017, MNRAS, 470, 3606
Hudson, R. D. 1971, Reviews of Geophysics and Space Physics, 9, 305
Hughes, A. M., Duchene, G., & Matthews, B. 2018, ArXiv e-prints
Ibukiyama, A., & Arimoto, N. 2002, A&A, 394, 927
Ida, S., Bryden, G., Lin, D. N. C., & Tanaka, H. 2000, ApJ, 534, 428
Ida, S., & Lin, D. N. C. 2010, ApJ, 719, 810
Ida, S., & Makino, J. 1993, Icarus, 106, 210
Isella, A., Guidi, G., Testi, L., et al. 2016, Phys. Rev. Lett., 117, 251101
Jackson, A. P., Wyatt, M. C., Bonsor, A., & Veras, D. 2014, MNRAS, 440, 3757
Johansen, A., & Lacerda, P. 2010, MNRAS, 404, 475
Johansen, A., & Lambrechts, M. 2017, Annual Review of Earth and Planetary Sciences, 45, 359
Johansen, A., Mac Low, M.-M., Lacerda, P., & Bizzarro, M. 2015, Science Advances, 1, 1500109
Johansen, A., Oishi, J. S., Mac Low, M.-M., et al. 2007, Nature, 448, 1022
Jurić, M., & Tremaine, S. 2008, ApJ, 686, 603
Kalas, P., Graham, J. R., Chiang, E., et al. 2008, Science, 322, 1345
Kalas, P., Graham, J. R., & Clampin, M. 2005, Nature, 435, 1067
Kalas, P., Graham, J. R., Fitzgerald, M. P., & Clampin, M. 2013, ApJ, 775, 56
Kass, R. E., & Raftery, A. E. 1995, Journal of the American Statistical Association, 90, 773
Kataoka, A., Tanaka, H., Okuzumi, S., & Wada, K. 2013, A&A, 557, L4
Kennedy, G. M., & Kenyon, S. J. 2008, ApJ, 682, 1264
Kennedy, G. M., Matrà, L., Marmier, M., et al. 2015a, MNRAS, 449, 3121
Kennedy, G. M., & Piette, A. 2015, MNRAS, 449, 2304
Kennedy, G. M., & Wyatt, M. C. 2010, MNRAS, 405, 1253
—. 2011, MNRAS, 412, 2137
—. 2014, MNRAS, 444, 3164
Kennedy, G. M., Wyatt, M. C., Bailey, V., et al. 2015b, ApJS, 216, 23
Kenyon, S. J., & Bromley, B. C. 2002, ApJ, 577, L35
—. 2008, ApJS, 179, 451
—. 2010, ApJS, 188, 242
Kiefer, F., Lecavelier des Etangs, A., Boissier, J., et al. 2014, Nature, 514, 462
Kirsh, D. R., Duncan, M., Brasser, R., & Levison, H. F. 2009, Icarus, 199, 197
Klahr, H., & Lin, D. N. C. 2005, ApJ, 632, 1113

Kóspál, Á., Moór, A., Juhász, A., et al. 2013, ApJ, 776, 77
Kral, Q., Krivov, A. V., Defrère, D., et al. 2017a, The Astronomical Review, 13, 69
Kral, Q., & Latter, H. 2016, MNRAS, 461, 1614
Kral, Q., Matrà, L., Wyatt, M. C., & Kennedy, G. M. 2017b, MNRAS, 469, 521
Kral, Q., Thébault, P., Augereau, J.-C., Boccaletti, A., & Charnoz, S. 2015, A&A, 573, A39
Kral, Q., Thébault, P., & Charnoz, S. 2013, A&A, 558, A121
Kral, Q., Wyatt, M., Carswell, R. F., et al. 2016, MNRAS, 461, 845
Kral, Q., Wyatt, M. C., Triaud, A. H. M. J., et al. 2018, ArXiv e-prints
Krijt, S., & Kama, M. 2014, A&A, 566, L2
Krist, J. E., Stapelfeldt, K. R., Bryden, G., & Plavchan, P. 2012, AJ, 144, 45
Krivov, A. V. 2010, Research in Astronomy and Astrophysics, 10, 383
Krivov, A. V., Eiroa, C., Löhne, T., et al. 2013, ApJ, 772, 32
Krivov, A. V., Ide, A., Löhne, T., Johansen, A., & Blum, J. 2018, MNRAS, 474, 2564
Krivov, A. V., Löhne, T., & Sremčević, M. 2006, A&A, 455, 509
Krivov, A. V., Mann, I., & Krivova, N. A. 2000, A&A, 362, 1127
Krivov, A. V., Müller, S., Löhne, T., & Mutschke, H. 2008, ApJ, 687, 608
Krivov, A. V., Queck, M., Löhne, T., & Sremčević, M. 2007, A&A, 462, 199
Kuchner, M. J. 2004, ApJ, 612, 1147
Kurucz, R. L. 1979, ApJS, 40, 1
Lacour, S., Biller, B., Cheetham, A., et al. 2016, A&A, 590, A90
Lagrange, A.-M., Desort, M., Galland, F., Udry, S., & Mayor, M. 2009a, A&A, 495, 335
Lagrange, A.-M., Gratadour, D., Chauvin, G., et al. 2009b, A&A, 493, L21
Lambrechts, M., & Johansen, A. 2012, A&A, 544, A32
Lebreton, J., Augereau, J.-C., Thi, W.-F., et al. 2012, A&A, 539, A17
Lebreton, J., Beichman, C., Bryden, G., et al. 2016, ApJ, 817, 165
Levanda, R., & Leshem, A. 2010, IEEE Signal Processing Magazine, 27, 14
Levison, H. F., & Duncan, M. J. 1997, Icarus, 127, 13
Levison, H. F., Duncan, M. J., & Wetherill, G. W. 1994, Nature, 372, 441
Levison, H. F., Duncan, M. J., Zahnle, K., Holman, M., & Dones, L. 2000, Icarus, 143, 415
Levison, H. F., Thommes, E., & Duncan, M. J. 2010, AJ, 139, 1297
Lewis, B. R., & Carver, J. H. 1983, J. Quant. Spec. Radiat. Transf., 30, 297
Li, A., & Greenberg, J. M. 1997, A&A, 323, 566
—. 1998, A&A, 331, 291
Lieman-Sifry, J., Hughes, A. M., Carpenter, J. M., et al. 2016, ApJ, 828, 25
Lissauer, J. J. 1987, Icarus, 69, 249
—. 1993, ARA&A, 31, 129
—. 2007, ApJ, 660, L149
Lissauer, J. J., & Stewart, G. R. 1993, in Protostars and Planets III, ed. E. H. Levy & J. I. Lunine,

1061–1088
Lisse, C. M., Wyatt, M. C., Chen, C. H., et al. 2012, ApJ, 747, 93
Löhne, T., Krivov, A. V., Kirchschlager, F., Sende, J. A., & Wolf, S. 2017, A&A, 605, A7
Löhne, T., Krivov, A. V., & Rodmann, J. 2008, ApJ, 673, 1123
Loukitcheva, M., Solanki, S. K., Carlsson, M., & Stein, R. F. 2004, A&A, 419, 747
Lyra, W., & Kuchner, M. 2013, Nature, 499, 184
MacGregor, M. A., Matrà, L., Kalas, P., et al. 2017, ApJ, 842, 8
MacGregor, M. A., Wilner, D. J., Rosenfeld, K. A., et al. 2013, ApJ, 762, L21
Mallik, S. V., Parthasarathy, M., & Pati, A. K. 2003, A&A, 409, 251
Mamajek, E. E., & Bell, C. P. M. 2014, MNRAS, 445, 2169
Mannings, V., & Barlow, M. J. 1998, ApJ, 497, 330
Marboeuf, U., Bonsor, A., & Augereau, J.-C. 2016, Planet. Space Sci., 133, 47
Marengo, M., Lisse, C. M., Hulsebus, A., et al. in prep
Marino, S., Casassus, S., Perez, S., et al. 2015, ApJ, 813, 76
Marino, S., Matrà, L., Stark, C., et al. 2016, MNRAS, 460, 2933
Marino, S., Wyatt, M. C., Kennedy, G. M., et al. 2017a, MNRAS, 469, 3518
Marino, S., Wyatt, M. C., Panić, O., et al. 2017b, MNRAS, 465, 2595
Marois, C., Macintosh, B., Barman, T., et al. 2008, Science, 322, 1348
Marois, C., Zuckerman, B., Konopacky, Q. M., Macintosh, B., & Barman, T. 2010, Nature, 468, 1080
Matrà, L., Dent, W. R. F., Wyatt, M. C., et al. 2017a, MNRAS, 464, 1415
Matrà, L., MacGregor, M. A., Kalas, P., et al. 2017b, ApJ, 842, 9
Matrà, L., Marino, S., Kennedy, G. M., et al. 2018, ApJ, 859, 72
Matrà, L., Panić, O., Wyatt, M. C., & Dent, W. R. F. 2015, MNRAS, 447, 3936
Matthews, B., Kennedy, G., Sibthorpe, B., et al. 2014a, ApJ, 780, 97
Matthews, B. C., Krivov, A. V., Wyatt, M. C., Bryden, G., & Eiroa, C. 2014b, Protostars and Planets VI, 521
Mayor, M., Marmier, M., Lovis, C., et al. 2011, ArXiv e-prints
Mayor, M., & Queloz, D. 1995, Nature, 378, 355
McMullin, J. P., Waters, B., Schiebel, D., Young, W., & Golap, K. 2007a, in Astronomical Society of the Pacific Conference Series, Vol. 376, Astronomical Data Analysis Software and Systems XVI, ed. R. A. Shaw, F. Hill, & D. J. Bell, 127
McMullin, J. P., Waters, B., Schiebel, D., Young, W., & Golap, K. 2007b, in Astronomical Society of the Pacific Conference Series, Vol. 376, Astronomical Data Analysis Software and Systems XVI, ed. R. A. Shaw, F. Hill, & D. J. Bell, 127
Meech, K. J., Yang, B., Kleyna, J., et al. 2013, ApJ, 776, L20
Meeus, G., Montesinos, B., Mendigutía, I., et al. 2012, A&A, 544, A78
Miles, B. E., Roberge, A., & Welsh, B. 2016, ApJ, 824, 126

Montgomery, S. L., & Welsh, B. Y. 2012, PASP, 124, 1042
Moór, A., Ábrahám, P., Derekas, A., et al. 2006, ApJ, 644, 525
Moór, A., Ábrahám, P., Juhász, A., et al. 2011, ApJ, 740, L7
Moór, A., Curé, M., Kóspál, Á., et al. 2017, ApJ, 849, 123
Moór, A., Henning, T., Juhász, A., et al. 2015a, ApJ, 814, 42
Moór, A., Kóspál, Á., Ábrahám, P., et al. 2015b, MNRAS, 447, 577
Morales, F. Y., Rieke, G. H., Werner, M. W., et al. 2011, ApJ, 730, L29
Morales, F. Y., Werner, M. W., Bryden, G., et al. 2009, ApJ, 699, 1067
Morbidelli, A. 2005, ArXiv Astrophysics e-prints
Morbidelli, A., Chambers, J., Lunine, J. I., et al. 2000, Meteoritics and Planetary Science, 35, 1309
Morbidelli, A., Lunine, J. I., O'Brien, D. P., Raymond, S. N., & Walsh, K. J. 2012, Annual Review of Earth and Planetary Sciences, 40, 251
Morbidelli, A., & Nesvorny, D. 2012, A&A, 546, A18
Moro-Martín, A., Carpenter, J. M., Meyer, M. R., et al. 2007, ApJ, 658, 1312
Moro-Martín, A., Marshall, J. P., Kennedy, G., et al. 2015, ApJ, 801, 143
Mouillet, D., Larwood, J. D., Papaloizou, J. C. B., & Lagrange, A. M. 1997, MNRAS, 292, 896
Muñoz-Gutiérrez, M. A., Pichardo, B., Reyes-Ruiz, M., & Peimbert, A. 2015, ApJ, 811, L21
Mumma, M. J., & Charnley, S. B. 2011, ARA&A, 49, 471
Murray, C. D., & Dermott, S. F. 1999, Solar system dynamics
Mustill, A. J., & Wyatt, M. C. 2009, MNRAS, 399, 1403
—. 2012, MNRAS, 419, 3074
Nesvold, E. R., Kuchner, M. J., Rein, H., & Pan, M. 2013, ApJ, 777, 144
Nesvorný, D., Jenniskens, P., Levison, H. F., et al. 2010, ApJ, 713, 816
Nesvorný, D., & Roig, F. 2001, Icarus, 150, 104
Nilsson, R., Liseau, R., Brandeker, A., et al. 2009, A&A, 508, 1057
Nordström, B., Mayor, M., Andersen, J., et al. 2004, A&A, 418, 989
Nuñez, P. D., Scott, N. J., Mennesson, B., et al. 2017, A&A, 608, A113
O'Brien, D. P., & Greenberg, R. 2003, Icarus, 164, 334
O'Brien, D. P., Morbidelli, A., & Levison, H. F. 2006, Icarus, 184, 39
Ootsubo, T., Kawakita, H., Hamada, S., et al. 2012, ApJ, 752, 15
Ormel, C. W., Ida, S., & Tanaka, H. 2012, ApJ, 758, 80
Ormel, C. W., & Klahr, H. H. 2010, A&A, 520, A43
Oudmaijer, R. D., van der Veen, W. E. C. J., Waters, L. B. F. M., et al. 1992, A&AS, 96, 625
Pan, M., Nesvold, E. R., & Kuchner, M. J. 2016, ApJ, 832, 81
Panić, O., Holland, W. S., Wyatt, M. C., et al. 2013, MNRAS, 435, 1037
Pantin, E., & Starck, J.-L. 1996, A&AS, 118, 575
Patel, B. H., Percivalle, C., Ritson, D. J., D., D., & Sutherland, J. D. 2015, Nat Chem, 7, 301
Pawellek, N., & Krivov, A. V. 2015, MNRAS, 454, 3207

Pawellek, N., Krivov, A. V., Marshall, J. P., et al. 2014, ApJ, 792, 65
Payne, M. J., Ford, E. B., Wyatt, M. C., & Booth, M. 2009, MNRAS, 393, 1219
Pearce, T. D., & Wyatt, M. C. 2014, MNRAS, 443, 2541
—. 2015, MNRAS, 453, 3329
Pecaut, M. J., Mamajek, E. E., & Bubar, E. J. 2012, ApJ, 746, 154
Perrin, M. D., Duchene, G., Millar-Blanchaer, M., et al. 2015, ApJ, 799, 182
Pinilla, P., Benisty, M., & Birnstiel, T. 2012, A&A, 545, A81
Pollack, J. B., Hubickyj, O., Bodenheimer, P., et al. 1996, Icarus, 124, 62
Pu, B., & Wu, Y. 2015, ApJ, 807, 44
Quillen, A. C. 2006, MNRAS, 372, L14
Rafikov, R. R. 2004, AJ, 128, 1348
Rameau, J., Chauvin, G., Lagrange, A.-M., et al. 2013, ApJ, 772, L15
Rappaport, S., Barclay, T., DeVore, J., et al. 2014, ApJ, 784, 40
Rappaport, S., Vanderburg, A., Jacobs, T., et al. 2018, MNRAS, 474, 1453
Raymond, S. N., Armitage, P. J., Moro-Martín, A., et al. 2011, A&A, 530, A62
Raymond, S. N., & Izidoro, A. 2017, Icarus, 297, 134
Raymond, S. N., O'Brien, D. P., Morbidelli, A., & Kaib, N. A. 2009, Icarus, 203, 644
Raymond, S. N., Quinn, T., & Lunine, J. I. 2005, ApJ, 632, 670
Raymond, S. N., Scalo, J., & Meadows, V. S. 2007, ApJ, 669, 606
Read, M. J., & Wyatt, M. C. 2016, MNRAS, 457, 465
Rebollido, I., Eiroa, C., Montesinos, B., et al. 2018, ArXiv e-prints
Reche, R., Beust, H., Augereau, J.-C., & Absil, O. 2008, A&A, 480, 551
Rein, H., & Liu, S.-F. 2012, A&A, 537, A128
Rhee, J. H., Song, I., & Zuckerman, B. 2007, ApJ, 671, 616
Ricci, L., Carpenter, J. M., Fu, B., et al. 2015a, ApJ, 798, 124
Ricci, L., Maddison, S. T., Wilner, D., et al. 2015b, ApJ, 813, 138
Richert, A. J. W., Lyra, W., & Kuchner, M. J. 2018, ApJ, 856, 41
Riviere-Marichalar, P., Barrado, D., Augereau, J.-C., et al. 2012, A&A, 546, L8
Riviere-Marichalar, P., Barrado, D., Montesinos, B., et al. 2014, A&A, 565, A68
Riviere-Marichalar, P., Pinte, C., Barrado, D., et al. 2013, A&A, 555, A67
Roberge, A., Feldman, P. D., Lagrange, A. M., et al. 2000, ApJ, 538, 904
Roberge, A., Feldman, P. D., Weinberger, A. J., Deleuil, M., & Bouret, J.-C. 2006, Nature, 441, 724
Roberge, A., Kamp, I., Montesinos, B., et al. 2013, ApJ, 771, 69
Roberge, A., Welsh, B. Y., Kamp, I., Weinberger, A. J., & Grady, C. A. 2014, ApJ, 796, L11
Rodigas, T. J., Debes, J. H., Hinz, P. M., et al. 2014, ApJ, 783, 21
Rollins, R. P., & Rawlings, J. M. C. 2012, MNRAS, 427, 2328
Rotelli, L., Trigo-Rodríguez, J. M., Moyano-Cambero, C. E., et al. 2016, 6, 38888

Ryan, E. V., Hartmann, W. K., & Davis, D. R. 1991, Icarus, 94, 283
Schneider, G., Grady, C. A., Hines, D. C., et al. 2014, AJ, 148, 59
Schneider, G., Silverstone, M. D., Hines, D. C., et al. 2006, ApJ, 650, 414
Schüppler, C., Krivov, A. V., Löhne, T., et al. 2016, MNRAS, 461, 2146
Schwarz, G. 1978, The annals of statistics, 6, 461
Scicluna, P., Rosotti, G., Dale, J. E., & Testi, L. 2014, A&A, 566, L3
Shakura, N. I., & Sunyaev, R. A. 1973, A&A, 24, 337
Shannon, A., Bonsor, A., Kral, Q., & Matthews, E. 2016, MNRAS, 462, L116
Shannon, A., Clarke, C., & Wyatt, M. 2014, MNRAS, 442, 142
Shannon, A., & Wu, Y. 2011, ApJ, 739, 36
Silverstone, M. D. 2000, PhD thesis, UNIVERSITY OF CALIFORNIA, LOS ANGELES
Simon, J. B., Armitage, P. J., Li, R., & Youdin, A. N. 2016, ApJ, 822, 55
Simpson, J. M., Smail, I., Swinbank, A. M., et al. 2015, ApJ, 799, 81
Slettebak, A. 1975, ApJ, 197, 137
Slettebak, A., & Carpenter, K. G. 1983, ApJS, 53, 869
Smith, A. W., & Lissauer, J. J. 2009, Icarus, 201, 381
Smith, B. A., & Terrile, R. J. 1984, Science, 226, 1421
Smith, R., Wyatt, M. C., & Haniff, C. A. 2009, A&A, 503, 265
Sousa, S. G., Santos, N. C., Mayor, M., et al. 2008, A&A, 487, 373
Stark, C. C., Schneider, G., Weinberger, A. J., et al. 2014, ApJ, 789, 58
Stencel, R. E., & Backman, D. E. 1991, ApJS, 75, 905
Stewart, S. T., & Leinhardt, Z. M. 2009, ApJ, 691, L133
Strubbe, L. E., & Chiang, E. I. 2006, ApJ, 648, 652
Su, K. Y. L., MacGregor, M. A., Booth, M., et al. 2017, AJ, 154, 225
Su, K. Y. L., Rieke, G. H., Malhotra, R., et al. 2013, ApJ, 763, 118
Su, K. Y. L., Rieke, G. H., Stansberry, J. A., et al. 2006, ApJ, 653, 675
Su, K. Y. L., Rieke, G. H., Stapelfeldt, K. R., et al. 2009, ApJ, 705, 314
Sylvester, R. J., Skinner, C. J., Barlow, M. J., & Mannings, V. 1996, MNRAS, 279, 915
Tanaka, H., Takeuchi, T., & Ward, W. R. 2002, ApJ, 565, 1257
Tazzari, M., Testi, L., Ercolano, B., et al. 2016, A&A, 588, A53
Terquem, C., & Papaloizou, J. C. B. 2007, ApJ, 654, 1110
Thébault, P., & Augereau, J.-C. 2007, A&A, 472, 169
Thébault, P., & Wu, Y. 2008, A&A, 481, 713
Thilliez, E., & Maddison, S. T. 2016, MNRAS, 457, 1690
Thureau, N. D., Greaves, J. S., Matthews, B. C., et al. 2014, MNRAS, 445, 2558
Tisserand, F. 1896, Traité de mécanique céleste, Traité de mécanique céleste No. v. 4 (Gauthier-Villars)
Toomre, A. 1964, ApJ, 139, 1217

Torres, C. A. O., Quast, G. R., da Silva, L., et al. 2006, A&A, 460, 695

Torres, C. A. O., Quast, G. R., Melo, C. H. F., & Sterzik, M. F. 2008, Young Nearby Loose Associations, ed. B. Reipurth, 757

Tremaine, S. 1993, in Astronomical Society of the Pacific Conference Series, Vol. 36, Planets Around Pulsars, ed. J. A. Phillips, S. E. Thorsett, & S. R. Kulkarni, 335–344

Tsiganis, K., Gomes, R., Morbidelli, A., & Levison, H. F. 2005, Nature, 435, 459

van Boekel, R., Min, M., Leinert, C., et al. 2004, Nature, 432, 479

van Leeuwen, F. 2007, A&A, 474, 653

van Lieshout, R., Dominik, C., Kama, M., & Min, M. 2014, A&A, 571, A51

Veras, D., & Evans, N. W. 2013, MNRAS, 430, 403

Verhoeff, a. P., Min, M., Pantin, E., et al. 2011, Astronomy & Astrophysics, 528, A91

Vican, L. 2012, AJ, 143, 135

Visser, R., van Dishoeck, E. F., & Black, J. H. 2009, A&A, 503, 323

Vogt, S. S., Wittenmyer, R. A., Butler, R. P., et al. 2010, ApJ, 708, 1366

Warmuth, A., & Mann, G. 2013, A&A, 552, A86

Weidenschilling, S. J. 1977a, MNRAS, 180, 57

—. 1977b, Ap&SS, 51, 153

Weiss, L. M., Marcy, G. W., Petigura, E. A., et al. 2018, AJ, 155, 48

Welsh, B. Y., Craig, N., Crawford, I. A., & Price, R. J. 1998, A&A, 338, 674

Wetherill, G. W., & Stewart, G. R. 1993, Icarus, 106, 190

Whipple, F. L. 1973, NASA Special Publication, 319, 355

Williams, J. P., & Cieza, L. A. 2011, ARA&A, 49, 67

Williams, J. P., Najita, J., Liu, M. C., et al. 2004, ApJ, 604, 414

Winn, J. N., & Fabrycky, D. C. 2015, ARA&A, 53, 409

Wisdom, J. 1980, AJ, 85, 1122

Wittenmyer, R. A., Horner, J., Tinney, C. G., et al. 2014, ApJ, 783, 103

Wright, N. J., Drake, J. J., Mamajek, E. E., & Henry, G. W. 2011, ApJ, 743, 48

Wyatt, M. C. 2003, ApJ, 598, 1321

—. 2005, A&A, 440, 937

—. 2006, ApJ, 639, 1153

—. 2008, ARA&A, 46, 339

Wyatt, M. C., Bonsor, A., Jackson, A. P., Marino, S., & Shannon, A. 2017, MNRAS, 464, 3385

Wyatt, M. C., Booth, M., Payne, M. J., & Churcher, L. J. 2010, MNRAS, 402, 657

Wyatt, M. C., Clarke, C. J., & Booth, M. 2011, Celestial Mechanics and Dynamical Astronomy, 111, 1

Wyatt, M. C., & Dent, W. R. F. 2002, MNRAS, 334, 589

Wyatt, M. C., Dermott, S. F., Telesco, C. M., et al. 1999, ApJ, 527, 918

Wyatt, M. C., Farihi, J., Pringle, J. E., & Bonsor, A. 2014, MNRAS, 439, 3371

Wyatt, M. C., Greaves, J. S., Dent, W. R. F., & Coulson, I. M. 2005, ApJ, 620, 492
Wyatt, M. C., Kennedy, G., Sibthorpe, B., et al. 2012, MNRAS, 424, 1206
Wyatt, M. C., Panić, O., Kennedy, G. M., & Matrà, L. 2015, Ap&SS, 357, 103
Wyatt, M. C., Smith, R., Greaves, J. S., et al. 2007a, ApJ, 658, 569
Wyatt, M. C., Smith, R., Su, K. Y. L., et al. 2007b, ApJ, 663, 365
Yang, C.-C., Johansen, A., & Carrera, D. 2017, A&A, 606, A80
Yelverton, B., et al. submitted
Youdin, A. N., & Goodman, J. 2005, ApJ, 620, 459
Zheng, X., Lin, D. N. C., Kouwenhoven, M. B. N., Mao, S., & Zhang, X. 2017, ApJ, 849, 98
Zsom, A., Ormel, C. W., Güttler, C., Blum, J., & Dullemond, C. P. 2010, A&A, 513, A57
Zuckerman, B., Forveille, T., & Kastner, J. H. 1995, Nature, 373, 494